School of Applied Chemistry

Silica Precipitation From Electrolytic Zinc Solutions

Ross Malcolm Gordon Cooper

"This thesis is presented as part of the requirements for
the award of the Degree of Doctor of Philosophy
of the
Curtin University of Technology"

December 1998

Acknowledgments

I wish to thank Professor Gordon Parkinson and Dr Mike Newman for their guidance and instruction throughout the course of this project.

Thanks also go to: Dave Walton for his time and effort in the workshop, Bill van Bronswijk for his advice on electrical circuitry, Eric Roche and Paul Freeman for their technical input and my fellow research students for their support.

I gratefully acknowledge the support of Curtin University of Technology - School of Applied Chemistry, Pasminco Group Technical Support, the A.J. Parker Cooperative Research Centre for Hydrometallurgy, the Australian Research Council and the Department of Employment, Education, Training and Youth Affairs.

To my best friend Nyree, who only knows me as a student. My greatest thanks goes to you. You are the one, who forced me to stop and rest when I was exhausted. You are the one, who encouraged me when I was disillusioned. You are the one, who slept alone at night while I toiled in the laboratory. You are the one who supported me through all this, thank you my love. You really are the one. May our lives now be much richer.

19 Down: "It sounds foolish to study this element" (6 letters)

"The Times" crossword puzzle n°. 13321.

Abstract

Silica is detrimental to the recovery of zinc from zinc bearing siliceous materials. The difficulties involved in the hydrometallurgical processing of silica are well documented, the major problem being the formation of gels. These are extremely difficult to separate from solution, creating serious problems. This work investigates the mechanism of the formation of granular silica precipitates and how this differs from the mechanism of formation of the gels.

Batch precipitation studies of silica from sulfuric acid solutions have revealed valuable information about the processes occurring. A solution of monosilicic acid ($Si(OH)_4$) was produced by leaching synthetic zinc orthosilicate (Zn_2SiO_4) in sulfuric acid. Precipitation was monitored by measuring the turbidity and silica concentration in solution at regular intervals. Electron microscopy was used to examine the precipitate morphology. Variables known to influence silica precipitation are supersaturation, temperature, seeding and the concentrations of sulfuric and hydrofluoric acids and zinc, iron (III) and aluminium sulfates. These were investigated by comparing their effects on precipitation with those of a control experiment. The evaluation criteria used were induction time, precipitation rate, precipitation time, product morphology and filterability. The results of this work define conditions that yield a granular silica precipitate in preference to a gel, low supersaturation being the most important condition. The product morphology is insensitive to precipitation rate over the range of conditions studied.

A laboratory scale continuous crystalliser was designed and constructed and used to carry out a series of experiments to determine the operating conditions for suitable processing of natural zinc orthosilicate ore to remove the silica impurity in an easily separable form. The variables examined were supersaturation as well as mixing and product removal conditions. The relationship between supersaturation and morphology discovered during the batch experiments was confirmed to also occur when employing a continuous basis. This finding has not been previously reported in the literature. The use of classified stirring and classified product removal led to the formation of the highest quality silica product with a reasonable residence time. The most important quality criterion being the filtration rate.

Insight into the mechanism of silica precipitation has been gained by analysing information from both batch and continuous experiments. Under the strongly acidic conditions studied, colloidal silica particles are initially formed. At low supersaturation ($S \leq 2.9$) the colloidal particles aggregate and cement together to form solid particles, while at higher supersaturation ($S \geq 4.3$) the colloidal particles aggregate to form a gel.

TABLE OF CONTENTS

1.0 INTRODUCTION

1.1 ZINC PRODUCTION

This section briefly outlines the production of zinc using hydrometallurgical processing and introduces Pasminco Limited, the industrial collaborator of this project.

Pasminco Limited is an Australian company formed in 1988 by the merger of CRA and North Broken Hill's lead and zinc operations, and is one of the world's largest vertically integrated base metal companies (Financial Times, 1997; McCristal, Manning and Sanderson, 1998). World production of zinc is approximately 7 000 000 tonnes per annum, of which Pasminco produces approximately 500 000 tonnes (Fitzgerald, 1997).

Greenwood and Earnshaw (1989) give a simplified view of the isolation of zinc, over 90% of which is extracted from sulfide ores. Sedimentation or flotation techniques are used to produce a concentrate from the run-of-mine ore (Pryor, 1965). An analysis of a typical zinc concentrate is shown in Table 1.1. This concentrate can be treated by either pyrometallurgical or hydrometallurgical techniques to recover the metallic zinc. The main smelting technique is the Imperial Smelting Process which uses a blast furnace to produce almost 99% pure zinc that is further vacuum distilled to 99.99% purity (Greenwood and Earnshaw, 1989). The Imperial Smelting Process overcomes the difficulty of zinc boiling below the carbon reduction temperature of zinc oxide, by using a lead splash condenser (Gordon, 1985) to minimise re-oxidation of zinc vapour leaving the furnace. Pasminco operates the Imperial Smelting Process at its Newcastle plant in New South Wales (Financial Times, 1997; Firkin, 1980; Staff of Pasminco Metals, 1993). Hydrometallurgical treatment of zinc concentrate is by the Electrolytic Process which has become the most popular method for the recovery of zinc (Gordon, 1985). Over 80 percent of world production is by this method (Dutrizac, 1990). Figure 1.1 shows a flow diagram of the process.

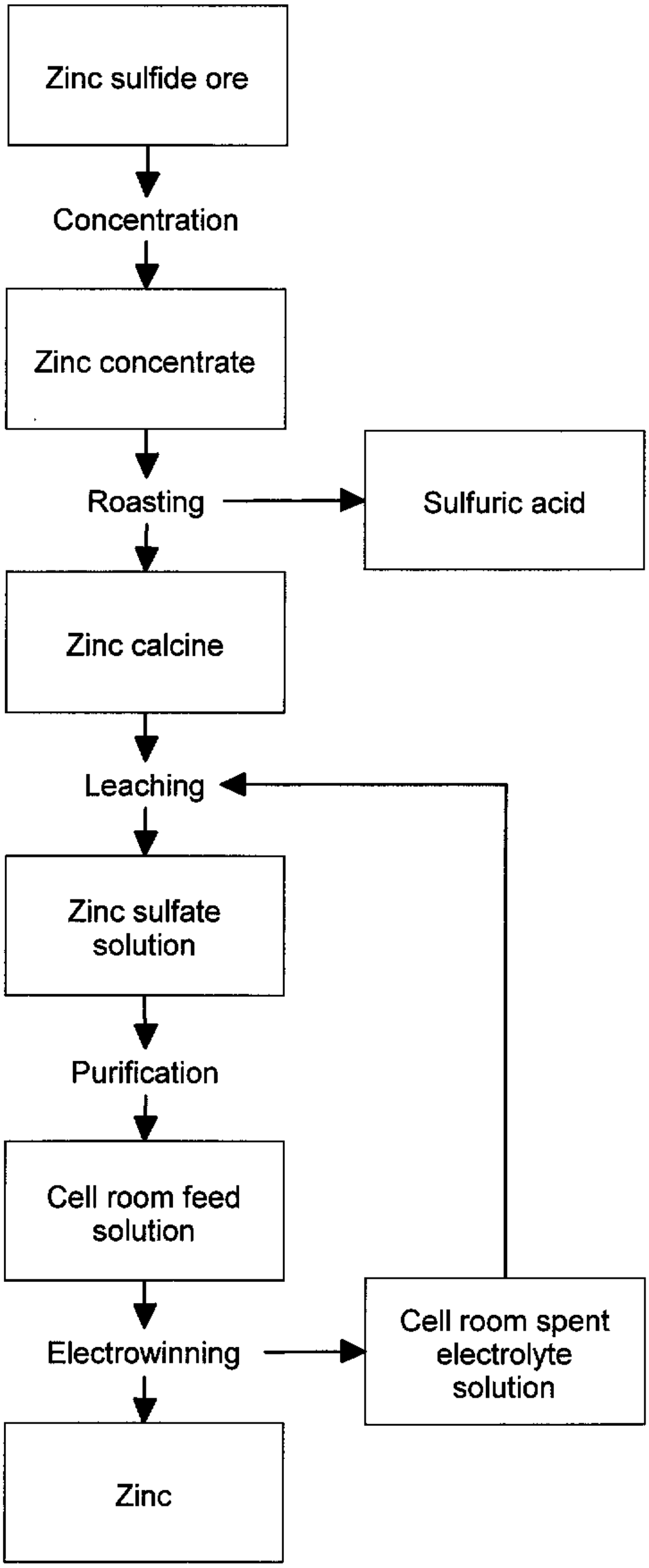

Figure 1.1: Flow diagram of the Electrolytic Process for the hydrometallurgical production of zinc (supplied by Pasminco).

The zinc concentrate is roasted to produce a calcine containing predominantly zinc oxide with smaller amounts of zinc ferrite, zinc sulfate and lead sulfate (Kershaw, 1995; Weimer, Wever and Lapee, 1959). A typical zinc calcine analysis is shown in Table 1.1. A by-product of roasting is sulfur dioxide gas which is used to make sulfuric acid. The calcine is then leached with Cell room spent electrolyte, containing sulfuric acid, to produce a zinc sulfate solution which is purified by precipitation and zinc cementation processes. The pure zinc sulfate solution, referred to as Cell room feed solution, is then electrolysed using lead anodes and aluminium cathodes to produce zinc of 99.995% purity. The electrowinning process regenerates the sulfuric acid in the Cell room spent electrolyte solution which is recycled to leach further calcine (Weimer, Wever and Lapee, 1959). Pasminco operates two plants using the Electrolytic Process, at Risdon in Tasmania and Budel in the Netherlands (Financial Times, 1997; Gilmour, 1993).

Table 1.1: Percentage composition and speciation of typical zinc concentrate and zinc calcine materials (supplied by Pasminco).

Analyte	Zinc concentrate (% w/w)	Zinc Calcine (% w/w)
Zn	51.50	55.11
S	31.92	0.25
Fe	9.18	10.37
Pb	2.58	2.66
SiO_2	1.55	1.72
Speciation	**Zinc concentrate (% w/w)**	**Zinc Calcine (% w/w)**
ZnS	77.34	0.79
ZnO	0.00	59.12
$ZnFe_2O_4$	0.00	22.82
FeS	14.92	0.00
$ZnSO_4.7H_2O$	0.03	8.37
PbS	2.97	4.04
SiO_2	1.55	1.72

Weimer, Wever and Lapee (1959) detail impurities in the calcine that are released during leaching and become problematic to electrolysis and zinc recovery. The recycling of Cell room spent electrolyte solution compounds this impurity problem. Such impurities are arsenic, antimony, copper, iron, cadmium, cobalt, nickel, tin, germanium, selenium, tellurium, silica, alumina and others. Many of these impurities can be removed by an iron precipitation stage with the residue separated by filtration.

Traditionally, the iron precipitation step was effected by raising the pH of the filtered leach liquor with zinc calcine from 1.7 to approximately 5.1 in conjunction with air sparging to precipitate all the iron as iron (III) hydroxide. Aluminium and part of the tin are also removed during this step as hydroxides. Copper is removed as a copper-zinc sulfate while arsenic, antimony and germanium are removed by ion exchange on the precipitated iron hydroxide (Bratt and Gordon, 1967).

Elimination of other impurities is achieved if the amount of iron present is in excess of ten times the amount of impurities to be removed. Iron (III) sulfate or other forms of iron maybe added if there is insufficient iron present in the calcine (Weimer, Wever and Lapee, 1959). Iron is the biggest impurity present in calcine, typically assaying at *ca* 10% (Allen, Haigh and Hamdorf, 1970; Kershaw, 1995). This is also shown in Table 1.1.

Filtration and washing difficulties associated with the iron (III) hydroxide residue (Gordon, 1985) and the need for improvements in zinc extraction from concentrates (Bryson, 1986; McCristal, Manning and Sanderson, 1998) forced further research to develop better methods for iron removal. Examples of these are the goethite, or paragoethite process, the haematite process and, most importantly at the time, the jarosite process (Gordon, 1985). Dutrizac (1990) notes that the jarosite process is the most widely used of the three iron removal methods because of its simplicity and low cost of operation.

The jarosite process was developed jointly by Asturiana de Zinc in Spain, Norzinc in Norway and the Electrolytic Zinc Company of Australasia (now part of Pasminco Limited) to remove iron as ammonium jarosite ($(NH_4)Fe_3(SO_4)_2(OH)_6$) (Gordon, 1985). Pasminco's Hobart smelter has produced jarosite since 1971 (Pammenter, 1993), which was land dumped until 1973 (McCristal, Manning and Sanderson, 1998). Following this, ocean dumping was introduced as a means of jarosite disposal under a special permit from the Australian Commonwealth Government (Pammenter, Gilmour and Salmon, 1993). Most of the world's jarosite production, however, is stored in ponds (Dutrizac, 1990; Elgersma, Witkamp and van Rosmalen, 1993).

Jarosite is precipitated in an easily filterable form (Dutrizac and Kaiman, 1976) from zinc leach liquor high in iron at a pH of 1.5 at 90°C by the addition of ammonium sulfate (Davey and Scott, 1976; Dutrizac and Jambor, 1985; Hutchison and Phipps, 1977). As well as removing the unwanted iron, jarosite also effectively removes the metallic impurities: arsenic, gallium, indium, lead, silver, cadmium, copper and cobalt from the leaching circuits to prevent their accumulation (Elgersma, Witkamp and van Rosmalen, 1993). This occurs with very low zinc incorporation in the jarosite, typically between 0.2 and 1.0%.

As a result of increasing environmental pressure, expiring dumping concessions and danger of heavy metals reporting to ground water from damaged ponds, pressure has been applied to the zinc industry to modify current hydrometallurgical practice and stop jarosite production and storage (Dutrizac, 1990; Elgersma, Witkamp and van Rosmalen, 1993; Reuter, Sudholter, Kruger and Koller, 1995). Pasminco, specifically, was forced to change its operation due to the expiration of its jarosite ocean disposal permit at the end of 1997 (It's over: Pasminco ends ocean dumping, 1997) even though, according to McCristal, Manning and Sanderson (1998), independent research could find no adverse effects from ocean disposal. Pasminco's permit to produce jarosite at its Budel smelter in the Netherlands also expired at the end of 1997 and an extension was granted to store jarosite until June 30, 2000 (Ball, 1998; Bell, 1997a).

The conversion of Pasminco's Hobart smelter from the jarosite process to the paragoethite process as the iron removal step in 1997 has alleviated this problem in Australia (McCristal, Manning and Sanderson, 1998).

The goethite, or paragoethite process was developed by the Electrolytic Zinc Company of Australasia and is outlined in a patent by Allen, Haigh and Hamdorf, (1970). The process involves adding the pregnant iron (III) solution to a reactor vessel containing zinc plant liquor at such a rate so as to match the iron (III) removal rate through precipitation of goethite. The iron (III) concentration in the reactor vessel should never exceed 1.0 g L^{-1}. The preferred operating temperature range is from 65 to 95°C, and the pH should be maintained in the range 2.0 to 3.0 by addition of a neutralising agent such as zinc calcine. Significant amounts of arsenic, antimony, germanium and fluorine are removed from the zinc plant liquor with the goethite. Davey and Scott (1975) detail production of the same precipitate by initially reducing the solution to form iron (II) and then oxidising at a controlled rate so as to not exceed 1.0 g L^{-1} iron (III). The precipitation products of the goethite process are crystalline α-goethite and on some occasions wholly or partly, very poorly crystalline β-goethite (Davey and Scott, 1975; Davey and Scott, 1976). The paragoethite precipitate formed at Hobart is typically amorphous and is further treated at Pasminco's Port Pirie plant to recover any entrained zinc and lead and produce a significantly more inert slag (McCristal, Manning and Sanderson, 1998). Johnson and Tyson (1993) describe the Port Pirie operation as a slag fuming plant which treats lead blast furnace slag, and now also paragoethite residue from Hobart, to produce zinc oxide fume. An electrolytic zinc plant is used to convert the fume to metallic zinc.

Read (1995) reports that the Budel smelter would have been forced to close because of the expiring jarosite storage permit, but now has a secure future due to Pasminco's purchase of the Century zinc project in August 1997 (Ball, 1998; Bell, 1997b). The Century orebody is, in world terms, a very large zinc sulfide deposit that is unique in that it contains very little iron (Irving, 1998; Waltho and Andrews, 1993) and would eliminate the need for jarosite production at Budel (Ball, 1998). Irving (1998) notes that the total resource is approximately 98.5 million tonnes assaying at 10.2% zinc. The Century mine is set to start producing zinc concentrate in late 1999 or early 2000 and half of the concentrate produced will be exported to the Budel plant (Bell, 1997a; Fitzgerald, 1997; Irving, 1998).

The Century zinc deposit has another unique, but this time undesirable feature, the presence of an unusually high concentration of silica associated with the sulfide mineralisation (Hamilton and Woodcock, 1993; Read, 1995; Waltho, Allnutt and Radojkovic, 1993). Main (1993) and Read (1995) mention the possibility of penalties from zinc smelters for the high silica content of Century concentrate, detracting from its otherwise high purity. The most likely method for overcoming the silica problem is by ultra-fine grinding of the ore to liberate the zinc sulfide and separate it from the silica during flotation to produce a low-silica concentrate. However, no concrete knowledge appears in the literature that could be used to completely overcome the silica problem at the Century mine.

Pasminco owns the Beltana mine in South Australia which also contributes to the company's silica problems. Carmichael (1993) describes the mine's zinc bearing mineral as zinc silicate instead of the more commonly treated zinc sulfide mineral. 380 000 tonnes of ore have already been mined, with the deposit now containing approximately 180 000 tonnes of ore; assaying 38% zinc. The ore mined to date has been sold to overseas smelters with a small amount having been treated at Pasminco's Hobart smelter (Rangott, 1980). Elliot (1991) mentions the difficulty in treating zinc silicate ore by conventional zinc smelting techniques. This, combined with the lack of a method for ore concentration at the mine site has caused the project to be shelved even though a new zinc silicate ore treatment method was developed by the Electrolytic Zinc Company of Australasia. This method is described in Section 1.2.

The above problems, combined with a lack of detailed knowledge in the suitable processing of zinc silicate ore to recover the zinc, prompted Pasminco to investigate the problem further. The diminishing world reserves of good zinc sulfide ores (Frenay, 1985) and the discovery of large deposits of zinc silicate ores (Abbruzzese, 1981) have no doubt contributed to Pasminco's decision. The global reserve of zinc sulfide ores is expected to last for several decades, but for future demand, zinc silicate ores are a significant alternative (Bodas, 1996).

1.2 SILICA IN ZINC HYDROMETALLURGY

The problems created by soluble silica in zinc hydrometallurgy are well documented in the literature. Abbruzzese (1981); Ashman, Delong and Jankola (1993); Betterton (1923); Bodas (1996); Dufresne (1976); Hutchison (1958); Matthew and Elsner (1977a; 1977b); Pus'ko, Ushakov and Khan (1979); Wood, Kern and Ashdown (1977) describe the formation of silica gels and the subsequent problems with poor settling, filtering and washing of these pulps when conventional zinc hydrometallurgy is applied to materials containing large amounts of soluble silica. This section details the current processes available to overcome these problems.

In the hydrometallurgical recovery of zinc, the source of soluble silica is the naturally occurring oxidised zinc ores; zinc orthosilicate (Zn_2SiO_4, mineral name willemite) and zinc pyrosilicate ($Zn_4Si_2O_7(OH)_2.H_2O$, mineral name hemimorphite) (Dufresne, 1976). Zinc concentrates containing quartz and other siliceous gangue material produce zinc orthosilicate upon roasting to form calcines (Ashman, Delong and Jankola, 1993; Pus'ko, Ushakov and Khan, 1979). Amorphous soluble silica is also present in other industrial residues that are treated to recover the zinc, such as slags (Fugleberg and Poijarvi, 1977 and 1979). Both zinc orthosilicate and pyrosilicate readily dissolve congruently in sulfuric acid (Terry, 1983a) to liberate monosilicic acid and disilicic acid, respectively (Matthew and Elsner, 1977a). Zinc orthosilicate dissolution is described by Margulis (1983) and many others as occurring by the following reaction:

$$Zn_2SiO_{4\,(s)} + 2H_2SO_{4\,(aq)} \rightarrow 2ZnSO_{4\,(aq)} + Si(OH)_{4\,(aq)}$$

Thus, zinc pyrosilicate dissolution would occur by the reaction:

$$Zn_4Si_2O_7(OH)_2.H_2O_{\,(s)} + 4H_2SO_{4\,(aq)} \rightarrow$$
$$4ZnSO_{4\,(aq)} + O(Si(OH)_3)_{2\,(aq)} + 3H_2O_{\,(aq)}$$

Monosilicic acid polymerises via a condensation type reaction between silanol groups (Si-OH) to form a siloxane bond of the dimer, disilicic acid, according to the reaction (Iler, 1979):

$$2Si(OH)_{4\ (aq)} \rightarrow O(Si(OH)_3)_{2\ (aq)} + H_2O_{\ (aq)}$$

Iler (1979) describes further polymerisation occurring between silanol groups of larger species to increase molecular weight.

Depending on conditions such as the pH, temperature, silica concentration, impurities, presence of seed, holding time and ionic strength, Matthew and Elsner (1977a; 1977b) describe the colloidal silica particles to be either stable or unstable. Stable particles may aggregate to form a fine precipitate. Alternatively, unstable colloidal silica particles may aggregate to form an open network structure or gel. It is the formation of silica gel that is responsible for the processing problems described previously. Accordingly, the electrolytic zinc industry has expended considerable effort in solving this problem. Several processes have been developed by various companies, manipulating the above variables to successfully treat feed stocks containing soluble silica. The most important of these will be discussed in turn. Note that processes that avoid dissolution of the silica or silicate material to liberate the zinc will not be discussed as they are not relevant to this study. Also not discussed here are processes that dehydrate the precipitated silica to render it filterable by using concentrations of sulfuric acid that are higher than those typically found in zinc plant Cell room spent electrolyte solutions, usually no higher than 200 g L^{-1}. Examples of such processes are the Reverse Leach process described by Zaitsev and Margulis (1985) and the Quick Leach process developed by Dufresne (1976).

One process to treat zinc silicate ores and lead furnace slags is the Vieille-Montagne process (Bodson, 1974). The process involves the suspension of the siliceous zinc material in water or zinc sulfate solution, stirring and heating to between 70 and 90°C. Over a period of three to ten hours with continual stirring and heating, Cell room spent electrolyte is slowly added until the final sulfuric acid concentration is in the range 1.5 to 15 g L^{-1}. An additional two to four hours of stirring and heating is specified. Bodson (1974) explains that the long acid addition stage is necessary to achieve complete ore dissolution, while complete silica precipitation is effected during the additional stirring and heating stage. To recover the zinc electrolytically, it is necessary to neutralise the solution pH. This can be done either prior to filtration to remove other impurities that will precipitate during neutralisation, such as iron, or after filtration. Neutralisation is achieved by progressively adding the entire slurry over the course of one to three hours to an aqueous suspension of lime, zinc oxide or calcine at 80°C maintaining the pH in the range 3 to 5. To precipitate the iron during neutralisation, finely dispersed air must be pumped through the solution. Filtration rates for the resulting silica precipitates, including iron precipitates on occasions, of up to 745 kg h^{-1} m^{-2} using a vacuum of 450 mm of mercury were achieved. In this instance the filter cake thickness was 35 mm and the pulp density was 557 g L^{-1}. This corresponds to a filtration rate of 1.34 m^3 m^{-2} h^{-1} for the filtrate.

Another process for treating zinc silicate ores is the Radino process (Radino, 1957). The process involves a semicontinuous leach of the ore with simultaneous precipitation of silica in the same vessel. Aluminium ions are used as a coagulant for the silica, being added at the rate of 1 to 50% by weight of the soluble silica. Processing begins by introducing Cell room spent electrolyte, containing aluminium sulfate, into a stirred reactor vessel at 90°C. Ground zinc silicate ore is added in slight excess of the acid so the final pH is approximately 4. The slurry is stirred for a further 30 minutes, maintaining 95°C. The Cell room spent electrolyte, always containing aluminium sulfate, and the additions of ore and the 30 minute stirring interval are repeated at least twice more, or until the reactor vessel is full. One third of the vessel contents are then removed, settled and filtered. Addition of Cell room spent electrolyte; always containing aluminium sulfate, the additions of ore, the 30 minute stirring period and the one third emptying process are then repeated continuously. Radino (1957) states that the 30 minute stirring period allows for complete coagulation of the silica. By removing one third of the vessel contents, a large amount of silica remains as seed for the next cycle. The silica precipitate can be classified into two separate types; coarse, hard sand-like grains and jelly-like grains. The jelly-like grains being produced in a single coagulation cycle and the sand-like grains being the product of multiple cycles. As a result, the sand-like grains are easy to filter. These different grains can be separated by settling in a thickener, with the sand-like grains settling rapidly and the jelly-like grains remaining essentially unsettled. By returning the jelly-like grains to the reactor vessel where they undergo further acidification and coagulation cycles, the sizes of subsequent filter cakes were reduced. A filtration test was performed and a rate of 1.53 $m^3\ m^{-2}\ h^{-1}$ for the filtrate was achieved. Matthew and Elsner (1977b) found the Radino process unsuitable for some types of zinc silicate ores. Other ores could be successfully treated without aluminium sulfate, providing the ionic strength was high enough.

Matthew and Elsner (1977a) of the Electrolytic Zinc Company of Australasia developed a continuous process for the treatment of zinc silicate ores and siliceous calcines. Feed stock is leached at 40 to 50°C with Cell room spent electrolyte in a series of three tanks, with the final tank having a pH in the range 1.8 to 2.0. Leaching time is in the range of one to three hours, mainly depending on the composition of the feed material. The low leaching temperature ensures that the silica remains in solution until the coagulation stage, as silica precipitation rate increases with temperature. Concentrations of up to 28 $g\ L^{-1}$ colloidal silica have been recorded. Silica coagulation takes place in three vessels, in series, with the pH raised to 4.0 to 5.5 via addition of a neutralising agent and a temperature of 50 to 65°C. Holding time is approximately three hours. The silica residue is then separated by filtration. During test work, filtration rates of 0.5 to 1.0 $m^3\ m^{-2}\ h^{-1}$ were achieved.

Fugleberg and Poijarvi (1977 and 1979) of the Outokumpu Oy company expressed concerns that other industrial processes for handling soluble silica had gelling problems if they were forced to shut down unexpectedly. This is especially problematic if the pH is in the range 1.0 to 3.5, and soluble silica concentrations are high, *ie.* 5 to 60 $g\ L^{-1}$ as SiO_2. The loss of zinc when neutralising silica bearing solutions with calcine was also of concern. As a result of these concerns, Fugleberg and Poijarvi (1977 and 1979) developed a process for treating soluble silicate bearing zinc materials. The process involves continuous operation of a single reactor vessel, stirred at 70°C, where dissolution and precipitation of silica occur simultaneously. Zinc silicate ore and Cell room spent electrolyte are slowly added to the reactor vessel to achieve a residence time of about 20 hours. The addition of Cell room spent electrolyte maintains the pH at less than 2.5 and certainly less than that needed to dissolve the zinc silicate material. The soluble silicate addition rate should be slow enough that its dissolution rate matches the silica precipitation rate and the silica concentration in solution remains fairly low, typically 0.9 to 1.6 g L^{-1} as SiO_2. The silicate bearing material, calculated as SiO_2, should not be added at a rate above 3 g L^{-1} h^{-1}. For the first several hours of operation, the product slurry is easy to filter; in the order of 1.9 m^3 m^{-2} h^{-1}. This is followed by a period where the silica gels and filtration is virtually impossible. After approximately one and a half residence times, filtration performance is constant in the range 0.2 to 0.4 m^3 m^{-2} h^{-1}. Upon addition of an anionic flocculant, followed by settling, the thickened silica precipitate can be filtered at 1.3 m^3 m^{-2} h^{-1}.

Recently, Bodas (1996) studied the extraction of zinc from a predominantly zinc pyrosilicate ore on a laboratory scale using simple batch processing. The ore was completely leached, maximum of 95.0% zinc extraction, in sulfuric acid at a pH of 2.0 and 70°C in three hours. The resultant leach slurry was virtually impossible to filter and very slow to settle, 0.5 cm^3 min^{-1} (units by Bodas). After addition of 40 mL of a 0.05% solution of Magnafloc 156 the slurry could be filtered in 30 seconds and the settling rate had improved to 20 cm^3 min^{-1} (units by Bodas).

The most significant aspect of all these processes is the lack of fundamental understanding of the silica precipitation process. The present study aims to address this issue. The process that is of most interest to Pasminco at present is the one developed at Outokumpu Oy (Fugleberg and Poijarvi, 1977 and 1979). This is because of its simplicity in equipment requirements and operation, and also the safety feature of not producing a silica gel if forced to shut down unexpectedly.

1.3 PRECIPITATION THEORY

A brief introduction to precipitation theory will be given in this section, and the distinction between crystallisation and precipitation will be addressed.

Precipitation is a difficult term to define according to Sohnel and Garside (1992), who liken it to very rapid crystallisation with several important features:

1. Relatively insoluble materials are precipitated as their insolubility creates high supersaturations when the material is produced by reaction precipitation, *ie.* the mixing of solutions of two, more soluble compounds.
2. Primary nucleation rates are usually very high due to the high supersaturations encountered and thus nucleation is a primary factor in precipitation.
3. Large numbers of crystals or particles are produced because of the high nucleation rates. This usually limits the overall particle size obtained.
4. If the particles are sufficiently small, ripening, ageing, agglomeration and coagulation can take place and dramatically alter the product size distribution. Colloidal intermediates maybe important.
5. The supersaturation generated for precipitation is usually the result of a chemical reaction, precipitation is therefore sometimes called reaction crystallisation.
6. Precipitation is usually carried out at constant temperature and does not therefore rely on cooling to produce supersaturation.

Mersmann (1995) defines precipitation as very rapid crystallisation where a large number of crystal nuclei are formed. Often, the process of precipitation can only be controlled to a small extent.

No generally accepted definition of the term precipitation exists, according to Mullin (1988; 1993), although it maybe referred to as very fast crystallisation, and is usually an irreversible process due to the insolubility of the products created. Another feature distinguishing precipitation from crystallisation systems is that they are usually initiated at high supersaturation, resulting in fast nucleation and the subsequent generation of a large number of very small crystals. Precipitation and crystallisation have much in common and share many of the same laws.

Sohnel and Garside (1992) note that precipitation involves many different steps and kinetic processes, as shown in Figure 1.2. However, it can be broken down into three major steps; supersaturation, primary nucleation or the birth of particles, and growth of these particles to adult particles. The time scale for precipitation can range from a few seconds to many days. Supersaturation is the driving force for precipitation, determining the rates of the different processes:

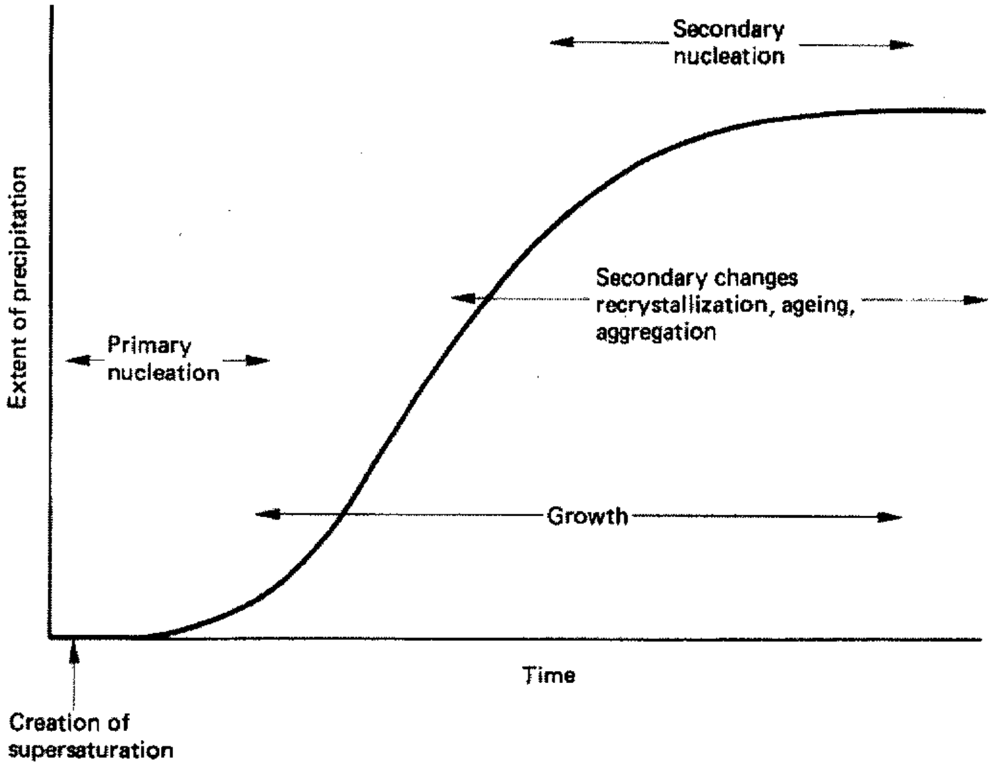

Figure 1.2: Kinetic precipitation processes (Sohnel and Garside, 1992).

Mersmann (1995) defines a supersaturated solution as one in which the solute is present in a concentration higher than equilibrium solubility. A solution that is saturated with solute in thermodynamic equilibrium is said to be at equilibrium solubility, represented as c^*, with respect to that particular solute. Crystallisation can only occur from a supersaturated solution, and the rate of crystallisation is usually dependent on the degree of supersaturation. Supersaturation can be expressed either as a difference in concentration, Δc, with the appropriate units:

$$\Delta c = c - c^*$$

or as a dimensionless supersaturation ratio, S:

$$S = \frac{c}{c^*}$$

or as a relative supersaturation, σ, also dimensionless:

$$\sigma = \frac{\Delta c}{c^*} = S - 1$$

In all cases, c is the concentration of the solute of interest. For this study the supersaturation ratio S will be used, with silica concentration expressed as the concentration of SiO_2. Supersaturation can be created by several methods; changing the temperature of the solution, *ie.* cooling a solution with a positive gradient for the solubility-temperature curve or heating a solution with a negative gradient for the solubility-temperature curve; the solvent can be removed by evaporation or by the addition of a drowning-out agent; by the addition of a salting-out agent, *ie.* a more soluble compound with a common ion; mixing of reaction partners.

This study uses the mixing of reaction partners to create supersaturation, but not in the traditional sense. A typical example of the mixing of reaction partners is in the precipitation of barium sulfate where supersaturation is created by mixing barium hydroxide and sulfuric acid (Mersmann, 1995). Supersaturation in this study is generated by dissolving a silicate ore in sulfuric acid, thus liberating monosilicic acid into solution at concentrations above its equilibrium solubility level.

Crystallisation typically involves supersaturation ratios of $1.01 < S < 2$, while precipitation typically involves $2 < S < 100$ (Mullin, 1993). A differentiation must be appreciated between global (bulk solution) and local supersaturation for precipitation systems, as very high local supersaturations can occur near the reactant inlets (Mersmann, 1995). This can result in very high nucleation rates, in the same order of magnitude, or faster, as mixing rates. This, in turn can lead to competition between mixing, reaction and nucleation. This is not such a problem with the silica system, as the silicate ore which provides silicic acid supersaturation must first dissolve in the liquor. Thus, it is expected that very high local supersaturations will be avoided.

As mentioned above, precipitation or crystallisation can be divided into supersaturation, nucleation and growth (including agglomeration which is typically less important in rapid precipitation than in slow crystallisation) processes. There are several types of nucleation that fit into two broad categories, primary and secondary nucleation (Mersmann, 1995). Primary homogeneous nucleation occurs from very pure, clean solution, free from crystals of its own type and solid foreign particles. This is the classic form of nucleation by successive addition of molecular units to form nuclei. Primary heterogeneous nucleation occurs on the surface of foreign solid particles. Both forms of primary nucleation occur when the metastable supersaturation ratio, S_{met}, is exceeded. Secondary nucleation occurs at lower supersaturations than the metastable supersaturation when solution-type crystals are present, either as added seed or as attrition fragments. According to Sohnel and Garside (1992), secondary nucleation may occur during precipitation by three mechanisms, aside from seeding:

1. Formation of nuclei on the surface of the solid phase, which grow to give structures, such as dendrites, which subsequently break off the crystal.
2. Nuclei formation in the liquid phase by structural changes in the liquid directly adjacent to the crystal surface.
3. Nuclei in the form of molecular aggregates forming in the adsorption layer on the crystal surface which are then washed into solution.

Figure 1.3 schematically shows the relationship between metastable supersaturation and temperature for primary and secondary nucleation (Mersmann, 1995). Clearly, primary homogeneous nucleation requires the highest supersaturation, followed by primary heterogeneous nucleation and then secondary nucleation. Thus, in an operational crystalliser, secondary nucleation is the most likely event to occur, followed by primary heterogeneous and finally primary homogeneous nucleation.

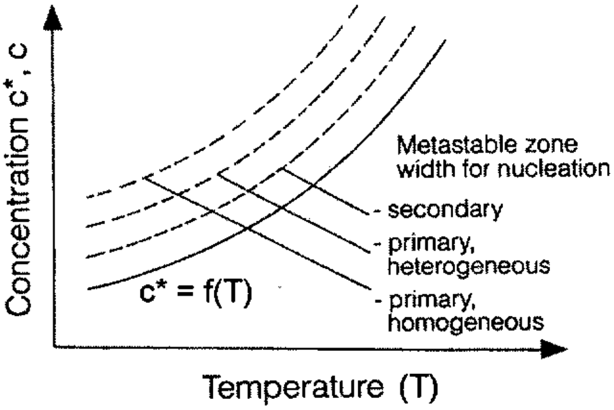

Figure 1.3: Metastable supersaturation versus temperature for different nucleation processes (Mersmann, 1995).

Once a stable nucleus has formed, *ie.* it has reached the critical nucleus size, it is capable of growing in supersaturated solution. Until the critical nucleus size has been reached the nuclei are in dynamic solubility equilibrium with the solution and are thus unstable (Mullin, 1993).

Growth of silica particles has been identified by Iler (1979) as occurring by the Ostwald ripening mechanism. This is not unexpected, due to the very small size of silica particles. Mersmann (1995) states that Ostwald ripening has a major influence on crystals below 1 μm in size and these sizes are very typical of precipitation systems. Ostwald ripening is defined by Mersmann (1995) as follows: The solute concentration is in equilibrium with the largest particles present in the system. Thus, the system is undersaturated with respect to the smallest particles which dissolve. Because of the additional dissolved solute, the system is now supersaturated with respect to the largest particles and hence, they grow. The overall effect is the growth of larger particles at the expense of the smaller ones. Mullin (1993) adds that, theoretically, the particle size distribution should change towards that of a monosized dispersion. The driving force for Ostwald ripening is the difference in solubility between small and large particles and the tendency of the solid phase to adjust itself to achieve a minimum surface free energy (Mullin, 1993).

The growth of crystalline precipitates can occur by several mechanisms. Fleming (1981) notes that silica precipitated under non-hydrothermal conditions is almost invariably amorphous, irrespective of the presence of other forms of solid silica. As a result of this, only growth of amorphous precipitates will be considered.

Mullin (1993), explains amorphous particle growth as a competition between the aggregation and orientation velocities of the molecular growth units, with aggregation dominating in the formation of amorphous particles. Aggregation and orientation are both influenced by supersaturation, temperature and in some instances by the precipitating species. For example, as mentioned previously, silica precipitated under non-hydrothermal conditions is almost invariably amorphous, while crystalline silica, quartz, can be precipitated under hydrothermal conditions (Baughman, 1991; Demazeau and Lafon, 1994). Very little information is available in the literature concerning the growth of amorphous particles from solution.

Agglomeration and ageing also play an important role in the growth of precipitates (Mullin, 1993). Agglomeration occurs soon after nucleation, and generally applies to small particles, *ie.* less than 1 μm in size, where van der Waals forces overcome Brownian motion. Interaction between the electrical double layers of particles would also play an important role (Hunter, 1987). Under these conditions interparticle collisions may result in permanent attachment and the agglomeration of particles. Colloidal silica precipitates are in the correct size range for agglomeration to be an important growth factor. Ageing is used to describe any irreversible process that occurs to a precipitate after it has formed, such as Ostwald ripening or phase transformations. Ostwald ripening has been discussed previously; however, phase transformations can be of equal or greater importance. When a metastable phase is precipitated initially and ages to yield a more stable product, a phase transformation has occurred. Examples of metastable phases undergoing transformations are amorphous precipitates ageing to crystalline products, metastable polymorphs of the final material precipitating first, a hydrated species ageing to a dehydrated species or a system contaminated substance ageing to a less contaminated substance. Ostwald's rule of stages is used to describe phase transformations: An unstable system does not transform itself directly into the most stable state, but into one which most closely resembles its own, associated with the smallest loss in free energy possible.

Precipitation processes can be operated on either a batch or continuous basis (Mullin, 1988). There are distinct advantages and disadvantages to both modes of operation. Batch operation offers simplicity of equipment and the ability to clean the crystalliser between batches, which minimises scale build up and ensures a contamination free product. In some cases only a batch crystalliser can produce the required product, in terms of morphology, particle size distribution (PSD) and purity. Continuous, steady state operation is often regarded as superior in industrial applications, with flexible control of temperature, supersaturation, nucleation, growth and other parameters that influence the PSD of the product. The operating costs of a continuous process maybe significantly less than those of a comparable batch process. A continuous crystalliser does not discharge its product under equilibrium conditions, whereas a batch crystalliser can. Unless a holding tank is used, this can cause problems down stream with further, unwanted, precipitation occurring when the system is trying to reach equilibrium. A holding tank may also be required if a phase transformation takes place. Variations in product quality between batches can be a problem that does not usually exist with continuous precipitation. In some instances, a combination of both batch and continuous precipitation, known as semicontinuous precipitation, can combine the best features of both operating modes.

On a laboratory scale, there are similar advantages and disadvantages for both batch and continuous operation as there are in the industrial case. A commonly operated continuous laboratory scale crystalliser is the mixed suspension mixed product removal (MSMPR) crystalliser. A diagram of a typical, laboratory scale, MSMPR crystalliser used for precipitation studies is shown in Figure 1.4.

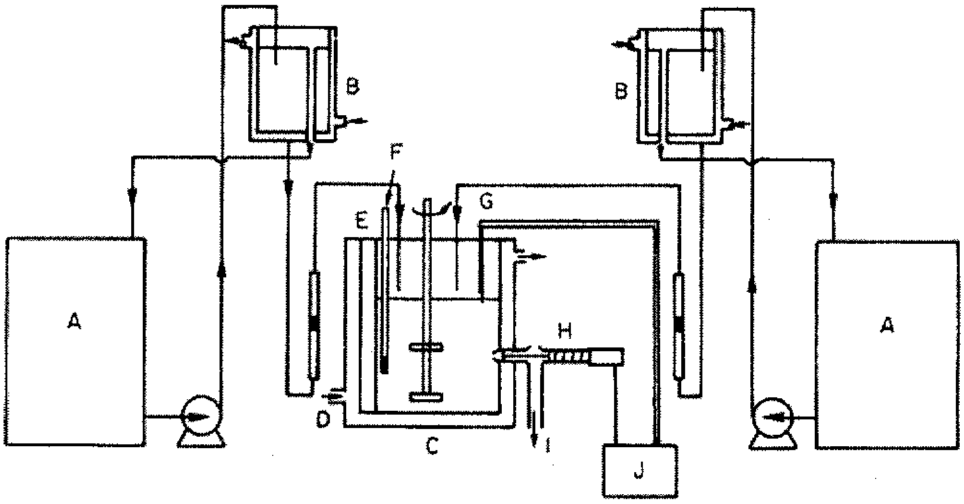

Figure 1.4: A typical laboratory scale MSMPR crystalliser: (A) reagent tank; (B) constant pressure tank; (C) reactor vessel; (D) water jacket inlet; (E) baffle; (F) thermometer; (G) level sensor; (H) discharge valve; (I) product removal; (J) controller (Mullin, 1988).

Randolph and Larson (1988) detail the requirements for MSMPR operation: proper mixing of suspension and mother liquor with minimum power input; product discharge should have the same characteristics as the slurry in the crystalliser (no size classification); the size of the crystalliser should be small enough so that reagent volumes are minimised but large enough to provide adequate samples without disturbing the system. These three main points will be further discussed shortly. Mullin (1988) states the following assumptions in regard to achieving MSMPR behaviour; no crystals present in the reagent streams, all crystals in the reactor are of the same shape, no attrition of crystals occurs, and growth rate is independent of crystal size.

A draft tube placed in the crystalliser is useful for reducing the power input for agitation required to achieve complete suspension; flow is typically down the draft tube and up the annular space (Randolph and Larson, 1988). The use of a crystalliser with a contoured base will also reduce the agitation power required to achieve proper mixing (Nyvlt, 1982a). The use of baffles reduces gross vortexing when agitating low viscosity liquids (Harnby, Edwards and Nienow, 1985). Baffles should be about one tenth the vessel diameter in width. Examples of these features are shown in Figures 1.5 and 1.6.

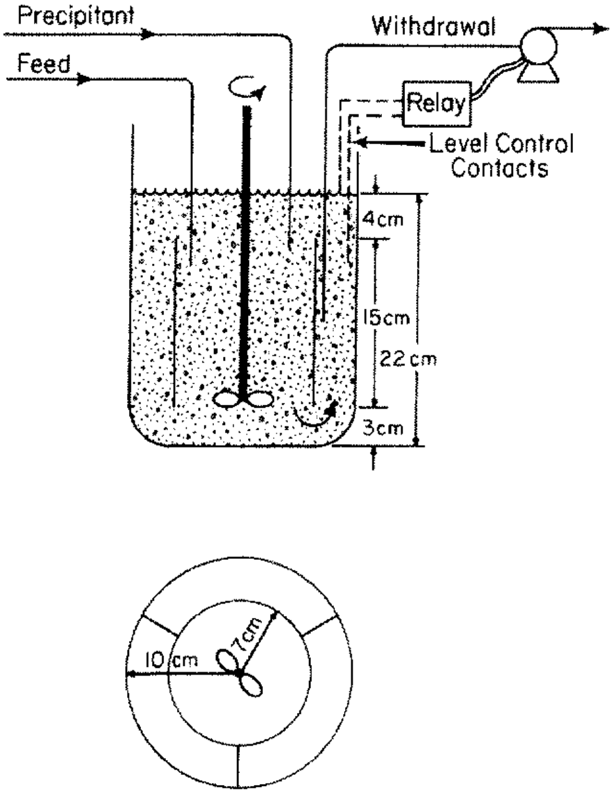

Figure 1.5: Diagram of laboratory scale MSMPR crystalliser vessel fitted with a draft tube, baffles, an electronic level sensing device and a pump for product removal (Randolph and Larson, 1988).

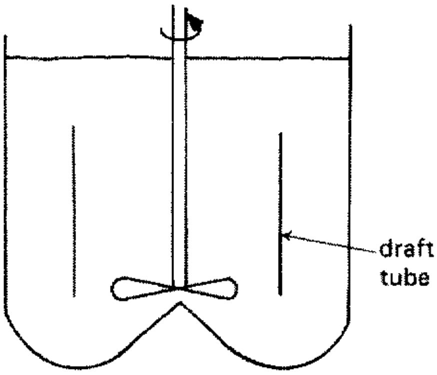

Figure 1.6: Diagram of a laboratory scale crystalliser vessel with a contoured base and fitted with a draft tube (Harnby, Edwards and Nienow, 1985).

An axial flow impeller is ideal for suspending solids and can therefore be used to agitate the magma (McDonough, 1992). Examples of axial flow impellers are the common marine propeller and the hydrofoil or fluidfoil, which produces the lowest shear at the highest flow rate (pumping capacity) of all impellers. A diagram of a Lightnin A-310 Fluidfoil impeller is shown in Figure 1.7. Of note is the decreasing blade width and blade angle from hub to tip, which provide constant shear across the blade.

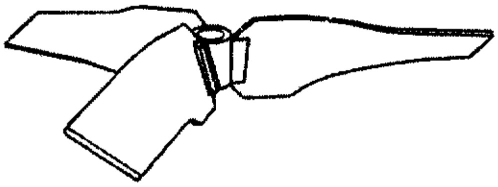

Figure 1.7: Lightnin A-310 Fluidfoil impeller (McDonough, 1992).

To obtain a product sample that is not classified with respect to the bulk magma, the product sample must be removed from the crystalliser isokinetically, *ie.* with the same velocity as the circulating magma at the point of removal (Randolph and Larson, 1988). This can be achieved by placing the product removal tube parallel to the circulation flow, with product removal in the direction of flow in the crystalliser. Due to the small volume of laboratory crystallisers, their subsequent very low through put rates and the need for very high withdrawal velocity to achieve isokinetic conditions, it is necessary to remove product intermittently. An electronic level sensing device and a pump can be used to accomplish this, as is shown in Figure 1.5. No more than 10% of the magma volume should be removed at one time. Nyvlt (1982a) recommends removing only 5% of the magma.

Crystalliser volumes as low as 250 mL right up to production size have been successfully used, according to Randolph and Larson (1988). Mullin (1988) recommends the use of about a four litre vessel for MSMPR determinations, smaller than this can cause poor scale up results and larger than this can make it difficult to achieve true MSMPR behaviour.

The MSMPR crystalliser is started and run until steady state is achieved. Randolph and Larson (1988) use 10 to 15 residence times to reach steady state, while Nyvlt (1982a) uses 6 to 10. Mullin (1993) and Sohnel and Garside (1992) both recommend 10 residence times to reach steady state. Once steady state has been reached, a sample of the magma can be removed and the particle size distribution (PSD), L, as a number function is determined (Mullin, 1988). Using the following relationships and the steady state residence time, τ, the nucleation and growth rates, B and G respectively, can be determined.

$$n = n_o \exp\frac{-L}{G\tau}$$

and

$$B = n_o G$$

Where n is the population density (number of crystals per unit size per unit volume of the system) and n_0 is the population density of nuclei (zero sized crystals).

The long time taken to reach steady state is a distinct disadvantage to operating a continuous laboratory scale crystalliser. However, the information that is obtained is suitable for scale up to industrial sized crystallisers. The product quality is more reflective of that produced by actual continuous industrial crystallisers, compared to that of batch crystallisers.

Laboratory scale experiments using a batch crystalliser are also a useful tool for understanding precipitation processes. Nyvlt (1982b) describes how batch precipitation experiments with a one-off, initial formation of supersaturation followed by a steady decrease in supersaturation can be used to compare precipitation performance on a relative scale between experiments. An example of this type of experimentation is given by Droppert, Demopoulos and Harris (1996) and Demopoulos, Droppert and Van Weert (1985 and 1995) in their work on producing crystalline scorodite ($FeAsO_4.2H_2O$) under ambient conditions, shown in Figures 1.8 and 1.9.

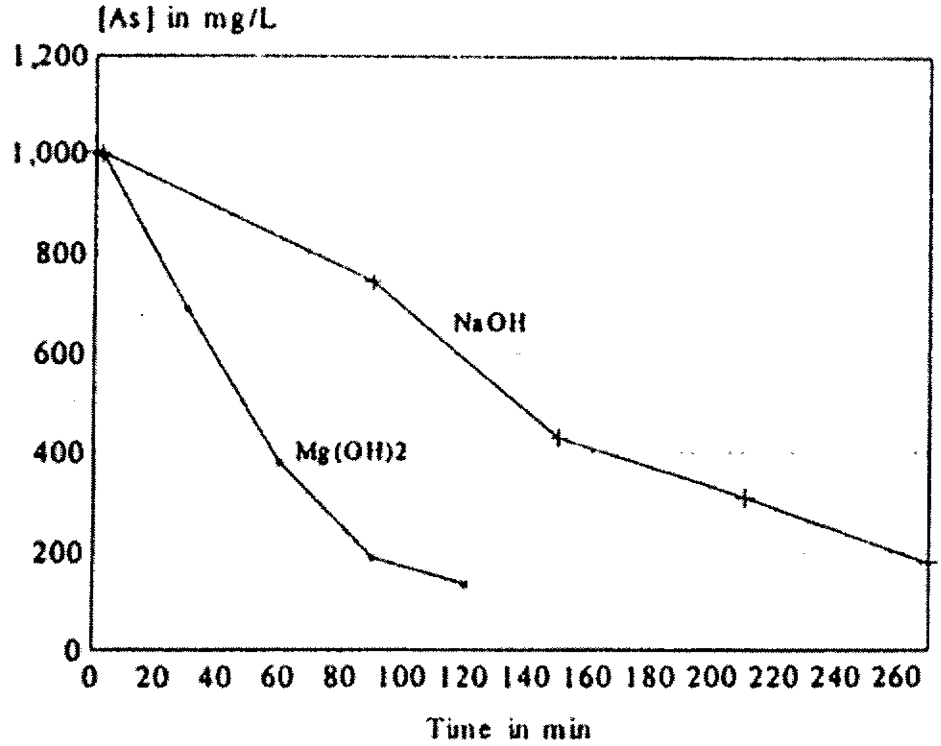

Figure 1.8 Precipitation curves for the production of scorodite using magnesium hydroxide and sodium hydroxide as neutralising agents (Droppert, Demopoulos and Harris, 1996).

A series of batch experiments were performed to investigate the effects of supersaturation, seed concentration, type of neutralising agent and other variables important to that particular system. Figures 1.8 and 1.9 show the precipitation curves produced to investigate two different neutralising agents, and differing seed concentrations, respectively. This method allows for easy determination of the relative rates of precipitation encountered.

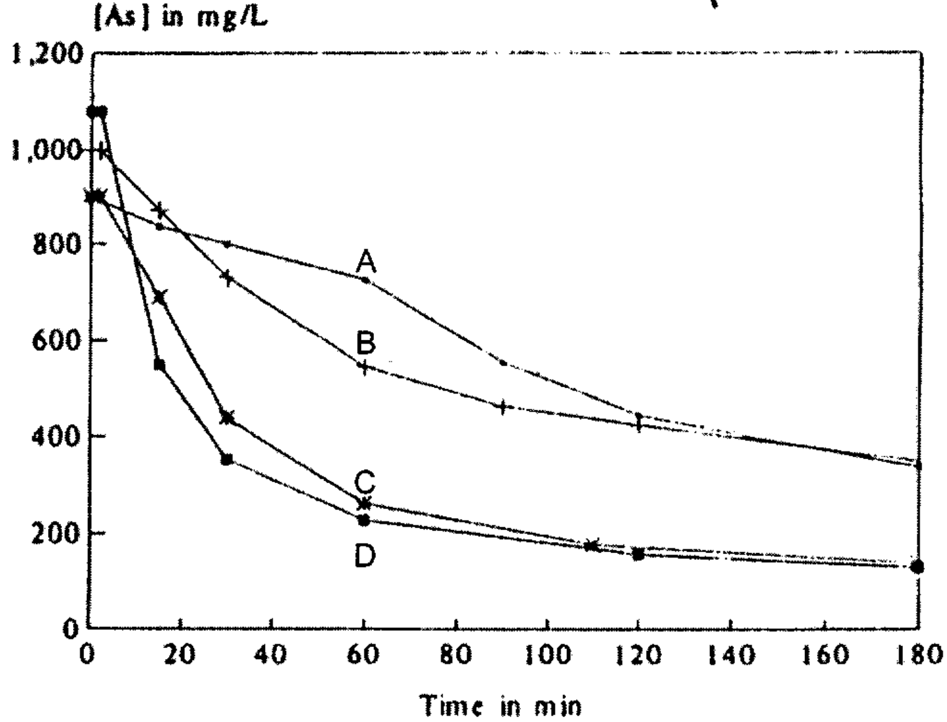

Figure 1.9: Precipitation curves for the production of scorodite with varying seed loadings; (A) 4 g L^{-1}, (B) 10 g L^{-1}, (C) 20 g L^{-1} and (D) 50 g L^{-1} (Droppert, Demopoulos and Harris, 1996).

In general, it maybe useful to use a combination of both batch and continuous experiments on a laboratory scale to gain a fundamental understanding of a precipitation system.

1.4 SILICA POLYMERISATION

1.4.1 General silica polymerisation theory

Soluble silica is defined by Iler (1979) as being monomeric; containing a single silicon atom, tetrahedrally surrounded by four hydroxide units, thus having the formula $Si(OH)_4$ and is commonly called monosilicic acid. Two monosilicic acid units polymerise via a condensation type reaction between silanol groups (≡Si-OH) to form a siloxane bond (≡Si-O-Si≡) and hence the dimer, disilicic acid, according to the reaction:

$$2Si(OH)_{4\,(aq)} \rightarrow O(Si(OH)_3)_{2\,(aq)} + H_2O_{\,(aq)}$$

The ionisation constant, pK_a, of monosilicic acid was found to be 9.8, while that of the disilicic acid was found to be 10.7 (Iler, 1979). Comparison with other inorganic acids would suggest that disilicic acid should be the stronger acid. This anomaly is thought to be a function of the instability of a solution of the dimer; preventing accurate determination of the pK_a. It should be noted that there is no similarity between aqueous silicic acid polymerisation and organic polymers formed by condensation reactions. Further condensation polymerisation occurs between silanol groups of larger species to increase molecular weight. Polymerisation refers to all types of silica growth that increase molecular weight, whether the growth forms spherical colloidal particles or aggregates under certain conditions or forms viscous gels under a different set of conditions. Both types of polymerisation can occur simultaneously. Iler's (1979) general theory of polymerisation will be presented and discussed in a series of steps; it is also diagrammatically represented in Figure 1.10.

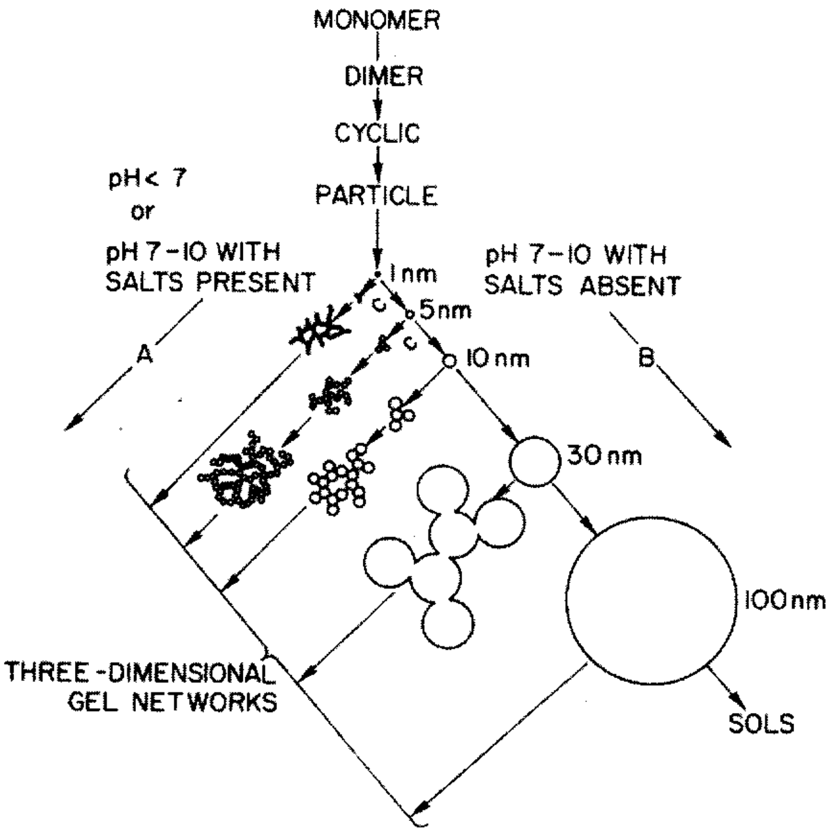

Figure 1.10: Polymerisation of silicic acid, (A) in acid solution or with flocculating salts present and (B) in basic solution (Iler, 1979).

1. When a solution of monosilicic acid becomes supersaturated, *ie.* the concentration is greater than 100 to 200 mg L^{-1} as SiO_2, polymerisation to form dimers and then cyclic, higher molecular weight species occurs. This is provided there is no suitable solid phase surface for the monomer to deposit on.
2. The polymerisation mechanism is ionic, and above pH 2 the rate of polymerisation is proportional to the hydroxide ion concentration, while below this pH it is proportional to the hydrogen ion concentration.
3. Polymerisation occurs to maximise the number of siloxane bonds and minimise the number of unreacted silanol groups, which leads to three dimensional structures with uncondensed silanol groups on the surface.
4. These spherical nuclei can then grow into larger particles. The solubility of these nuclei is dependent upon their size and also upon the extent of

internal dehydration. Nuclei formed above 80°C, and especially those formed above pH 7, are internally almost anhydrous.

5. Nuclei grow by the Ostwald ripening mechanism, *ie.* smaller particles dissolve to produce monosilicic acid which deposits on the surface of larger particles. The higher solubility of smaller particles is only pronounced when the particle size is less than about 5 nm. Above pH 7, where silica reactivity is high, growth continues at ambient temperatures up to sizes of 5 to 10 nm; above this pH, growth is slow. At low pH, where silica reactivity is low, particle growth is minimal after 2 to 4 nm particles have formed. However, larger particle sizes are achieved at higher temperatures and especially above pH 7. Silica reactivity is a function of zeta potential, which in turn varies with the solution pH (Iler, 1979). Zeta potential is described as the potential at the surface of shear between the charged surface and the electrolyte solution (Hunter, 1987; Shaw, 1980).
6. In the pH range 6 or 7 to 10.5, silica particles have a negative zeta potential and repel each other, allowing growth without aggregation due to a lack of particle interaction. Above pH 10.5 silica begins to dissolve.
7. At low pH, or pH 6 or 7 to 10.5, with salts present, silica particles have a low zeta potential and readily collide, thus aggregating and forming gels. If the SiO_2 concentration is above 1%, aggregation may occur as soon as small particles form. At lower concentrations, and at a pH of about 2, monosilicic acid forms discrete particles which then aggregate. At pHs of about 5 to 6, the monomer is rapidly converted to particles which aggregate and gel simultaneously. The aggregation rate increases with silica concentration, and above a concentration of 1% aggregation probably occurs between particles and higher order oligomers.

Iler (1979) represents the overall effect of pH on polymerisation in Figure 1.11. A long gel time is synonymous with silica stability in solution, or a slow rate of polymerisation. The gel time is defined as, the time taken for a gel to form that will not flow when the container in which it is contained is tilted. Curve ABC represents the silica-water system with maximum temporary stability (A) over the pH range 1.5 to 3.0 and a minimum in stability (B) at pH 5 to 6. Stability is infinite (C) above pH 7. Curve DEF represents the silica-water system with an electrolyte present above 0.2 M in concentration. At low pH there is no effect on the temporary stability maximum (D) from the electrolyte. The stability minimum (E) has increased to pH 7 while the region of infinite stability (F) has increased to pH 10 and above. Both of these shifts are caused by the electrolyte lowering the zeta potential of the silica particles.

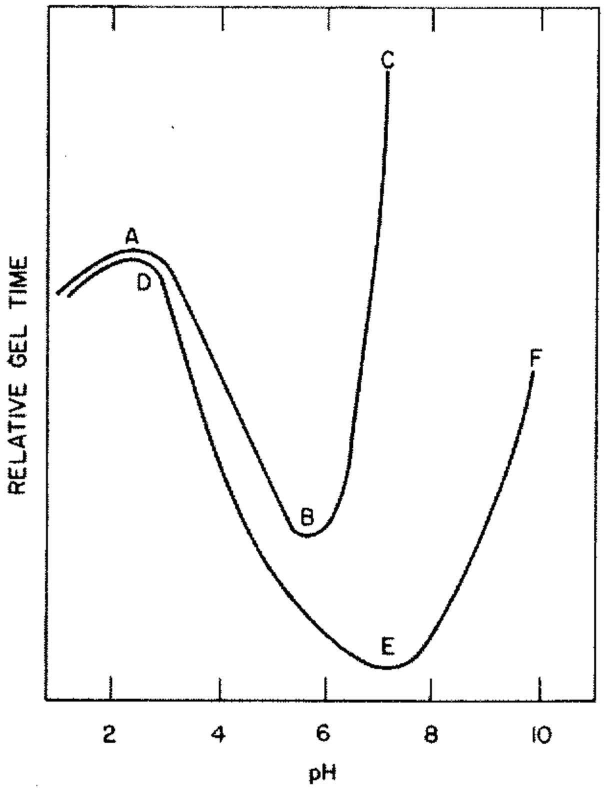

Figure 1.11: The effect of pH on the gelling of silica sols. Curve ABC in the absence of electrolyte and DEF with electrolyte present (Iler, 1979).

1.4.2 Gellation or precipitation

Silica removal from solution can be divided into stages, the polymerisation of silicic acid to a colloidal sol, and the possible aggregation of this sol to form amorphous silica in the form of a gel, a precipitate or a flocculate (Fleming, 1981; Queneau and Berthold, 1985).

Aggregation is used to describe all methods of colloidal silica particles linking together (Iler, 1979). Hence, aggregation includes gelling, coagulation and flocculation. Gelling is described as the linking of particles together in branched chains that consume the entire liquid volume. There is no increase in silica concentration in any region of the sol; instead, the whole medium becomes viscous and then solidifies into a coherent network of particles. The capillaries between particles retain the liquid medium within the gel. Coagulation is described as the coming together of particles to form relatively close packed clumps which settle as a relatively dense precipitate. As would be expected, the silica concentration is higher in the precipitate than in the original sol. Flocculation describes the traditional process of linking together particles by bridging them with a long, flexible molecule, typically organic. The resulting structure is open and voluminous, but sufficiently large to settle. Flocculation is outside the scope of this study and therefore will be discussed no further. Figure 1.12 shows diagrammatic, two-dimensional representations of a gel and a precipitate.

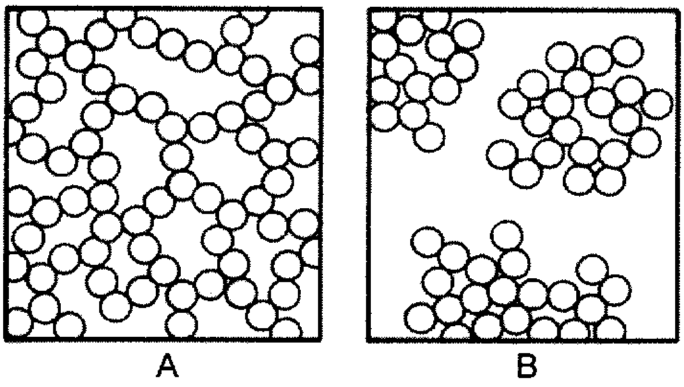

Figure 1.12: Diagrammatic two-dimensional representations of (A) a gel and (B) a precipitate (Iler, 1979).

Colloidal silica refers to stable dispersions or sols of discrete particles of amorphous silica (Iler, 1979). By definition, it does not include solutions of polysilicic acid where the polymer molecules or particles are unstable due to their extremely small size and therefore high solubility. These particles are referred to as oligomers. In general, colloidal particles are in the size range 1 nm to 1 μm (Shaw, 1980).

If the colloidal sol is stable, the silica particles are too small to settle and remain suspended in solution indefinitely (Queneau and Berthold, 1985). The stability of a colloidal sol of silica particles is dependent on several variables, such as pH, temperature, particle size and sol concentration, and the concentration of electrolytes (Iler, 1979). Depending on some or all of these variables, an unstable colloidal sol can either gel or precipitate. The effect of these variables, particularly electrolyte concentration, can be related back to the DLVO (Deryaguin-Landau-Verwey-Overbeek) theory of colloid stability (Hunter, 1987; Shaw, 1980). This theory quantifies the stability of a sol in terms of the energy changes that occur when colloid particles approach each other. Estimations of: the energy due to overlap of the electric double layers, and London-van der Waals energy, both in terms of interparticle distance are summed to give the total interaction energy as a function of interparticle distance. The stability of a colloidal sol is then interpreted from the interaction energy-interparticle distance curve.

The effect of pH on the colloidal silica-water system is best described by Figure 1.13 (Iler, 1979).

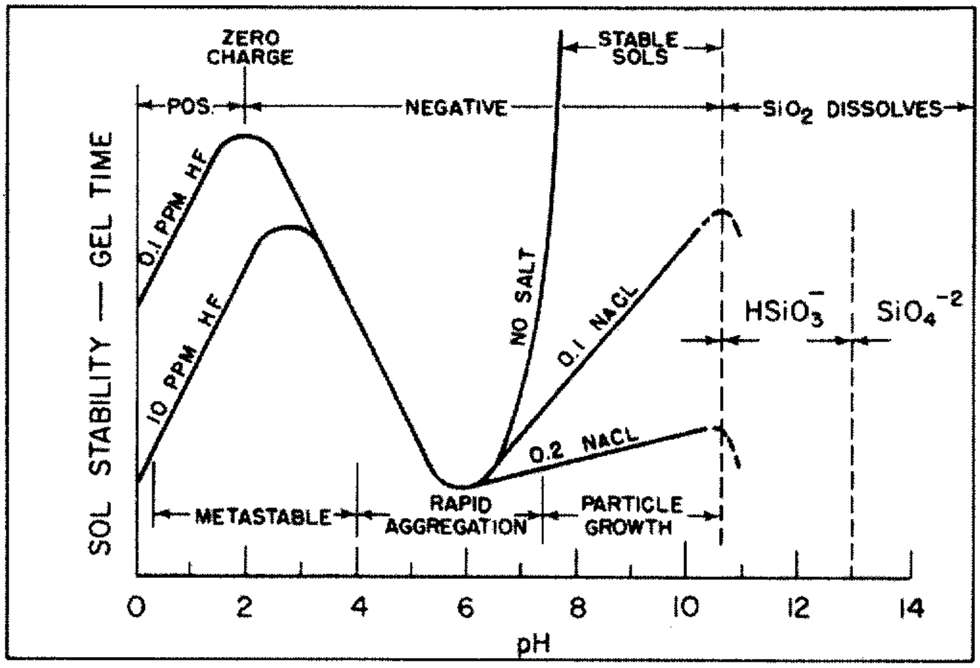

Figure 1.13: Effects of pH in the colloidal silica-water system (Iler,1979).

The basic step in gelling or precipitation is the collision of two particles, with sufficiently low zeta potential, and chemical reaction through the formation of siloxane bonds to hold them together (Iler, 1979). As the zeta potential changes, so to does the frequency of collisions, and thus the rate of reaction. Above pH 6, the negative zeta potential on particles increases, thus increasing their mutual repulsion and drastically reducing the frequency of collisions. Hence, the sol is increasingly stable with respect to gelling or precipitation at a pH above 3.5. At pHs less than 6, the zeta potential is quite low and has minimal impact on the rate of reaction. Below pH 2, the rate of reaction is proportional to the hydrogen ion concentration and is catalysed by traces of fluoride ion. A temporary (short term) stability maximum, or alternatively a reaction rate minimum, occurs at pH 2, the point of zero charge. Above pH 2, the rate of reaction is proportional to the hydroxide ion concentration until the zeta potential predominates from pH 6 onwards. This produces a maximum rate of reaction, a stability minimum, at pH 6.

The isoelectric point and the point of zero charge for silica are both at about pH 2 (Iler, 1979). Thus, the zeta potential is positive below this pH and negative above it. The temporary stability of silica at pH 2 is explained by the lack of $(OH)_3SiO^-$ ions present, which are necessary for condensation and dissolution reactions between silanol groups. This by far outweighs the collision and interaction of particles, due to the lack of zeta potential, which is not strongly present until pHs in excess of 7.

Since aggregation involves a kinetic mechanism, the rates of gelling and precipitation increase with increasing temperature (Iler, 1979).

According to Iler (1979), the effect of particle size and sol concentration on the rate of reaction are interrelated. The rate appears to be proportional to the specific surface area of silica available within the sol. Surface area is inversely proportional to particle diameter, therefore sols having the same ratio of concentration to particle size react at the same rate.

If an electrolyte is present, the zeta potential is reduced at a pH above 3.5, and thus stability is reduced and the reaction rate increases rapidly, as seen in Figure 1.13 (Iler, 1979). Below pH 3.5, electrolytes have very little effect; according to Iler (1979) this is presumably due to a hydration layer on the surface.

Similar findings to those of Iler (1979), have been found by other workers, as described below.

Queneau and Berthold (1985) found, that the formation of a gel or precipitate is a function of the silicic acid supersaturation, availability of a seed surface, temperature, pH and ionic strength.

Terry (1983b) reviewed silica behaviour in hydrometallurgy and concluded that under acidic conditions and high silicic acid concentrations (greater than 1000 mg L^{-1} as SiO_2) either a colloidal sol, a silica gel or a filterable precipitate could be formed. Ordinarily, a gel will be formed at higher pHs, but a precipitate can be formed under conditions of rapid coagulation by having high pH, temperature and ionic strength.

A study of particle nuclei from the polymerisation of silicic acid to colloidal silica was made by Iler (1980). Silicic acid concentration was 6000 mg L^{-1} or 0.1 M as SiO_2, the temperature was 25°C and several experiments were carried out over the pH range 0 to 3. However, most data were collected at pH 1.75 (considered to be the iso-electric point (Iler, 1980)) where polymerisation is slowest. The initial nuclei appeared after a two hour induction period, and were about 1 nm in size. These grow at the expense of monomer and by depolymerising oligomers forming more monomer. When the oligomers have been consumed, the particles grow by Ostwald ripening. After 20 days, 97% of the silica is in the form of particles 4 nm in size in temporary equilibrium solubility with 200 mg L^{-1} SiO_2 present as silicic acid. When the pH is changed to either side of pH 1.75, polymerisation becomes rapid with a ten times increase in the rate at pH 0.

Providing supersaturation is not so great that monomer polymerises to form a gel, precipitation of monosilicic acid from supersaturated solution can occur by two methods (Iler, 1979):

The first is by formation of a sol of colloidal particles. Nucleation is by polymerisation of an ionised monomer with a nonionised monomer to form a dimer. Below pH 2, monomer is ionised to $(HO)_3SiO^-$ and above this to $(HO)_3Si^+$. At low pHs, ionisation occurs only to a small degree and thus dimerisation is very slow. This was also noted by Fleming (1981). At pHs less than 2, the reaction is described as:

$$(HO)_3SiO^- + HOSi(OH)_3 \rightarrow (HO)_3SiOSi(OH)_3 + OH^-$$

If the dimer is a stronger acid than the monomer, it too can become ionised and react with monomer to produce the linear trimer, according to:

$$(HO)_3SiOSi(OH)_2O^- + HOSi(OH)_3 \rightarrow (HO)_3SiOSi(OH)_2OSi(OH)_3 + OH^-$$

Ionised monomer can react with either dimer or trimer and similarly, ionised dimer can react with monomer, dimer or trimer to increase molecular weight.

The end silanol groups of the linear tetramer and higher linear polymers condense to form the respective cyclic molecules. Bond angle strain makes the formation of a cyclic trimer unlikely. Monomer and dimer preferentially condense with the more highly ionised cyclic molecules to further increase their molecular weight. Adjacent silanol groups now condense wherever possible to make ring closures, leading to more compact, three-dimensional molecules. Molecules such as the double-three-ring hexamer and larger are considered to be the core of future particles. They are not yet described as silica particles as they do not contain an anhydrous core. When an oligomer such as an octamer or decamer is to be the core of a particle, further deposition of 40 to 50 monomer units is necessary to render the original oligomer almost anhydrous as the core. This is considered to be a stable nucleus, and is approximately 1.6 nm in diameter. Growth of nuclei to colloidal dimensions is by further condensation with monomer, either directly from solution or by the dissolution of other oligomers. Growth is more rapid, and condensation and internal dehydration more complete at higher temperatures. It should be remembered that up until the critical nucleus size is achieved, the molecules are soluble with solubility being inversely proportional to size. Nucleation will only occur if there is insufficient suitable surface for deposition.

Deposition on a solid surface is the second method for the removal of monosilicic acid from supersaturated solution. Once again, it is assumed that supersaturation is not so great that monomer polymerises to form a gel. Monosilicic acid condenses with hydroxide groups of any pre-existing solid surface that it can react with, specifically silica, but alternatively any metal hydroxide surface that will form a silicate under the conditions involved. This is described by the following equation where M is silicon or any suitable metal:

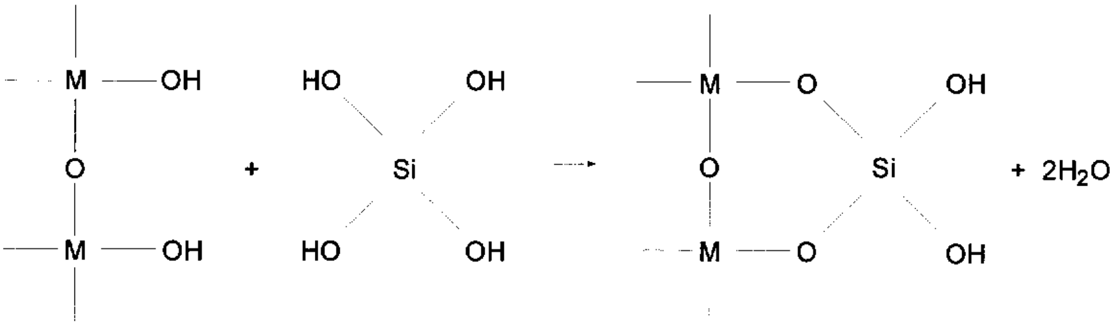

Once a layer of silica has deposited on the surface, further deposition is simply silica on silica. Due to deposition of monomeric silica, the film will be impervious. Deposition onto a surface is thought to be the reverse process of dissolution (Iler, 1979). Although monosilicic acid is believed to be the deposited material, it is possible that "active silica", consisting of low molecular weight polysilicic acids (including extremely small colloids) dissolves to liberate monomer for deposition. Deposition is faster at higher temperatures, and is fastest between pH 8 and 11; below this deposition is slow, and above this silica is soluble.

According to Iler (1979), colloidal silica particles can deposit on a surface if the pH and electrolyte conditions are similar to those for coagulation or precipitation. Deposition occurs when a colloid particle collides and bonds to the surface by formation of a siloxane bond. Due to the relatively large size of the colloidal particles, and hence poor packing, the deposited film will be porous. The concentration of colloid particles in suspension must not be too great, otherwise coagulation and gelling will occur.

It is possible for colloidal silica to deposit on a surface in the presence of monosilicic acid (Iler, 1979). This is a greatly accelerated reaction, and results in dense, hard deposits that are cemented together by the deposition of monomer. These deposits are usually microporous as there is insufficient monomer to completely fill the pores between individual colloid particles. However, if conditions are suitable, further deposition of monomer can fill the pores to form an impervious surface.

Fleming (1981) studied the kinetics of silica precipitation from solutions of silicic acid and found that the polymerisation rate constant for silicic acid was a function of the pH over the range 0.12 to 5.11. The rate constant function was observed to be symmetrical near the isoelectric point. Precipitation experiments, with and without seed, over the silicic acid concentration range 80 to 930 mg L^{-1} as SiO_2 were carried out. The temperature was 18±2°C, and equilibrium solubility is 100 mg L^{-1} as SiO_2 under these conditions. No mention of stirring was made. As is shown in Figure 1.14 precipitation is quicker at low pHs and higher silicic acid concentrations. Precipitation is mainly due to deposition on seed surfaces, rather than by nucleation. Nucleation only predominates until sufficient surface growth sites have been generated, with the transition from nucleation to growth occurring very early on in the process. This is evident by comparing Figure 1.14 and Figure 1.15, where the precipitation rates are slightly higher at all pHs when seed is present. The precipitation rate is described as the gradient of the tangent to the precipitation curve at the beginning of the experiment.

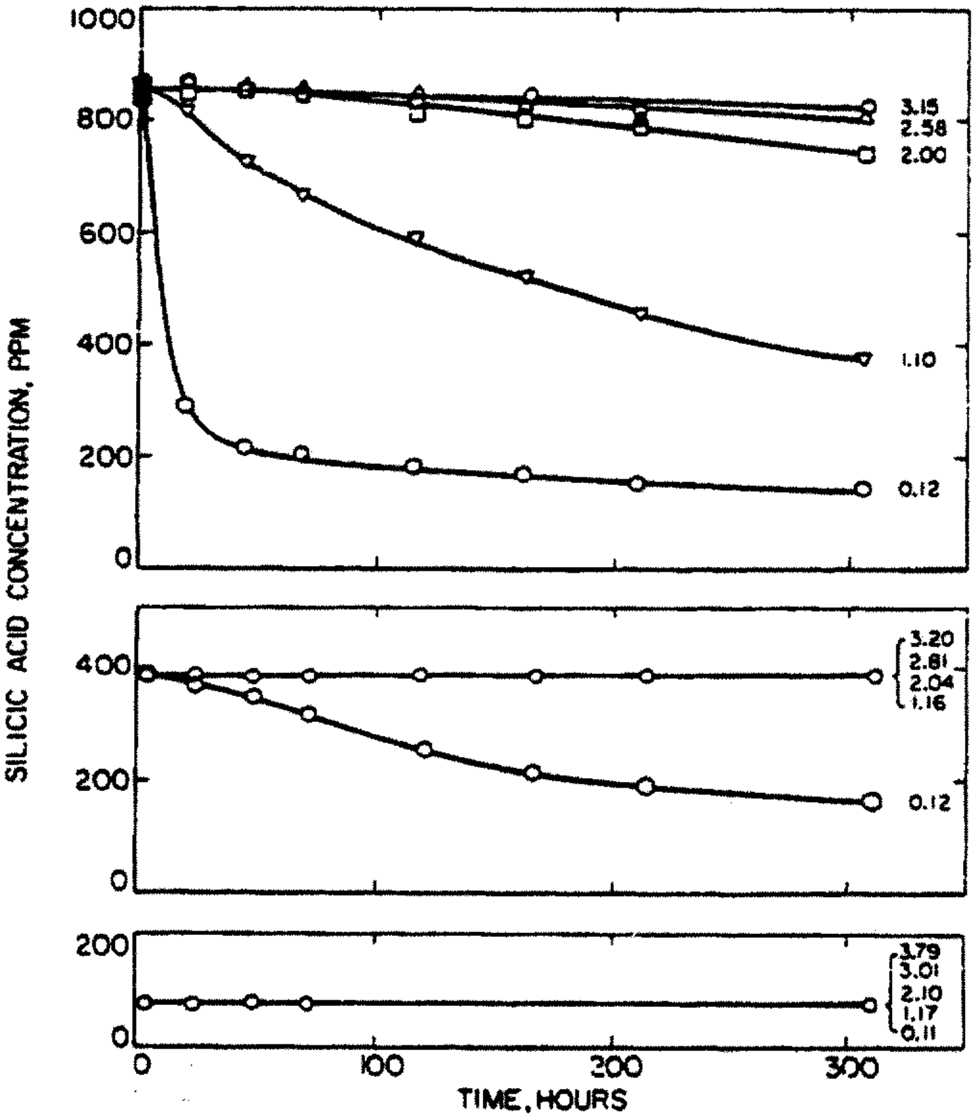

Figure 1.14: Unseeded silica precipitation experiments, silicic acid concentration versus time, as a function of pH, which is displayed down the right hand side of the graph (Fleming, 1981).

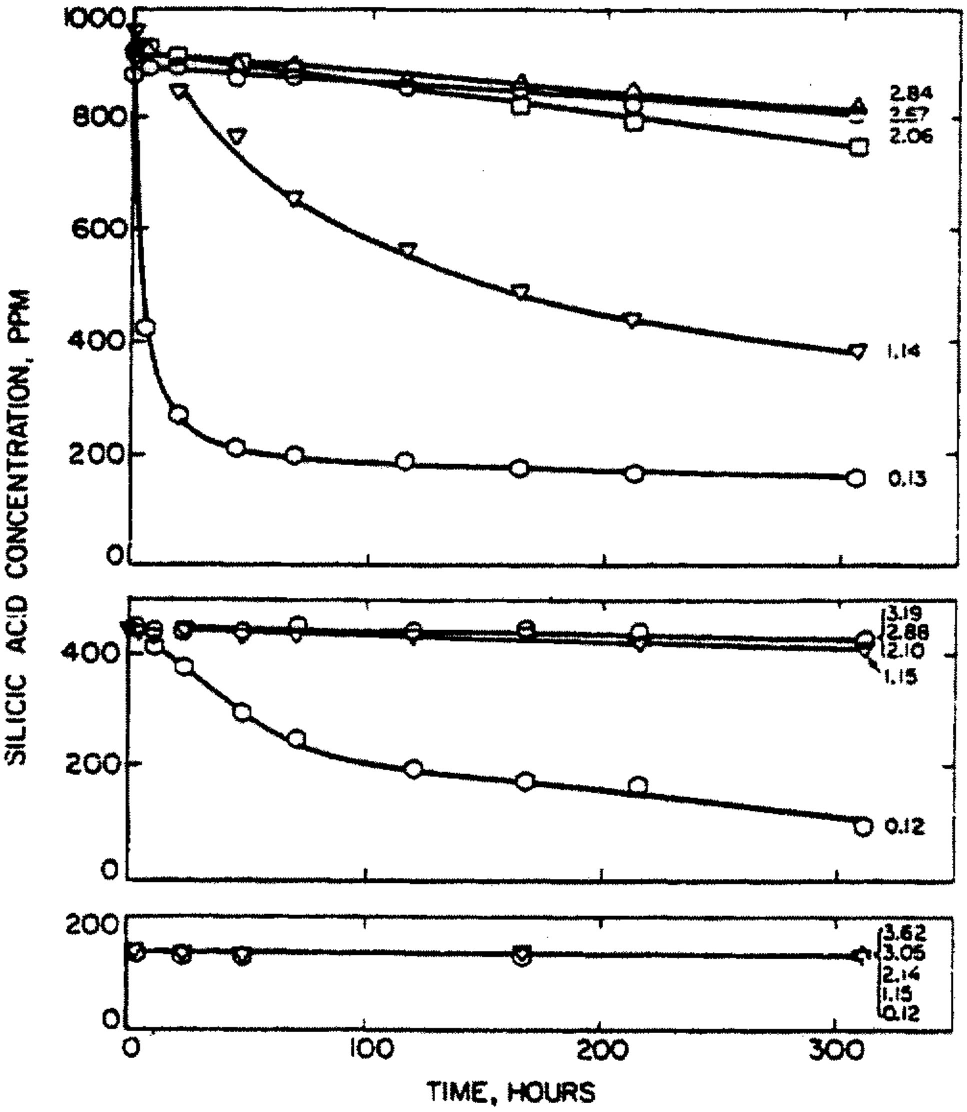

Figure 1.15: Seeded silica precipitation experiments, silicic acid concentration versus time, as a function of pH, which is displayed down the right hand side of the graph (Fleming, 1981).

In their review of zinc silicate ore processing, Matthew and Elsner (1977b) noted that precipitation of colloidal silica can be assisted by controlling or changing the pH, increasing the temperature, using a long conditioning time, adding ionic coagulants - such as aluminium or ferric iron, increasing ionic strength, use of seed and minimising the concentration of colloidal silica.

Chen, Dong and Yang (1997) investigated the size-dependence of the growth rate of monodisperse silica particles produced from tetraalkoxysilane.

Under conditions free of nucleation, particles of different size grew at the same rate, and thus growth is surface reaction limited (growth rate is size independent). When nucleation was present, smaller particles grew faster than larger ones, indicating growth to be diffusion limited. New particles were 70 nm in diameter while the largest particles grew to 1250 nm. It is not known whether the same situation exists when silica is precipitated from aqueous solution.

1.4.3 Factors influencing silica polymerisation

Betterton (1923) studied soluble silica, from zinc pyrosilicate ore, in the preparation of zinc sulfate solution for the electrolytic recovery of zinc. Upon experiencing problems with silica gelation, a series of tests were performed to evaluate sulfuric acid, zinc sulfate and soluble silica concentrations and their effect on the time taken to form a gel. It was found that increasing the concentration of either sulfuric acid or zinc sulfate led to a reduction in the time taken to form a gel. The time taken to form a gel decreased with silica concentrations from 8 to 10 g L^{-1} and increased with concentrations from 10 to 13 g L^{-1}. From this work, Betterton (1923) was able to calculate the time taken to form a gel if the concentrations of these three variables were known. Solutions containing 100 g L^{-1} zinc, 5 g L^{-1} sulfuric acid and 20 g L^{-1} silica have been successfully handled on a pilot plant scale.

Hurd and Letteron (1932) studied the formation time of silica gels from sodium silicate and acetic acid. They measured the time taken to form a gel, or the time of set as they call it, by placing a stirring rod in the solution at about 20° to vertical. If the stirring rod remained standing then the gel was considered to have set. Using this tilted rod method, they studied the effect of temperature on gelling, and found the time of set to decrease with increasing temperature. The concentration of acetic acid ranged from 0.50 to 0.75 M, temperature ranged from 13 to 80°C and silica concentration ranged from 0.4 to 0.8 M.

Hurd and Barclay (1940) investigated the time of set of silica gels containing high concentrations of mineral acids using the tilted rod technique. Sulfuric acid containing gels were studied in the pH range -0.5 to 0.5 and temperatures from 0 to 40°C at a silica concentration of 0.67 M. A linear relationship was found between the logarithm of time of set and the pH, with time of set decreasing with decreasing pH (increasing sulfuric acid concentration). An increase in temperature also decreases the time of set.

Hurd and Sheffer (1941) studied the effect of silica concentration on gelling from solutions of sodium silicate and acetic acid over the pH range 4.8 to 6.5. The silica concentration ranged from 0.25 to 1.00 M as SiO_2 and the temperature ranged from 0 to 40°C. Once again, the tilted rod technique was used to determine the time of set. It is apparent that at a given pH and temperature, an increase in the concentration of silica results in a decrease in the time of set.

Chan (1989) reviewed silicic acid polymerisation under various conditions, and found that the length of the induction period (time for gelation to begin) decreased with increasing supersaturation. The polymerisation rate was found to increase with temperature over the range from ambient to boiling. Queneau and Berthold (1985) also note the presence of an induction period before polymerisation occurs. This can be removed by seeding, increased supersaturation and/or higher temperature.

Ashman, Delong and Jankola (1993) report that the treatment of calcines containing up to 6% silica, in the form of zinc orthosilicate, is only possible with the addition of iron (III) at a concentration of between 1.5 and 2.0 g L^{-1}.

As mentioned earlier, Matthew and Elsner (1977b) noted that the precipitation of colloidal silica can be assisted by controlling or changing the pH, increasing the temperature, using a long conditioning time, adding ionic coagulants - such as aluminium or iron (III), increasing ionic strength, the use of seed and minimising the concentration of colloidal silica.

The Radino process uses aluminium ions as a coagulant for silica, dramatically improving its filtration performance (Radino, 1957). Aluminium is added at the rate of 1 to 50 % by weight of the silica present.

Iler (1952; 1979) warns of the catalytic effect of fluoride on silica polymerisation to form gels. Iler (1952) produced silicic acid sols, 1.0 M in SiO_2, in the pH range 0.5 to 3.0 using sulfuric acid at 25°C and studied the effect of sodium fluoride additions on gel times. Gel time was deemed to have been reached when the beaker was tilted and the solution no longer flowed. Fluoride ion concentrations up to 45 mg L^{-1} were investigated, and reductions in gel time in the order of five times were observed at pH 2. The addition of aluminium ions, as sulfate, stabilises silicic acid sols by removing the fluoride ions *via* formation of complexes such as $[AlF_6]^{3-}$. Beryllium and thorium ions have a slightly lesser effect than aluminium ions, while iron (III) ions have a slightly smaller but still significant effect on stabilisation. Iler (1952) suggests that below pH 2 the rate of silica polymerisation is catalysed by hydrogen and fluoride ions.

Hutchison (1958) studied the effect of aluminium and iron (III) ions on the gelation of silica in zinc leach pulp, catalysed by fluoride. It was concluded that one atom of aluminium has a marked influence on restraining one atom of fluoride and a partial influence on restraining two atoms of fluoride. Five to ten atoms of iron (III) were required to fully neutralise one atom of fluoride, while smaller quantities have a lesser effect.

1.4.4 Solubility of silica

The solubility of silica is higher when the surface of a particle is convex and lower when it is concave (Iler, 1979). This observation also applies to drops of liquid in a vapour, and bubbles in a liquid, as well as colloidal solids in a liquid, and is based upon the Kelvin equation, shown below (Hunter, 1987; Shaw, 1980).

$$\ln\frac{a}{a_o} = \frac{2\gamma V_m}{rRT}$$

Where α is the activity of a species at a surface with radius of curvature r (positive for convex surfaces, negative for concave surfaces), γ is the surface energy, and V_m is the molar volume of the species. R is the Universal gas constant and T is the temperature.

It is the relationship of the degree of curvature to the radius that is the important factor in this case, with the smaller the radius the larger the effect on solubility. Thus, a small spherical particle, with a small, positive radius of curvature, is more soluble than a larger particle, with its larger positive radius of curvature. This explains the instability of oligomers of silica and also the growth of silica particles by Ostwald ripening. Similarly, the crevice between two aggregated particles has an extremely small, negative radius of curvature and is thus a region of very low solubility. Silica will therefore dissolve from other regions of the particle and deposit in the crevice, cementing the particles together. This explains the tendency of silica particles to grow by aggregation when the zeta potential is low, such as low pH or pH 6 or 7 to 10.5 with electrolyte present. Initial adhesion of colliding particles is thought to be by the formation of siloxane bonds.

The equilibrium solubility of amorphous silica in water is dependent on the particle size, the state of internal hydration and the presence of impurities in the system (Iler, 1979). Due to these factors, reported values range from 70 to 150 mg L^{-1} SiO_2 at 25°C, with a figure of 321 mg L^{-1} quoted for a temperature of 100°C (Iler, 1979). As can be seen in Figure 1.16 various results have been reported for solubility as a function of pH at ambient temperatures. However, there is a general trend of decreasing solubility with increasing pH, with a minimum at about pH 7.

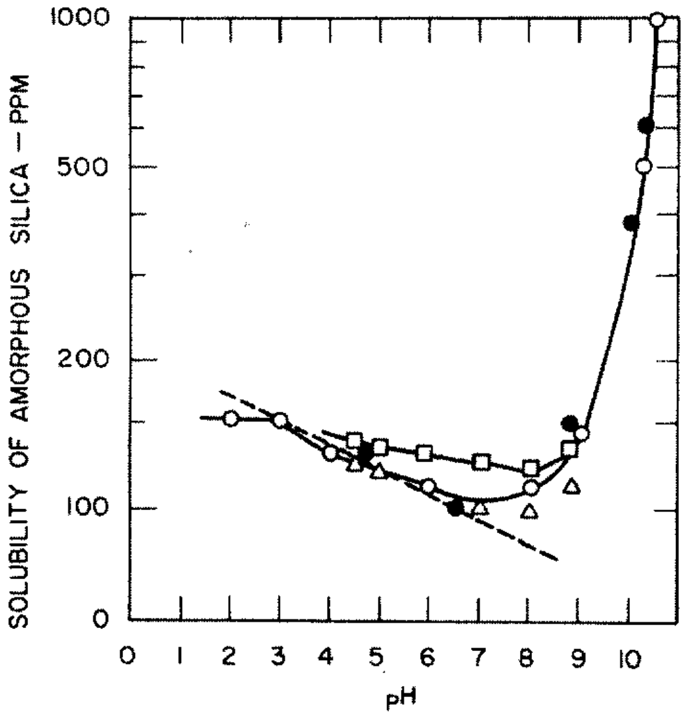

Figure 1.16: Solubility of amorphous silica in water as a function of pH at ambient temperatures, from several studies (Iler, 1979).

Iler (1979) states that fluorine and sulfate ions have no effect on the solubility of silica, but aluminium ions reduce the solubility somewhat.

Queneau and Berthold (1985) reviewed silica in hydrometallurgy and noted that of all forms of silica, amorphous silica has the highest solubility, as shown in Figure 1.17. They also noted that up to a pH of about 8, the solubility of amorphous silica was essentially constant with pH, Figure 1.18. However, increasing the temperature of a silica solution at a given pH increases solubility, as shown in Figure 1.19. It should be noted that the ion-product constant for water, K_w, is also temperature dependant (Skoog, West and Holler, 1988).

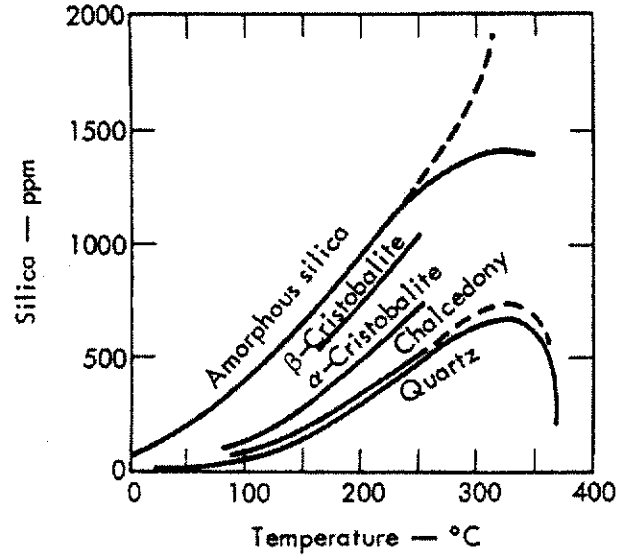

Figure 1.17: Solubilities of various forms of silica in water as a function of temperature (Queneau and Berthold, 1985).

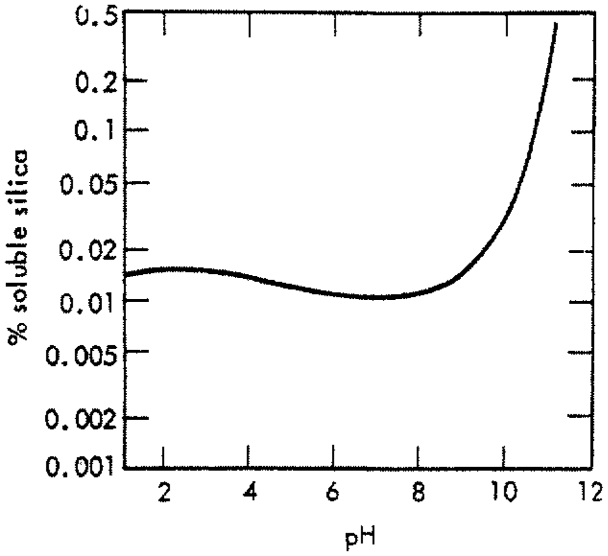

Figure 1.18: Solubility of amorphous silica in water at 25°C as a function of pH (Queneau and Berthold, 1985).

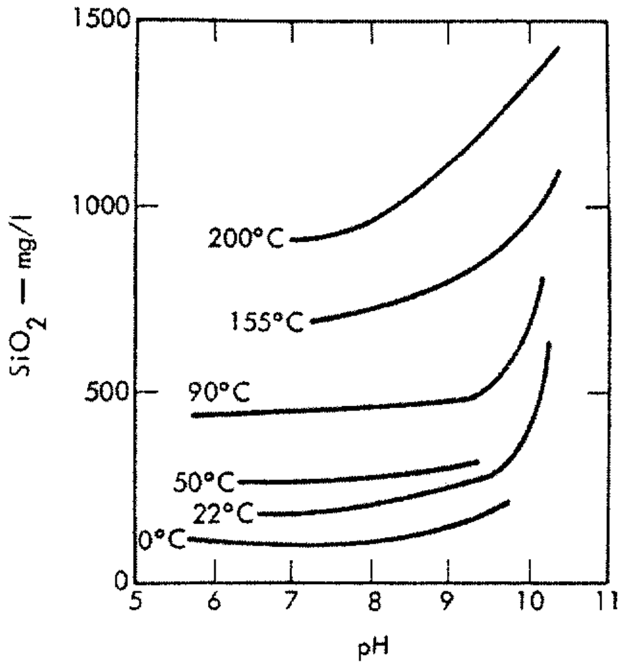

Figure 1.19: Solubility of amorphous silica in water at various pHs as a function of temperature (Queneau and Berthold, 1985).

The equilibrium solubility of amorphous silica precipitated from hydrometallurgical zinc liquors varies greatly, with those values quoted in the literature displayed in Table 1.2.

Table 1.2: Equilibrium solubility of amorphous silica precipitated from hydrometallurgical zinc solutions.

Amorphous Silica - Equilibrium Solubility (mg L^{-1} as SiO_2)	Amorphous Silica - Equilibrium Solubility (M as SiO_2)	Temperature (°C)	Reference
100	1.66×10^{-3}	Not quoted	Hutchison (1958)
290 to 380	4.83×10^{-3} to 6.32×10^{-3}	90	Bodson (1974)
100	1.66×10^{-3}	80	Bodson (1974)
80	1.33×10^{-3}	75	Bodson (1974)
350 to 400	5.83×10^{-3} to 6.66×10^{-3}	95 to 100	Radino (1957)

1.4.5 Summary

Iler's (1979) comprehensive monograph on the chemistry of silica is unfortunately lacking in detailed information covering polymerisation at pHs less than 2. This relatively unexplored area of silica precipitation is commonly found in hydrometallurgical processing. Many workers have investigated this region, and their research provides much qualitative theory and information concerning polymerisation and variables that influence it. However, very little quantitative information is given, concerning the formation of dense, easily separable precipitates. What is also unclear is the reason for formation of a gel as opposed to a precipitate. It appears to be mainly a function of silica concentration and other variables such as pH, temperature and the presence of electrolytes, but is not well quantified. These shortcomings provide further evidence of the need for the current investigation.

1.5 DISSOLUTION OF ZINC ORTHOSILICATE

Zinc orthosilicate is the source of monosilicic acid for this study, and hence a knowledge of its dissolution is important for the investigation.

The dissolution of oxidised zinc ores in various media has been studied by several workers (Abbruzzese, 1981; Frenay 1985; Pus'ko, Ushakov and Khan 1979). However, the most thorough investigation of silicate dissolution has been made by Terry. In his literature review of silicate dissolution Terry (1983a) divides silicate decomposition by leaching, into three broad categories:

1. Complete breakdown of the silicate structure with liberation of the metal cations and silica.
2. Partial decomposition of the silicate structure with liberation of only the metal ions, thus leaving an insoluble siliceous residue.
3. No reaction.

Both zinc orthosilicate and zinc pyrosilicate are group 1 silicates that dissolve stoichiometrically, a process called congruent dissolution. The strength of the silicon-oxygen bond compared to the metal cation-oxygen bond plays a part in the relative solubility of a particular silicate. For example, the zirconium-oxygen bond is much stronger than the zinc-oxygen bond, explaining the inertness of zirconium oxide ($ZrSiO_4$) to acid attack while zinc orthosilicate and zinc pyrosilicate are quite soluble. Complexation of the metal cation of the silicate and the anion of the solublising acid enhances the solubility of silicates. This explains the order of reactivity of the following acids on zinc orthosilicate and zinc pyrosilicate: Zinc orthosilicate: phosphoric acid > sulfuric acid > perchloric acid > hydrochloric acid. Zinc pyrosilicate: phosphoric acid > sulfuric acid > hydrochloric acid. Complexation of the metal cation of the silicate with sulfate ions explains the increase in the dissolution rate of zinc orthosilicate and zinc pyrosilicate upon addition of sulfate.

From this literature study, it can be concluded that the zinc industry is fortunate to have a most suitable solvent in sulfuric acid, in the form of zinc plant Cell room spent electrolyte, for the dissolution of zinc orthosilicate and zinc pyrosilicate. The high sulfate loading in hydrometallurgical zinc plant liquors is also advantageous to dissolution of these minerals.

The mineral acid dissolution of zinc orthosilicate and zinc pyrosilicate was studied by Terry and Monhemius (1983) over a range of temperatures and pHs. The stoichiometric dissolution is described according to the following, respective reactions:

$$Zn_2SiO_{4\,(s)} + 4H^+_{(aq)} \leftrightarrow 2Zn^{2+}_{(aq)} + Si(OH)_{4\,(aq)}$$

$$Zn_4Si_2O_7(OH)_2.H_2O_{(s)} + 8H^+_{(aq)} \leftrightarrow 4Zn^{2+}_{(aq)} + O(Si(OH)_3)_{2\,(aq)} + 3H_2O_{(aq)}$$

The dissolution of zinc orthosilicate occurs under mixed chemical-diffusional control over pHs from 0.15 to 3.00, and temperatures from ambient up to 80°C. The predominance of chemical or diffusional control is dependent on the temperature and pH conditions used for leaching. At low temperatures and low pH, dissolution is chemically controlled, while at high temperatures and high pH, diffusion is the rate controlling step of dissolution. Dissolution follows the shrinking core model under all conditions studied. Dissolution of zinc pyrosilicate is much more rapid than zinc orthosilicate, and is controlled predominantly by diffusion control over the pH range 2.0 to 3.5. This pH range was used, as dissolution was too rapid to accurately measure below pH 2.0.

Terry (1983c) summarised his own work and that of others on the rates of dissolution of various oxides and silicates in mineral acids. The specific chemical rate, k_s with units of mol Zn cm^{-1} s^{-1}, for the dissolution of zinc orthosilicate by sulfuric acid was expressed as:

$$k_s = 216\exp\frac{-49x10^3}{RT}\left\{H^+\right\}^{0.5}$$

R is the Universal gas constant (J mol^{-1} K^{-1}), T is the temperature (K) and $\{H^+\}$ is the hydrogen ion activity (mol cm^{-3}). This correlation is based on the gas adsorption method for determining the particle surface area. If the correlation is normalised with respect to the geometric area for a smooth sphere, the value of k_s should be increased by a factor of 4.3. No results for zinc pyrosilicate are reported.

Zinc orthosilicate was chosen as the source of soluble silica for this study for three reasons:

1. It readily liberates monosilicic acid, which is the base unit for silica polymerisation.
2. Pasminco had a ready supply of run-of-mine ore available for use.
3. Synthetic zinc orthosilicate of reasonably high purity can be easily produced using an adaptation of a method reported by Yatabe, Yamada, Ikawa and Kageyama (1992). The method reacts zinc chloride and sodium metasilicate solutions in an aqueous precipitation stage, followed by a heat treatment to 1250°C.

1.6 AIM OF THE WORK

The aim of this project was to gain an understanding of silica precipitation from electrolytic zinc plant solutions, and also investigate the factors that affect silica precipitation under these conditions. More specifically, it was an investigation into the mechanism of the formation of granular silica precipitates and how this differs from that of unwanted, but more easily produced, silica gels.

The research involved studying the precipitation of silica from supersaturated monosilicic acid solutions obtained by the treatment of zinc orthosilicate with sulfuric acid in the form of Cell room spent electrolyte from a zinc plant. The literature describes several hydrometallurgical processes regarding this treatment, none of which are well understood on a fundamental level, or suitable for Pasminco's specific needs. Beginning with the most appropriate method for Pasminco's purposes, the project involved precipitation studies of silica using actual process reagents and also synthetic reagents. The use of synthetic reagents in an essentially pure system allowed for the effect of impurities and commonly found zinc plant chemicals to be studied. The precipitation studies were carried out on a laboratory scale using a batch and also a continuous crystalliser, both of which were specifically constructed for this project.

The batch crystalliser was used to produce a batch precipitation curve under ideal conditions, with no impurities or additives present, and this was used as a control. This was achieved by leaching synthetic zinc orthosilicate in pure sulfuric acid to produce a supersaturated solution of monosilicic acid. This was aged at temperature in a stirred, jacketed reactor vessel with precipitation monitored by measuring the turbidity and monosilicic acid and silica concentrations in solution at regular intervals. Electron microscopy was used to examine the precipitate morphology and the filterability quantified. Further batch experiments were used to investigate the effect of the fundamental precipitation parameters of supersaturation, sulfuric acid concentration and temperature; additives such as zinc, iron (III) and aluminium sulfates and hydrofluoric acid; and various types of silica seeds. These variables were investigated by comparing their effects on precipitation with those of the control experiment. The criteria used were the length of the induction period, precipitation rate, precipitation time, product morphology and filterability.

The continuous crystalliser was used to apply the knowledge gained from batch experiments to process industrial reagents. This provided industrially relevant information for Pasminco, such as precise flow rates and concentrations of reagents, operating temperature, residence time and mixing and product removal conditions. It also produced relevant information on silica product quality, measured as filterability, settling rate, thickened solids loading, water content of the filter cake and impurity entrainment in the precipitate.

Insight into the mechanism of silica precipitation was gained by analysing information from both the batch and continuous experiments.

The formation of a gel-like silica precipitate, and the subsequent processing problems this causes, is a major limiting factor to increasing production throughput of materials high in soluble silica. In some instances it is enough to prevent processing of such materials altogether. Thus, through gaining fundamental and practical knowledge, this project elucidated the factors that cause gel formation, and help derive strategies to avoid its formation while optimising productivity. Hence, this has provided a sound basis for improving industrial operations.

1.7 DEFINITION OF SILICA STRUCTURES

For the purposes of this research, silica gel refers to dissolved silica that polymerises to consume the contents of the vessel and sets to a thick rubbery mass, much like cured, silicone sealant. Silica micro-gel refers to dissolved silica that has polymerised in a similar fashion to silica gel. However, the silica concentration in micro-gel is much lower than that in silica gel and while the micro-gel entrains all the liquid in the vessel, it still remains fluid although somewhat viscous. A solution of silica micro-gel is extremely difficult to filter. The references to silica gel in this section, generally apply to both silica gel and silica micro-gel, as defined here. Silica precipitate has a completely different structure to that of silica gel or micro-gel, and resembles a traditional precipitate, *ie.* a closely packed structure, excluding most of the mother liquor with each particle essentially independent of the next. As would be expected, a suspension of silica precipitate is easily filtered, in comparison to a suspension of silica micro-gel.

2.0 PREPARATION OF ZINC ORTHOSILICATE MATERIALS

2.1 PRODUCTION AND CHARACTERISATION OF SYNTHETIC ZINC ORTHOSILICATE

Synthetic zinc orthosilicate, to be used in the batch precipitation experiments, was produced from zinc chloride and sodium metasilicate using an adaptation of the method described by Yatabe, Yamada, Ikawa and Kageyama (1992). The actual method used to produce 10 kg of material is described below.

Zinc chloride (25 kg) was dissolved, with stirring, in 73 L of water in a 200 L drum. Similarly, 19.4 kg of sodium metasilicate was dissolved in 122 L of water. The resulting solutions were pressure filtered through a 1.0 μm membrane to remove insoluble impurities. The zinc chloride solution was added to the sodium metasilicate solution over the course of four hours, with constant stirring. An additional three hours of stirring followed, after which the slurry was allowed to settle for 24 hours. The supernatant liquor was decanted, and the remaining slurry pressure filtered (1.0 μm membrane). The recovered solid was repulped in 30 L of water, stirred for one hour, pressure filtered (1.0 μm membrane) and dried at 100°C in an oven for 24 hours. The intermediate solid was sintered at 1250°C for eight hours in clay pots. A large amount of material fused to the clay pots and could not be recovered. The remaining solid was crushed using a rod mill to pass a 53 μm screen. Batches of the solid product, weighing approximately 1 kg, were leached with stirring in 4 L of sodium hydroxide solution (3 M in Milli-Q^{TM} water) at 85°C for 3 hours. A 5 L glass beaker covered with a watchglass was used. This step was used to remove amorphous silica that had co-precipitated with the zinc orthosilicate. Following this, the slurry was pressure filtered (0.45 μm membrane) and washed with water. Re-leaching, under the previous conditions, followed by pressure filtering (0.45 μm membrane) and washing with Milli-Q^{TM} water were carried out and finally the zinc orthosilicate product was dried in an oven at 60°C for 24 hours. The yield was 6 kg, the major loss of product occurring during the sintering stage.

The particle size of -53 μm was chosen to allow for rapid dissolution in the batch experiments. The particle size distribution (PSD) of the synthetic zinc orthosilicate after screening is shown in Figure 2.1. The ordinate in Figure 2.1, and all other PSDs in this thesis, represents the frequency of particles of a specific size.

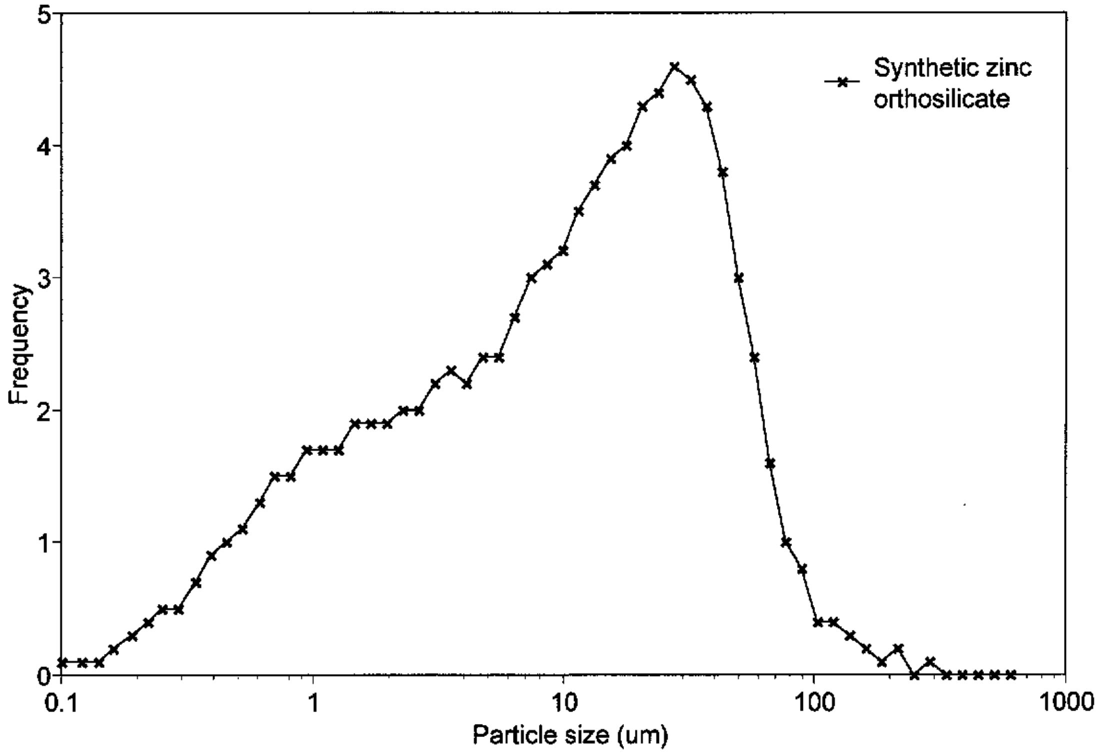

Figure 2.1: PSD of the synthetic zinc orthosilicate after preparation.

The synthetic zinc orthosilicate has a PSD centred at about 30 μm, with a gradual decline in the distribution towards the smaller particle sizes and a sharp decline in the distribution towards the larger particle sizes, a result of screening the material through a 53 μm screen. The small amount of material reporting over 53 μm in size is the result of particles with one dimension greater than 53 μm, passing through the screen.

The synthetic zinc orthosilicate was characterised using X-ray diffraction (XRD). The diffractogram is shown in Figure 2.2, with the identified peaks labelled. Clearly, the predominant phase is willemite, Zn_2SiO_4. Table 9.1 details the minor element composition of the synthetic zinc orthosilicate. The presence of several unidentified peaks in the XRD is indicative of other minor phases present. However, nothing conclusive could be identified until the synthetic material was treated to determine the percentage of insoluble material, the method detailed in Section 9.2.2.5. XRD of the insoluble residue indicated that the phase tridymite (SiO_2) was present. It is therefore assumed that the 10.1% (w/w) insoluble material listed in Table 9.1, is tridymite.

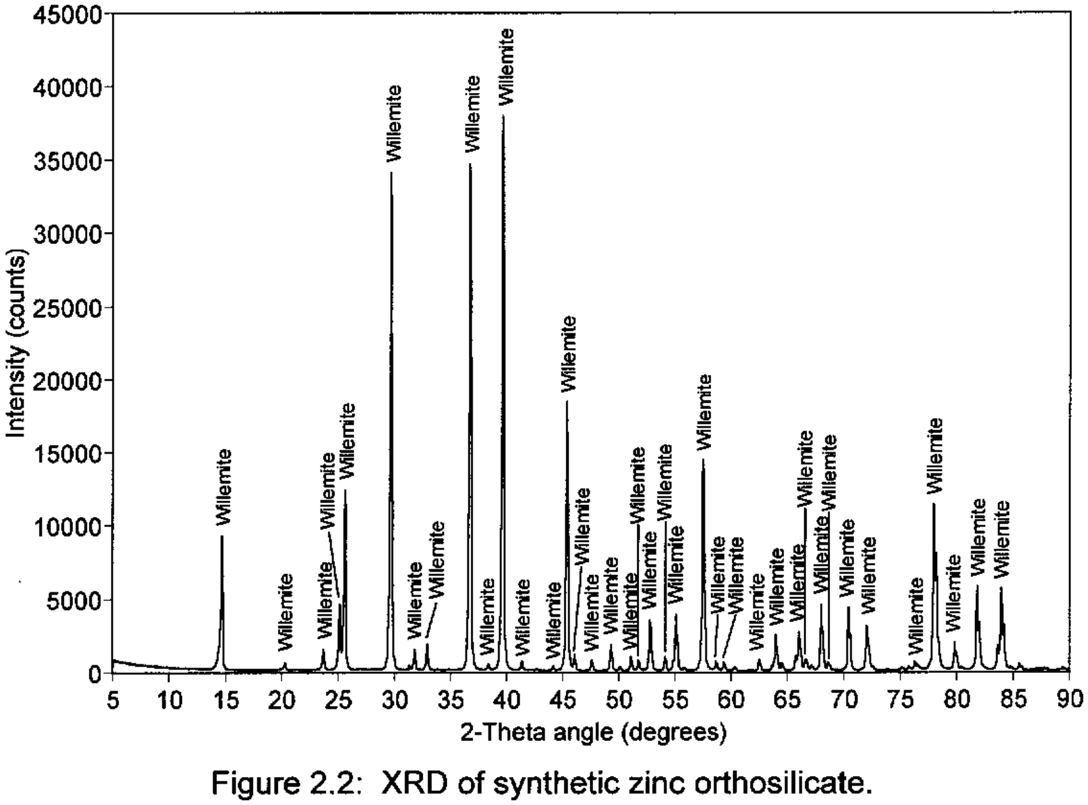

Figure 2.2: XRD of synthetic zinc orthosilicate.

A scanning electron microscopy (SEM) analysis of the synthetic zinc orthosilicate and associated tridymite phase was not conducted as the batch experiments that used the zinc orthosilicate removed the insoluble tridymite phase by filtration prior to silica precipitation. Thus, a knowledge of the interaction between the zinc orthosilicate and the tridymite is not important.

2.2 PREPARATION AND CHARACTERISATION OF NATURAL ZINC ORTHOSILICATE

The natural zinc orthosilicate ore (50 kg) was supplied by Pasminco. The particle size was less than 10 mm. A jaw crusher with a set of 4 mm was used to crush the ore initially. The ore was air dried in an oven at 60°C for 24 hours and then pulverised using a continuous ring mill. The material was screened using a vibrating screen separator fitted with a 100 μm screen. Oversize material was repeatedly reground until all material passed through the screen. A riffle splitter was used to split the ore into approximately 1.25 kg packets.

The chosen particle size of -100 μm was a compromise between the length of time required to prepare the ore and a small enough particle size that would not block the peristaltic pump tubing in the continuous crystalliser, Section 4.0. The PSD of the natural zinc orthosilicate material after sample preparation is shown in Figure 2.3. Also shown, is the PSD of the insoluble material after its separation from the soluble zinc orthosilicate by the method described in Section 9.2.2.5. A knowledge of the PSD of the insoluble material is needed for the continuous precipitation experiments, detailed in Section 4.0. The percentage of insoluble material was found to be 16.8% (w/w).

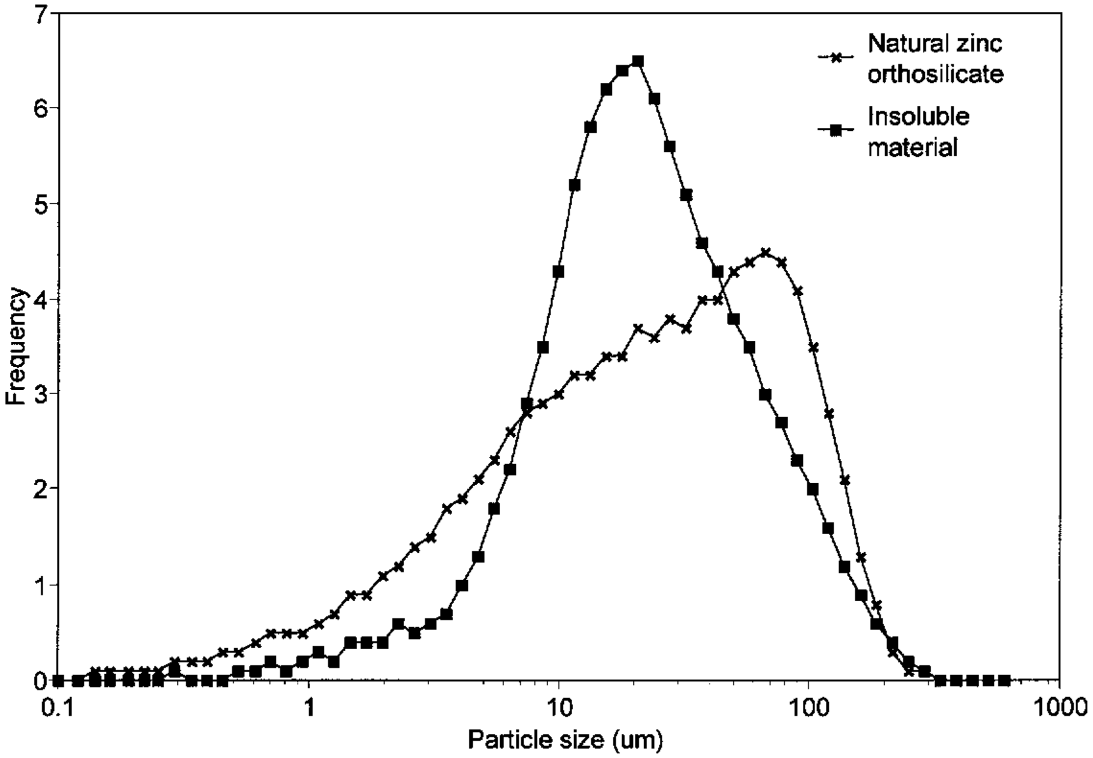

Figure 2.3: PSDs of the natural zinc orthosilicate after sample preparation and the insoluble material remaining after leaching in 50 g L^{-1} sulfuric acid at 95°C.

The PSD of the natural zinc orthosilicate is centred at about 60 to 70 μm, with a gradual decline towards the smaller particle sizes and a sharp decline towards the larger particle sizes, a result of screening the material to pass 100 μm. The presence of the small fraction of material above 100 μm in size has been discussed previously. The PSD of the insoluble material is much narrower than that of the natural zinc orthosilicate material prior to leaching, and has its distribution centred at about 20 μm. Again, the distribution shows particles larger than the expected 100 μm in size.

The natural zinc orthosilicate was characterised using XRD. The diffractogram is shown in Figure 2.4 with the identified peaks labelled.

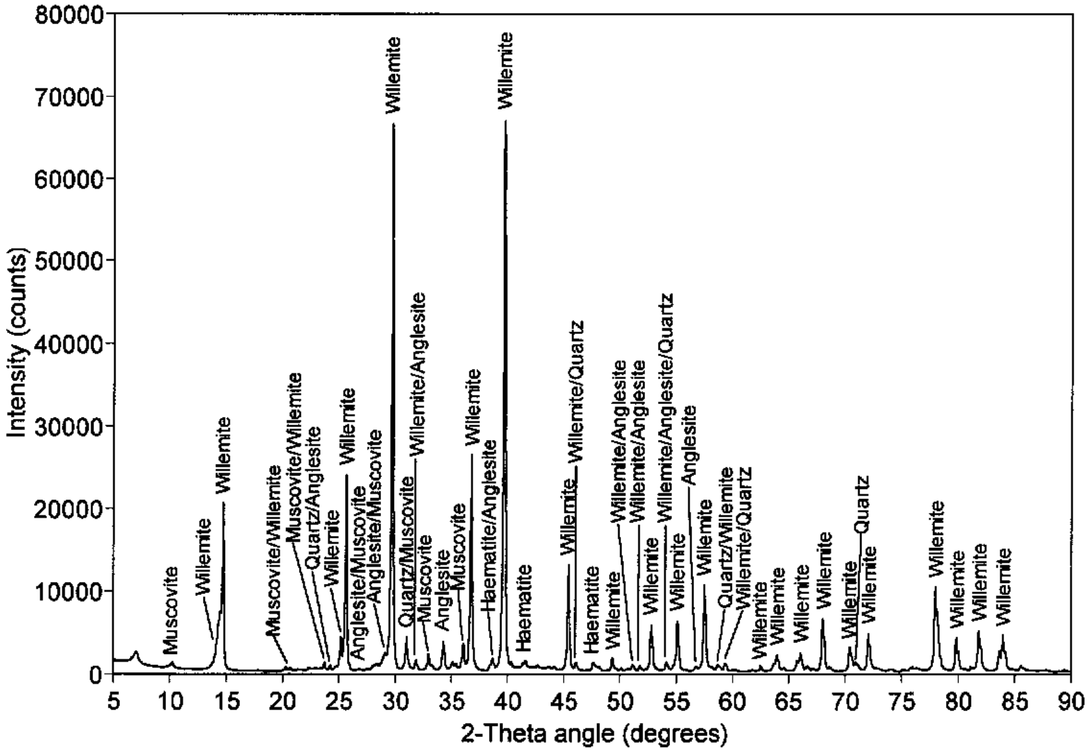

Figure 2.4: XRD of the natural zinc orthosilicate.

The diffractogram in Figure 2.4 clearly shows the most abundant phase to be willemite (Zn_2SiO_4) with traces of quartz (SiO_2), haematite (Fe_2O_3), anglesite ($PbSO_4$) and muscovite ($Al_{2.9}H_2KO_{12}Si_{3.1}$) also being present. Table 9.1 details the minor element composition of the natural zinc orthosilicate material. The presence of these minor phases was confirmed by an XRD analysis of the insoluble residue mentioned above. This analysis also indicated the complete leaching of zinc orthosilicate from the ore.

SEM-energy dispersive X-ray analysis (EDX) was used to characterise a sample of the natural zinc orthosilicate ore that had been set in a resin block which was ground and polished to cross section the particles. In the description that follows, elements are listed in decreasing order of concentration, according to their peak height in the EDX spectrum. It should be noted that this is only a qualitative examination to determine the elements present, not a quantitative determination. Peak height or area is not an accurate method of determining elemental composition because of the dependence of X-ray emission intensity on atomic number and differential absorption of X-rays; particularly those emitted by the light elements because of their relatively low energy. The resin material contains mostly carbon, with a much lesser amount of oxygen and a trace amount of chloride. The EDX spectrum is shown in Figure 2.5. All of the spectra in this section exhibit a trace amount of carbon from the coating process required to enable successful imaging.

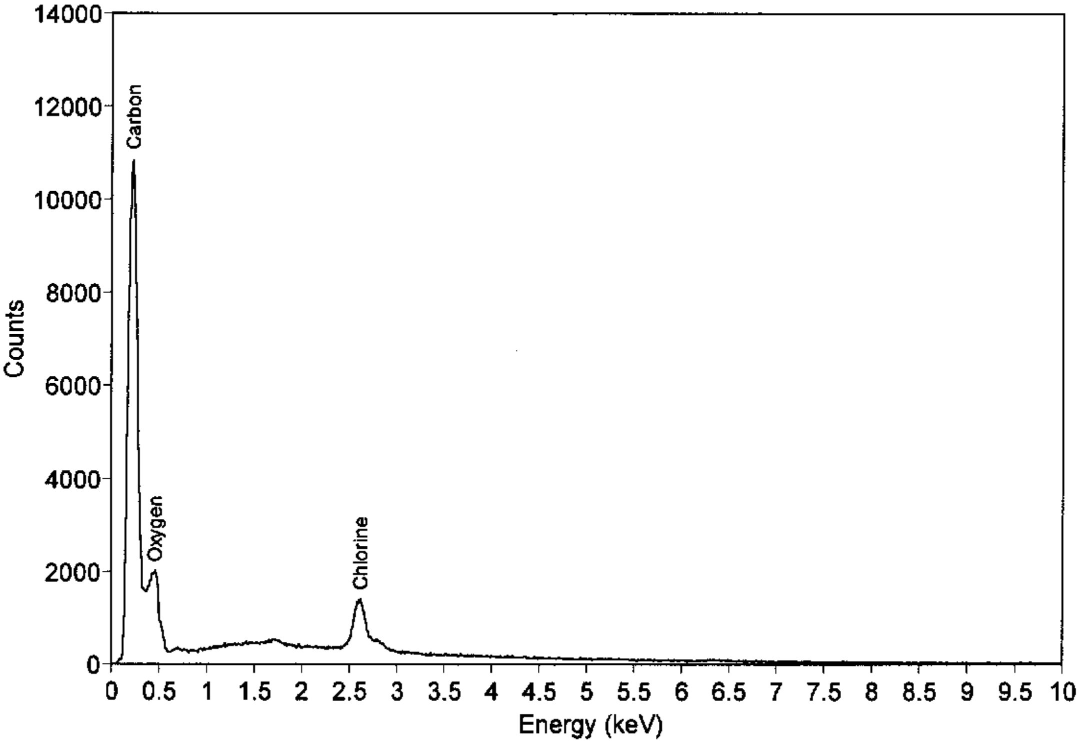

Figure 2.5: EDX spectrum of the resin used to mount the natural zinc orthosilicate sample.

As would be expected, the composition of most of the particles in the sample suggests that they are zinc orthosilicate. Figure 2.6 shows a micrograph of a typical zinc orthosilicate particle, imaged using backscattered electron imaging, as are all micrographs in this section. The resin appears as the black areas surrounding other particles. The EDX spectrum of a typical zinc orthosilicate particle is shown in Figure 2.7. The particles contain zinc, silicon and oxygen, with traces of aluminium and a second unidentified element at 2.7 keV. A double peak for zinc is also present. This result confirms the XRD analysis that the predominant phase is zinc orthosilicate. The majority of the zinc orthosilicate particles present are very pure, containing almost no impurity inclusions. This is evident in Figure 2.6.

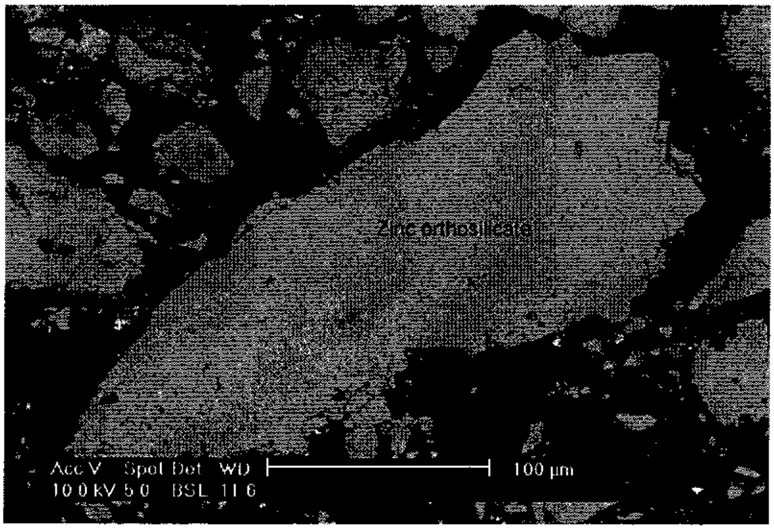

Figure 2.6: SEM micrograph of a typical zinc orthosilicate particle, imaged using backscattered electron imaging.

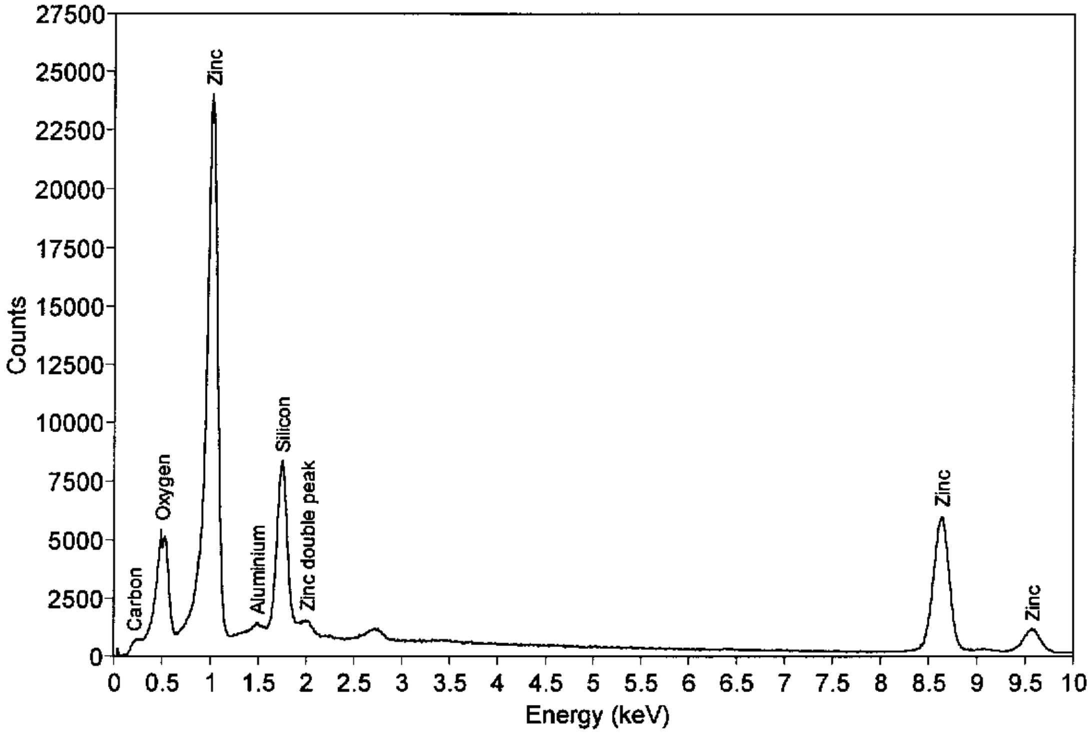

Figure 2.7: EDX spectrum of a typical zinc orthosilicate particle.

XRD identified the mineral anglesite, $PbSO_4$, as being present. This compound was easily detected by atomic number contrast, being white in colour compared to the grey zinc orthosilicate particles. This is clearly shown in Figure 2.8.

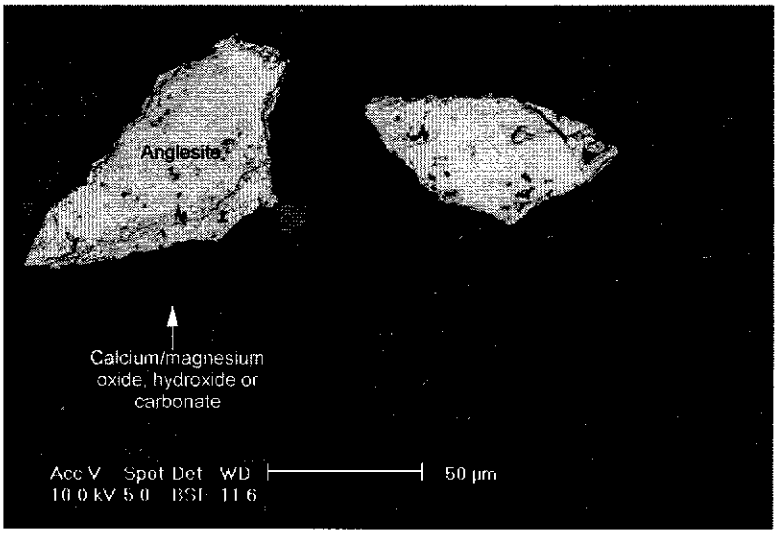

Figure 2.8: SEM micrograph of anglesite, zinc orthosilicate and calcium/magnesium oxide, hydroxide or carbonate particles, imaged using backscattered electron imaging.

The anglesite particles, as determined by SEM-EDX, were found to be composed of arsenic, lead, sulfur, oxygen and calcium, with a trace of zinc present. The EDX spectrum is shown in Figure 2.9. A double peak for lead/sulfur is also present in the spectrum. The results of the ICP-AES analysis of the natural zinc orthosilicate material, shown in Table 9.1, indicate that 2.0% lead and 0.92% arsenic are present in the ore. It is reasonable to infer therefore, that this phase is arsenic rich anglesite, containing calcium and zinc as impurities.

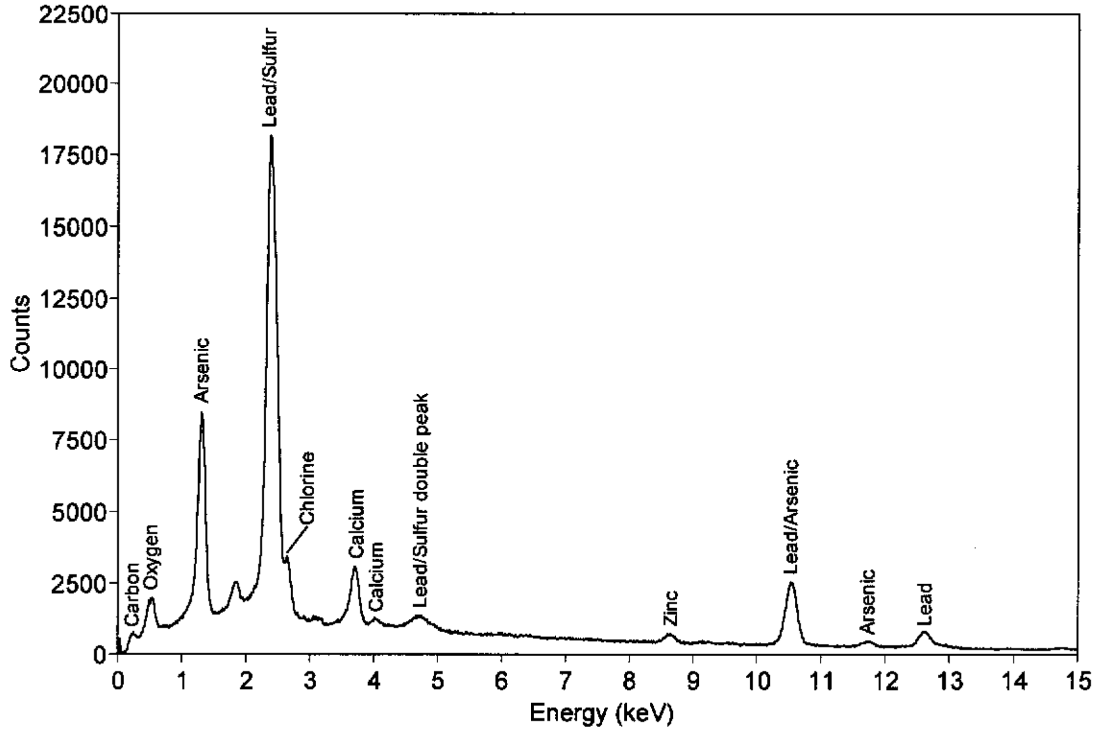

Figure 2.9: EDX spectrum of a typical anglesite particle.

Also visible in Figure 2.8 is another impurity phase, darker in atomic number contrast than the zinc orthosilicate. The EDX spectrum for this material is shown in Figure 2.10 and contains peaks for calcium, magnesium and oxygen, with lesser amounts of carbon, silicon, manganese, iron and zinc. It is assumed this phase is some type of calcium/magnesium oxide, hydroxide or carbonate. This phase was not identified by XRD and is of very low occurrence.

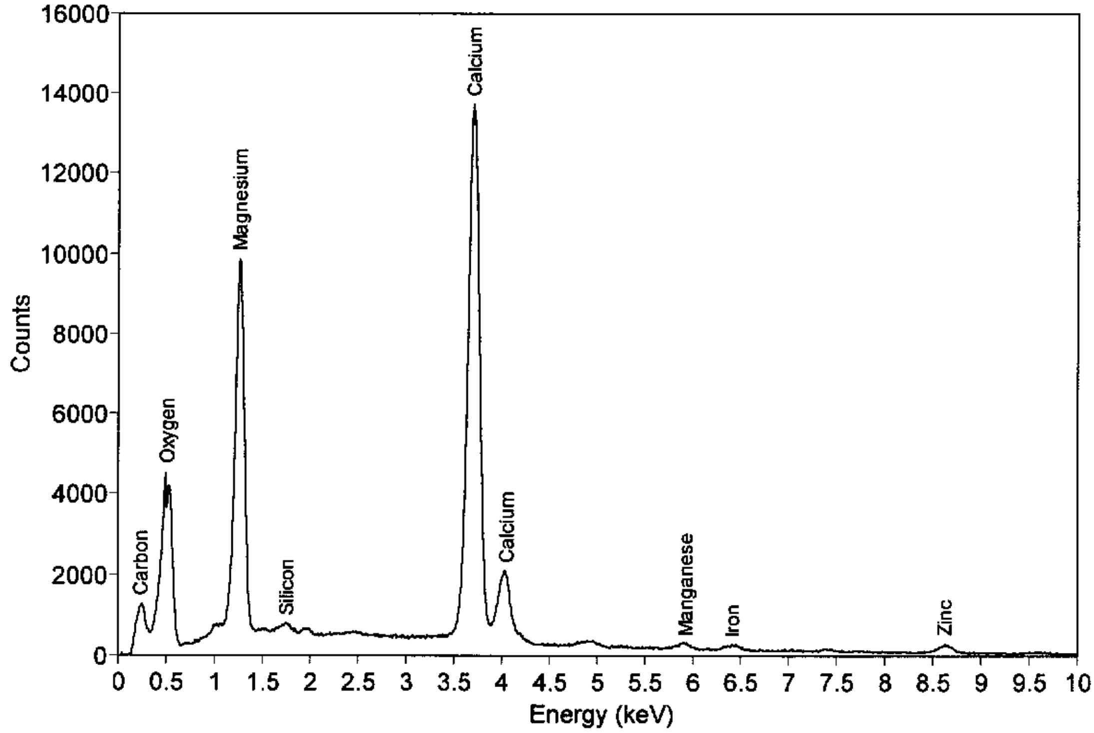

Figure 2.10: EDX spectrum of calcium/magnesium oxide, hydroxide or carbonate impurity phase.

Figure 2.11 shows the EDX spectrum of another impurity phase detected in the natural zinc orthosilicate ore. This phase contains silicon, oxygen and a small amount of mercury, a silicon double peak is also present. This material is most likely to be quartz (SiO_2), as this phase was detected using XRD.

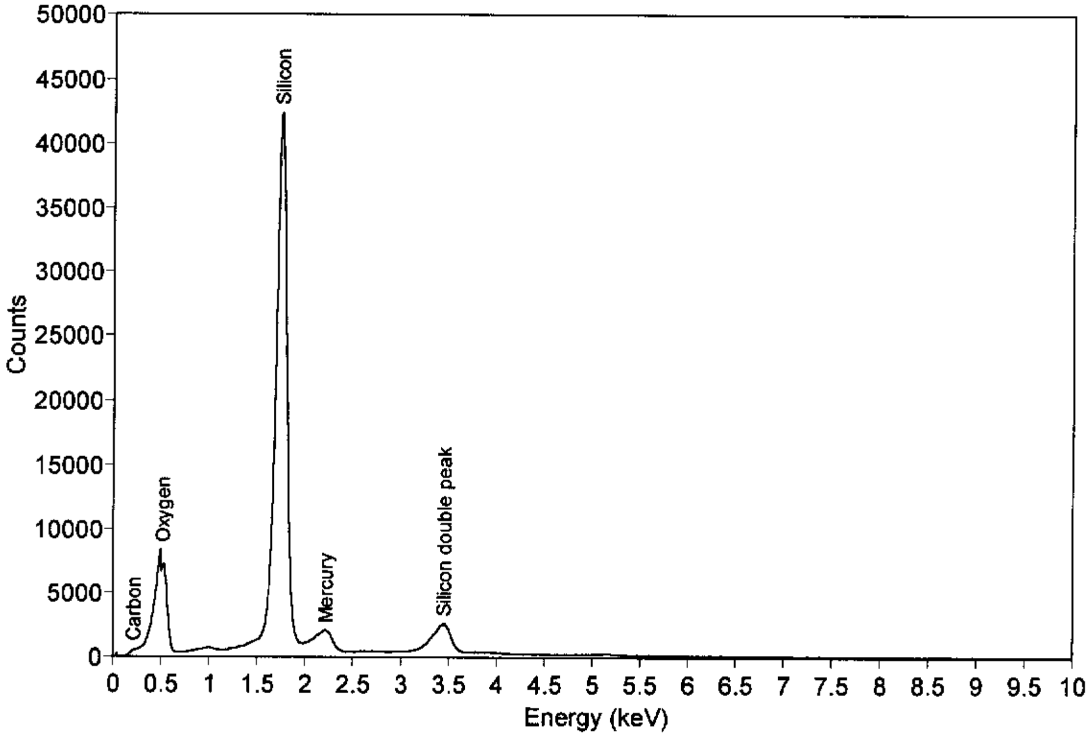

Figure 2.11: EDX spectrum of a typical quartz particle.

Figure 2.12 shows a micrograph of a quartz particle with several zinc orthosilicate particles. Two of the zinc orthosilicate particles have quartz associated with them. Another impurity phase is present in Figure 2.12. Its EDX spectrum is shown in Figure 2.13, and contains peaks for iron and oxygen and much smaller ones for silicon, aluminium and zinc. The use of XRD identified the presence of haematite (Fe_2O_3) in the ore sample. Thus, this impurity detected by SEM-EDX is probably haematite.

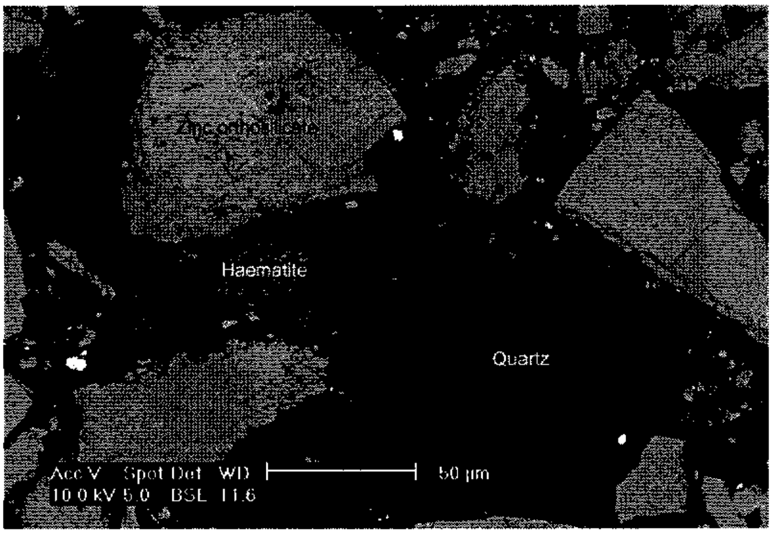

Figure 2.12: SEM micrograph of a quartz particle, several zinc orthosilicate particles, some with associated quartz and a haematite particle, imaged using backscattered electron imaging.

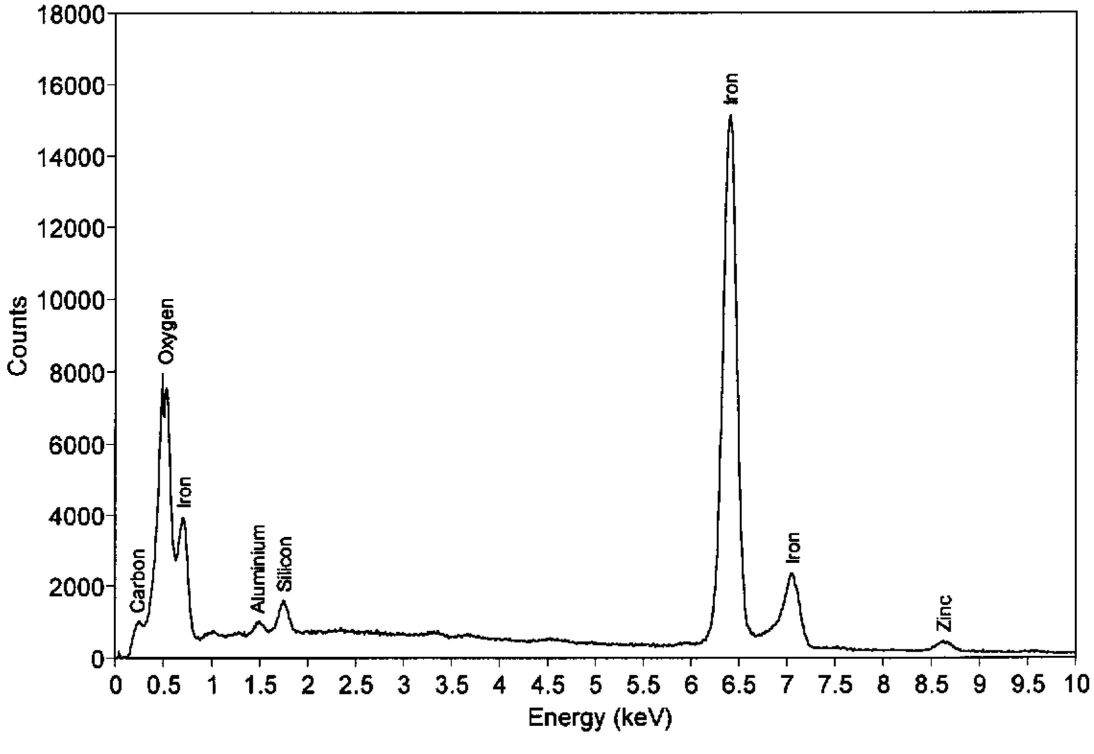

Figure 2.13: EDX spectrum of a typical haematite particle.

The remaining impurity phase identified in the natural zinc orthosilicate by XRD is muscovite ($Al_{2.9}H_2KO_{12}Si_{3.1}$). This presence of this phase was confirmed by SEM-EDX, with a typical spectrum shown in Figure 2.14. Peaks are present for silicon, aluminium, potassium and oxygen. Other minor peaks are present; however, they are too weak to be accurately identified.

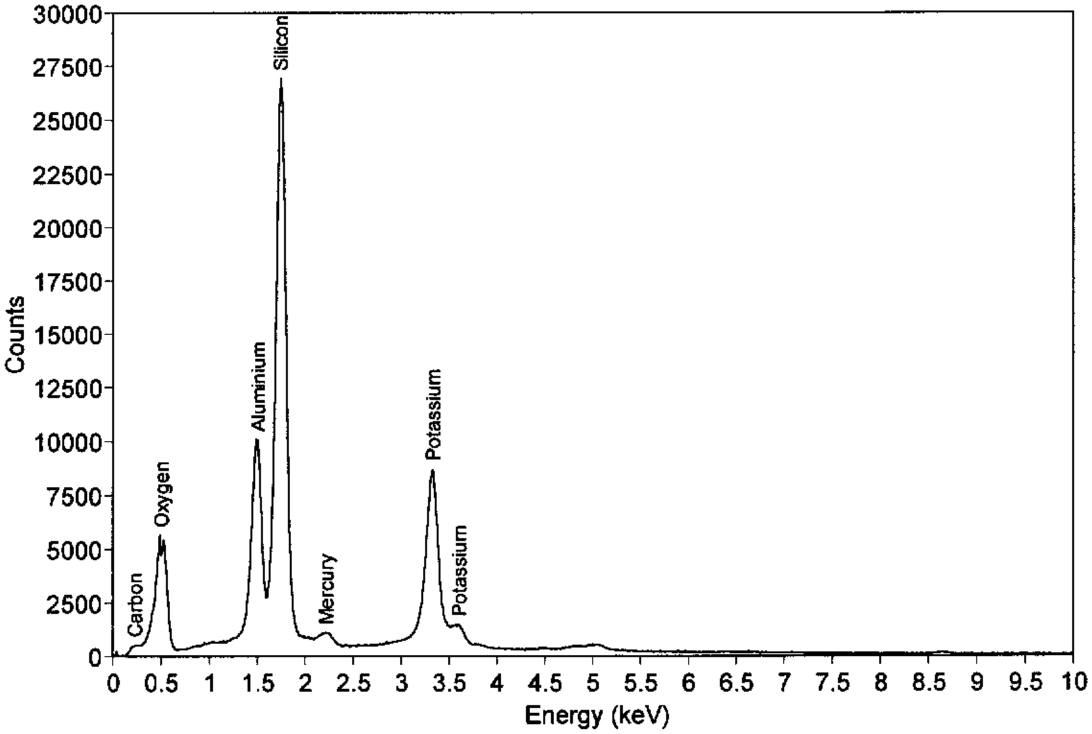

Figure 2.14: EDX spectrum of a typical muscovite particle.

Muscovite was found both associated with quartz, as is shown in Figure 2.15, and also on its own.

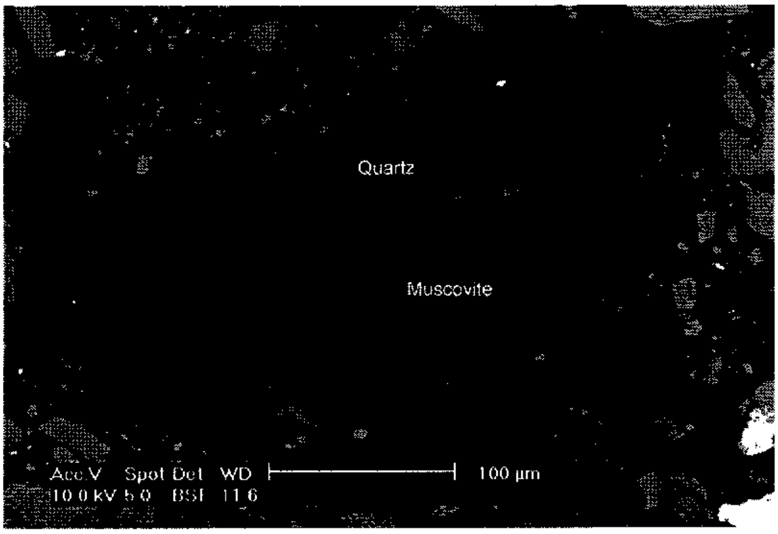

Figure 2.15: SEM micrograph of a quartz-muscovite particle, imaged using backscattered electron imaging.

As seen in some of the previous micrographs, some particles contain multiple phases; an example of this is shown in Figure 2.16.

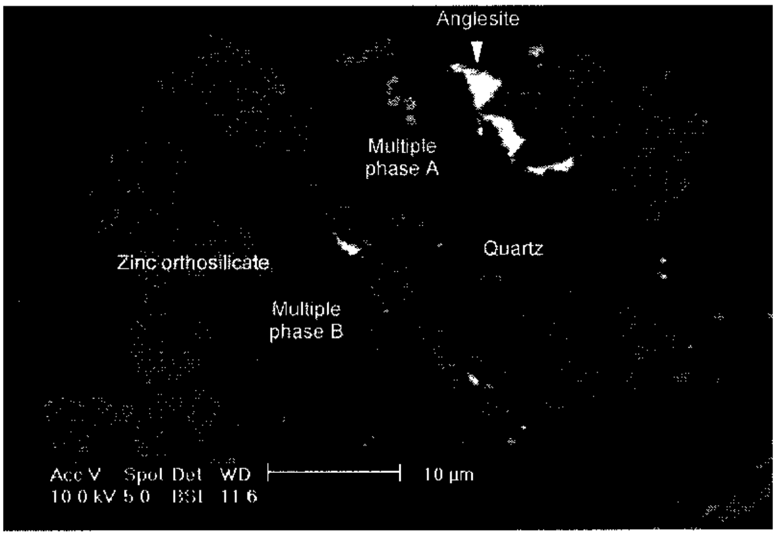

Figure 2.16: SEM micrograph of a particle containing multiple phases, imaged using backscattered electron imaging.

This particle (Figure 2.16) contains zinc orthosilicate, anglesite, quartz and two other impurity phases, the EDX spectra of which are shown in Figure 2.17 and Figure 2.18.

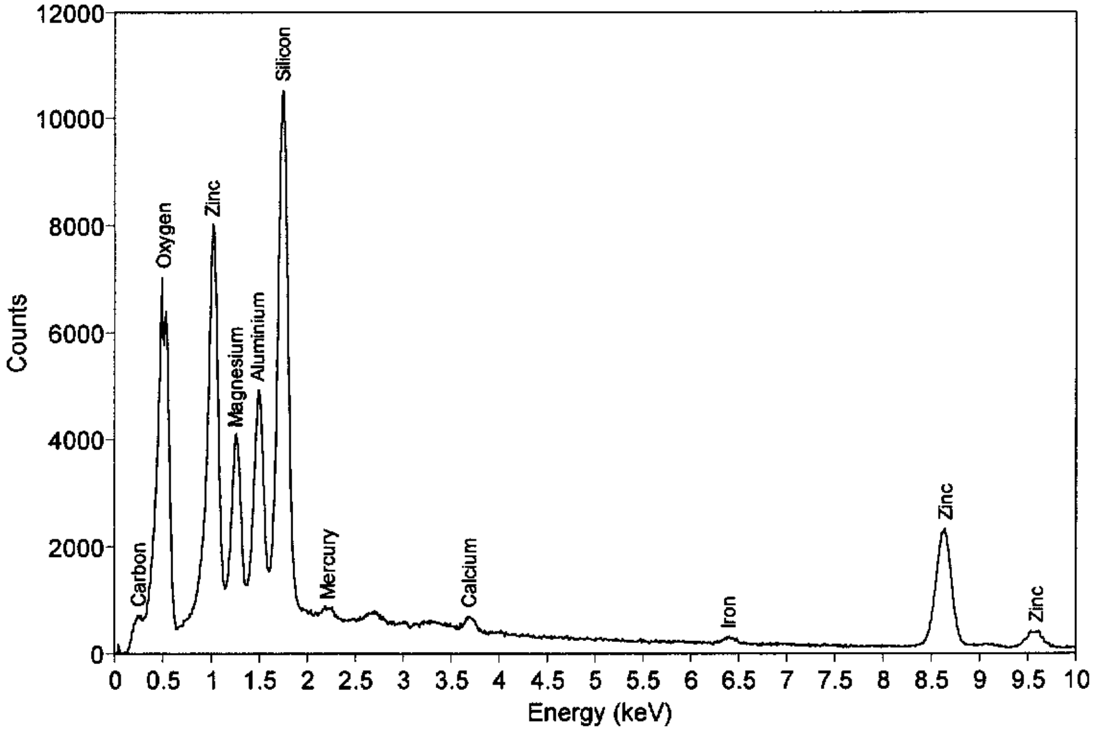

Figure 2.17: EDX spectrum of multiple phase A.

Multiple phase A contains silicon, zinc, oxygen, aluminium and magnesium, with traces of calcium, mercury and iron.

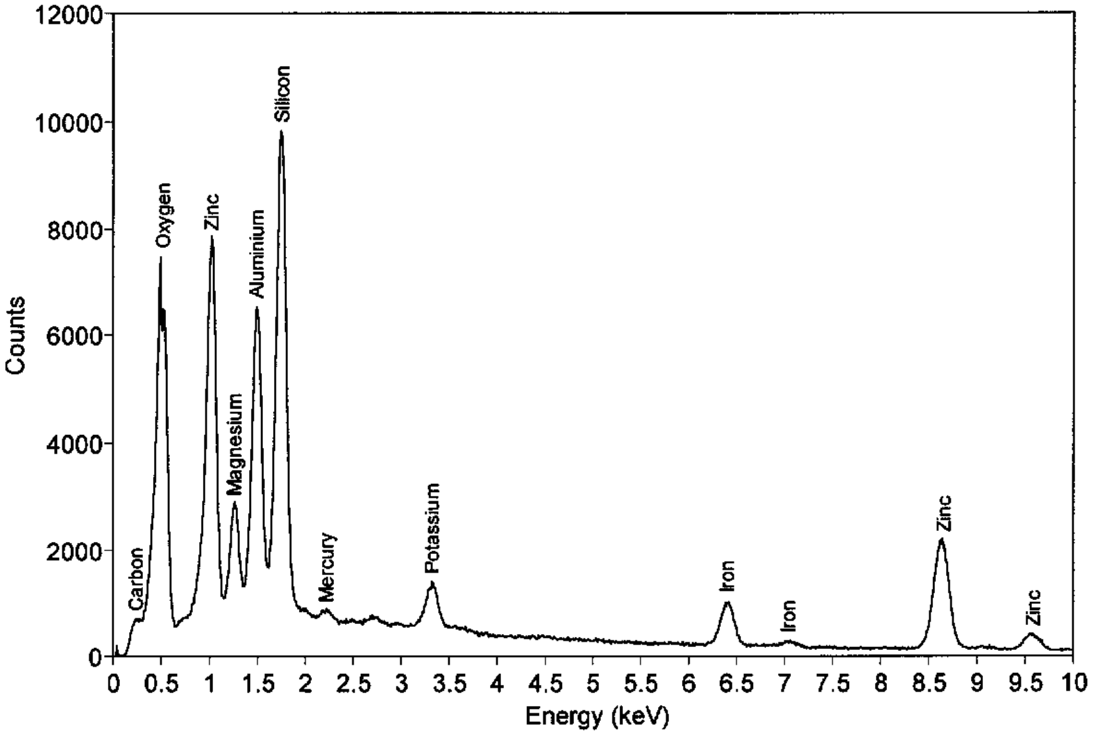

Figure 2.18: EDX spectrum of multiple phase B.

Multiple phase B is very similar in composition to multiple phase A, except that it contains potassium instead of calcium as a minor constituent. These two phases appear to be heterogeneous, as is shown in Figure 2.16, and could be mixtures of several other phases that have already been identified. They are present in very low concentration and were not identified by XRD.

Several other impurity phases were also identified in the natural zinc orthosilicate sample in relatively low concentrations. The EDX spectrum of one of these phases is shown in Figure 2.19; peaks are present for the elements manganese, sulfur and oxygen, with smaller ones present for lead, zinc, calcium and iron. It is likely that this compound is impure manganese sulfate; however, XRD did not detect this phase.

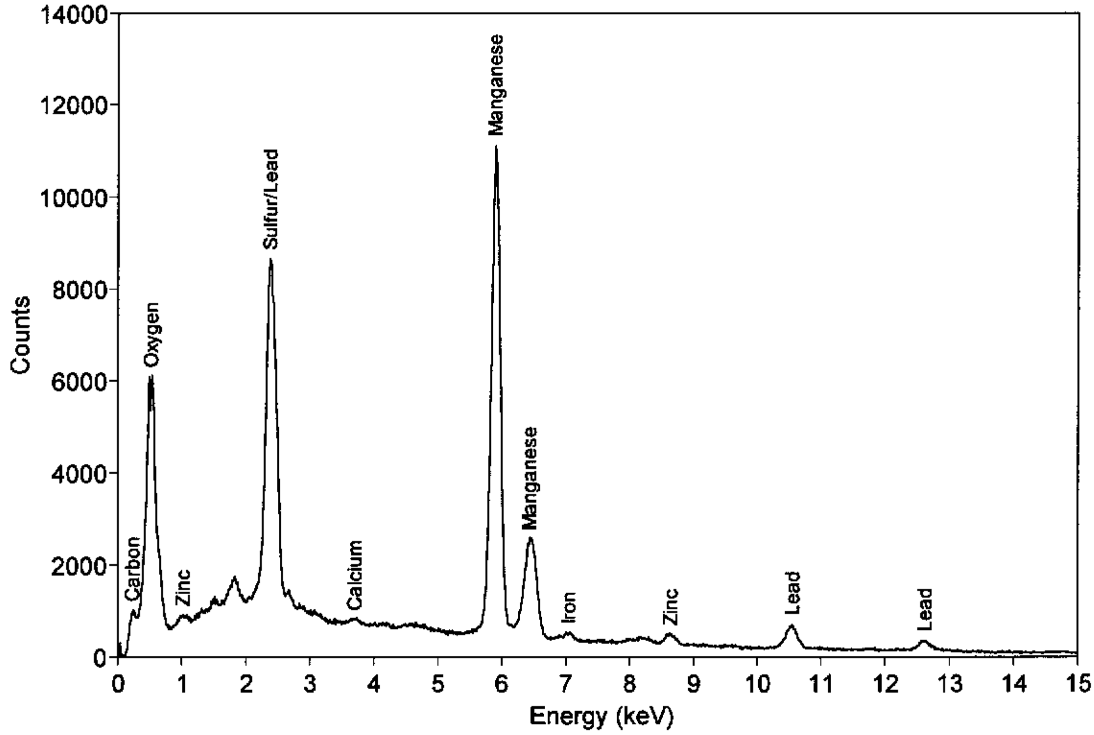

Figure 2.19: EDX spectrum of manganese sulfate.

Manganese sulfate is usually associated with other phases. An example of this is shown in Figure 2.20 where it is imaged associated with a calcium/manganese sulfate phase, the EDX spectrum for which is shown in Figure 2.21. The internal structure of the manganese sulfate is most unusual.

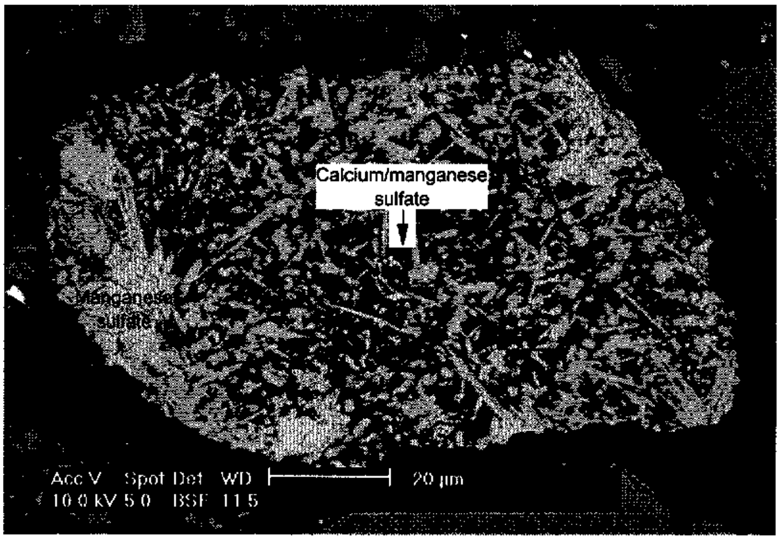

Figure 2.20: SEM micrograph of manganese sulfate associated with a calcium/manganese sulfate phase, imaged using backscattered electron imaging.

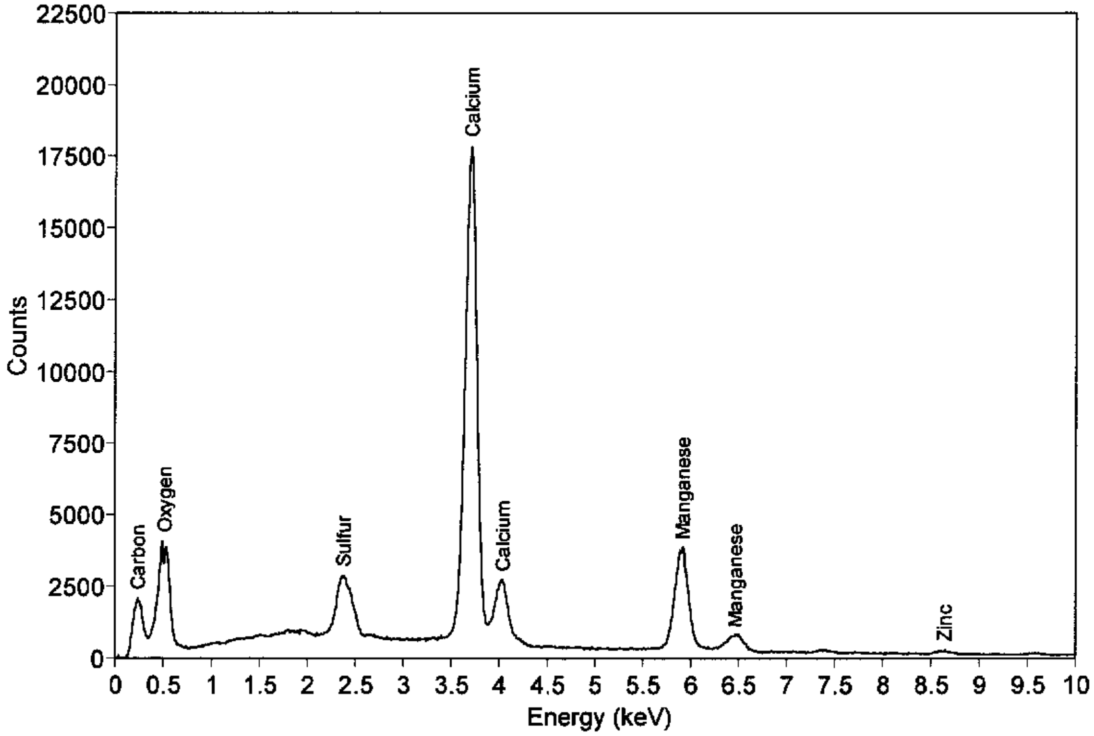

Figure 2.21: EDX spectrum of a calcium/manganese sulfate phase.

Since the EDX spectrum shows calcium, manganese, oxygen and sulfur to be present, the phase is thought to be a calcium/manganese sulfate phase. Small amounts of carbon and zinc are also present.

Manganese sulfate has also been imaged associated with multiple phase C, the EDX spectrum for which is shown in Figure 2.22. Figure 2.23 shows multiple phase A (Figure 2.17) and multiple phase C, intimately associated with a manganese sulfate particle. Once again, the very distinct morphology of the manganese sulfate is visible.

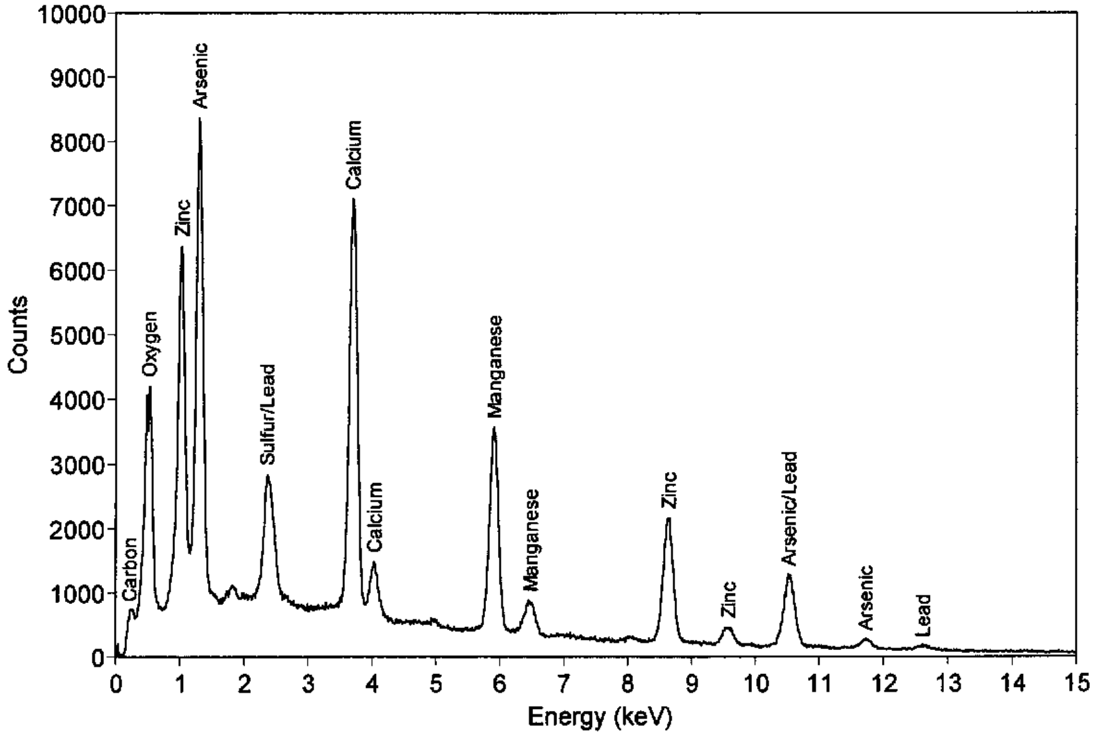

Figure 2.22: EDX spectrum of multiple phase C.

Multiple phase C contains arsenic, calcium, zinc, oxygen, manganese, lead and sulfur. The manganese and some of the sulfur and oxygen detected in the EDX spectrum maybe from the manganese sulfate particle as it is entrained in the multiple phase, as is shown in Figure 2.23. This phase appears to be homogeneous in its nature.

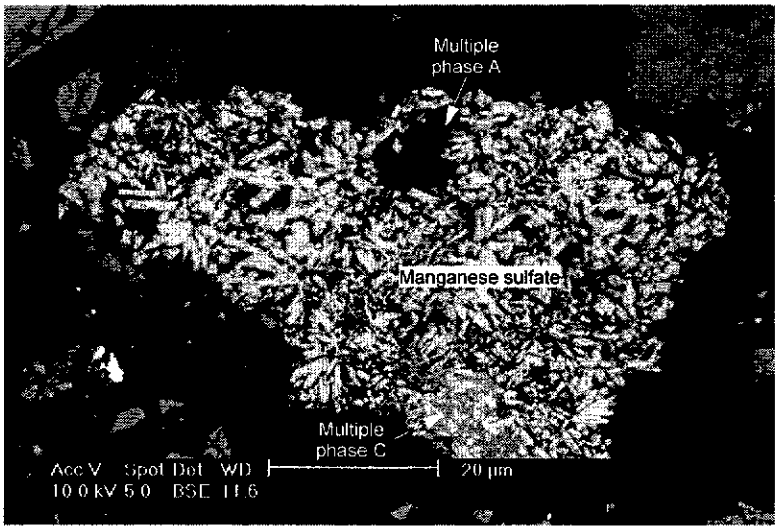

Figure 2.23: SEM micrograph of multiple phases A and C associated with a manganese sulfate particle, imaged using backscattered electron imaging.

3.0 BATCH PRECIPITATION

3.1 INTRODUCTION

This section describes the construction and use of a laboratory scale batch crystalliser to study silica precipitation. The aims of these batch precipitation experiments are described below.

This section of work investigated the mechanism for the formation of silica precipitates, rather than micro-gels. Zinc orthosilicate was leached in sulfuric acid to produce a solution supersaturated with respect to monosilicic acid. The solution was aged at temperature in a stirred, jacketed reactor vessel while the precipitation was monitored by measuring the turbidity and silica concentration in solution at regular intervals. The monosilicic acid concentration was also studied during the reaction. The morphology of the precipitate was examined using Electron microscopy, and the filtration performance quantified when precipitation had ceased.

This section described the effects of supersaturation, sulfuric acid concentration and temperature. Also of interest were the impact of zinc, aluminium and iron (III) sulfates, hydrofluoric acid and various types of silica seeds. These variables were investigated by comparing their effects on precipitation with the results of a control experiment. The comparison criteria to be used were induction time, precipitation rate, precipitation time, product morphology and filterability.

3.2 EXPERIMENTAL OUTLINE

3.2.1 Description of the batch crystalliser

The batch crystalliser consisted of a simple, beaker like reactor vessel, of 400 mL capacity, that was custom fabricated from glass with an integral water jacket for heating the precipitation mixture. A photograph of the crystalliser appears in Figure 3.1.

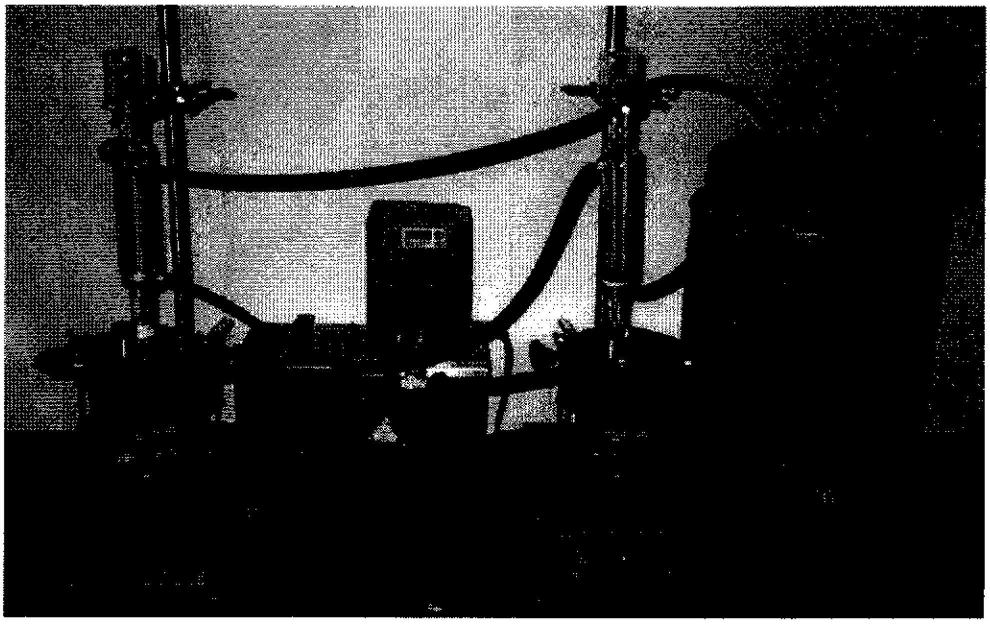

Figure 3.1: Photograph of the batch crystalliser. Note two separate crystallisers are shown.

Figure 3.1 shows a duplicate set-up with two batch crystallisers set up side by side. This enabled higher productivity by performing two experiments simultaneously. The two reactor vessels share common heating water that is circulated through the reactor vessel jackets to maintain the desired precipitation temperature by a Grant heater/circulator fitted to a Grant W6 water bath. Thus, both experiments must be carried out at the same temperature. The heating water is split into two parallel streams by a "Y" connector and delivered to the reactor vessels through equal length tubing to ensure that both reactors operate at the same temperature. The heating water exiting the reactor vessels is recombined in a second "Y" connector before returning to the water bath. Each reactor vessel is fitted with a dual surface condenser to prevent evaporation. In Figure 3.1, 50 mL glass beakers can be seen inverted, atop the condensers to prevent any dust entering the reactor vessels. Cooling water is recirculated through the condensers, which are plumbed in series, from a 20 L drum using a Uno Powerhead submersible pump. The large volume of cooling water used prevents it from becoming heated and losing efficiency. The precipitation liquor in the reactor vessels is stirred at 210 RPM (measured using an optical tachometer) by a magnetic stirrer bar measuring 41 x 12 mm using an IEC hotplate/stirrer.

A 316 stainless steel lid was secured to the glass reactor vessel via a clamping mechanism consisting of two vertical 316 stainless steel shafts, 6 mm in diameter, attached to the base of the clamp. The reactor vessel was placed on the base and a silicone rubber seal placed atop this. The holes in the lid were fitted over the vertical shafts and 316 stainless steel wing nuts (6 mm metric thread) were screwed onto each shaft and tightened to hold the lid in place and compress the seal to create an airtight joint. A cross sectional-view, dimensional drawing of the reactor vessel and lid, with its clamping mechanism is shown in Figure 3.2.

The lid contains two holes to clamp it to the base, a sampling port and another port fitted with a polypropylene fixture to accept the dual-surface condenser. A plan-view, dimensional drawing of the reactor vessel lid is shown in Figure 3.3.

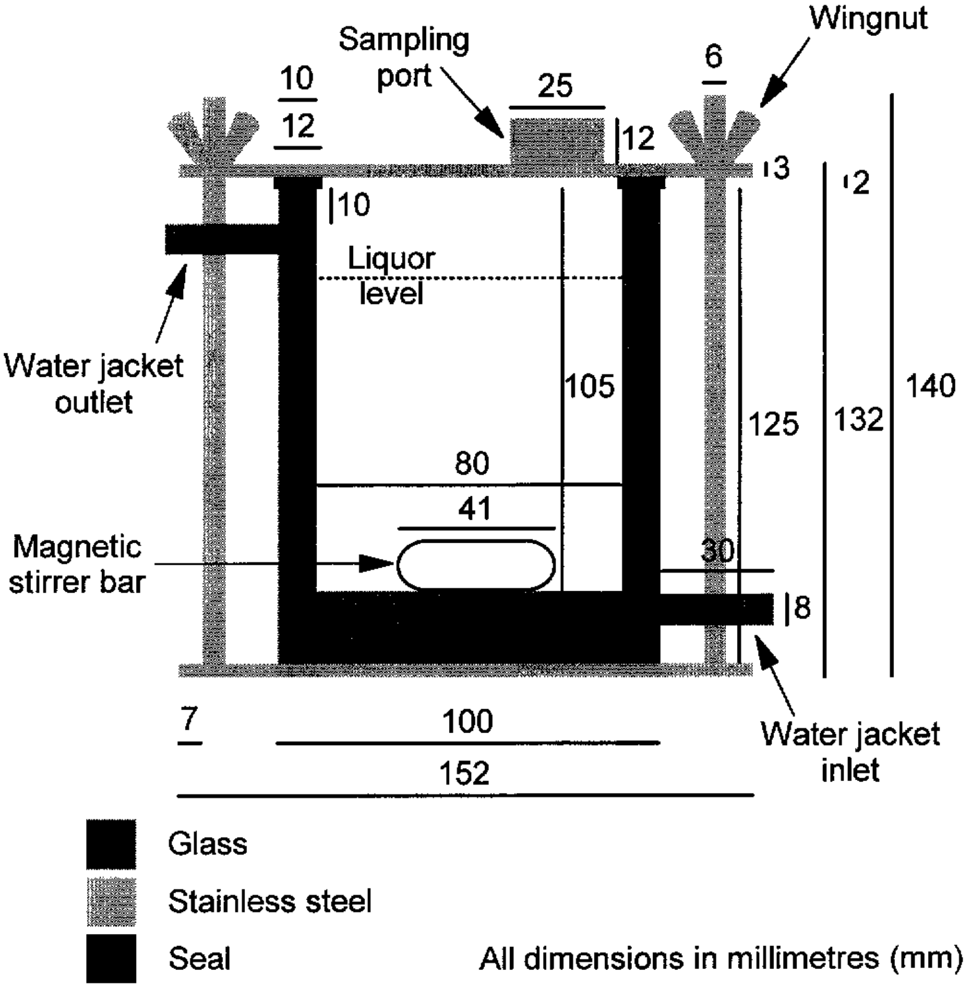

All dimensions in millimetres (mm)

Figure 3.2: Cross sectional-view, dimensional drawing of the reactor vessel and lid with its clamping mechanism.

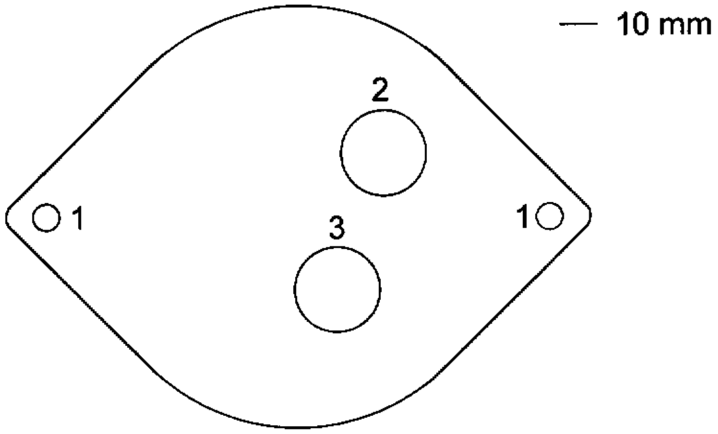

1 Fixing to secure lid to reactor vessel, 7.0 mm.
2 Sampling port, 22.0 mm.
3 Condenser, 23.0 mm.

Figure 3.3: Plan-view, dimensional drawing of the reactor vessel lid.

Details of the sampling port and condenser fitting are shown in Figure 3.4 A and B, respectively. The sampling port, hole 2 in Figure 3.3 is shown in further detail in Figure 3.4 A. It is constructed from 316 stainless steel and is welded to the lid of the reactor vessel. The plug that seals the sampling port is also manufactured from 316 stainless steel and uses a nitrile rubber O-ring to form a seal and simply presses into the lid recess. The large size of the port allows for the turbidity probe to be inserted directly into the reactor vessel.

The dual-surface condenser is connected to the reactor vessel lid using a polypropylene fitting, through hole 3 in Figure 3.3. The fitting is threaded (22 mm metric thread) and is secured to the lid by means of a nut on the underside of the lid; details of both are shown in Figure 3.4 B. The fitting and the nut contain nitrile rubber O-rings for sealing. The lower ground glass joint (Quickfit 19/26) of the condenser is wrapped in Teflon tape and firmly pressed into the tapered polypropylene fitting, with the outside of the joint also being wrapped in Teflon tape. Polypropylene was used for this fitting as it is much softer than stainless steel and is therefore more compatible with a glass fitting.

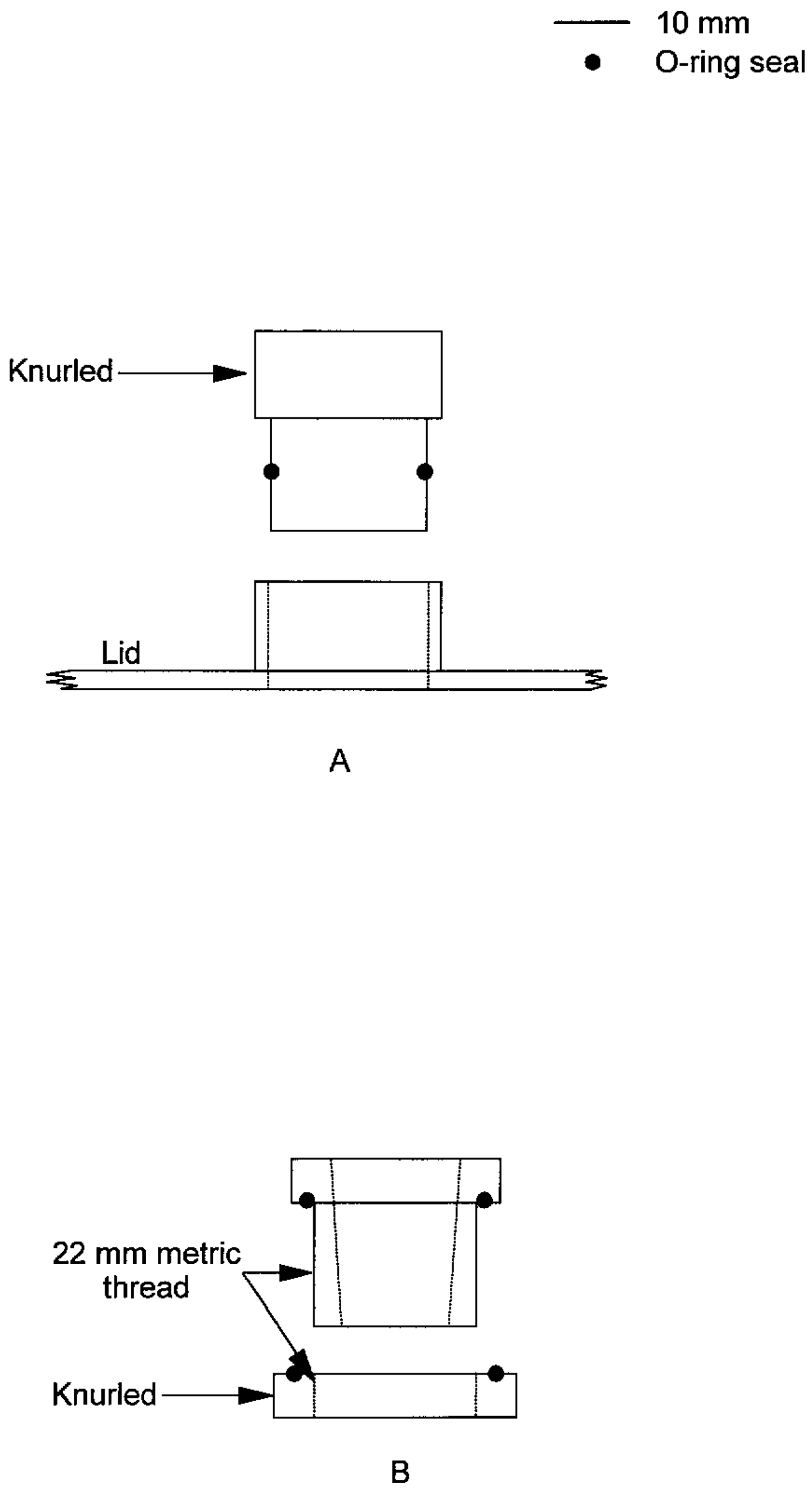

Figure 3.4 A-B: Cross sectional-view, dimensional drawings of the fittings for the reactor vessel lid.

3.2.2 Operation of the crystalliser

The crystalliser components are assembled as shown in Figure 3.1 and the water bath filled. The heater/circulator is switched on and the temperature set on the controller to achieve the correct precipitation temperature, bearing in mind the temperature loss between the water bath and precipitation liquor inside the reactor vessel. The temperature of precipitation liquor is measured directly, using an accurate thermometer, as a check. The condenser cooling water pump is also switched on.

A typical 400 mL precipitation liquor for a batch experiment was produced according to the following procedure. In this example the liquor contains 7000 mg L^{-1} silica as SiO_2 and 50 g L^{-1} sulfuric acid. Synthetic zinc orthosilicate (11.15 g), prepared using the method outlined in Section 2.1, was slurried in 20.0 mL of Milli-Q^{TM} water. An acid solution containing 15.5 mL of sulfuric acid (98% w/v AR grade) and 314.5 mL of Milli-Q^{TM} water was produced. Of the 15.5 mL of sulfuric acid, 10.9 mL is required to achieve the background acidity, while 4.6 mL is needed to dissolve the synthetic zinc orthosilicate. The method to determine the volume of sulfuric acid required to dissolve a set mass of the synthetic zinc orthosilicate is outlined in Section 9.2.2.6. The acid solution was heated to 95°C in a covered, 1000 mL glass beaker and stirred magnetically. The synthetic zinc orthosilicate slurry was washed into the hot acid solution with 50.0 mL of Milli-Q^{TM} water and stirred until dissolution was complete; requiring five minutes at 95°C. When the synthetic zinc orthosilicate slurry was added to the acid solution, the time was noted, as this constituted the start of the precipitation experiment. The liquor was pressure filtered through a Gelman Supor 0.45 μm filter membrane and transferred to the reactor vessel. The sulfuric acid concentration was determined according to the titration method outlined in Section 9.2.2.4 as a quality measure to determine if solution volumes were correct. When differing amounts of synthetic zinc orthosilicate, sulfuric acid or other additives or seeds were used, the volume of Milli-Q^{TM} water was varied accordingly, to maintain the total liquor volume at 400 mL. When the precipitation temperature was lower than 95°C, the acid solution was heated to the required temperature and the leaching time increased to ensure complete dissolution of the synthetic zinc orthosilicate.

Once the precipitation liquor was in the reactor vessel, the magnetic stirrer was switched on and samples were taken at regular intervals throughout the experiment. Individual precipitation curves were constructed using turbidity, silica concentration by ICP-AES and monosilicic acid concentration data. These data were collected using the methods outlined in Sections 9.2.2.1, 9.2.2.2 and 9.2.2.3, respectively. For some experiments, samples were prepared for transmission electron microscopy (TEM) examination at all sampling points, as outlined in Section 9.2.2.7. On several occasions it was necessary to examine a sample using SEM or SEM-EDX. In such cases the sample was prepared according to the method outlined in Section 9.2.2.8.

The relationship between turbidity and particle size and concentration has been described by Gregory and Nelson (1986). The turbidity of a suspension of particles much smaller than the wavelength of the turbidity instrument (in this case 900 nm), increases with the particle size. When the particle size is comparable to the wavelength of the turbidity instrument, the turbidity decreases with increasing particle size. Turbidity is also related to the number of particles in suspension, with an increase in the concentration of particles resulting in an increase in turbidity. The inverse also applies for these three relationships.

The precipitation experiment was considered finished when the liquor turbidity had reached equilibrium. At the end of each experiment a sample was prepared for TEM examination, according to the method in Section 9.2.2.7. The filtration rate of the product was determined using the method described in Section 9.2.2.12.

3.3 RESULTS AND DISCUSSION

3.3.1 Typical precipitation curves

The precipitation curves for the silica and monosilicic acid concentrations, and the turbidity for the experiment described in Section 3.2.2 are shown in Figure 3.5. The turbidity curve reflects changes in the physical nature of the precipitate, and exhibits an induction period followed by a precipitation period which is followed by a small reduction in turbidity associated with ageing of the precipitate. The silica concentration curve reflects changes in solution chemistry, and exhibits an induction period and precipitation period after which equilibrium solubility of 350 mg L^{-1} SiO_2 is attained. The monosilicic acid curve also reflects changes in the solution chemistry, albeit on a different molecular scale. Within nine minutes of the start of the experiment about 80% of the monosilicic acid has reacted, and after about five hours the concentration has reached equilibrium solubility of 350 mg L^{-1} expressed as SiO_2. It is clear from this result that only monomer is present at equilibrium, and no higher silica species are present. Due to the very rapid reaction and disappearance of the monosilicic acid from solution, it was decided not to pursue this method as a means of monitoring precipitation.

The equilibrium solubility value of 350 mg L^{-1} SiO_2 at 95°C is close to that reported by Iler (1979) of 321 mg L^{-1} at 100°C. It is also within the ranges 350 to 400 mg L^{-1} at 95 to 100°C reported by Radino (1957) and 290 to 380 mg L^{-1} at 90°C reported by Bodson (1974). These last two literature values were determined from precipitation in hydrometallurgical zinc liquors. The value of 350 mg L^{-1} will be used in this research and in all calculations of silica supersaturation ratio, as described in Section 1.3. Thus, the silica supersaturation ratio for this particular experiment is 20.0, which corresponds to 7000 mg L^{-1} SiO_2. For the remainder of this section, silica concentrations will be expressed as supersaturation ratios.

The silica concentration and turbidity curves, in Figure 3.5, describe different processes, as their induction and precipitation periods do not coincide. This experiment was performed in duplicate to test experimental reproducability of the silica concentration and turbidity measurements which, as can be seen in Figure 3.5, was very good.

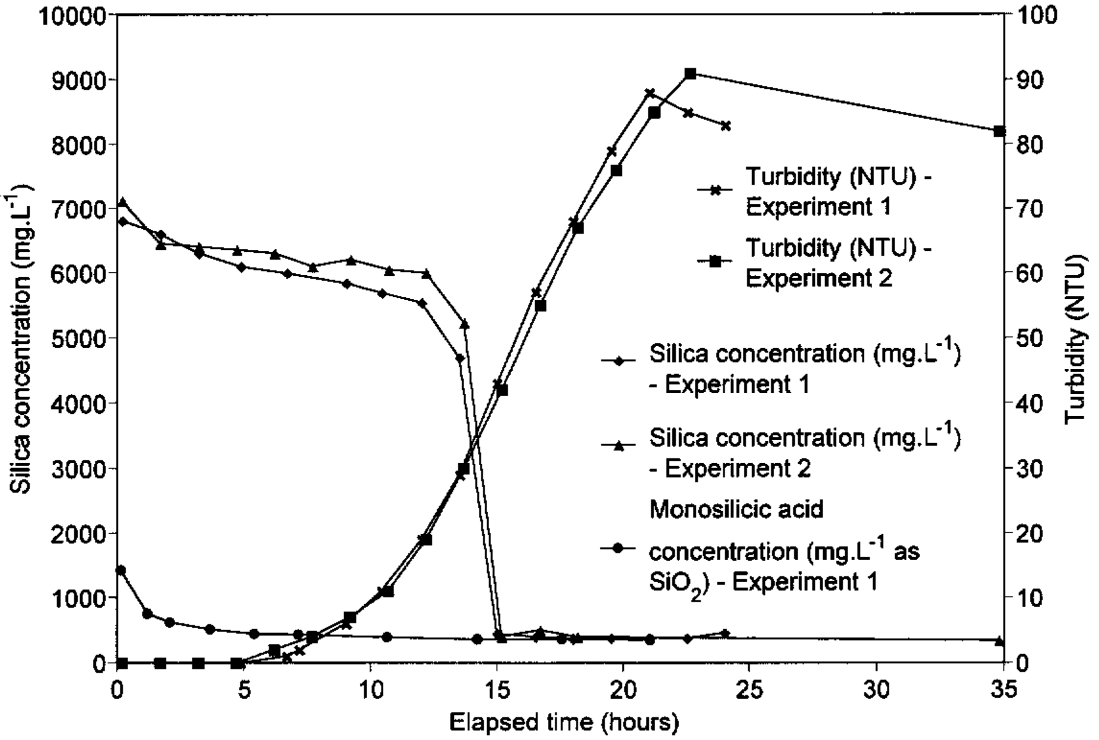

Figure 3.5: Silica precipitation curves. Turbidity, and silica and monosilicic acid concentrations versus time, testing experimental reproducability. Precipitation conditions for both experiments: S = 20.0, 50 g L^{-1} H_2SO_4 and 95°C.

Analysis of the qualitative filtration data, recorded at each sampling point when the liquor was filtered for ICP-AES analysis, indicates that the liquor became extremely difficult to filter when equilibrium solubility of silica (SiO_2) was reached. The poor filtration performance of the silica product would suggest that a micro-gel had formed. The morphology of a typical micro-gel particle from this experiment is shown in Figure 3.6, and appears as a very porous structure of approximately 500 nm in size.

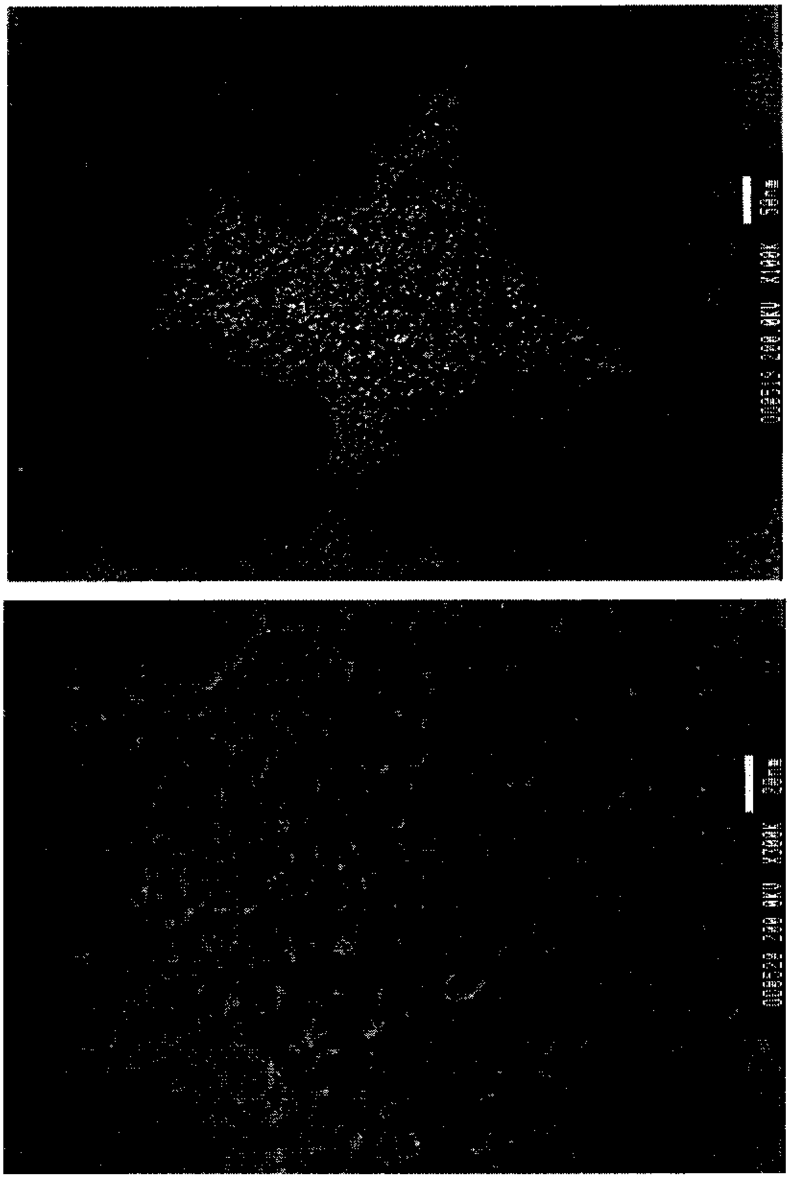

Figure 3.6: Transmission electron micrograph of a typical micro-gel particle, imaged at two different magnifications. The scale bar is displayed on the upper right hand side of the micrograph. Precipitation conditions: S = 20.0, 50 g L^{-1} H_2SO_4 and 95°C.

It must be appreciated that the particle in Figure 3.6 has become dehydrated from the high vacuum of the TEM and appears two dimensional from being laid out on the specimen grid, and because of the nature of TEM imaging. The use of XRD has confirmed that these particles are amorphous.

After further experimentation, it was discovered that the silica concentration curve could be shifted along the time axis depending on the pore size of the membrane filter used. An example of this is shown in Figure 3.7, where the samples collected for silica determination were filtered successively through 0.45, 0.20 and 0.10 μm filter membranes prior to analysis. All samples were collected from the same experiment.

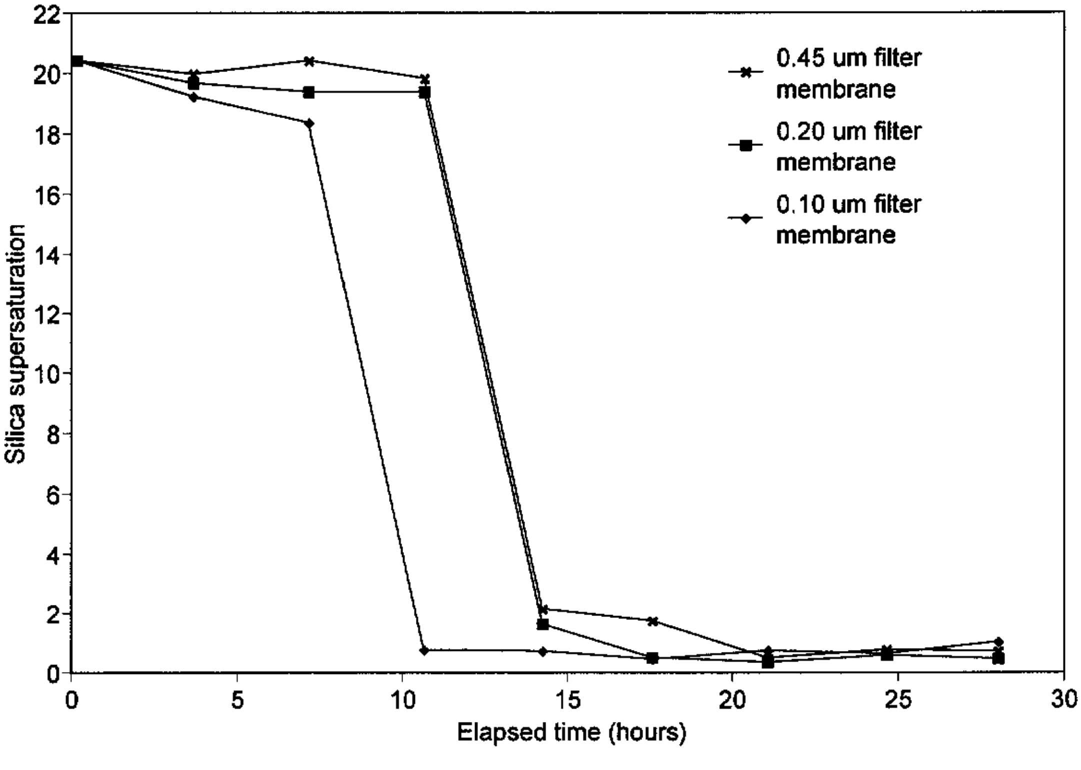

Figure 3.7: Silica precipitation curves. Silica concentration versus time as a function of filter membrane pore size. Precipitation conditions: S = 20.0, 50 g L^{-1} H_2SO_4 and 95°C.

The samples filtered through the 0.45 μm membrane exhibit the highest silica concentration throughout the experiment and are the slowest to reach equilibrium solubility. The smaller the pore size of the membrane used to filter the sample, the lower the apparent silica concentration. This is strong evidence that a micro-gel is precipitated under these conditions. The general shape of the silica concentration curve is a result of micro-gel forming and, as time progresses, the micro-gel becomes stronger and is less readily forced through the filter membrane. At some particular point in time, most of the micro-gel is unable to be forced through the filter and thus a massive decrease in the apparent silica concentration is measured. When using a smaller pore sized membrane, this event will appear much earlier in the precipitation experiment. As a result of this, this method does not measure true SiO_2 concentration in solution but the solution SiO_2 concentration plus the mass of silica particles passing through the pores of the particular membrane used. This method is thus suitable for the comparison of precipitation curves between experiments that are analysed using the same pore size filter membrane; assuming the same behaviour of micro-gel, *eg.* same particle size distribution, aggregation behaviour *etc.*. A membrane pore size of 0.45 μm was chosen for experiments in this section as this behaviour was only discovered when most experiments had already been completed.

The silica concentration and turbidity curves shown in Figure 3.5 are used as the control experiment with which future experiments are compared. The results from this experiment are shown in Table 3.1.

Table 3.1: Mean results from the duplicate control precipitation experiment. Precipitation conditions: S = 20.0, 50 g L^{-1} H_2SO_4 and 95°C.

	Measured by Turbidity	Measured by Silica Concentration
Induction Period (hours)	10	12
Precipitation Time (hours)	22	15
Filtration Rate (m^3 m^{-2} h^{-1})	<0.05	

Of the criteria employed for comparing precipitation performance mentioned in Section 3.1, those in Table 3.1 are the most commonly used for this work. The most significant is the filtration rate, followed by the precipitation time. The precipitation time is defined as the time taken, from the start of the experiment, until equilibrium is achieved. For the silica concentration curve equilibrium is reached when equilibrium solubility is attained and for the turbidity curve, equilibrium is reached when maximum turbidity is attained.

3.3.2 Silica precipitation - fundamental aspects

Three fundamental aspects of silica precipitation have been examined and assessed: the precipitation time, by both turbidity and silica concentration; the filtration rate; and the precipitate morphology (using TEM). Changes in these parameters that resulted from varying initial supersaturation, sulfuric acid concentration and temperature were assessed by comparing the results with those of the control experiment detailed in Section 3.3.1.

3.3.2.1 Effect of supersaturation

The results of the experiments comparing initial silica supersaturation and those of the control are shown in Table 3.2.

Table 3.2: Effect of initial silica concentration (supersaturation) on precipitation time and filterability. Precipitation conditions for all experiments: 50 g L^{-1} H_2SO_4 and 95°C, with * denoting the control experiment.

Initial Silica Concentration (mg L^{-1} SiO_2)	Supersaturation Ratio	Precipitation Time - Turbidity (hours)	Precipitation Time - Silica Concentration (hours)	Filtration Rate (m^3 m^{-2} h^{-1})
7000*	20.0	22	15	<0.05
5000	14.3	40	30	<0.05
3000	8.6	91	60	<0.05
2000	5.7	214	141	<0.05
1500	4.3	267	194	<0.05
1000	2.9	348	120	1.47

A definite trend is evident between initial silica concentration (supersaturation) and precipitation time, whether measured by silica concentration or turbidity. As would be expected from crystallisation theory, the time for precipitation increases as the supersaturation, or driving force for precipitation, decreases (Randolph and Larson, 1988). Hurd and Sheffer (1941) similarly report an increase in the time of set of silica gels (*cf.* precipitation time) with decreasing silica concentration.

An anomaly occurs at $S = 2.9$ when the precipitation time, as determined by silica concentration, is less than that at $S = 4.3$ or 5.7 and a dramatic improvement in filterability occurs. A TEM examination of the product, Figure 3.8, clearly shows well resolved granular, spheres of silica, 25 nm in diameter.

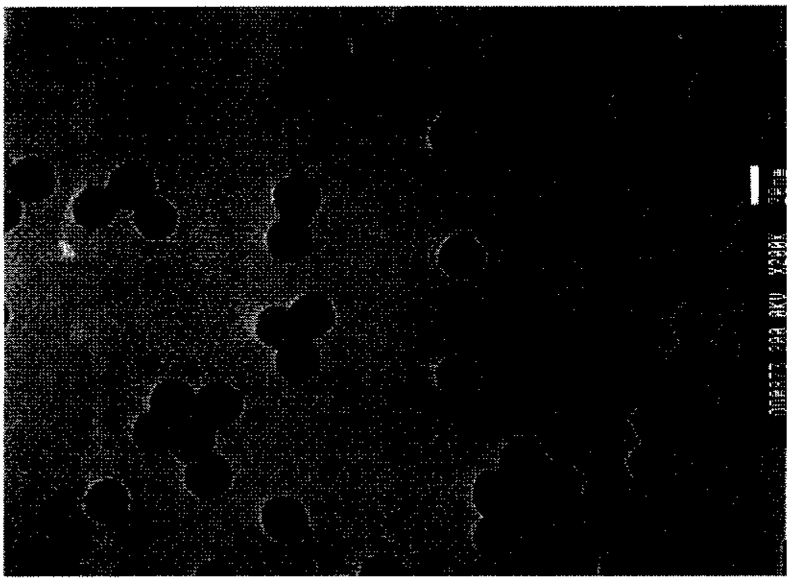

Figure 3.8: TEM micrograph of a typical granular precipitate. The scale bar is displayed on the upper right hand side of the micrograph. Precipitation conditions: S = 2.9, 50 g L^{-1} H_2SO_4 and 95°C.

This morphology has previously been reported (Stober, Fink and Bohn, 1968; Iler, 1979; Brinker and Scherer, 1990; Chen, Dong and Yang, 1997), and accounts for the improved filterability. The very narrow particle size distribution (PSD) can be explained in terms of the metastable supersaturation diagram shown in Figure 1.2. Primary nucleation, either homogeneous or heterogeneous, has occurred and nuclei have been formed. As a result of nucleation, the supersaturation has now dropped below the metastable zone for primary nucleation and into the region of growth on existing particles. The supersaturation is now too low for nucleation to occur and thus the initial nuclei all grow to the same size. These particles are also amorphous to X-rays. All particles precipitated from supersaturations above S = 2.9 have the same morphology as shown in Figure 3.6.

There appear to be different mechanisms for the formation of silica particles from solutions with initial supersaturations between S = 2.9 and 4.3 and above. This is supported by the different shapes of the silica concentration and turbidity curves at different initial supersaturations (Figure 3.9 and Figure 3.10, respectively).

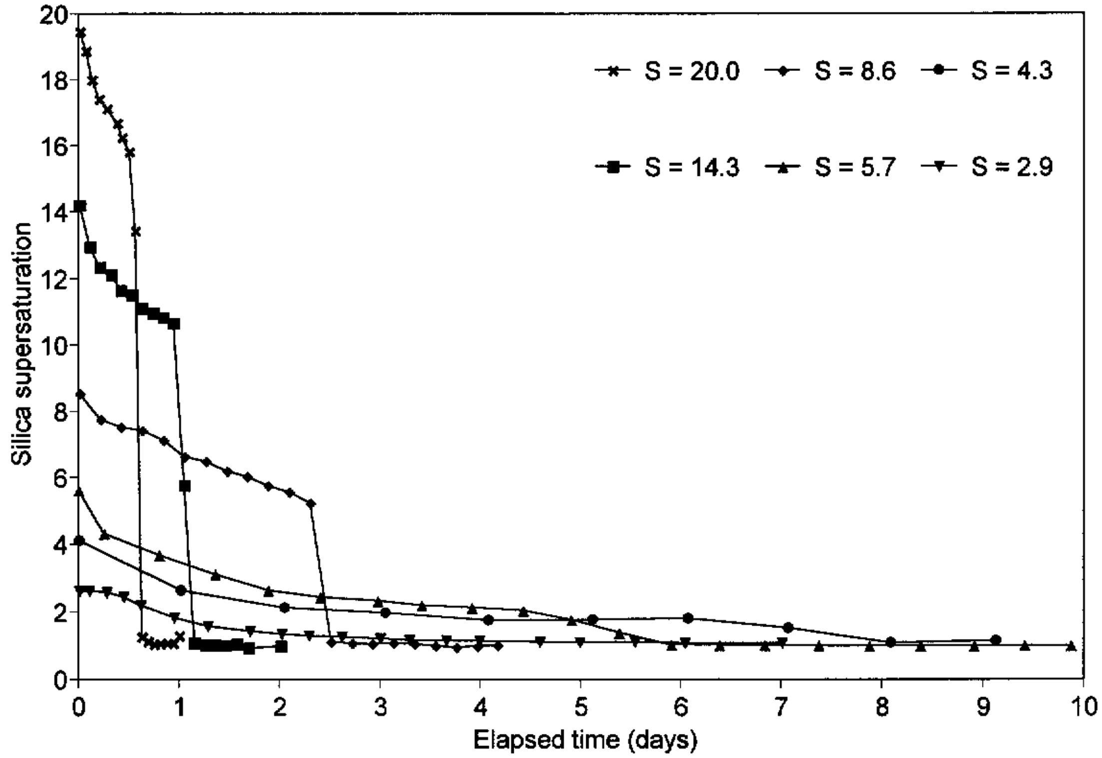

Figure 3.9: Silica supersaturation versus elapsed time, as a function of initial supersaturation. Precipitation conditions for all experiments: 50 g L^{-1} H_2SO_4 and 95°C.

The precipitation curve for S = 2.9 in Figure 3.9 shows a much less sharply defined precipitation period following the induction period, reinforcing the difference between that curve and those produced at higher supersaturations.

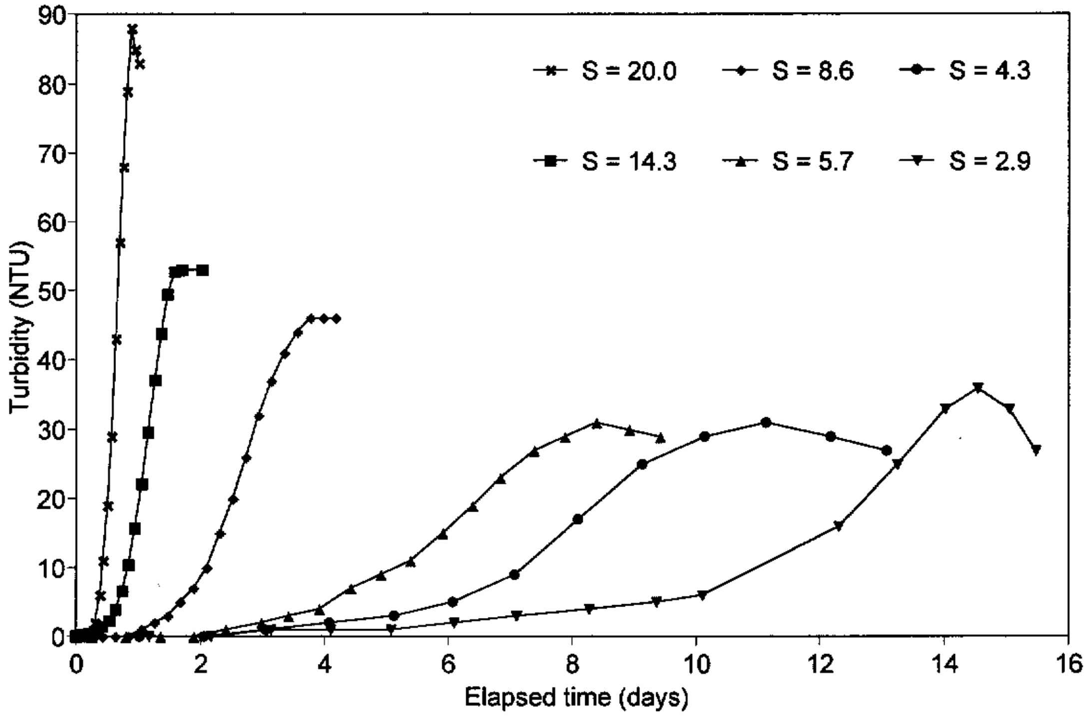

Figure 3.10: Turbidity versus elapsed time, as a function of initial supersaturation. Precipitation conditions for all experiments: 50 g L^{-1} H_2SO_4 and 95°C.

The precipitation curve for S = 2.9 in Figure 3.10 shows a higher final turbidity and a much narrower peak in the curve when compared to the curves produced at the higher supersaturations of S = 4.3 and S = 5.7. This reinforces the proposal that different mechanisms operate at the different supersaturations. The anomaly at S = 2.9 is more clearly visible in a plot of precipitation time, determined by turbidity and silica concentration, versus initial supersaturation. This is shown in Figure 3.11, where the precipitation time, as determined by silica concentration, reverses its trend at S = 2.9.

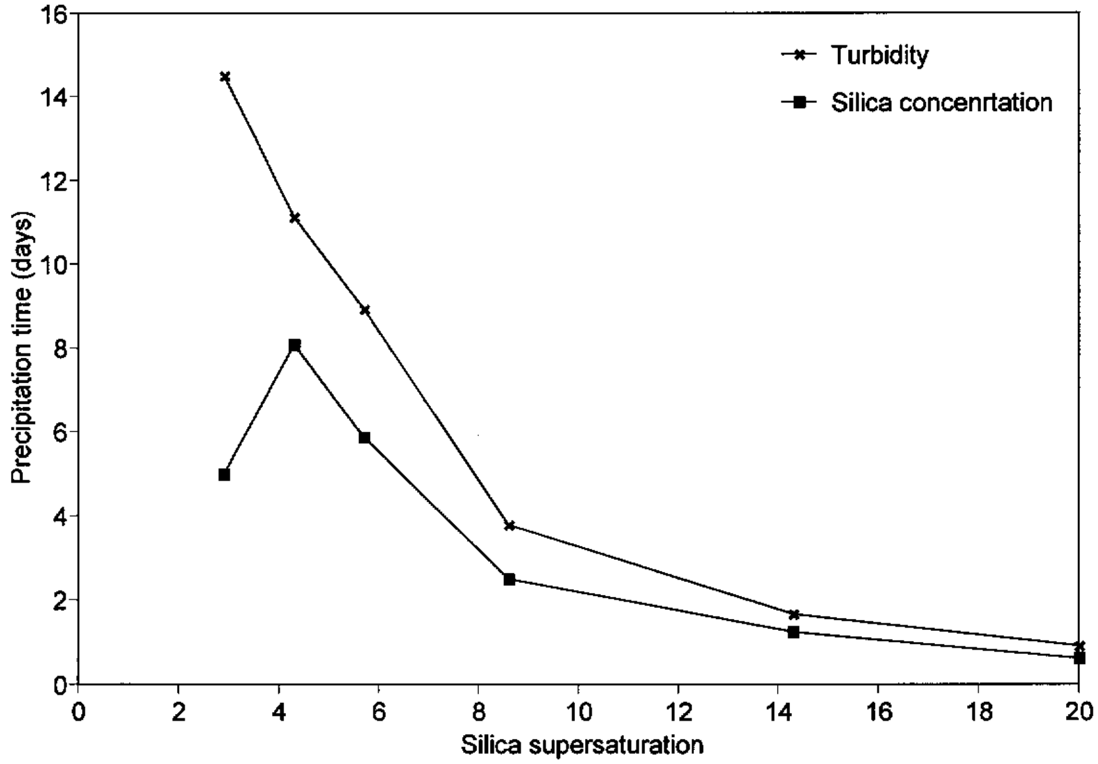

Figure 3.11: Precipitation time versus initial supersaturation, determined by turbidity and silica concentration. Precipitation conditions for all experiments: 50 g L^{-1} H_2SO_4 and 95°C.

As reported by Chan (1989), the induction period for silica precipitation can be reduced by increasing the initial supersaturation ratio. This is clearly shown in Figures 3.9 and 3.10, thus reinforcing this statement.

In an attempt to determine the mechanism of precipitation, and how it differed at S = 2.9 compared to supersaturation ratios above this value, samples from each sampling point of the two experiments carried out at supersaturation ratios of S = 2.9 and S = 5.7, were examined by TEM. Unfortunately, the resolution of the available instrument was such that only the full grown silica particles could be imaged clearly. Despite this, two useful observations were made.

It was observed that the experiment at S = 2.9 contained full grown colloidal silica particles, 25 nm in diameter, approximately 24 hours after the commencement of the experiment. These particles are very similar to those shown in Figure 3.8. While smaller particles could be imaged earlier in the experiment, the image quality was extremely poor and hence the micrographs are not shown here. It should be noted that these colloidal particles were visible before the peak in the turbidity signal arose. This peak was actually the result of aggregation of the colloidal silica to form larger particles. This is not unexpected, as Mullin (1988) suggests agglomeration/aggregation of precipitates, particularly if they are in the colloidal size range. Typical aggregate structures are shown in Figure 3.12. After aggregation it was very unusual to image single silica particles, as most particles had aggregated to form larger particles. In Figure 3.12, colloidal silica particles can be seen cemented to neighbouring particles. This is presumably a result of the dissolution of monosilicic acid from regions with large positive radii of curvature and re-deposition in the crevices between particles (regions with a small, negative radii of curvature). This phenomenon was described in Section 1.4.4.

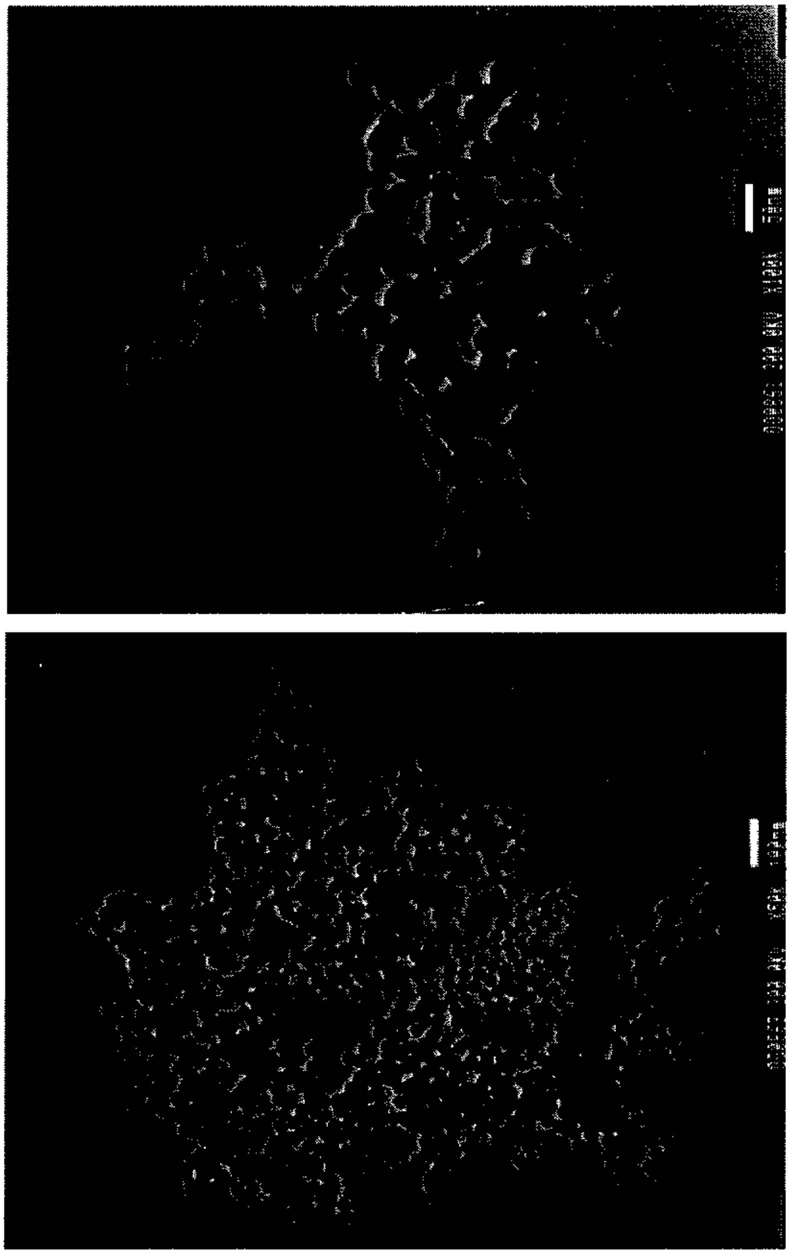

Figure 3.12: TEM micrographs of typical aggregates of colloidal silica particles. The scale bar is displayed on the upper right hand side of the micrograph. Precipitation conditions: S = 2.9, 50 g L^{-1} H_2SO_4 and 95°C.

A very interesting observation was made with the S = 5.7 experiment. The precipitate behaved as expected, in that micro-gel had formed by the time the solution became difficult to filter (supersaturation ratio decreasing to S = 1.0). However, after the turbidity peaked and began to decrease, the precipitate became easier to filter and the micro-gel network began to break up and densify into individual particles with a filtration rate of 0.65 m^3 m^{-2} h^{-1}. The sequence of TEM micrographs in Figure 3.13 A-D show this ageing event as a function of time. The precipitate became difficult to filter after approximately six days, and over the following ten days the ageing process occurred.

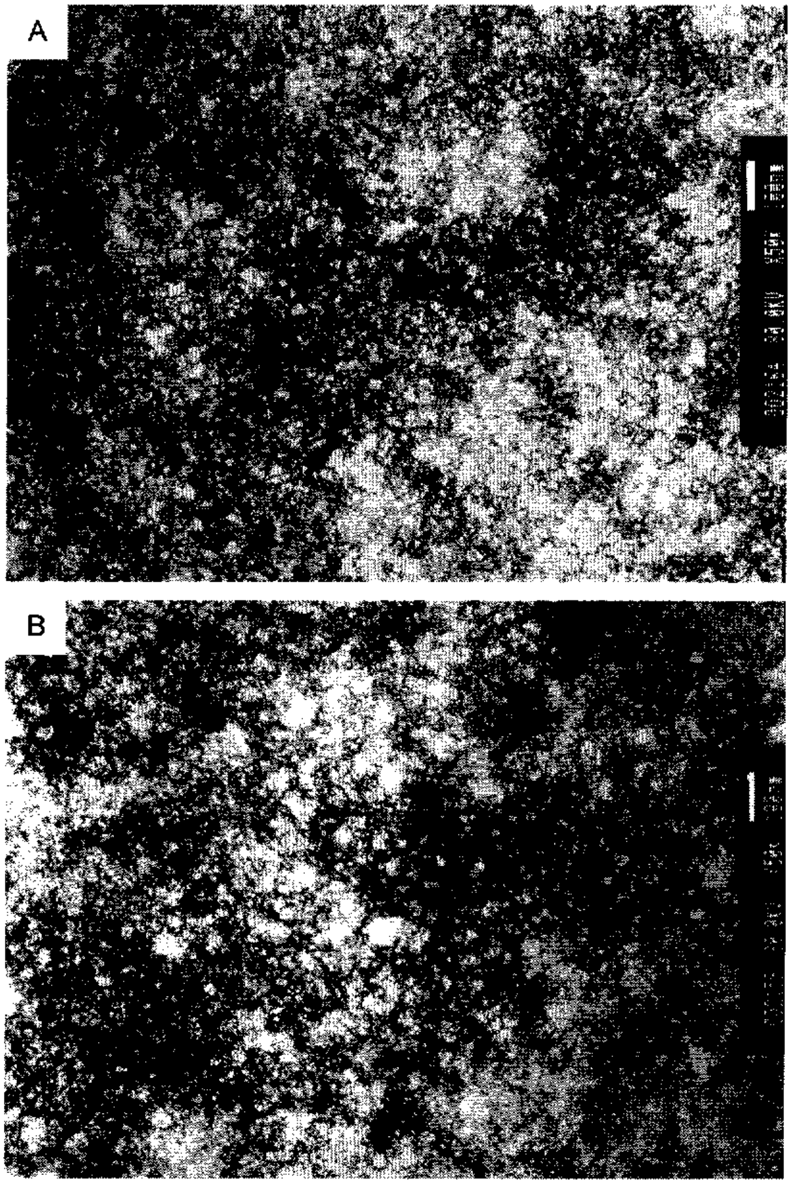

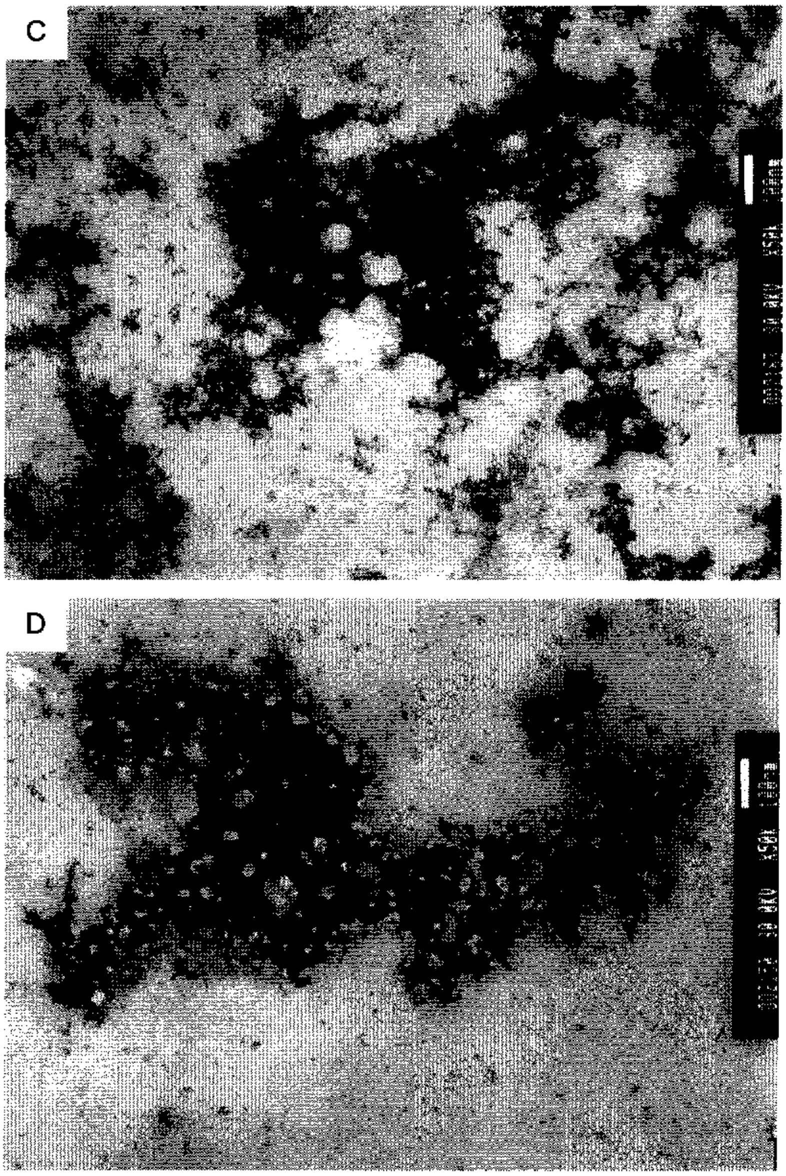

Figure 3.13 A-D: TEM micrographs of silica micro-gel ageing to dense particles that filter readily. (A) - 6 days, (B) - 9 days, (C) - 13 days and (D) - 20 days. The scale bar is displayed on the upper right hand side of the micrograph. Precipitation conditions: S = 5.7, 50 g L^{-1} H_2SO_4 and 95°C.

Those particles precipitated at the lower supersaturation of S = 2.9 are obviously more desirable in a hydrometallurgical sense; however, the precipitation time is very long at this supersaturation.

After the completion of this series of experiments with varying supersaturation at 95°C and 50 g L^{-1} sulfuric acid, the equilibrium solubility value of 350 mg L^{-1} SiO_2, was assigned an error range of ±50 mg L^{-1} SiO_2

based on the actual fluctuation in results. It is assumed that this error is a result of experimental errors associated with the experiments themselves, and the determination of the SiO_2 concentration by ICP-AES.

3.3.2.2 Effect of sulfuric acid concentration

The results of the experiments of varying sulfuric acid concentration, and their comparison with those of the control are shown in Table 3.3 and also in Figure 3.14.

Table 3.3: Effect of sulfuric acid concentration on precipitation time and filterability. Precipitation conditions for all experiments: S = 20.0 and 95°C, with * denoting the control experiment.

Sulfuric Acid Concentration (g L^{-1} H_2SO_4)	Precipitation Time - Turbidity (hours)	Precipitation Time - Silica Concentration (hours)	Filtration Rate (m^3 m^{-2} h^{-1})
50*	22	15	<0.05
65	15	10	<0.05
100	7	5	<0.05
215	1.2	1.2	<0.05

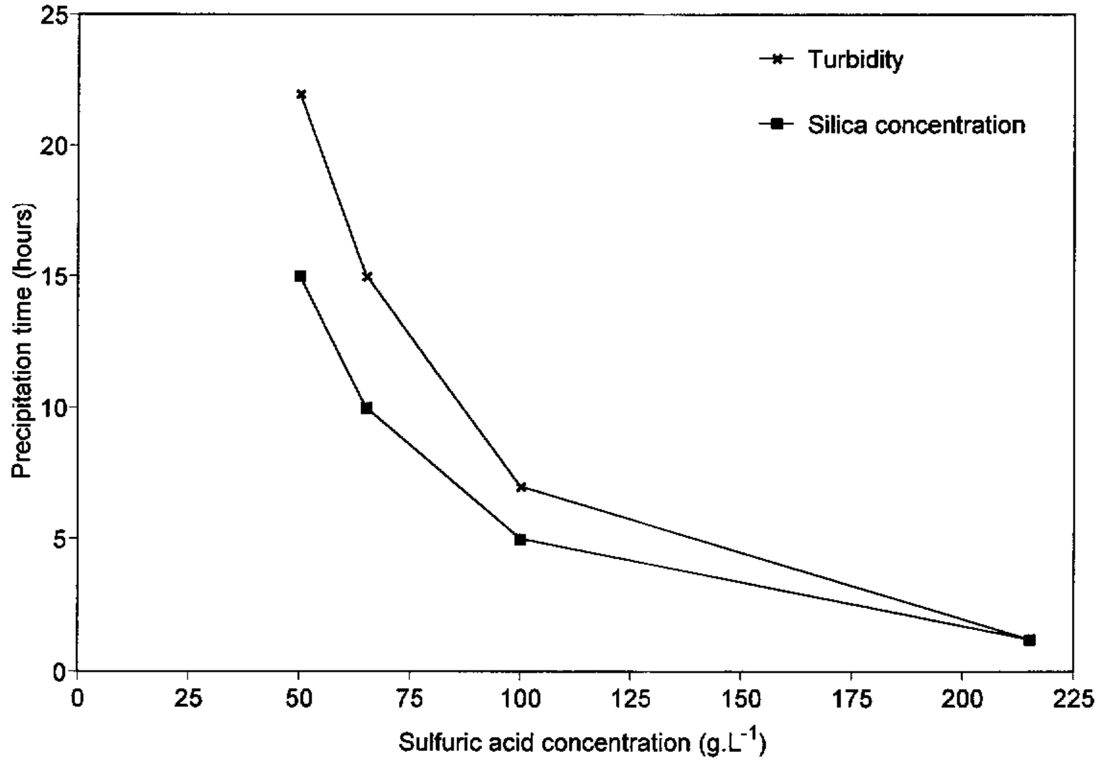

Figure 3.14: Precipitation time versus sulfuric acid concentration, determined by turbidity and silica concentration. Precipitation conditions for all experiments: S = 20.0 and 95°C.

Again, a clear trend is evident, with precipitation time decreasing with increasing sulfuric acid concentration. This has previously been reported (Betterton, 1923; Hurd and Barclay, 1940; Iler, 1979). Based on all previous experiments, it would be expected that the precipitation time at 215 g L^{-1} sulfuric acid, as determined by silica concentration, would be less than that determined by turbidity. However, due to the very short duration of this experiment and the number of sampling points, these results can not be differentiated. There is no change in filterability or morphology (examined by TEM) as a function of sulfuric acid concentration. However, a significant reduction in precipitation time can be achieved by operating at higher acid concentration.

It would appear from these experiments, covering the sulfuric acid range 50 to 215 g L^{-1}, that the equilibrium silica solubility decreases with increasing sulfuric acid concentration at which the precipitation was carried out. This is a general observation and no evidence is shown here to support this statement, as replicate experiments were not carried out to determine the exact equilibrium solubility value. This is because of experimental fluctuations observed in the silica concentration at equilibrium. As a result of this, the equilibrium solubility used in the calculation of the supersaturation ratios in Table 3.3 is 350 mg L^{-1} SiO_2. Solubility data for this temperature and pH range are not available in the literature to enable a comparison to be made.

3.3.2.3 Effect of temperature

The results of the experiments of varying temperature and their comparison with those of the control are shown in Table 3.4, and graphically in Figure 3.15.

Table 3.4: Effect of temperature on precipitation time and filterability. Precipitation conditions for all experiments: S = 20.0 and 50 g L^{-1} H_2SO_4, with * denoting the control experiment.

Temperature (°C)	Precipitation Time - Turbidity (hours)	Precipitation Time - Silica Concentration (hours)	Filtration Rate (m^3 m^{-2} h^{-1})
95*	22	15	<0.05
70	77	59	<0.05
25	2500	1100	<0.05

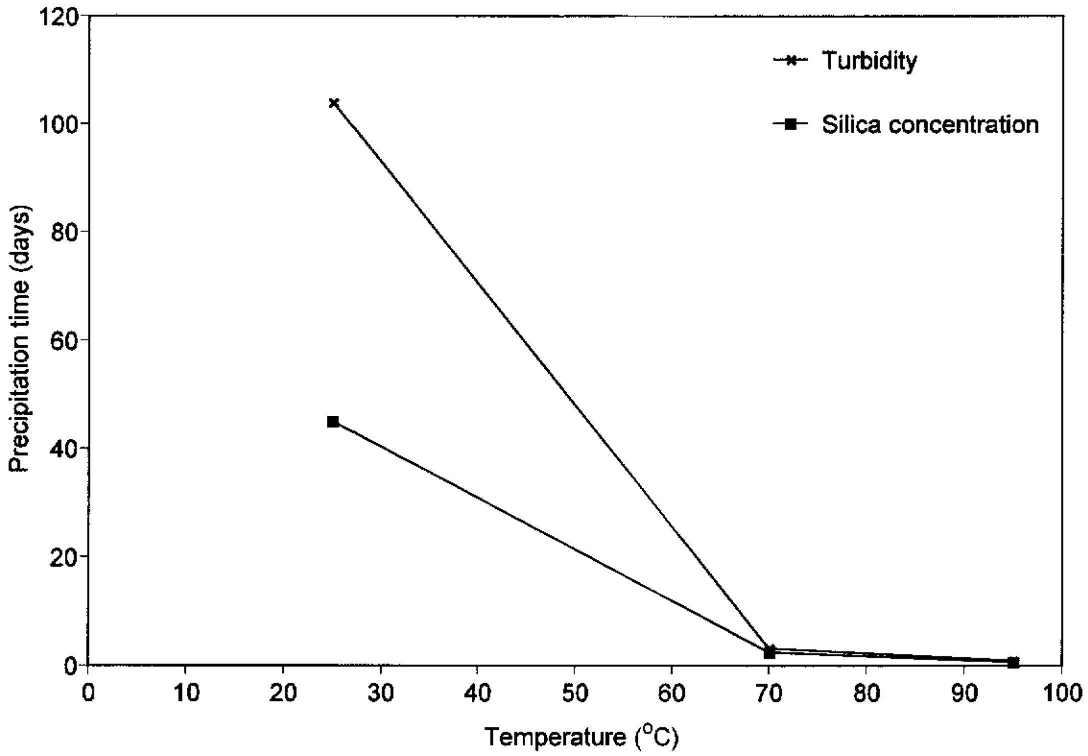

Figure 3.15: Precipitation time versus temperature, determined by turbidity and silica concentration. Precipitation conditions for all experiments: S = 20.0 and 50 g L^{-1} H_2SO_4.

Hurd and Letteron (1932) and Hurd and Barclay (1940) both report an increase in the time of set of silica gels (*cf.* precipitation time) with a decrease in temperature, in agreement with these results. Although the precipitation curves are not shown here, the length of the induction period was shortened by using a higher precipitation temperature, as reported by Chan (1989). The rate of silica precipitation was found to increase with temperature, as reported by Matthew and Elsner (1977a). It is obvious that as high a temperature as possible should be chosen to achieve the shortest precipitation time. No change in morphology as a function of temperature was observed by TEM, and no change in filterability was detected.

Queneau and Berthold (1985) and also Bodson (1974) report an increase in the equilibrium solubility of silica with an increase in temperature, at a fixed pH. This trend was also observed in the experiments discussed in this section. However, as with the experiments of varying sulfuric acid concentration, fluctuation in the silica concentration at equilibrium made it difficult to determine an accurate value for the equilibrium solubility. Once again the equilibrium solubility has been taken as 350 mg L^{-1} SiO_2 in the calculation of the supersaturation ratios for the various temperatures listed in Table 3.4.

3.3.3 Silica precipitation - effects of additives

The results of this suite of experiments conducted at 95°C with S = 20.0, 50 g L^{-1} H_2SO_4 and various additives are shown in Table 3.5. The additives tested were zinc sulfate, aluminium sulfate, iron (III) sulfate and hydrofluoric acid. Zinc sulfate was chosen as an additive for investigation as it is typically present in solutions found in a hydrometallurgical zinc plant. The other three additives investigated were selected as they are known to influence silica polymerisation, as detailed in Section 1.0.

Table 3.5: Effect of additives on precipitation time and filterability. Precipitation conditions for all experiments: S = 20.0, 50 g L^{-1} H_2SO_4 and 95°C.

Additive and Concentration	Precipitation Time - Turbidity (hours)	Precipitation Time - Silica Concentration (hours)	Filtration Rate (m^3 m^{-2} h^{-1})
Control	22	15	<0.05
$ZnSO_4$ 0.50 M	18	14	<0.05
$ZnSO_4$ 1.00 M	10	8	<0.05
$Al_2(SO_4)_3$ 0.25 M	13	10	<0.05
$Al_2(SO_4)_3$ 0.50 M	6	4	0.20
$Fe_2(SO_4)_3$ 0.25 M	15	10	<0.05
$Fe_2(SO_4)_3$ 0.50 M	8	6	<0.05
HF 130 mg L^{-1}	2	1.7	<0.05
HF 195 mg L^{-1}	1.2	1.0	<0.05

Zinc sulfate causes a decrease in precipitation time, which is in agreement with Betterton (1923) who observed a decrease in the time of set of silica gels (*cf.* precipitation time) with increasing zinc sulfate concentration. This result is encouraging, because a hydrometallurgical zinc plant operates in a zinc sulfate medium which is favourable to silica precipitation. However, no change in filterability or morphology, as observed by TEM, were detected, at either concentration of zinc sulfate investigated.

Aluminium sulfate produces a significant reduction in the precipitation time at both concentrations studied and an improvement in filterability at an addition level of 0.5 M. Radino (1957) used aluminium as a silica coagulant to improve filterability, but no record is made of any effect on precipitation time. The success of the Radino process relies on aluminium ions added at 1 to 50% by weight of the mass of silica present. In this study 200 and 400% by weight of aluminium ions were added and it was only at the higher concentration that a coagulation effect was seen. TEM examination revealed both precipitates to be morphologically similar to the micro-gel particle in Figure 3.6, with no reason for the improved filterability at the higher addition level apparent from the images.

Iron (III) ions have been reported as assisting in the precipitation of silica by acting as a coagulant (Ashman, Delong and Jankola, 1993; Matthew and Elsner, 1977b). In this instance the addition of iron (III) sulfate has improved the precipitation times, however the lack of change in morphology and filterability does not support the literature findings that it acts as a coagulant to improve filtration performance.

Of the three metal sulfates tested, aluminium sulfate shows the greatest improvement in precipitation times, followed by iron (III) sulfate and then zinc sulfate. This comparison is made at the same molar concentration of metal species, 1.00 M in Table 3.5. It should be noted however, that the concentration of sulfate ion, added as the metal sulfate is not constant for the three metals of interest.

Hydrofluoric acid, even at low concentrations, is known to catalyse the formation of silica gels (Iler, 1952). The addition of 130 mg L^{-1} of hydrofluoric acid produced an exceptional reduction in the precipitation time, while the addition of 195 mg L^{-1} had an even greater effect. There was however, no change in filterability or morphology as examined by TEM.

No new findings in regard to Iler's (1979) statement concerning the solubility of silica in the presence of fluoride, aluminium and sulfate ions have been made as a result of this section of work. As mentioned previously, the silica concentration at equilibrium fluctuates, and as a result, an accurate equilibrium solubility value can not be reported without additional replicate experiments being performed. Thus, the equilibrium solubility has been taken as 350 mg L^{-1} SiO_2 in the calculation of the supersaturation ratios listed in Table 3.5.

The solution samples collected during these experiments for silica analysis were also analysed for the particular additive of interest for that experiment. In all cases there was no detectable decrease in the concentration of the additive material throughout the course of the precipitation. SEM-EDX also found no traces of the additive materials present in the respective silica precipitates. These additive materials maybe acting as catalysts for improving precipitation performance and are thus, not consumed in the process. It is also possible that the additives are affecting the electric double layer interactions between the silica particles and this accounts for their effect on silica precipitation. Due to the high ionic strengths present in these experiments, the electric double layer of the silica particles will be highly compressed; reducing the importance of electrical interactions.

Following the successes of the precipitation experiments at $S = 2.9$, in terms of filterability, and those using additives to improve precipitation time at $S = 20.0$, these conditions were combined to try and produce a filterable precipitate in a shorter time. The results of this work, from $S = 2.9$, are shown in Table 3.6. The second experiment in Table 3.6 was used to investigate two important aspects of silica precipitation. The first concerns the investigation into the mechanism of silica precipitation. Namely, is silica micro-gel formed at $S = 2.9$, if the rate of precipitation is extremely rapid? The second area of importance is the role of the insoluble impurity particles that are present in the natural zinc orthosilicate ore used for the continuous precipitation experiments, detailed in Section 4.0. For this experiment it was therefore decided to use the natural zinc orthosilicate ore instead of the synthetic zinc orthosilicate. This will provide an understanding of the role of these impurity particles on silica precipitation. The precipitation liquor was not filtered before the experiment as had been done previously and hence the insoluble impurity particles remained in the liquor. The concentration of additives for this experiment were selected to enable the duration of the experiment to be as short as possible but still allow enough sampling points to construct accurate precipitation curves. It was thought that the two different aspects of the experiment would not interfere with each other.

Table 3.6: Effect of additives on precipitation time and filterability. Precipitation conditions for all experiments: S = 2.9, 50 g L^{-1} H_2SO_4 and 95°C.

Additive and Concentration	Precipitation Time - Turbidity (hours)	Precipitation Time - Silica Concentration (hours)	Filtration Rate ($m^3\ m^{-2}\ h^{-1}$)
Control	348	120	1.47
HF 195 mg L^{-1}	58	30	3.92
$ZnSO_4$ 0.5 M, $Al_2(SO_4)_3$ 0.25 M and HF 130 mg L^{-1}	NA	5	14.70

The addition of hydrofluoric acid at S = 2.9 results in a dramatic improvement in both precipitation time and filterability. The spherical morphology observed by TEM in Figure 3.8 was maintained; however, the particle size increased to approximately 50 nm. This is thought to account for the improved filterability, but the reason why remains unclear. It is not known why the addition of fluoride ions increases the PSD. Iler (1979) states that hydrofluoric acid catalyses silica polymerisation and this result reinforces that finding. This result also implies that all forms of silica precipitation (yielding silica gel, micro-gel or granular precipitate) occur by very similar mechanisms, as they appear to be influenced by the same factors. It should be remembered that it was proposed in Section 3.3.2.1 that silica micro-gel and silica precipitate formed by similar mechanisms.

The effect of the three additives and the presence of the insoluble material had a very dramatic effect on the silica precipitation of the second experiment. Turbidity measurements could not be used to monitor precipitation due to the high turbidity signal present from the insoluble material. The precipitation time, determined by silica concentration, was about 4% of that without the soluble and insoluble impurities present. The filtration rate indicates that silica micro-gel did not form. Thus, over the range of conditions studied, the structure of the silica precipitate is chemically controlled, not kinetically controlled, as may have been expected. It is not unreasonable to expect the structure of a precipitate to be a function of the rate of its formation. The exceptional filterability is explained by examining the precipitate morphology using SEM, the particle size being too large for TEM. Figure 3.16 shows a typical silica precipitate approximately 30 µm in size and somewhat spherical in shape.

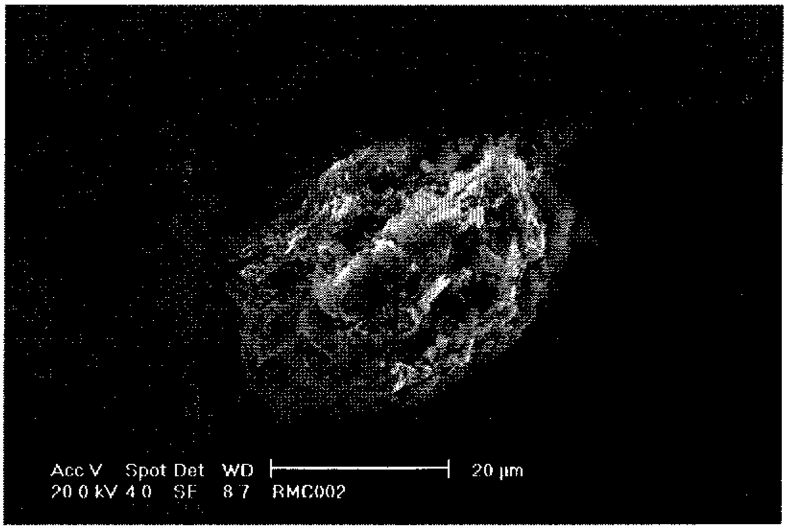

Figure 3.16: SEM micrograph of a typical silica particle precipitated in the presence of zinc and aluminium sulfates, hydrofluoric acid and various solid impurity particles. Precipitation conditions: S = 2.9, 50 g L^{-1} H_2SO_4 and 95°C.

The silica particles from this particular precipitation experiment appear to be aggregates of colloidal particles. These colloids are presumably of the same structure as those precipitated from S = 2.9 without additives, shown in Figure 3.8. A sample of the dried precipitate was mounted in a resin block and ground and polished to cross-section the particles. Examination using SEM revealed the silica aggregates to contain the insoluble impurity particles. A micrograph showing this behaviour is shown in Figure 3.17. These impurities were seen to be nucleation or aggregation centres for silica precipitation or aggregation, respectively. Since none of the other soluble additives had this effect on the silica, it is assumed to be a result of the solid impurities. The additional precipitation and or aggregation of the colloidal silica particles leads to a much larger particle size which in turn explains the very high filtration rate. This behaviour is the same as that observed in the continuous experiments, detailed in Section 4.3.10.2, and thus no detailed analysis is provided here.

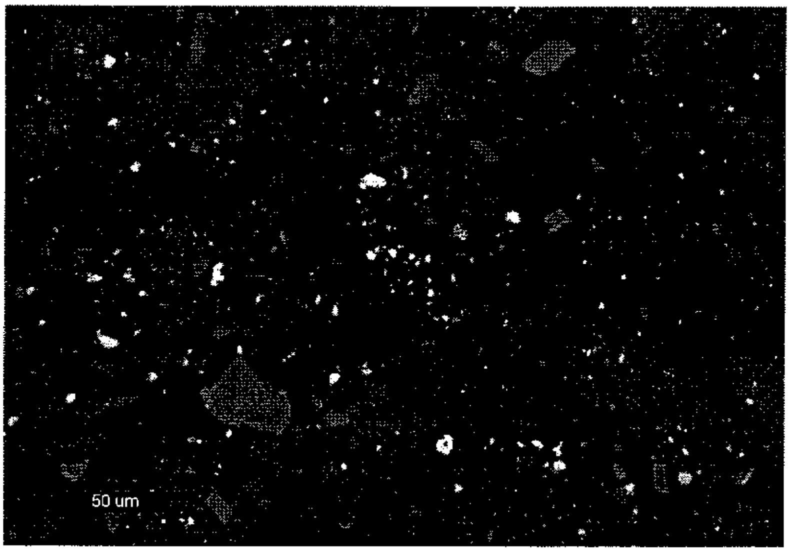

Figure 3.17: SEM micrograph of typical silica particles precipitated in the presence of zinc and aluminium sulfates, hydrofluoric acid and various solid impurity particles, imaged using backscattered electron imaging. Precipitation conditions: S = 2.9, 50 g L^{-1} H_2SO_4 and 95°C.

3.3.4 Silica precipitation - effect of seed

Several silica seeds were trialed, with the aim of improving both precipitation time and the filterability of the silica product. The seeds used were a mix of commercially available pyrogenic and precipitated silicas; a precipitated silica produced from a dried micro-gel that was the product of an earlier precipitation experiment; and also a precipitated silica micro-gel that had always remained in solution. The experiments were carried out at S = 20.0 to provide a relatively short experiment duration. The seed solids loading was 3.3 g L^{-1}. This value represents the seed solids loading for the experiment where silica micro-gel, that had always remained in solution, was used as the seed source; this value was maintained for the other seeded experiments in this suite. The results of these experiments are shown in Table 3.7 and Figure 3.18. Turbidity measurements were not made for these experiments, as the seed material produced a background turbidity over which the small change in turbidity associated with precipitation could not be detected.

Table 3.7: Silica precipitation as a function of different silica seeds. Precipitation conditions for all experiments: S = 20.0, 50 g L^{-1} H_2SO_4, 95°C and 3.3 g L^{-1} seed loading.

Seed Type	Precipitation Time - Silica Concentration (hours)	Filtration Rate ($m^3 m^{-2} h^{-1}$)
Control - unseeded	15	<0.05
Pyrogenic silica - commercial	12	<0.05
Precipitated silica - commercial	12	<0.05
Precipitated silica - dried micro-gel	19	<0.05
Precipitated silica - wet micro-gel	18	<0.05

The data contained in Table 3.7 indicate that the commercial pyrogenic and precipitated silicas show promise as potential seed materials with precipitation times shorter than those of the control experiment, whereas the two silica micro-gels appear not to be functioning very well as seeds, as their precipitation times have increased over that of the control experiment. The reason for this unusual result is not known.

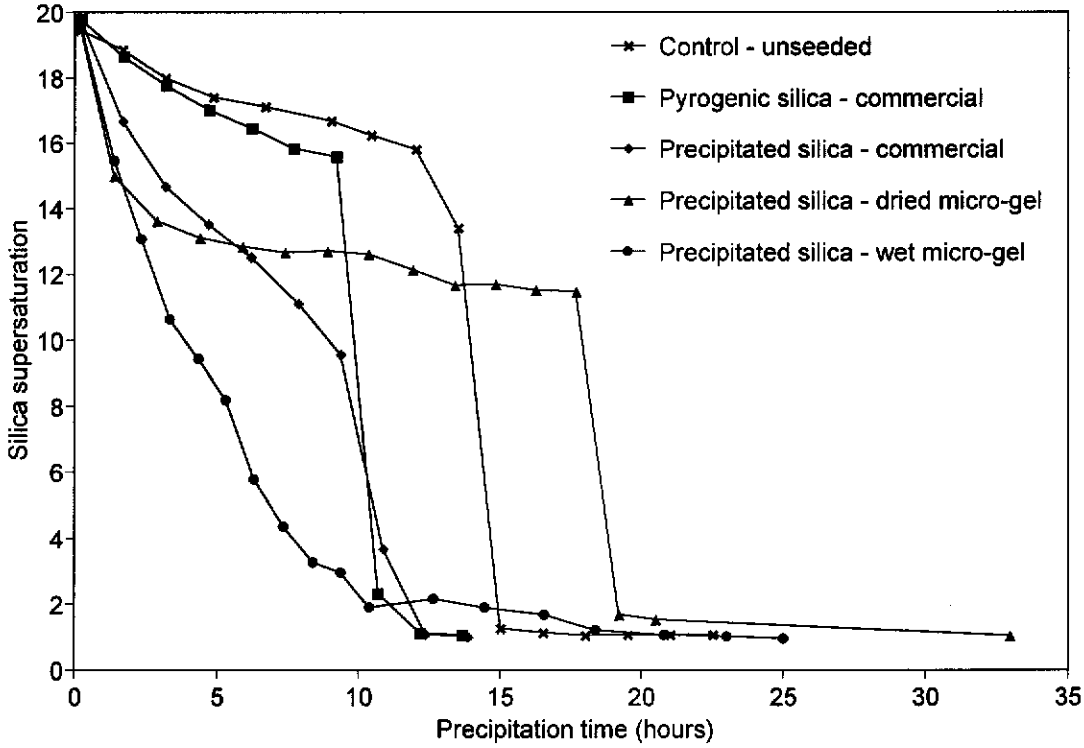

Figure 3.18: Silica supersaturation versus precipitation time as a function of different silica seeds. Precipitation conditions for all experiments: S = 20.0, 50 g L^{-1} H_2SO_4, 95°C and 3.3 g L^{-1} seed loading.

However, the extra data in Figure 3.18 suggest a different conclusion. The commercially available pyrogenic silica produced a precipitation curve similar in shape to that of the control experiment, providing good evidence that the seed material was relatively inactive. However, the precipitation time was reduced by about three hours, as shown in Table 3.7, which indicates that the seed was having some effect. It would be expected that an effective seed would remove the induction period from the silica precipitation curve altogether (Queneau and Berthold, 1985).

The commercial precipitated silica had the best performance of all the dried silicas with a precipitation time about three hours shorter than that for the control experiment. Although the precipitation curve appears to have no induction period, the overall shape of the curve is similar to that of the control experiment, which indicates the precipitated silica is not acting as a fully effective seed.

The dried micro-gel silica was the least effective seed trialed. The shape of the precipitation curve with this seed was the same as that for the control experiment, indicating an ineffective seed. The precipitation time was approximately four hours longer than that for the control experiment.

The precipitated micro-gel that had always remained in solution was an effective seed, with no induction period present before precipitation. The exponential shape of the precipitation curve differs from that of the control markedly, and because of that, combined with the absence of an induction period, indicates that growth on seed is occurring. The precipitation time for this seed is about six hours longer than that of the control experiment. While this seems unusual, it maybe a result of the very early, rapid precipitation, that reduced supersaturation to the extent that further precipitation to achieve equilibrium would be very slow. The seed and product particles from this experiment were examined by TEM and found to be very similar to the particle shown in Figure 3.6, Section 3.3.1. Due to the irregular nature of the seed particles, it was not possible to detect any evidence of further growth using TEM.

As is shown in Table 3.7, the resulting precipitates from these experiments all had filtration rates of less than 0.05 $m^3\ m^{-2}\ h^{-1}$. This was expected of the wet micro-gel, as it had this filtration rate to start with, but it is further evidence that the well filtering dry seeds were not participating to any great extent in the precipitation of micro-gel.

The important result from the seeding experiments concerns the initial precipitation rate, measured as the gradient of the tangent to the precipitation curve in the initial stages of precipitation. The steeper the gradient, the higher the precipitation rate. However, this is only applicable when secondary nucleation and growth is predominant, not primary nucleation. For this series of experiments the precipitated micro-gel that had always remained in solution was the most effective seed and was the only one that has been conclusively found to have acted as an efficient seed.

It was assumed from these experiments that the surface of the dry seeds had somehow become deactivated by removing them from their aqueous environments, and this accounted for their inertness. A further avenue for investigation is that of reactivating the silica surface in a suitable solvent prior to use as a seed. However, for the remainder of this thesis it is recommended that only seeds that have remained in solution from their production should be used.

In an attempt to reduce the very long precipitation time encountered at S = 2.9, and still produce a filterable product without the use of any foreign additives, it was decided to pursue seeding with the colloidal silica precipitate produced at S = 2.9 as an alternative. The precipitation experiment at S = 2.9, 50 g L^{-1} sulfuric acid and 95°C that produced the colloidal precipitate that filtered very well, was repeated on an increased scale at six times the original volume. After precipitation and settling, enough seed was collected to carry out a batch experiment at 3.3 g L^{-1} seed loading. The filtration rate of this seed was 0.74 m^3 m^{-2} h^{-1}, which is less than the expected value of about 1.47 m^3 m^{-2} h^{-1} achieved previously. The lower filtration rate is a result of aggregation during the settling period. Due to the extended period of time needed to produce this seed, it was also decided to test some already available precipitated silica product from one of the continuous experiments in Section 4.0. This material was collected from Industrial run number 5 (IRN-5) during a period when the filtration rate was good, the resultant seed slurry at 3.3 g L^{-1} solids loading having a filtration rate of 1.76 m^3 m^{-2} h^{-1}. The results of these experiments are compared with that of the control and displayed in Table 3.8 and Figure 3.19.

Table 3.8: Effect of different seeds at 3.3 g L^{-1} seed solids loading on precipitation time and filterability. Precipitation conditions for all experiments: S = 2.9, 50 g L^{-1} H_2SO_4 and 95°C.

Seed Type	Precipitation Time - Silica Concentration (hours)	Precipitation Rate (mg SiO_2 L^{-1} h^{-1})	Filtration Rate - Initial (m^3 m^{-2} h^{-1})	Filtration Rate - Final (m^3 m^{-2} h^{-1})
Control - unseeded	120	16	NA	1.47
Synthetic seed	46	94	0.74	1.02
Industrial seed	40	51	1.76	1.08

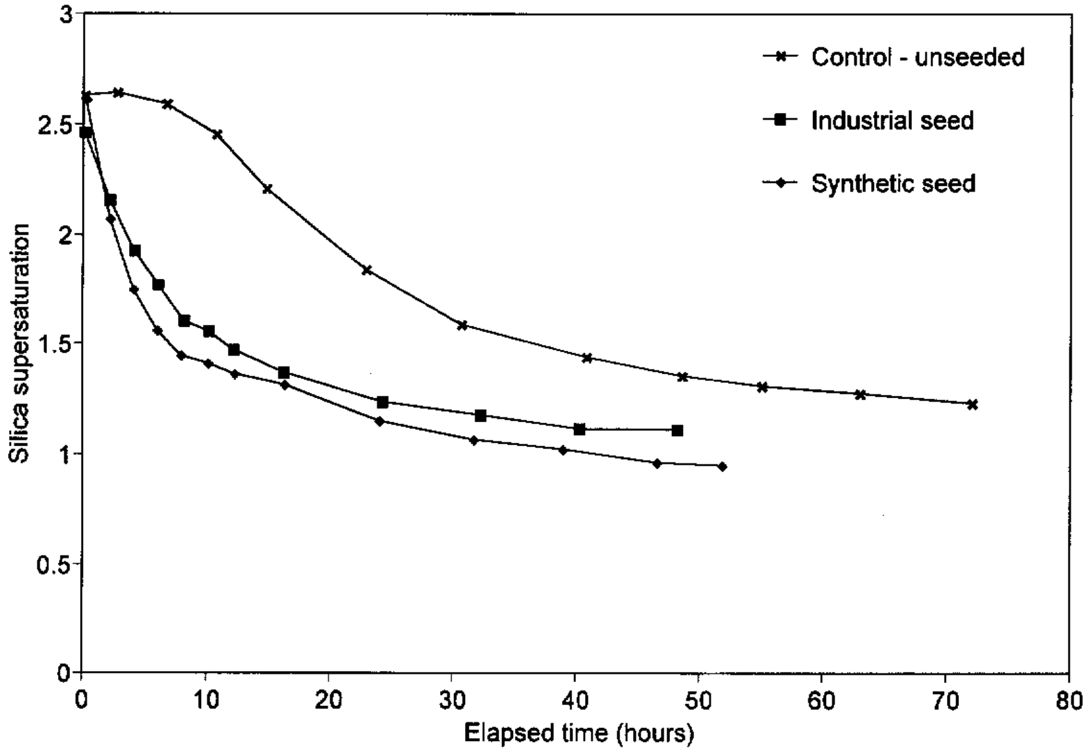

Figure 3.19: Silica supersaturation versus elapsed time, as a function of seed type at 3.3 g L^{-1} seed solids loading. Precipitation conditions for all experiments: S = 2.9, 50 g L^{-1} H_2SO_4 and 95°C.

The results in Figure 3.19 show that both the industrial and synthetic seeds increase the rate of precipitation over that of the control (unseeded); the synthetic seed being almost twice as efficient as the industrial seed, in terms of precipitation rate. Compared to the control, an induction period is not present in the seeded systems. The final filtration rates of the two products is very similar, even though their initial filtration rates were quite different. The final filtration rates are also less than that for the control, the reason for both these results is not known. Thus, with an effective seed it is possible to reduce the precipitation time considerably when precipitating from S = 2.9.

TEM examination of the synthetic seed and resultant product confirmed that the growth of silica particles is by the mechanism outlined by Iler (1979) in Section 1.4. The supporting micrographs are shown in Figure 3.20. During the TEM examination of the initial seed material, many individual particles were visible; however, after further precipitation virtually no individual particles were visible. Clearly, growth is by aggregation of colloidal particles and further deposition of monosilicic acid in the crevices between the particles to rigidly bond the aggregates together. Under the conditions of this experiment, growth is predominant over nucleation. This conclusion is supported by the lack of any new nuclei forming during the experiment, as detected by TEM. Examination of the industrial seed and the resultant product using TEM revealed no differences in the particles: they are both very irregular in shape and surface structure. Surface area analysis of the industrial seed and resultant product may have detected the presence of growth on the seed particles. However, this was not considered necessary as seeded growth has already been confirmed in Figure 3.19.

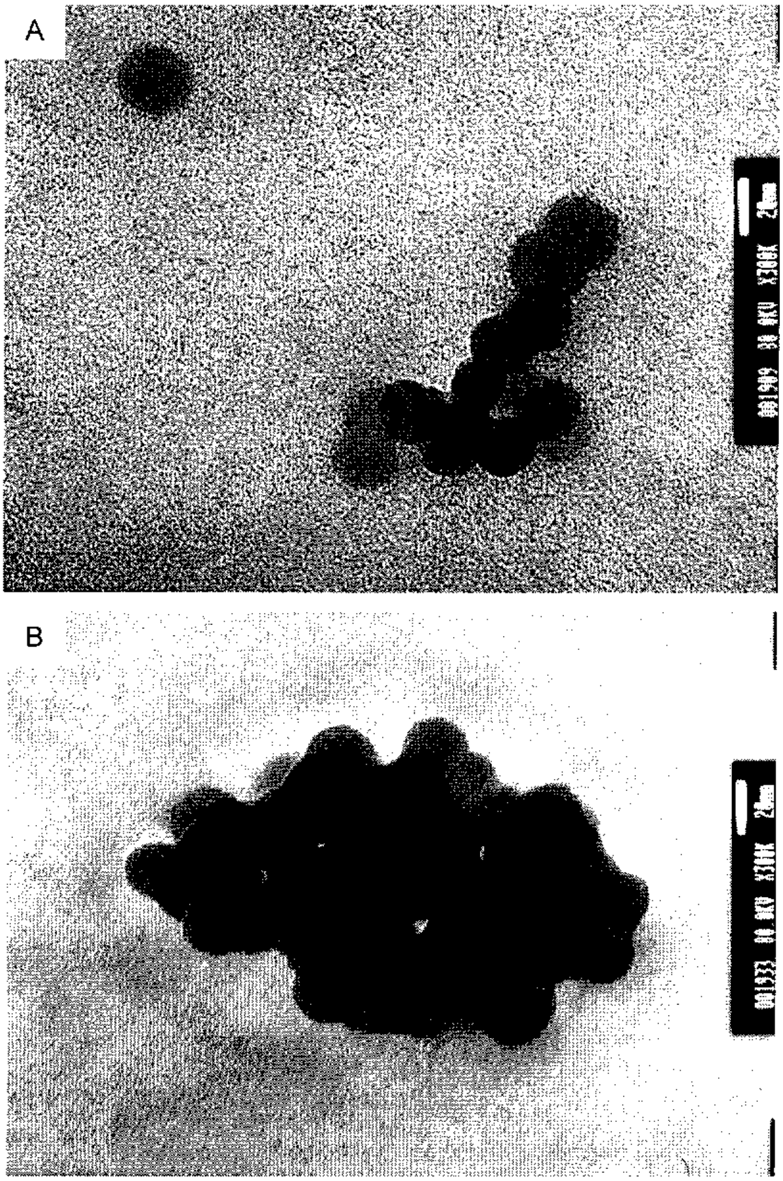

Figure 3.20: TEM micrographs of (A) initial seed particles precipitated from $S = 2.9$, 50 g L^{-1} H_2SO_4 and 95°C and (B) particles after 6 hours of growth under the same conditions. The scale bar is displayed on the upper right hand side of the micrograph.

Due to the length of time needed to produce even small quantities of the synthetic seed, the large volume of readily available industrial seed and the similarities in their performance it was decided to use the industrial seed for the remaining seeding experiments.

It is desirable to know the effect of seed loading on silica precipitation from an initial supersaturation ratio of $S = 2.9$. The results of experiments investigating seed loadings of 3.3 and 6.6 g L^{-1} of industrial seed, are shown in Figure 3.21 and Table 3.9.

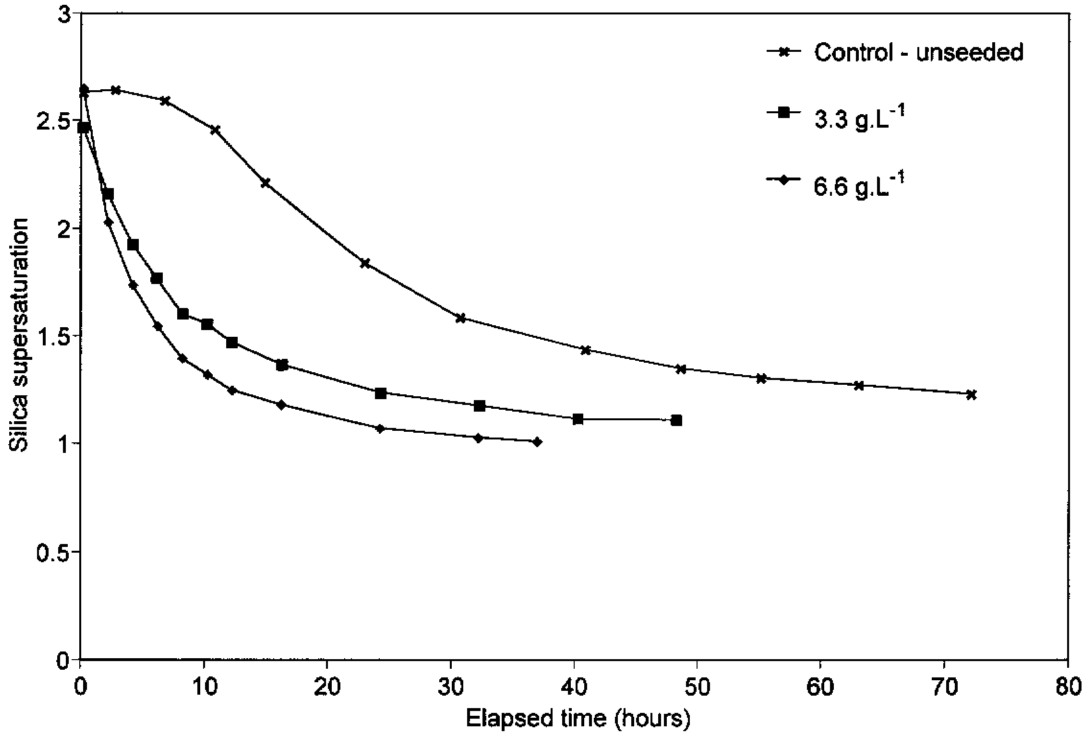

Figure 3.21: Silica supersaturation versus elapsed time, as a function of industrial seed loading. Precipitation conditions for all experiments: S = 2.9, 50 g L^{-1} H_2SO_4 and 95°C.

Table 3.9: Effect of industrial seed loading on seeded silica precipitation. Precipitation conditions for all experiments: S = 2.9, 50 g L^{-1} H_2SO_4 and 95°C.

Industrial Seed Loading (g L^{-1})	Precipitation Time - Silica Concentration (hours)	Precipitation Rate (mg SiO_2 L^{-1} h^{-1})	Filtration Rate - Initial (m^3 m^{-2} h^{-1})	Filtration Rate - Final (m^3 m^{-2} h^{-1})
Control - unseeded	120	16	NA	1.47
3.3	40	51	1.76	1.08
6.6	37	107	1.04	2.20

Clearly, the higher seed loading has improved the precipitation performance, both in terms of precipitation and filtration rates. The precipitation rate at the higher seed loading is almost double that at 3.3 g L^{-1}. Whilst filterability only improved at 6.6 g L^{-1} seed loading, it was still acceptable at 3.3 g L^{-1}. Precipitation theory would predict an increased precipitation rate with increased seed loading due to increased surface area available for growth, as observed in these experiments (Randolph and Larson, 1988). Once again, TEM was unable to detect any significant changes between the seed and the precipitation product.

With such a dramatic improvement in the precipitation rate with an increase in seed loading, it is logical to think that perhaps seed can be used to prevent the formation of silica micro-gel at supersaturations higher than S = 2.9. Seeded precipitation experiments were conducted from S = 8.6 to ensure a relatively short reaction time; the results with 3.3 and 6.6 g L^{-1} seed loadings are shown in Figure 3.22 and Table 3.10.

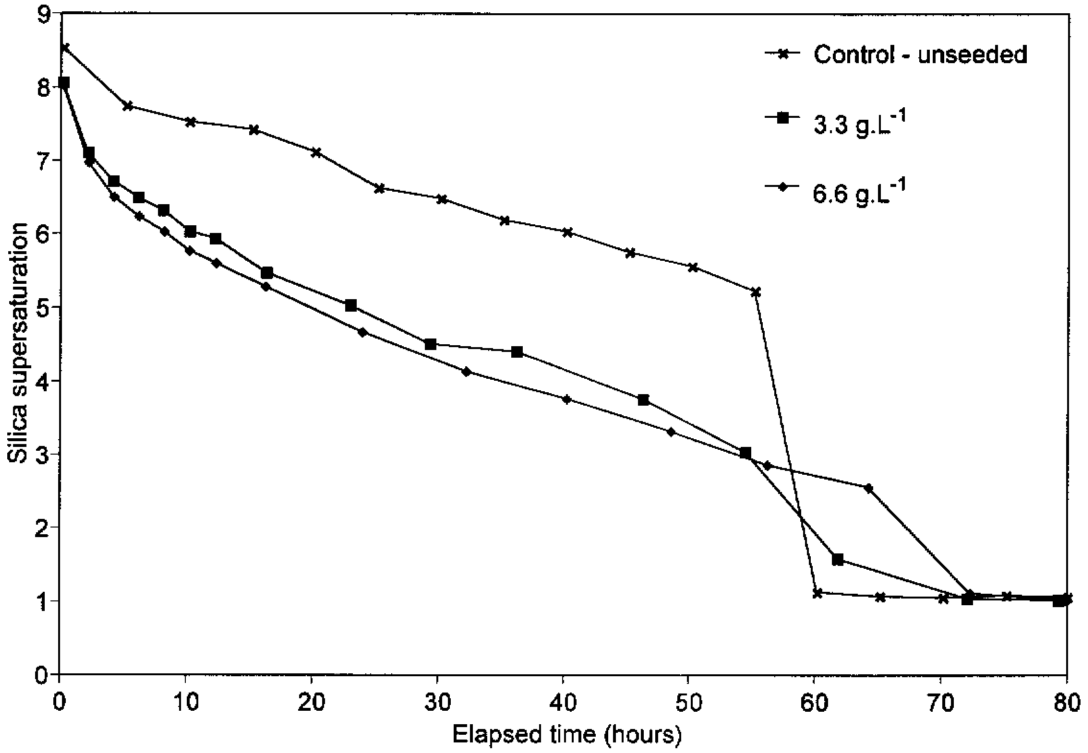

Figure 3.22: Silica supersaturation versus elapsed time, as a function of industrial seed loading. Precipitation conditions for all experiments: S = 8.6, 50 g L^{-1} H_2SO_4 and 95°C.

The shape of the precipitation curves in Figure 3.22 for the two seeded experiments indicate that they were unsuccessful in trying to achieve improvements of the magnitude observed at S = 2.9 (Figure 3.21). The curves are similar to that of the control and exhibit an induction period of similar duration to that of the control, albeit the curve is a different shape. This is followed by a precipitation period, prior to equilibrium solubility being reached. This indicates that the seed was ineffective in preventing the nucleation and growth of micro-gel. In fact, the seed has had a detrimental effect on precipitation with the precipitation time, shown in Table 3.10, being longer than that for the control.

Table 3.10: Effect of industrial seed loading on seeded precipitation. Precipitation conditions for all experiments: S = 8.6, 50 g L^{-1} H_2SO_4 and 95°C.

Seed Loading ($g\ L^{-1}$)	Precipitation Time - Silica Concentration (hours)	Filtration Rate - Initial ($m^3\ m^{-2}\ h^{-1}$)	Filtration Rate - Final ($m^3\ m^{-2}\ h^{-1}$)
Control	60	NA	<0.05
3.3	72	1.76	<0.05
6.6	72	1.04	<0.05

The filtration rates for the seeded products are the same as that for the control, further evidence that the seed was ineffective in preventing micro-gel precipitation from this supersaturation. The precipitation rates are not shown in Table 3.10 because these experiments had induction periods in which primary nucleation of micro-gel is occurring and not exclusively growth on seed. Thus, the tangent to the precipitation curves in Figure 3.22 does not exclusively represent the precipitation rate due to growth on seed, as it does in Figures 3.19 and 3.21.

It would be advantageous if increased seed loadings could be used to precipitate silica from concentrations above the S = 2.9 cut-off to producing a micro-gel. However, the results of the experiments shown here indicate that this is not possible, although increased seed loadings do permit much higher precipitation rates from S = 2.9.

3.4 CONCLUSIONS

A series of simple batch experiments from strong sulfuric acid solutions have revealed much valuable information about the silica precipitation process. Monosilicic acid and silica concentrations, and turbidity measurements were used to follow the progress of precipitation, while filtering tests and electron microscopy were used to determine the precipitate quality and morphology, respectively.

The equilibrium solubility of silica precipitated from 50 g L^{-1} sulfuric acid, at 95°C with a range of initial silica concentrations from 1000 to 7000 mg L^{-1} was determined to be 350±50 mg L^{-1}, expressed as SiO_2. The presence of aluminium, iron (III) or fluoride ions did not influence the equilibrium solubility. Further experimentation determined the only solution species present at equilibrium to be monosilicic acid.

The inductively coupled plasma - atomic emission spectroscopy (ICP-AES) method used to determine the aqueous silica concentration was in fact also measuring a proportion of solid silica that passes through the membrane filter during sample preparation. Only at equilibrium does the ICP-AES value truly represent the monosilicic acid concentration in solution.

The rate of silica precipitation is proportional to the supersaturation. It is also proportional to the concentrations of sulfuric acid, zinc sulfate, iron (III) sulfate, aluminium sulfate and hydrofluoric acid, and the precipitation temperature, all at a fixed silica supersaturation. None of these additives appear to be incorporated in the silica precipitate, nor noticeably consumed from the liquor; their effect would therefore appear to be catalytic. Studies on the effect of supersaturation revealed a dramatic change in the precipitate morphology between $S = 2.9$ and $S = 4.3$. At $S = 4.3$ and above, unfilterable, porous, micro-gel particles are formed, while at $S = 2.9$ and below granular, colloidal particles that filter rapidly are formed. The filtration rate of silica micro-gel particles can be increased by addition of aluminium sulfate during precipitation, but only at concentrations of 0.5 M $Al_2(SO_4)_3$ and above. While some of these additives may not willingly be used in a hydrometallurgical zinc plant, they are, however, present in solution and a knowledge of their effects is important.

Only silica that has an activated surface is suitable for secondary precipitation, with the rate being proportional to the seed loading. Silica seed particles that have remained in solution and were precipitated under similar conditions to those used for further growth make the best seeds. While seed can be used to increase the rate of silica precipitation from any supersaturation, it cannot be used to prevent the precipitation of micro-gel from supersaturations above S = 2.9. The insoluble impurity phases present in the natural zinc orthosilicate ore are acting as either nucleation or aggregation centres for silica precipitation.

The structure of precipitated silica is independent of the rate of precipitation. Micro-gel particles always form at S = 4.3 or above, whether it be in one hour or 2500 hours. Similarly, granular, colloidal particles always form at S = 2.9 or below, whether it be in seven hours or 350 hours. Therefore, the structure of the silica precipitate is controlled by chemical means rather than kinetic means, with supersaturation being the most dominant factor. *ie.*, The rate at which the product is formed does not determine its structure, the chemical conditions under which it is formed are responsible for this.

It would appear that hydrofluoric acid catalyses all forms of silica precipitation (gel, micro-gel or granular precipitate) and not just gelation. The mechanism for the formation of silica micro-gels and granular precipitates is essentially the same, but is dominated by supersaturation. There were previously thought to be two completely separate mechanisms, but since the same chemical factors have a similar influence on both, it is likely that they are similar.

A suspension of poorly filtering, micro-gel particles can be aged at 95°C to form a suspension of dense particles that have greatly improved filtration performance. The time frame for this to occur is about double the time taken for precipitation to reach equilibrium (as determined by silica concentration), *eg.* from S = 5.7 the time for precipitation is approximately six days, while the ageing process occurred over the following ten days.

4.0 CONTINUOUS PRECIPITATION

4.1 INTRODUCTION

This section describes the construction and use of a laboratory scale continuous crystalliser to study silica precipitation. The crystalliser is loosely based on the design of those used by Pasminco in their pilot plant, but on a smaller scale. The aims of these continuous precipitation experiments are described below.

First, the major finding from the batch experiments, Section 3.0, needed to be tested on a continuous basis. *ie.*, the hypothesis stating "The silica supersaturation limit of $2.9 \leq S \leq 4.3$ (equivalent to a silica concentration between 1000 and 1500 mg L^{-1} SiO_2) is the gel point for silica. Above this limit silica gel is formed and below this silica precipitate is formed" needed to be accepted or rejected. This was essentially an investigation of the effect of supersaturation on silica precipitation.

Secondly, the effect of mixing and product removal conditions on continuous silica precipitation needed to be determined. Pasminco had indicated that this could be a major problem in scaling up to pilot plant and full plant scale. More specifically, there was concern about the quality of mixing and product removal in a pilot plant or plant scale crystalliser compared to a laboratory scale crystalliser.

Thirdly, a set of conditions needed to be determined for successful operation of the crystalliser. This was a request from Pasminco, with successful operation being defined as that producing a silica product that: has a filtration rate in the order of 1.0 m^3 m^{-2} h^{-1}; has a dense structure not incorporating zinc ions; settles readily when flocculated, at a rate of at least 1.0 m h^{-1}; has a thickened solids loading in the order of 300 g L^{-1} after settling; contains 20 to 25% moisture after filtering; contains as many impurities as possible so as to purify the resulting solution. Ideally, the process would have a residence time of approximately 20 hours or less. This objective may well be achieved as a result of the information learned from the first two steps.

The batch experiments, detailed in Section 3.0, have revealed that increasing the sulfuric acid concentration increases the rate of silica precipitation. This would seem an obvious avenue to explore using continuous experiments; however, industrially, it is not economically feasible for Pasminco to operate at an acidity higher than 50 g L^{-1} sulfuric acid.

The last aim of this section of work was to gain further insights into the mechanism of silica precipitation.

4.2 EXPERIMENTAL OUTLINE

4.2.1 Description of the continuous crystalliser

The continuous crystalliser, a photograph of which is shown in Figure 4.1, was of the mixed suspension mixed product removal (MSMPR) type and utilised a draft tube baffle reactor vessel. The working volume of the crystalliser was 2050 mL. Agitation was provided by an impeller, driven by an overhead mechanical stirrer. The crystalliser is depicted schematically in Figure 4.2. The entire system was operated from the Control computer which is linked to send signals to, and receive signals from, the various electrical components via the Transfer box.

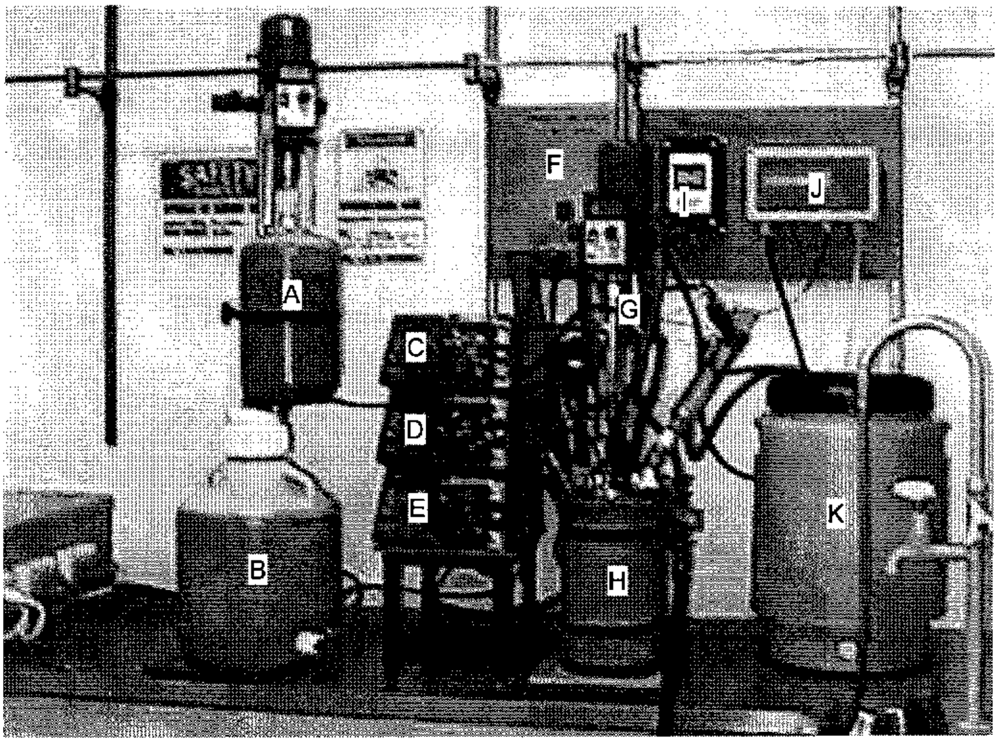

Figure 4.1: Photograph of the continuous crystalliser with the major components labelled: (A) ore slurry storage, (B) acid storage, (C) product pump, (D) ore slurry pump, (E) acid pump, (F) transfer box, (G) product removal valve, (H) reactor vessel, (I) pH transmitter, (J) conductivity transmitter and (K) condenser cooling water storage. The control computer is not shown.

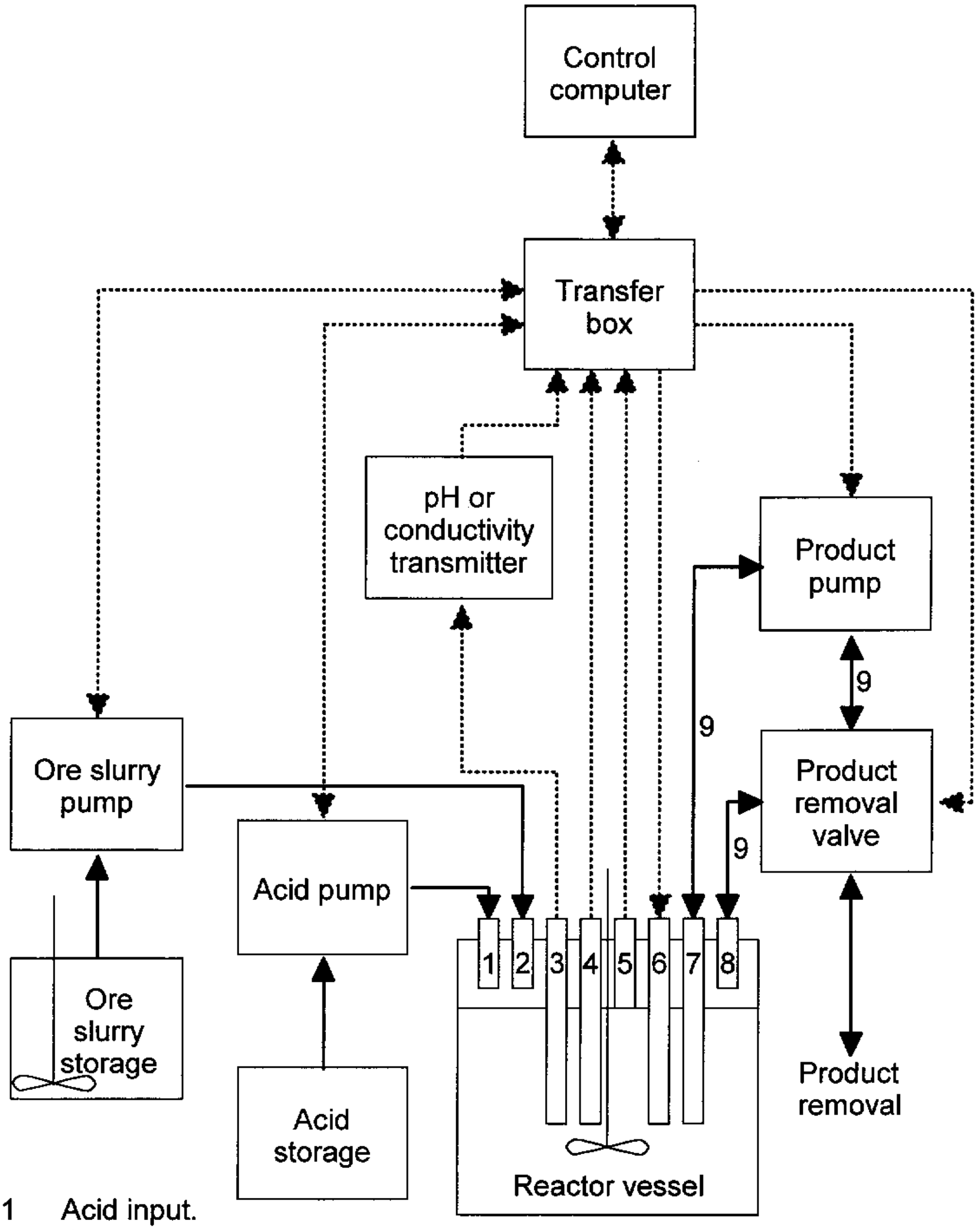

1 Acid input.
2 Ore slurry input.
3 pH electrode or Conductivity sensor.
4 Temperature probe and transmitter.
5 Liquor level sensing electrode.
6 Immersion heater.
7 Product removal.
8 Product return.
9 Product loop.

—▶ Liquid/slurry transport, one way.
◀—▶ Liquid/slurry transport, two way.
······▶ Electrical signal, one way.
◀···▶ Electrical signal, two way.

Figure 4.2: Schematic diagram of the continuous crystalliser.

A stable operating temperature was achieved by measuring the temperature and transmitting it to the Control computer which then switched the Immersion heater on and off as required to maintain the set-point temperature. The precipitation process began with ore slurry, that was agitated by an impeller, driven by an overhead mechanical stirrer, being fed into the reactor vessel at constant rate by a peristaltic pump, the Ore slurry pump. The pump returned the ore slurry flow rate to the Control computer. As the ore was dissolved in the reactor vessel, acid was consumed and the pH increased and the conductivity decreased. Either of these parameters could be used to control the acidity. By keeping the acidity and the Ore slurry flow rate constant, constant silica supersaturation was achieved. The pH or the conductivity was measured and transmitted to the computer which in turn switched on a second peristaltic pump, the Acid pump, to dose acid into the reactor vessel to maintain the set-point pH or conductivity. The further the pH or conductivity was from the set-point the faster the Acid pump was operated to correct it. This pump also returned a flow rate to the computer which is added to the ore slurry flow rate to determine the cumulative volume of reagents dosed into the crystalliser, which was used to determine the residence time of the process. When the liquor in the reactor vessel reached the Liquor level sensing electrode, a signal was sent to the Control computer which turned on a third peristaltic pump, the Product pump. For 20 seconds the product flowed through the Product loop and returned to the reactor vessel to allow for homogeneity in the Product loop to be achieved. The Control computer activated the Product removal valve and product was discharged into a receiver. When the liquor fell below the Liquor level sensing electrode, the Product pump was reversed in flow direction to clear the Product removal tubing. Following this, with the Product pump still operating in reverse, the Product valve was deactivated thus emptying the contents of the Product loop back into the reactor vessel. Five seconds after the Product valve was deactivated, the Product pump was switched off and awaited the next product removal cycle. The whole process was carried out continuously for approximately six residence times, upon which steady state was achieved and a true steady state sample could be taken.

4.2.2 Description of the reactor vessel

The reactor vessel was of the draft tube baffle type and had a working volume of 2050 mL. Figure 4.3 shows a cross sectional-view, dimensional drawing of the reactor vessel and lid. The general design follows that outlined in Section 1.3. Note the contoured reactor vessel bottom and draft tube to minimise the power input to achieve homogeneous suspension, one of the requirements for MSMPR operation. The slurry in the reactor vessel travels down the draft tube and up the annulus. The diameter of the draft tube was thus 2/3rd of the diameter of the reactor vessel. The draft tube had three integral 316 stainless steel support shafts, 4 mm in diameter, protruding from the upper end of the tube and was suspended from the lid using these shafts. This arrangement allowed for vertical adjustment of the draft tube within the reactor vessel to vary mixing conditions. Four baffles, 14 mm wide or approximately 1/10th the internal vessel diameter, were located at 90° intervals in the draft tube anulus to prevent excessive vortexing. The 316 stainless steel impeller consists of a Lightnin A310 Fluidfoil, 66 mm in diameter, mounted on an 8 mm shaft. The diameter of the impeller was 3/4 the diameter of the draft tube. This type of axial flow impeller produced very low, and constant shear across the full width of each blade, resulting in minimal attrition of suspended solids.

The reactor vessel and draft tube were manufactured by Whickam Fibreglass from Hetron 197 glass reinforced plastic. This material was chosen because of its excellent resistance to acid and high temperature, its ease of manufacture to produce intricate designs and its overall low cost. The lid was manufactured from 316 stainless steel due to its strength, inertness to chemical attack and machinability.

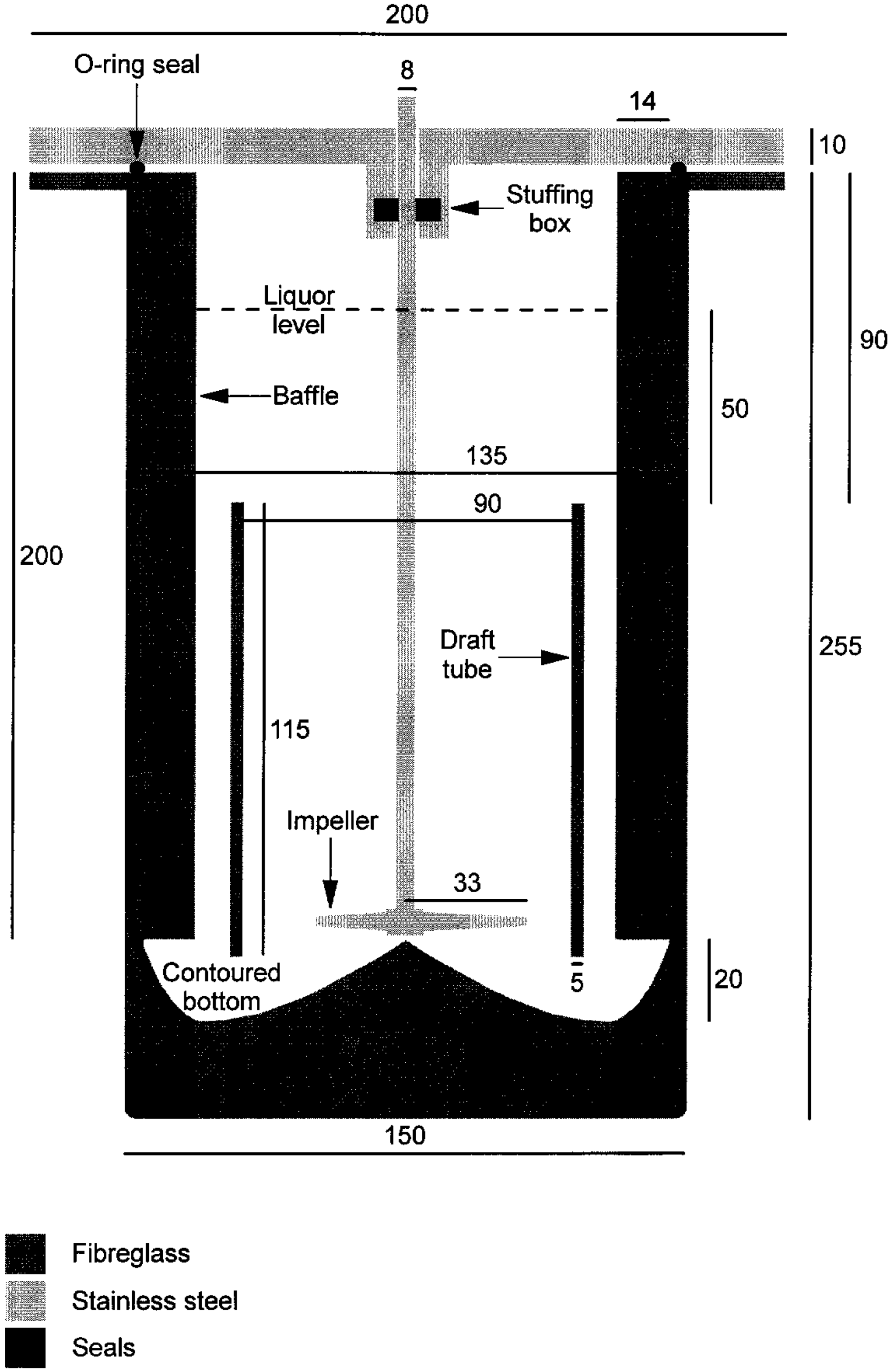

All dimensions in millimetres (mm)

Figure 4.3: Cross-sectional view, dimensional drawing of the reactor vessel and lid.

Further detail on the construction and optimisation of the mixing and product removal conditions in the continuous crystalliser is shown in Section 9.3.

4.2.3 Operation of the crystalliser

The Ore slurry reagent was made up by dispersing, with stirring, 1400 g of natural zinc orthosilicate ore in approximately 2000 mL of Cell room feed solution. Details of the preparation and characterisation of the natural zinc orthosilicate ore are given in Section 2.2, while the Cell room feed solution is described in Section 9.2.1. The resultant slurry was washed into the Ore slurry storage tank with further Cell room feed solution and made up to the 3500 mL mark to produce a slurry of 400 g L^{-1} solids loading. A two blade, centrifugal impeller, driven by an overhead stirrer at 1000 rpm was used to homogenise the suspension. The Ore slurry was agitated for at least 12 hours prior to the commencement of operation to ensure complete dispersion of the ore as a preventative measure against the peristaltic pump tubing becoming blocked.

The Acid storage tank was filled with Cell room spent electrolyte, detailed in Section 9.2.1, and weighed. The density was 1.27 g cm^{-3} and thus the volume of Cell room spent electrolyte can be easily calculated.

The crystalliser components were assembled as shown in Figure 4.1, and all electrical and tubing connections were made. The stuffing box seals, described in Section 9.3.1, were replaced at the beginning of each experiment, as was all the peristaltic pump tubing. Each piece of tubing was wrapped in electrical tape on the up-flow side of the pump head next to the tubing clamp. This prevented the tubing slipping through the pump head during operation. The desired mixing and product removal conditions were set, from those in Table 9.4.

An initial mixture of Cell room spent electrolyte and Cell room feed solutions totaling 2000 mL was prepared and placed in the crystalliser. The mixture had the same acidity as the desired operating acidity for the experiment, in all cases 50 g L^{-1} sulfuric acid. To begin a precipitation experiment, the Control computer and printer were switched on and the software loaded. The overhead stirrer to agitate the reactor vessel and the condenser cooling water pump were switched on, along with power to the Transfer box. The software was started, but at this stage only heating of the reactor vessel was occurring. The temperature was under control after about 60 minutes of operation. At this stage, the three peristaltic pumps were switched on and the process started. The residence time for the process was determined by the flow rate of Ore slurry into the reactor vessel, and this was set accordingly to provide the desired residence time. The computer controlled all aspects of the operation of the crystalliser, and all that was required was routine sampling and preventative maintenance. The crystalliser was typically operated for at least six residence times to achieve steady state before being shut down. Upon completion of the experiment the remaining volume of Ore slurry and the remaining mass of Cell room spent electrolyte were recorded. Once again, the volume of Cell room spent electrolyte was calculated, from the known density, and the volume of reagents consumed was compared with that determined by the Control computer. This allowed for a check on the accuracy of the computer, and also provided the volumetric ratio of Cell room spent electrolyte to Ore slurry, which is an important figure for Pasminco to know.

Sampling was performed at intervals of one quarter the duration of the residence time and involved waiting for the crystalliser to discharge product from the product loop, this material then became the sample. Sampling in this manner did not disturb the operation of the crystalliser. Approximately 4 mL of sample was collected and the acidity determined and a sample filtered and diluted for ICP-AES analysis. The sample preparation methods for these analyses are described in Section 9.2.2.4 and 9.2.2.2, respectively. During filtration of the sample for ICP-AES analysis, a qualitative estimate of the filtration performance was recorded. The acidity determination was used as a check on the computer's control of that parameter.

At the end of each residence time, more extensive sampling was conducted, in addition to the sampling described above. While the crystalliser was discharging product, approximately 50 mL was collected directly from the discharge tube, to prevent any classification, in a plastic bottle for the determination of the PSD as outlined in Section 9.2.2.11. A sample was prepared for TEM imaging according to the method in Section 9.2.2.7. A further 50 mL of the raw sample was used to determine the quantitative filtration rate, the method is supplied in Section 9.2.2.12. When steady state had been reached at the end of six residence times, the crystalliser was shut down, and all the above samples collected and tests performed. A settling test, outlined in Section 9.2.2.15, was also performed using 500 mL of the remaining product in the reactor vessel.

Preventative maintenance was carried out at intervals of one half the duration of the residence time to ensure smooth, uninterrupted operation of the crystalliser. The Liquor level sensing electrode, Conductivity sensor and Product removal tube were removed from the reactor vessel and wiped clean of any deposits that might hinder their successful operation. While the Product removal tube was removed, the product loop was flushed with Milli-Q^{TM} water to remove any product deposits that might build up in the loop, particularly in the Product removal valve. The tubing for the Ore slurry peristaltic pump was back-flushed with Cell room feed solution into the Ore slurry tank to remove any particles that might have been lodged in the tubing that causing it to become blocked. Only a very small volume of Cell feed solution was used, so as not to dramatically alter the solids loading of the Ore slurry.

4.3 RESULTS AND DISCUSSION

In total, 12 continuous precipitation experiments were carried out. However, the first six experiments were used to identify and eliminate any faults in the system, in order to improve operating proficiency and develop a reliable crystalliser. During this period, it was determined that pH control of acidity was not suitable for this high acid concentration, and thus conductivity control was employed. No useful precipitation results could be obtained from these experiments, and they are not discussed any further. The remaining six experiments are discussed in turn.

4.3.1 Industrial run number 7 (IRN-7)

The aim of this experiment was to formulate a standard experiment against which all future experiments could be compared. The conditions used for this experiment were based on the results of the batch experiments detailed in Section 3.0 and the Patents of Fugleberg and Poijarvi (1977 and 1979) of the Outokumpu Oy company. The batch experiments clearly show the rate of silica precipitation to be proportional to temperature, thus the highest possible temperature, at ambient pressure, was chosen. The Outokumpu Oy Patent suggests a residence time of approximately 20 hours. The conditions used are tabulated in Table 4.1. Detail of the MSMPR configuration of the reactor vessel is shown in Section 9.3.4.

Table 4.1: Operating parameters for IRN-7.

Parameter	Value
Mixing and product removal conditions	MSMPR
Silica feed rate (g SiO_2 L^{-1} h^{-1})	1.20
Temperature (°C)	95
Acidity (g L^{-1})	50
Residence time (hours)	18

Figure 4.4 shows a plot of the main process variables as a function of elapsed time for the entire experiment. The residence time intervals are also shown. The variables graphed on the primary Y axis are recorded in the

legend on the left-hand side of the figure, while those graphed on the secondary Y axis are recorded in the legend on the right-hand side of the figure. This also applies to Figures 4.7, 4.8, 4.10, 4.11 and 4.14.

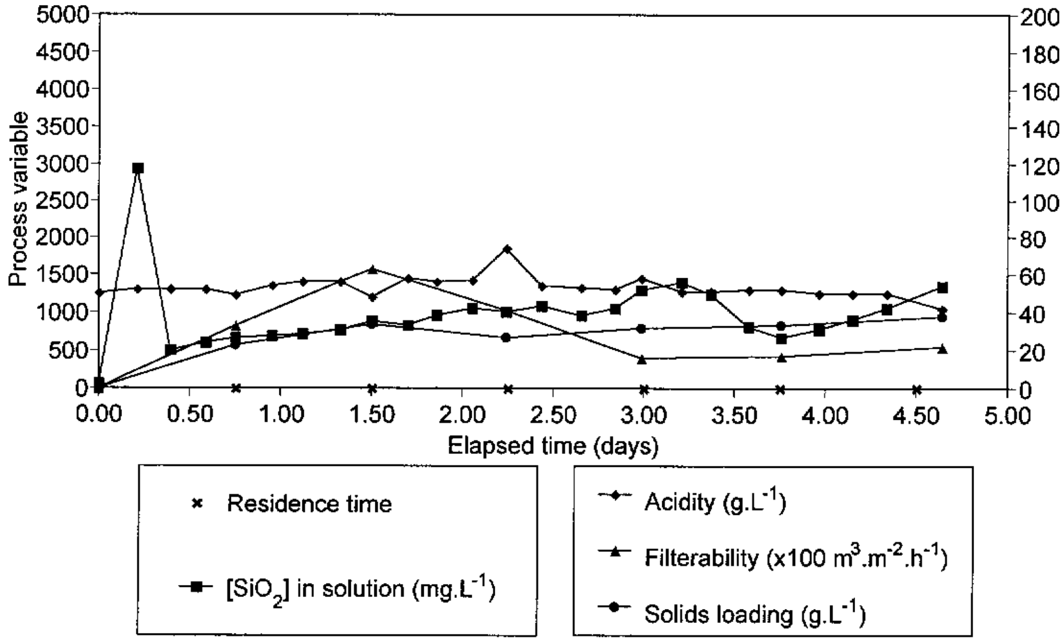

Figure 4.4: Main process variables versus elapsed time for IRN-7.

Control of acidity during the experiment was satisfactory, at best, with a couple of excursions outside the expected operating zone of 50±2 g L^{-1} sulfuric acid. Control for the steady state period however, was very good. Temperature control was excellent at 95.0±0.2°C for the duration of the experiment. The solids loading in the reactor vessel increased for the first two residence times, decreased during the third residence time and increased for the remainder of the experiment. The silica concentration fluctuates throughout the experiment with a massive initial spike, and does not reach equilibrium at any stage. It should be remembered that the silica concentration was determined by filtration of a liquor sample followed by ICP-AES analysis and contains, as well as the soluble silica, a portion of the solid silica that passes through the filter membrane as well. Further detail of this is given in Section 3.3.1. The filtration performance of the silica product was found to be similar to that reported in the literature (Fugleberg and Poijarvi, 1977 and 1979). For the first several hours of operation the product slurry is easy to filter. This is followed by a period where the silica gels and filtration is virtually impossible. By the end of the first residence time filtration performance is much improved. These observations are qualitative only and were made when filtering the sample for ICP-AES analysis. Figure 4.4 shows the filterability improving for the first two residence times, decreasing for the next two and staying roughly constant at about 0.25 $m^3\ m^{-2}\ h^{-1}$ for the remainder of the experiment. This filtration performance is in the range 0.2 to 0.4 $m^3\ m^{-2}\ h^{-1}$ as reported by Fugleberg and Poijarvi (1977 and 1979). Pasminco states a filtration rate in the order of 1.0 $m^3\ m^{-2}\ h^{-1}$ as being satisfactory, so clearly the conditions used in this experiment do not produce a satisfactory product. The fluctuation in silica concentration and the unsatisfactory filtration performance at steady state might be linked to the hypothesis detailed in Section 4.1. However, further experiments are needed to qualify this.

More detailed results from the sixth residence time, the steady state period, are shown in Table 4.2.

Table 4.2: Results at steady state for IRN-7.

Parameter	Value
Silica concentration (mg L^{-1})	850
Temperature (°C)	95.0±0.2
Acidity (g L^{-1})	50±2
Filterability ($m^3\ m^{-2}\ h^{-1}$)	0.22
Reactor solids loading (g L^{-1})	37.9
Filter cake thickness (mm)	2
Filter cake water content (%w/w)	68
Filtrate clarity	46+
Settling rate (m h^{-1})	5.0
Thickened solids loading, after 60 minutes (g L^{-1})	156
Supernatant clarity, after 60 minutes	28

The settling rate, determined at steady state on a portion of the reactor contents, was found to be very good at 5.0 m h^{-1}; well above the 1.0 m h^{-1} target figure of Pasminco. The thickened solids loading after 60 minutes of settling was 156 g L^{-1}, and is approximately half the desired 300 g L^{-1}

typically found in these types of settled slurries. The water content of the wet filter cake was very high at 68% and is much higher than the 20 to 25% quoted by Pasminco as being a reasonable value. The major disadvantage of a high water content of the filtered product is that a large volume of wash water will be needed to wash the material free of trapped mother liquor, which contains the valuable zinc sulfate solution. The transportable moisture limit of the product is also of consideration. This is the moisture limit, above which the material can liquefy. This value is not known for silica but is expected to be in the order of 20 to 25%, which is similar to other hydrometallurgical precipitation products.

Figure 4.5 shows the PSDs for the insoluble material in the natural zinc orthosilicate ore and at the end of the first residence time for IRN-7, while Figure 4.6 shows the PSDs at the end of each residence time for all of IRN-7.

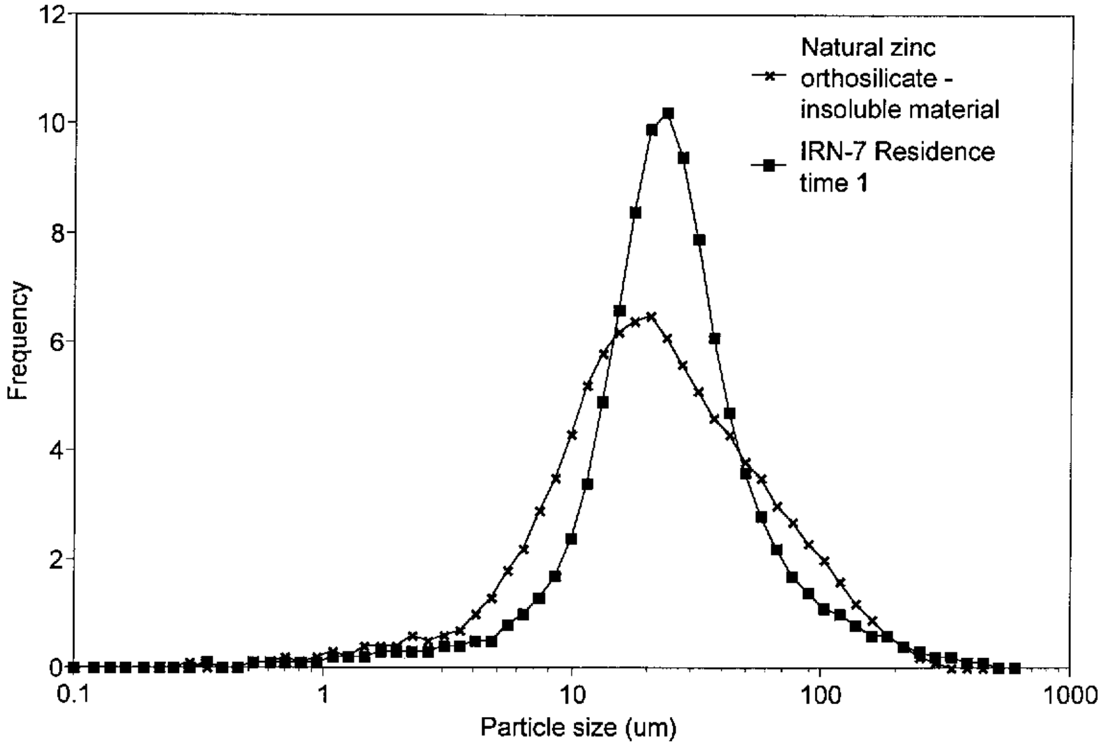

Figure 4.5: PSDs for the insoluble material in the natural zinc orthosilicate ore and at the end of the first residence time for IRN-7.

A comparison of the PSD from the insoluble material in the natural zinc orthosilicate ore and that at the end of the first residence time for this experiment clearly show their mean particle sizes to be approximately the same. However, there is some additional material present that has narrowed the PSD in the IRN-7 sample. It should be noted that only a small portion of the IRN-7 sample is the insoluble material from the natural zinc orthosilicate. Thus, the PSD curve for the insoluble material in the natural zinc orthosilicate, shown in Figure 4.5, is disproportionately large. The silica concentration curve in Figure 4.4 has a massive spike during the first residence time that would indicate silica precipitation had occurred, thus indicating the additional material seen in the PSD could be silica. The fact that the mean size of the initial silica particles, about 20 μm, is the same as the insoluble particles form the ore suggests that these insoluble particles might be acting as primary heterogeneous nucleation centres for silica precipitation.

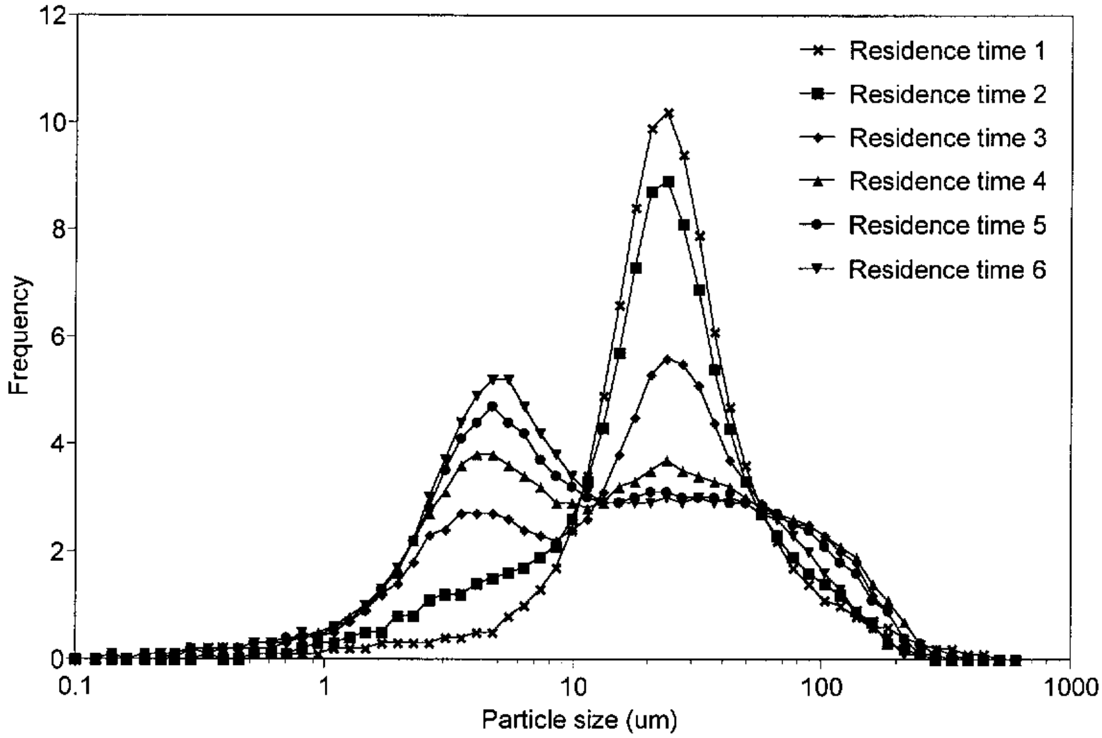

Figure 4.6: PSD at the end of each residence time for IRN-7.

After the first residence time, the peak centred at 20 μm becomes less intense and another peak centred at 4 μm increases in intensity, as is shown in Figure 4.6. The PSD appears to reach equilibrium as a bi-modal distribution during the fifth and sixth residence times. The fluctuation in silica concentration during the experiment, shown in Figure 4.4, does not appear to affect the PSD of the product.

4.3.2 Industrial run number 8 (IRN-8)

The aim of this experiment was to trial a higher volumetric, silica feed rate to the crystalliser, or in other words a shorter residence time. These changes are reflected in the operating conditions, outlined in Table 4.3. The reason for this was to investigate the Outokumpu Oy patent (Fugleberg and Poijarvi, 1977 and 1979) where a silica feed rate as high as 3.0 g L^{-1} h^{-1}, calculated as SiO_2, can be used, producing silica with filtration rates in the range 0.2 to 0.4 m^3 m^{-2} h^{-1}.

Table 4.3: Operating parameters for IRN-8.

Parameter	Value
Mixing and product removal conditions	MSMPR
Silica feed rate (g SiO_2 L^{-1} h^{-1})	2.37
Temperature (°C)	95
Acidity (g L^{-1})	50
Residence time (hours)	8

Figure 4.7 shows a plot of the main process variables as a function of elapsed time for the entire experiment; residence time intervals are also shown.

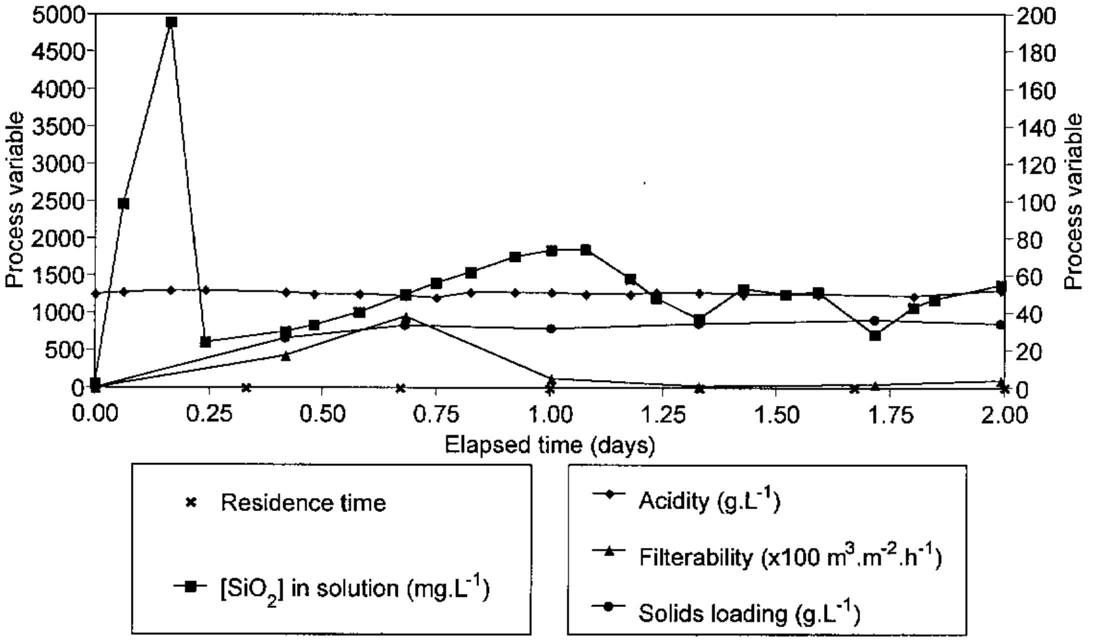

Figure 4.7: Main process variables versus elapsed time for IRN-8.

Much better control of acidity was achieved with this experiment compared to IRN-7; within the operating zone of 50±2 g L^{-1} sulfuric acid for the entire experiment. Once again, temperature control was excellent at 95.0±0.2°C for the duration of the experiment. The solids loading in the reactor vessel remained very constant in the range 30 to 35 g L^{-1} after building up for the first residence time. As with IRN-7, the silica concentration fluctuates throughout the experiment with a massive initial spike, this time up to 5000 mg L^{-1} SiO_2. Once again equilibrium is not reached at any stage of the experiment. The filtration performance was much worse than that in IRN-7, but followed the same trend. The 0.2 to 0.4 m^3 m^{-2} h^{-1} reported by Fugleberg and Poijarvi (1977 and 1979) was achieved only at the end of the second residence time. Following this, the filtration rate was in the range 0.01 to 0.05 m^3 m^{-2} h^{-1}, appalling by any standard. Obviously, under these conditions, the feed rate of silica cannot be raised to the maximum level of 3.0 g L^{-1} h^{-1} as suggested by Fugleberg and Poijarvi (1977 and 1979). The same qualitative filtration observations were made as for those in IRN-7, except that the steady state filterability was far worse. A possible trend maybe discerned in regard to the fluctuation in silica concentration and the unsatisfactory filtration performance at steady state. It would appear that, after the initial spike in silica concentration, the filtration performance is satisfactory until approximately such time as the silica concentration rises above 1000 mg L^{-1}. When this occurs, an unfilterable silica product is formed. This observation is in line with the hypothesis detailed in Section 4.1. Further experiments are needed, with the silica concentration remaining below 1000 mg L^{-1} to qualify this.

More detailed results from the sixth residence time, the steady state period, are shown in Table 4.4.

Table 4.4: Results at steady state for IRN-8.

Parameter	Value
Silica concentration (mg L^{-1})	1080
Temperature (°C)	95.0±0.2
Acidity (g L^{-1})	50±2
Filterability (m^3 m^{-2} h^{-1})	0.04
Reactor solids loading (g L^{-1})	34.0
Filter cake thickness (mm)	2
Filter cake water content (%w/w)	67
Filtrate clarity	46+
Settling rate (m h^{-1})	7.1
Thickened solids loading, after 60 minutes (g L^{-1})	92
Supernatant clarity, after 60 minutes	37

A very good settling rate was achieved for this experiment, 7.1 m h^{-1}. Despite this good result, the thickened solids loading was poor at less than 100 g L^{-1}. The moisture content of the filter cake was almost identical to that of IRN-7, and is most unsatisfactory.

The PSDs for this experiment were almost identical to those of IRN-7 (Figure 4.6) and thus, are not shown. The same initial, single peak at 20 μm was present which transformed into the bi-modal distribution with peaks at approximately 4 and 20 μm by the steady state period.

4.3.3 Industrial run number 9 (IRN-9)

The aim of this particular experiment was to use mixed suspension classified product removal (MSCPR) conditions to selectively leave a higher proportion of the larger fraction of the product in the crystalliser (see Section 9.3.4). The idea being to increase the PSD of the silica and produce a better filtering product. Thus, the parameters used for this experiment are the same as those for the control, IRN-7, with the exception of the mixing and product removal conditions, and these are displayed in Table 4.5.

Table 4.5: Operating parameters for IRN-9.

Parameter	Value
Mixing and product removal conditions	MSCPR
Silica feed rate (g SiO_2 L^{-1} h^{-1})	1.20
Temperature (°C)	95
Acidity (g L^{-1})	50
Residence time (hours)	18

Figure 4.8 shows a plot of the main process variables as a function of elapsed time for the entire experiment; residence time intervals are also shown.

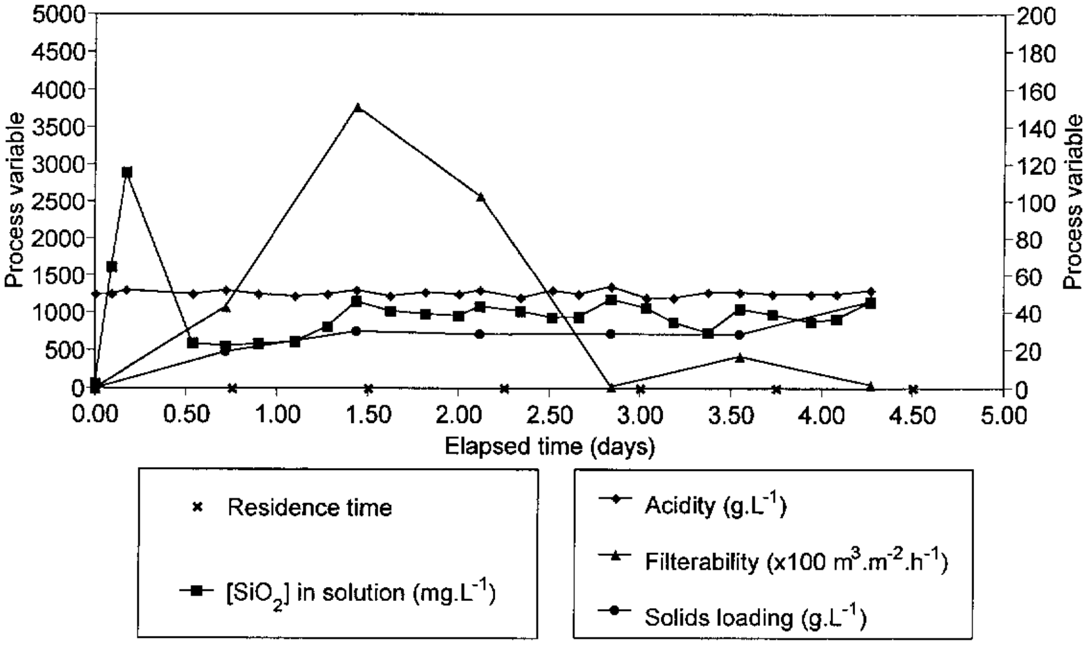

Figure 4.8: Main process variables versus elapsed time for IRN-9.

Very good control of acidity was maintained throughout the experiment, with only one minor excursion out side the operating zone of 50±2 g L^{-1} sulfuric acid, to 54 g L^{-1} sulfuric acid. Excellent control of temperature was achieved to 95.0±0.2°C for the experiment. The solids loading followed the same trend as in previous experiments, and was constant at about 30 g L^{-1} from the second residence time onwards. However, at the end of the sixth residence time the solids loading is much higher than expected and is most likely to be in error as this did not occur in IRN-7 (Figure 4.4) or IRN-8 (Figure 4.7). The reason for this increase is not known and thus, the value quoted in Table 4.5 is from the fifth residence time. The relationship between silica concentration and filterability seen in previous experiments continues with this one. Once again, as soon as the silica concentration rises above 1000 mg L^{-1} the filterability decreases dramatically. This is after the initial silica concentration spike, where the filterability, determined qualitatively, is extremely poor. The encouraging result from this experiment was the high level of filterability achieved until the third residence time, indicating that using classified product removal conditions improves silica filterability. Since the silica concentration rose above 1000 mg L^{-1} during this experiment, no further conclusions relating to the supersaturation hypothesis can be made.

More detailed results from the sixth residence time, the steady state period, are shown in Table 4.6.

Table 4.6: Results at steady state for IRN-9.

Parameter	Value
Silica concentration (mg L^{-1})	980
Temperature (°C)	95.0±0.2
Acidity (g L^{-1})	50±2
Filterability (m^3 m^{-2} h^{-1})	0.02
Reactor solids loading (g L^{-1})	28.6
Filter cake thickness (mm)	2
Filter cake water content (%w/w)	61
Filtrate clarity	46+
Settling rate (m h^{-1})	16.4
Thickened solids loading, after 60 minutes (g L^{-1})	130
Supernatant clarity, after 60 minutes	46+

An exceptional settling rate of 16.4 m h^{-1} was achieved for the silica product during steady state. However, the thickened solids loading was lower than desired at 130 g L^{-1}. Once again the water content of the filter cake was very high.

The PSDs for this experiment are shown in Figure 4.9. There is a higher proportion of larger product present at steady state than there was in previous experiments without product classification, *ie.* IRN-7, Figure 4.6.

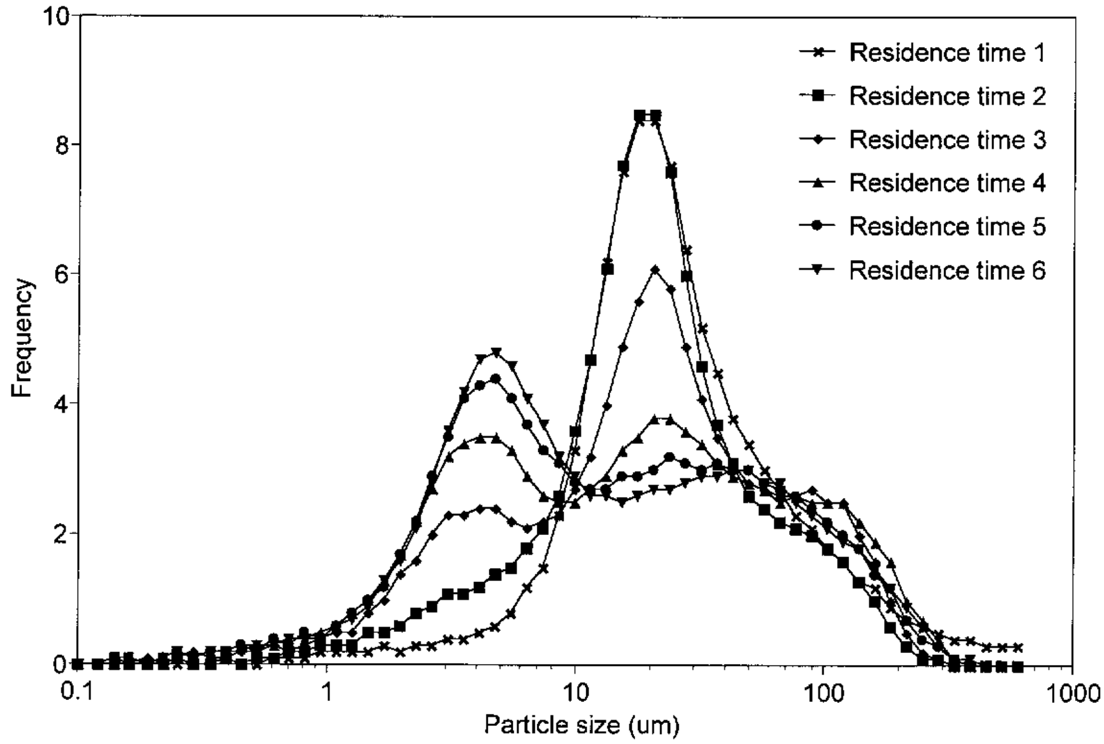

Figure 4.9: PSD at the end of each residence time for IRN-9.

4.3.4 Industrial run number 10 (IRN-10)

In an attempt to run an experiment without the silica concentration rising above 1000 mg L^{-1} in order to test the hypothesis concerning the relationship between filterability and silica concentration, the residence time for this experiment was increased by reducing the silica feed rate to the reactor vessel. The parameters for this experiment are displayed in Table 4.7.

Table 4.7: Operating parameters for IRN-10.

Parameter	Value
Mixing and product removal conditions	MSMPR
Silica feed rate (g SiO_2 L^{-1} h^{-1})	0.66
Temperature (°C)	95
Acidity (g L^{-1})	50
Residence time (hours)	29

Figure 4.10 shows a plot of the main process variables as a function of elapsed time for the entire experiment; residence time intervals are also shown.

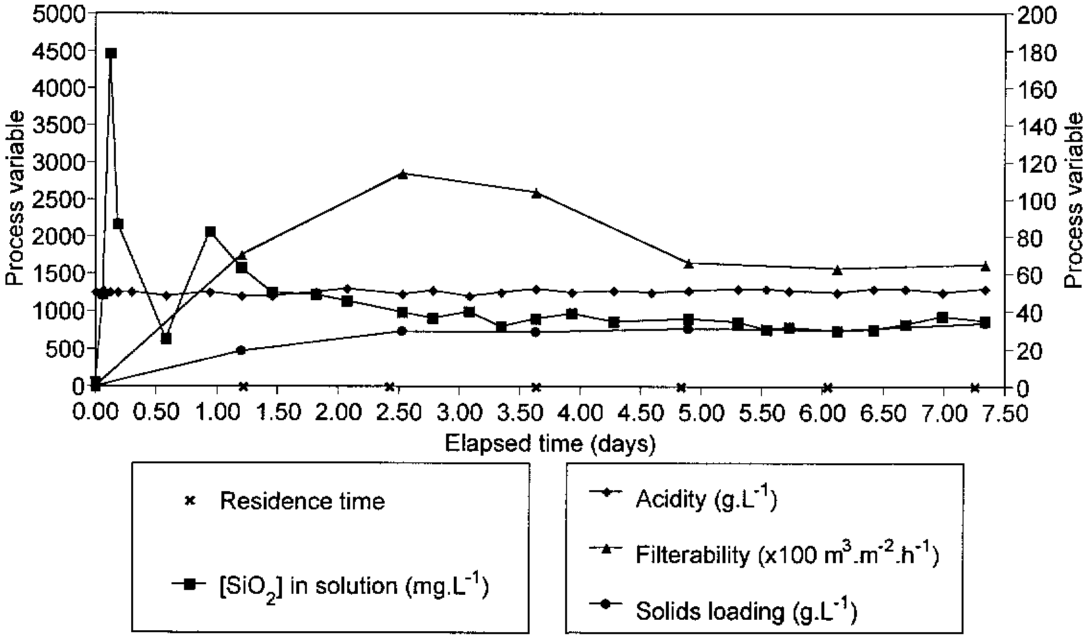

Figure 4.10: Main process variables versus elapsed time for IRN-10.

As a result of increasing operating proficiency, acidity and temperature were controlled to within their respective operating zones for the entire experiment. The solids loading remained essentially constant at 30 to 35 g L^{-1} from the second residence time. The silica concentration appears to reach equilibrium from the second or third residence time onwards, at a level just below 1000 mg L^{-1}. There is some unusual behaviour occurring with the silica concentration during the first residence time that hasn't previously appeared. The initial spike is still present, but it appears as if there is now a second one as well. However, this is most likely due to sampling or analysis error and will therefore be ignored. As a result of the silica concentration remaining below 1000 mg L^{-1} after the first residence time the filterability has also reached equilibrium at an acceptable level of about 0.6 m^3 m^{-2} h^{-1} at steady state. This is the first time filterability has reached equilibrium. While this level of filtration is not as high as the ideal 1.0 m^3 m^{-2} h^{-1}, it is still acceptable to Pasminco and is better than that reported by Fugleberg and Poijarvi (1977 and 1979). Unfortunately, to obtain this level of filtration performance the residence time is undesirably long. The results of this experiment now confirm the hypothesis concerning silica supersaturation and morphology. However, the supersaturation range for the gel point of silica, quoted in the hypothesis, can be narrowed to a single decimal point figure of

S = 2.9 (equivalent to a silica concentration of 1000 mg L^{-1} expressed as SiO_2).

More detailed results from the sixth residence time, the steady state period, are shown in Table 4.8.

Table 4.8: Results at steady state for IRN-10.

Parameter	Value
Silica concentration (mg L^{-1})	655
Temperature (°C)	95.0±0.2
Acidity (g L^{-1})	50±2
Filterability (m^3 m^{-2} h^{-1})	0.65
Reactor solids loading (g L^{-1})	33.8
Filter cake thickness (mm)	2
Filter cake water content (%w/w)	66
Filtrate clarity	46+
Settling rate (m h^{-1})	11.5
Thickened solids loading, after 60 minutes (g L^{-1})	152
Supernatant clarity, after 60 minutes	46+

As with previous experiments, a very good settling rate of 11.5 m h^{-1} was achieved, combined with a less than ideal, but typical, thickened solids loading of 152 g L^{-1}. The very high filter cake water content is, once again, quite typical of these experiments.

The PSDs for this experiment were almost identical to those of IRN-7 (Figure 4.6) and IRN-9, and thus are not shown. The same initial, single peak at 20 μm was present which transformed into the bi-modal distribution with peaks at approximately 4 and 20 μm by steady state.

4.3.5 Industrial run number 11 (IRN-11)

After the success in improving filterability by using MSCPR conditions in IRN-9, it was the aim of this experiment to improve upon that by using classified stirring classified product removal (CSCPR) conditions. This mixing and product removal configuration is detailed in Section 9.3.4. It is hoped to be able to achieve filtration performance close to that required by Pasminco. The conditions used for this experiment are outlined in Table 4.9. The slightly different values for the silica feed rate and consequently the residence time, for this experiment compared to IRN-7 and IRN-9, are due to the use of a different method of programming the Ore slurry pump. It is believed that these small changes will not dramatically affect the validity of comparing these three experiments, based on their silica feed rates.

Table 4.9: Operating parameters for IRN-11.

Parameter	Value
Mixing and product removal conditions	CSCPR
Silica feed rate (g SiO_2 L^{-1} h^{-1})	0.96
Temperature (°C)	95
Acidity (g L^{-1})	50
Residence time (hours)	20

Figure 4.11 shows a plot of the main process variables as a function of elapsed time for the first six residence times. The duration of this experiment was nine residence times in total; however, there was very little change in product quality once steady state had been reached. Thus, results after the sixth residence time are not shown. Since CSCPR conditions were used, the solids loading for both the product and reactor are shown. The samples from the reactor were taken by briefly returning the crystalliser to MSMPR conditions to remove a small representative sample to enable determination of the solids loading and PSD.

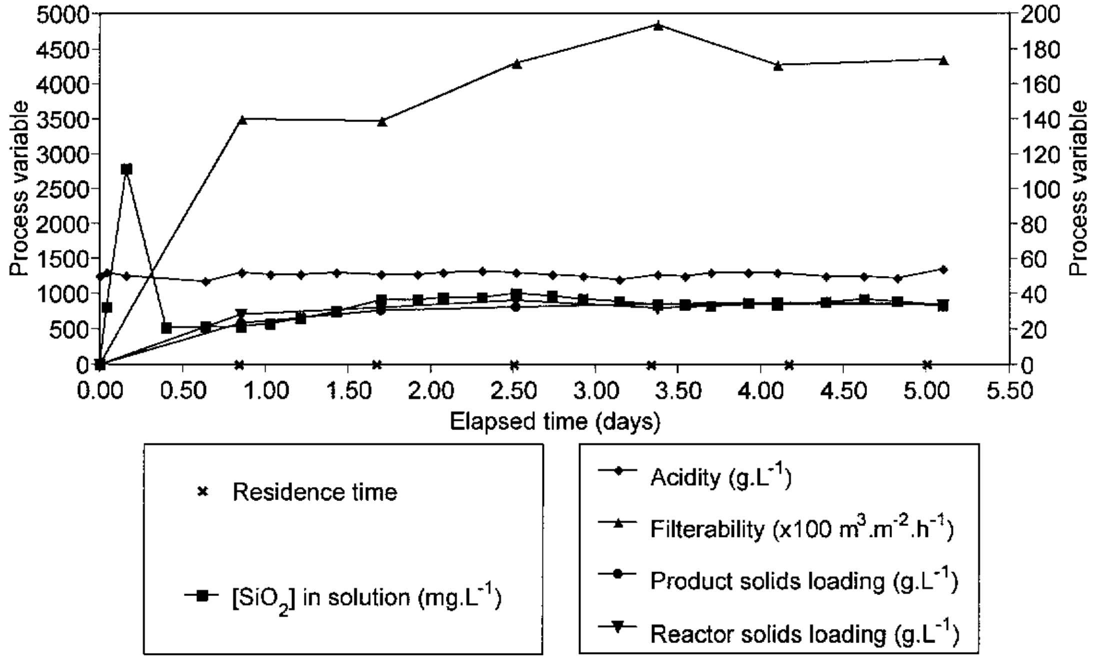

Figure 4.11: Main process variables versus elapsed time for IRN-11.

Temperature control for the experiment was once again excellent at 95.0±0.2°C. Acidity control was good with only two small excursions outside the prescribed operating zone of 50±2 g L^{-1} sulfuric acid. The solids loadings for the experiment are interesting. As would be expected under CSCPR conditions the solids loading for the product is less than that for the reactor; however, the difference is not as great as was expected on the basis of the wash-out tests described in Section 9.3.4. From the fourth residence time onwards, the solids loadings reverse with the reactor ones being higher. It is difficult to draw definite conclusions from these results as there is a 5% error in the solids loading value and some values are within experimental error. The solids loadings reach equilibrium at the end of the third residence time for this experiment, compared with the end of the second residence time for experiments using MSMPR conditions. The silica concentration reached equilibrium after the third residence time and never rose above 1000 mg L^{-1} for the entire experiment, apart from the initial spike during the first residence time. As a result of the silica concentration, the filterability for the experiment was exceptionally good, remaining above the ideal 1.0 m^3 m^{-2} h^{-1} for the duration and reaching an equilibrium value of 1.7 m^3 m^{-2} h^{-1} at steady state.

This is further reinforcement of the supersaturation hypothesis proved in IRN-10.

More detailed results for the product and reactor samples from the sixth residence time, the steady state period, are shown in Table 4.10.

Table 4.10: Results at steady state for IRN-11.

Parameter	Value
Silica concentration (mg L^{-1})	900
Temperature (°C)	95.0±0.2
Acidity (g L^{-1})	50±2
Reactor filterability (m^3 m^{-2} h^{-1})	1.47
Product filterability (m^3 m^{-2} h^{-1})	1.74
Reactor solids loading (g L^{-1})	33.4
Product solids loading (g L^{-1})	34.0
Reactor filter cake thickness (mm)	2
Product filter cake thickness (mm)	2
Reactor filter cake water content (%w/w)	70
Product filter cake water content (%w/w)	71
Reactor filtrate clarity	46+
Product filtrate clarity	46+
Settling rate (m h^{-1})	2.2
Thickened solids loading, after 60 minutes (g L^{-1})	124
Supernatant clarity, after 60 minutes	46+

The settling rate for this experiment, 2.2 m h^{-1}, was much lower than that for previous experiments, but still good and very acceptable according to Pasminco's standards. The thickened solids loading was once again low, but typical of this series of experiments. The water content of the filter cake, both for the reactor sample and the product sample, at steady state were very similar and typically high. The filterability of the reactor contents was determined and as is shown in Table 4.10 was slightly less than that of the product, for the same residence time. This would, no doubt, be a result of the CSCPR conditions, but the reason is unknown.

The PSDs for both the product samples and reactor samples are shown in Figures 4.12 and 4.13, respectively, and exhibit only minor changes between the product and reactor samples at the end of each residence time. The use of CSCPR conditions has produced a product with excellent filterability, the most important quality criterion specified by Pasminco. The difference in filtration performance, compared to other experiments using different mixing and product removal conditions, may not be a function of the PSD, or the differences in the PSDs of IRN-11 may lie outside the detectable range of the Malvern Mastersizer X instrument (0.1 to 600 μm for all previous experiments and 1.2 to 600 μm for IRN-11). The author believes the filtration performance of the silica precipitate from continuous experiments is independent of small changes in the PSD, as we have seen previously in all continuous experiments dramatic changes in the filtration performance without corresponding changes in the PSD. It is believed that the improved filtration performance experienced with this experiment is a result of the mixing and product removal conditions. The major point of difference when examining the PSDs between this experiment and the MSMPR experiment, IRN-7, is the shift in the mean particle sizes of the two main peaks. The initial peak appears at 30 μm whereas it was at 20 μm in the MSMPR experiments, while the secondary peak, forming after the third residence time is centred at 10 μm as apposed to 4 μm. It is also clear that the peak size ratios of the two size fractions are different between the two mixing and product removal conditions at steady state. It is therefore concluded that the differences in the PSDs between IRN-7 and IRN-11 are the result of the different mixing and product removal conditions employed for these two experiments. This is reinforced by the three experiments carried out using MSMPR conditions; IRN-7, IRN-9 and IRN-10, having the same PSDs at the end of each residence time.

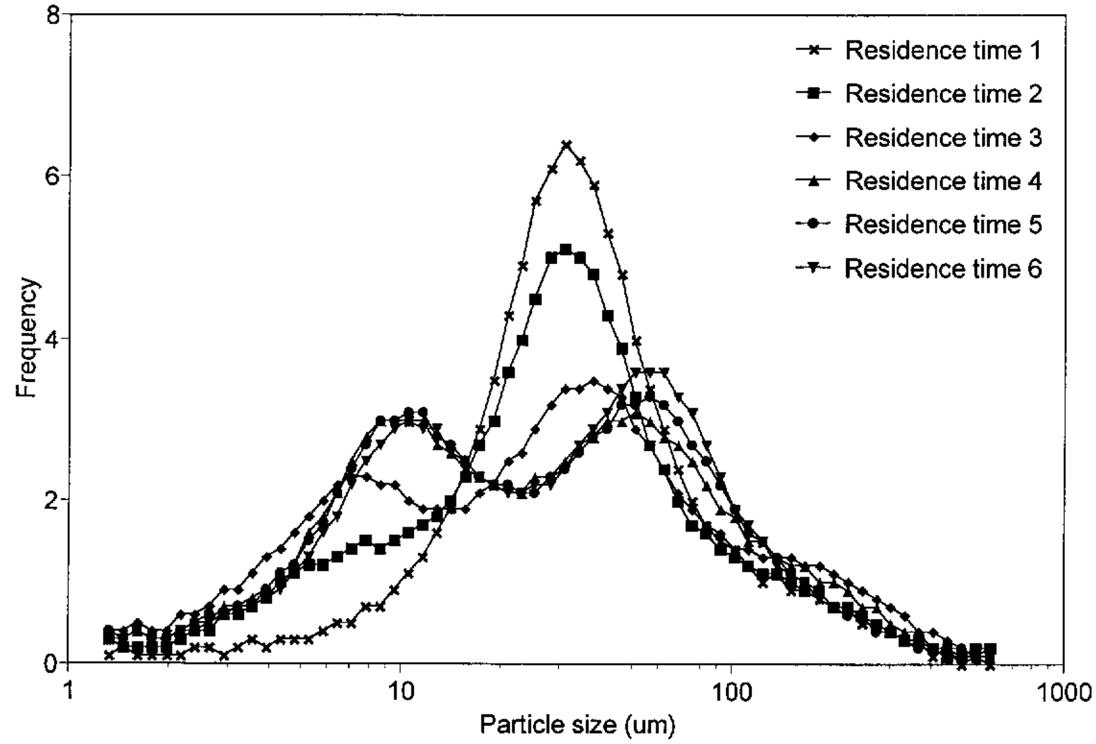

Figure 4.12: PSD at the end of each residence time for IRN-11, product samples.

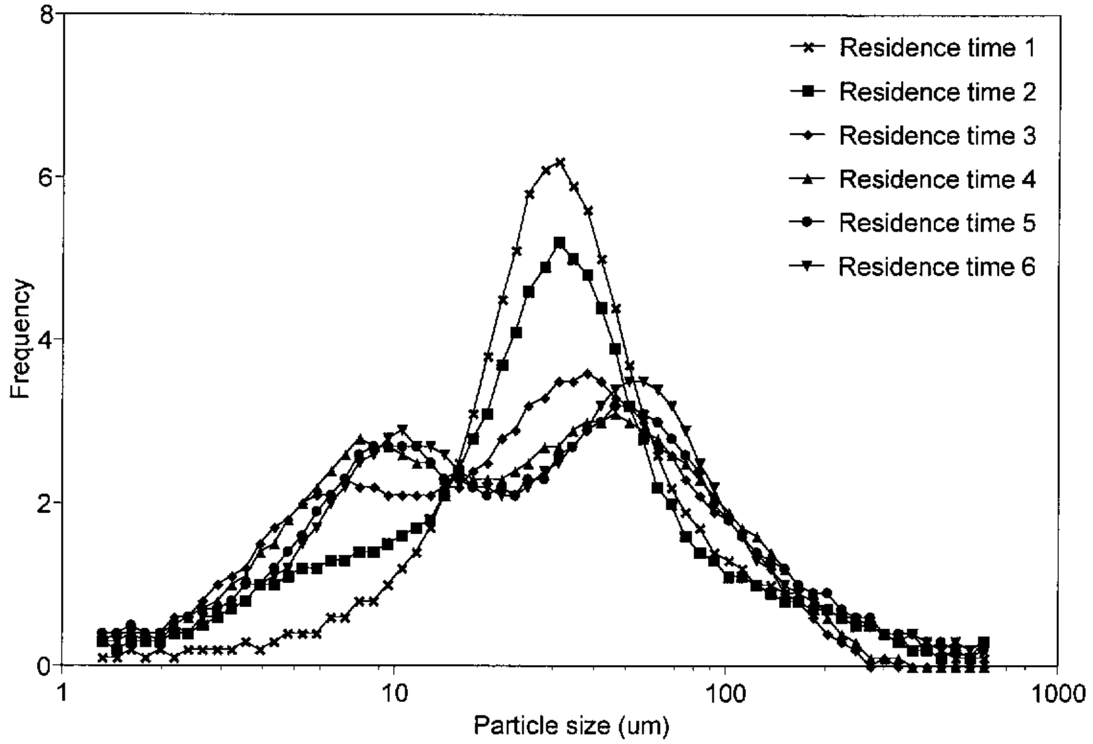

Figure 4.13: PSD at the end of each residence time for IRN-11, reactor samples.

The use of CSCPR conditions may not have had a very dramatic impact on the PSD between the reactor and product samples, but it might have impacted on the residence times for the solid and liquid products. The stunning improvement in filterability of the product is most likely a result of an increase in the residence time for the solid product with respect to the liquid product. It is believed that, under CSCPR conditions the liquor in the reactor vessel is well mixed and representatively removed, while the solid particles settle and become concentrated at the bottom of the reactor vessel and subsequently only the smaller particles are mixed and removed from the reactor vessel. The result of this is that the residence time for the liquid portion of the product is the actual operating residence time, while the residence time of the solid portion of the product is somewhat greater than this. In turn, this allows for the solids to age more than under MSMPR conditions and subsequently become more filterable. This would also account for the increased particle sizes seen in this experiment, due to additional growth and or agglomeration; but, as explained previously, this is not the reason for the improved filterability.

4.3.6 Industrial run number 12 (IRN-12)

The aim of this experiment is to eliminate the massive silica over-supersaturation and resultant poor product filterability experienced during the first residence time of all the previous experiments. Solving this problem will overcome what will no doubt be a big industrial problem, that is; what to do with the poorly filtering material produced during the first residence time? The use of a one-off batch of seed in the reactor vessel at start up and the use of a long residence time until the solids loading had built up to a normal level are seen as the most effective means to eliminate this problem. It is planned to shorten the residence time duration, at the end of each residence time. The seed is to be produced by a similar method to that used in Section 3.3.2.1 which provided a well filtering colloidal precipitate, *ie.* batch precipitation at S = 2.9, 50 g L^{-1} sulfuric acid and 95°C. The aim is to produce a seed that has never been through the initial gelling period and thus having superior filtration performance.

In order to produce this seed, the crystalliser was set up as described in Section 4.2.3, and addition of Ore slurry and Cell room spent electrolyte solution started as normal. After a specified period of time, determined so that the silica concentration would not exceed 1000 mg L^{-1}, the reagent pumps were switched off and the experiment allowed to continue as a batch type experiment. From batch experiments in Section 3.3.2.1, the time to reach equilibrium solubility was established. After this period had elapsed, further addition of reagents commenced and the reagent addition cycle was repeated approximately 50 times over a period of almost two months. During this time, the silica concentration never exceeded 1000 mg L^{-1} and the silica never gelled. Before commencement of the continuous period of this experiment the properties of the seed slurry were determined, and the results are shown in Table 4.11.

Table 4.11: Results for the batchwise seed production stage of IRN-12.

Parameter	Value
Final SiO_2 concentration (mg L^{-1})	410
Temperature (°C)	95.0±0.2
Acidity (g L^{-1})	50±2
Filterability (m^3 m^{-2} h^{-1})	1.64
Reactor solids loading (g L^{-1})	22.0
Filter cake thickness (mm)	1
Filter cake water content (%w/w)	63
Filtrate clarity	46+

The seed produced had similar filterability and product characteristics to that of the steady state product from IRN-11. The relatively low solids loading is the reason for starting the continuous phase of the experiment with such a long residence time, this allows for the solids loading to build up. Due to the time taken to manufacture this seed, there is no advantage in pursuing this as an industrial source of seed. A better source would presumably be the steady state product from the reactor, suitably thickened and recycled into the reactor vessel to increase the solids loading.

The parameters used for the continuous phase of this experiment are shown in Table 4.12.

Table 4.12: Operating parameters for the continuous stage of IRN-12.

Parameter	Value
Mixing and product removal conditions	MSMPR
Silica feed rate (g SiO_2 L^{-1} h^{-1})	0.43, 0.66 then 0.96
Temperature (°C)	95
Acidity (g L^{-1})	50
Residence time (hours)	45, 29 then 20
Initial seed concentration (g L^{-1})	22.0

Due to the failure of the Level sensing electrode, the experiment was stopped after only one 45 hour residence time had been completed. The results for this period are shown in Figure 4.14 and Table 4.13.

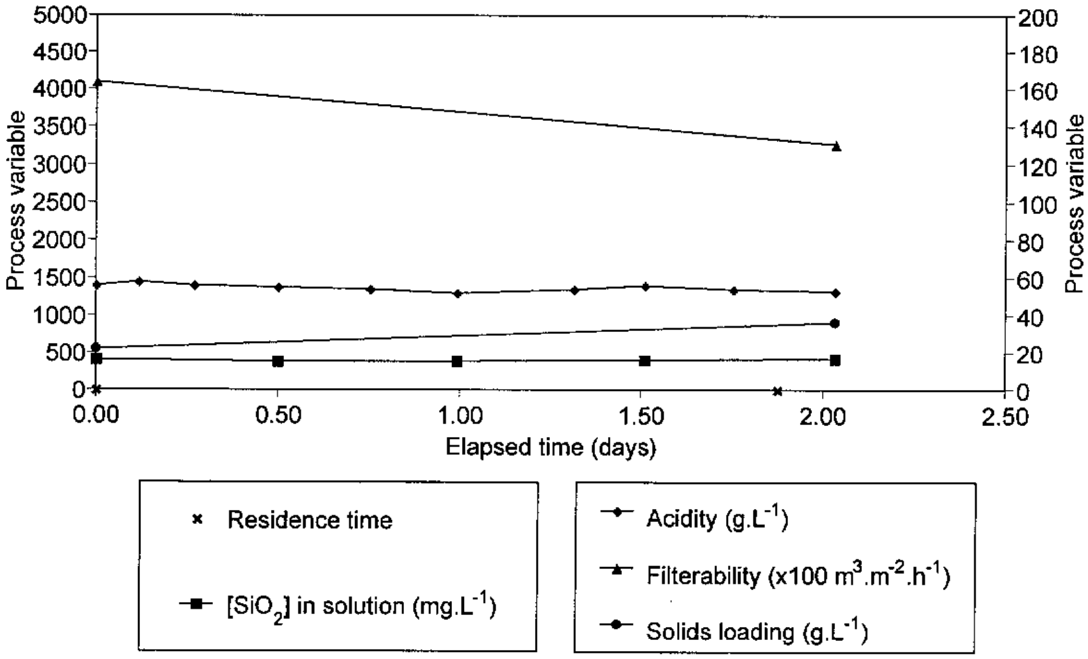

Figure 4.14: Main process variables versus elapsed time for IRN-12.

Table 4.13: Results for residence time one of IRN-12.

Parameter	Value
Silica concentration (mg L^{-1})	395
Temperature (°C)	95.0±0.2
Acidity (g L^{-1})	50+8
Filterability (m^3 m^{-2} h^{-1})	1.31
Reactor solids loading (g L^{-1})	36.3
Filter cake thickness (mm)	2
Filter cake water content (%w/w)	73
Filtrate clarity	46+

Temperature control, as always was excellent at 95.0±0.2°C for the experiment. Acidity control was not ideal, with the concentration rising as high as 58 g L^{-1} during the shortened experiment. This is because this was the first time a residence time as long as 45 hours had been trialed, and reagent flow rates were unknown. The initial acidity was higher than desired at 56 g L^{-1} and this contributed to the problem. This is not considered to be a major problem however, because, as seen in previous experiments, the silica product quality is independent of acid concentration. The solids loading rose to a nominal level by the end of the first residence time. As a result of this, the second residence time would have been shortened to 29 hours if the experiment had continued. The silica concentration remained essentially constant throughout the experiment at a level close to the equilibrium solubility; no massive concentration spike was observed. Thus, the use of a very long residence time and the initial presence of adequate seed is sufficient to prevent a concentration spike. Subsequently, the filterability remained very good for the experiment and probably only decreased due to the increase in solids loading. The filtration performance, observed qualitatively, throughout this period was also very good. Since the experiment was not run to steady state a settling test was not carried out. The water content of the filter cake was typically high.

The PSD for the initial seed and the product sample after one residence time are not shown as they are very similar to one another and also to the steady state samples from IRN-7 (Figure 4.6), which was also operated under

MSMPR conditions. This is further reinforcement that the filterability is independent of PSD, which is itself a function of the mixing and product removal conditions.

4.3.7 Cell room spent electrolyte to ore slurry ratio

The ratio of Cell room spent electrolyte to Ore slurry was determined at the end of each continuous experiment. All experiments were carried out at an acidity of 50 g L^{-1} sulfuric acid. In all cases the volumetric ratio was determined to be 3.00±0.05:1.00. The sulfuric acid concentration in the cell room spent electrolyte was 170 g L^{-1}, while the Ore slurry solids loading was 400 g L^{-1} and was slurried in Cell room feed solution.

4.3.8 Chemical composition of solution and solid products

The analysis for zinc and other elements of interest to Pasminco was performed by ICP-AES on the solution samples previously examined for their silica content and on the solid samples recovered from the filtration tests at the end of each residence time. Samples were collected and analysed according to the method detailed in Section 9.2.2.2. Fluorine was determined using ion selective electrode measurements. Due to the lack of suitable equipment, these samples were out-sourced to a commercial laboratory for analysis. The behaviour of the analytes throughout the progress of each experiment were very similar, so only the results for IRN-11 are shown (Table 4.14). The figures in parentheses are the percentage distribution between solution and solid for each analyte. The solution concentration of all species for this experiment reached equilibrium by the end of the second residence time, hence the results shown are the mean of the values at the end of each residence time after this. The concentration of all species in the precipitated solids remained constant for the duration of each experiment, thus the results shown in Table 4.14 are the mean values at the end of all residence times.

Table 4.14: Concentrations of important analytes in solution and in the silica precipitate. Figures in parentheses are the percentage distribution between solution and solid for each analyte.

Analyte	Solution concentration (mg L^{-1})	Solid concentration (%w/w)
SiO_2	885 (4%)	59.5 (96%)
Zn	125 000 (>99.5%)	1.10 (<0.5%)
As	735 (96%)	0.088 (4%)
Pb	45 (5%)	2.60 (95%)
Al	360 (38%)	1.73 (62%)
Fe	270 (14%)	4.77 (86%)
Ge	<1.0	<0.005
Sb	<1.0	<0.005
F	57 (98%)	0.0036 (2%)

No relationship between filterability and the concentration of any other analyte, apart from silica, is observed. The fact that filterability fluctuates with silica concentration, while the concentration of all other elements remains constant, is evidence of that. The behaviour of silica has been previously discussed in detail, and it is sufficient to mention here that the distribution between solution and precipitate is excellent with almost all the silica reporting to the precipitate, as would be expected.

The concentration of zinc in solution remains essentially constant throughout any given experiment. This is simply an artefact of the zinc concentration in the initial solution being the same as the steady state zinc concentration. At any given time approximately 40%, by weight, of the zinc entering the reactor vessel is liberated from the ore. The low level of zinc reporting to the solid product is very encouraging, and would presumably be due to a combination of entrained zinc sulfate solution and undigested natural zinc orthosilicate.

It is desirable for the impurity elements to report to the silica precipitate, as this helps to purify the resultant zinc sulfate solution. This reduces the amount of downstream purification required. Arsenic and fluorine do not report to the silica residue and remain almost exclusively in solution, while lead reports almost completely to the solid product. Approximately one third of the aluminium present remains in solution, while the remainder reports to the solid product. Iron is mostly concentrated in the solid product during these experiments. The reason for the distribution of these elements is discussed in the following sections. The silica precipitate is very effective in removing lead and iron, and moderately effective in removing aluminium from solution. Arsenic and fluorine, and to a lesser degree aluminium, may present a cumulative problem in solution as they are not being recovered with the solid residue, and hence will need to be removed downstream before electrowinning to recover the zinc. Arsenic and aluminium are leached from the natural zinc orthosilicate ore and were not present in the aqueous reagent streams. The source of the fluorine is not known. Germanium and antimony are both below the detection limit of the ICP-AES instrument, and therefore no conclusions can be drawn as to their behaviour.

It should be remembered from Section 3.3.3 that the presence of zinc, aluminium and iron (III) as sulfates and fluorine in solution increases the silica precipitation rate. While the presence of aluminium sulfate in solution improves filterability, the concentration in a typical continuous experiment is well below the 0.5 M $Al_2(SO_4)_3$ required for this to happen.

4.3.9 Speciation of solid products by X-ray diffraction (XRD)

Since all solid products from the continuous experiments have been so similar in nature, only two experiments were selected for analysis by XRD. IRN-9 was selected as it had a dramatic change in filtration performance between the third and fourth residence times: from 1.03 to 0.01 $m^3\ m^{-2}\ h^{-1}$, respectively. It is desirable to know if this change can be detected by XRD and its cause then determined. The second experiment selected was IRN-11, as this was the most stable experiment with very good product qualities.

The XRDs for both experiments were almost identical and thus only one series is shown here. There was no detectable change in the XRD as a result of the decrease in filterability in IRN-9. Since the chemical composition of IRN-11 was discussed earlier in Section 4.3.8, it seems logical to focus on the XRD for this experiment also. The XRDs for this experiment are shown in Figure 4.15. The peaks for the crystalline phases identified have been labelled.

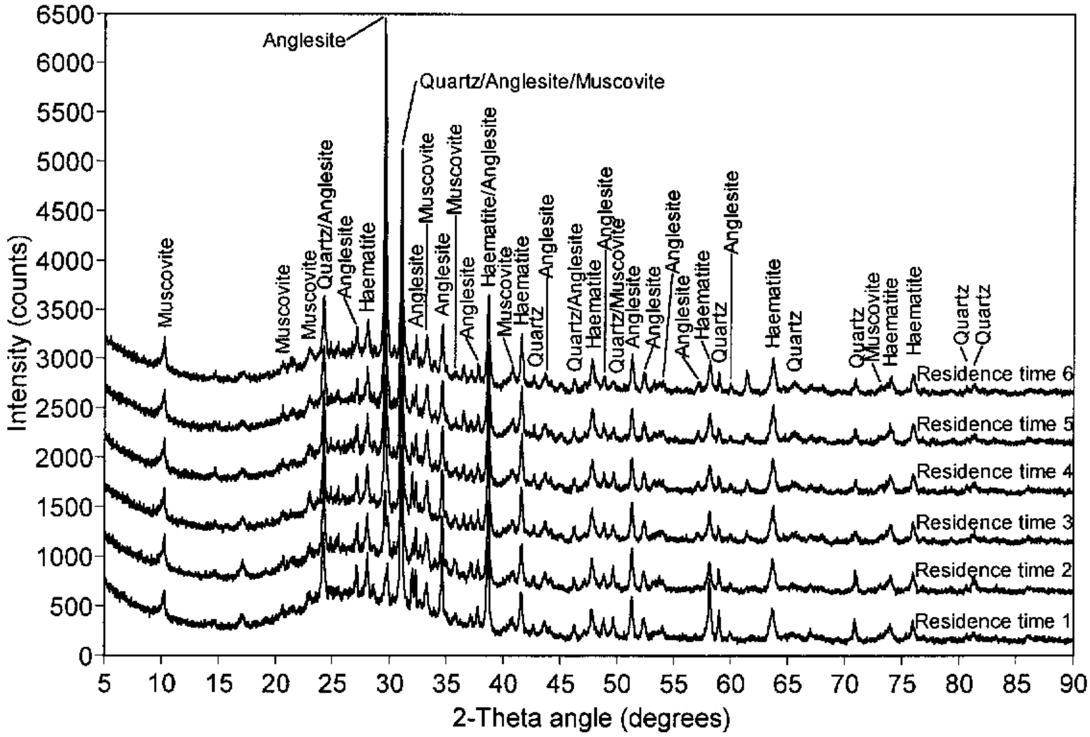

Figure 4.15: XRDs recorded at the end of each residence time for IRN-11. Peaks for the crystalline phases identified have been labelled.

It is evident from Figure 4.15 that the six XRDs are virtually identical, with only minor changes in some peak intensities between residence times. The most noticeable feature is the broad amorphous peak from approximately 15 to 40°, 2θ, due to the large proportion of amorphous silica in the solid product from the crystalliser. The formation of amorphous silica was expected and reinforces Fleming's (1981) finding that silica precipitated under non-hydrothermal conditions is almost invariably amorphous. There are four minor crystalline phases present in the solid residue. These phases are, in order of approximate decreasing abundance: quartz (SiO_2), haematite (Fe_2O_3), anglesite ($PbSO_4$) and muscovite ($Al_{2.9}H_2KO_{12}Si_{3.1}$). The order of abundance was determined from both the XRDs and the chemical composition of the solid product by ICP-AES shown in Table 4.14. All the crystalline phases are present in similar quantities at each residence time. These four crystalline phases were also detected in the natural zinc orthosilicate reagent, details of which are given in Section 2.2.

Quartz and anglesite are virtually insoluble and slightly soluble (respectively) (Lide, 1994) components of the natural zinc orthosilicate ore, under the operating conditions used here. They simply pass through the crystalliser essentially unreacted and report to the solid residue. Muscovite, known for its chemical inertness (Greenwood and Earnshaw, 1989), would behave in a similar manner to anglesite. The low concentrations of lead and aluminium, as determined by ICP-AES and shown in Table 4.14, present in the product solution from the continuous experiments, would be as a result of the slight solubility of anglesite and muscovite, respectively. Haematite, on the other hand, is soluble in sulfuric acid (Lide, 1994). Despite this, the ICP-AES results, shown in Table 4.14, indicate only a small proportion of the iron, *ie.* haematite, is solublised, with the majority reporting to the solid residue. The reason for this is not known, at this stage.

There is no XRD evidence to support the presence of any unreacted zinc orthosilicate in the solid residue. There is also no zinc sulfate detectable in the residue, indicating that the entrained water soluble zinc concentration in the residue is very low. The absence of these two zinc phases in the solid product reinforces the very low concentration of zinc present in the solid product, as determined by ICP-AES (Table 4.14). No jarosite type compounds, which maybe expected to precipitate under these conditions, were detected. It should be remembered that the detection limit for XRD is in the order of a few percent. The presence of any amorphous species present in the solid residue will also not be detected.

4.3.10 Examination of solid products by electron microscopy

4.3.10.1 Field emission scanning electron microscopy (FESEM)

The solid residue from the end of each residence time for each of the six experiments in this section was examined by FESEM. As with other characteristics of the precipitates, there were no visible differences between samples obtained at different residence times and from different experiments. In short, all the precipitates looked very similar. A micrograph of typical silica particles of a range of sizes is shown in Figure 4.16.

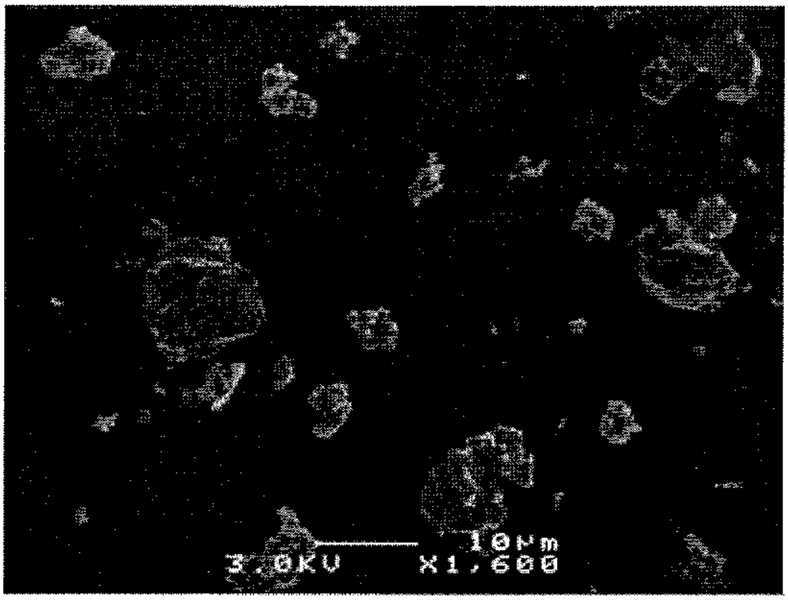

Figure 4.16: FESEM micrograph of typical precipitated, silica particles.

The silica particles appear to be porous aggregates of colloidal sub-particles. Aggregation of colloidal silica particles was evident during batch precipitation, as discussed in Section 3.3.2.1, and is not unexpected for colloidal sized precipitates (Mullin, 1988). The range of particle sizes observed, from 1 to approximately 500 μm, reinforces the particle size range determined by the Malvern Mastersizer instrument (Sections 4.3.1 to 4.3.6). The large aggregates display no distinct morphology. They appear to be somewhat spherical, possibly as a result of attrition. A micrograph of a typical aggregate is shown in Figure 4.17.

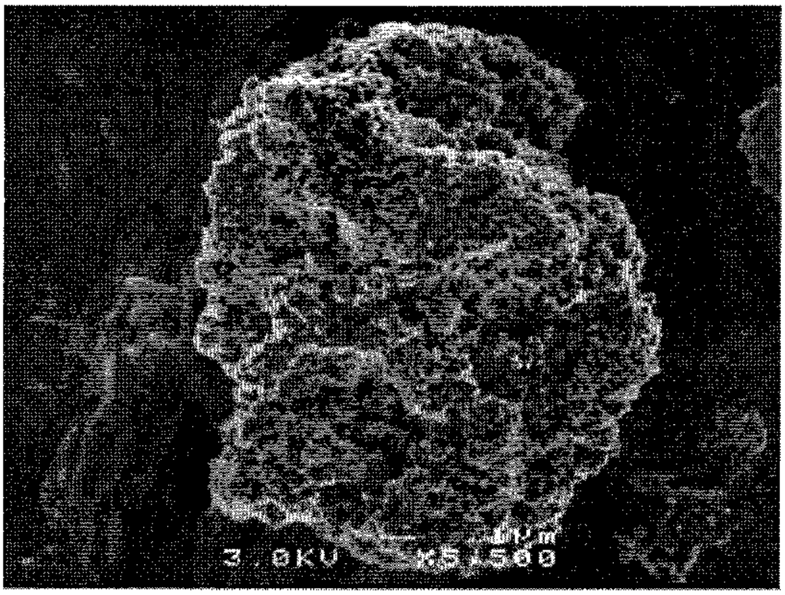

Figure 4.17: FESEM micrograph of a typical silica aggregate.

Upon closer examination of an aggregate, the sub-particle structure is clearly evident; a micrograph showing this in Figure 4.18. The aggregate substructure is made up of particles approximately 50 nm in diameter. The structure appears to be quite dense on the colloidal scale, but porous on a larger scale. Figure 4.18 was taken at the useable limit of the instrument's resolution and thus it is not possible to image any finer sub-structure detail. The structure of these aggregates is consistent with the growth mechanism outlined in Section 1.4. That is, initial formation of colloidal particles and subsequent aggregation of these particles to form larger particles.

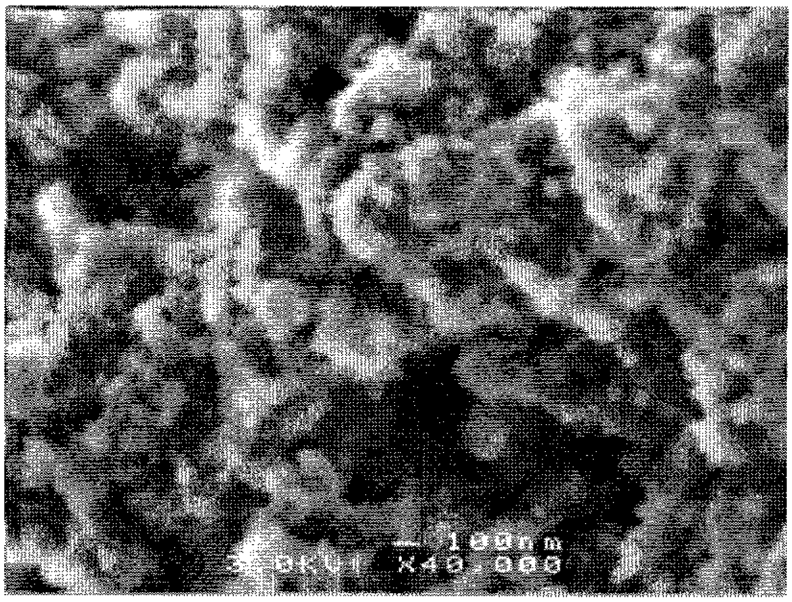

Figure 4.18: FESEM micrograph of a typical silica aggregate, showing fine structure detail.

The same structure is evident in all particles, independent of their size. Upon further examination, some particles are found to have smooth areas present in the structure as well as the aggregated structure just discussed. This is shown in Figure 4.19.

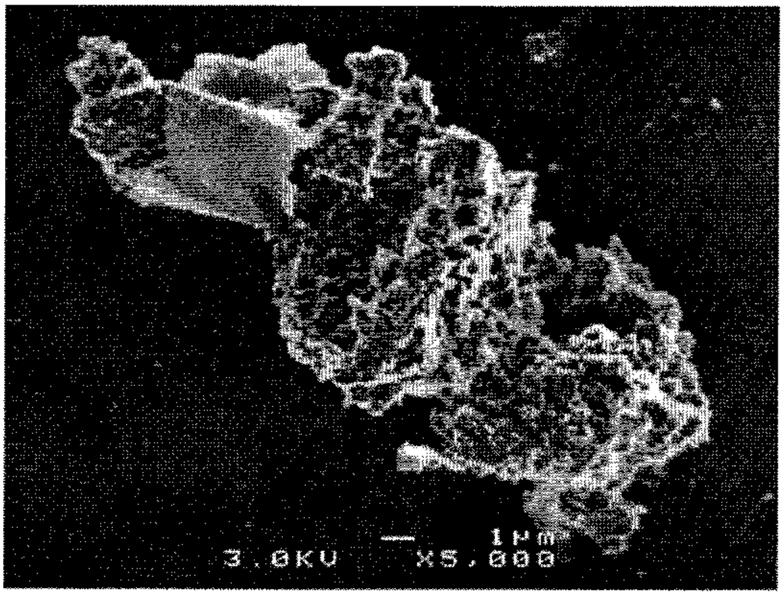

Figure 4.19: FESEM micrograph of a silica aggregate containing two structure types.

Examination of this particle at higher magnification reveals the aggregated area to have the same structure as previous particles, while the smooth area is quite different and is shown in Figure 4.20.

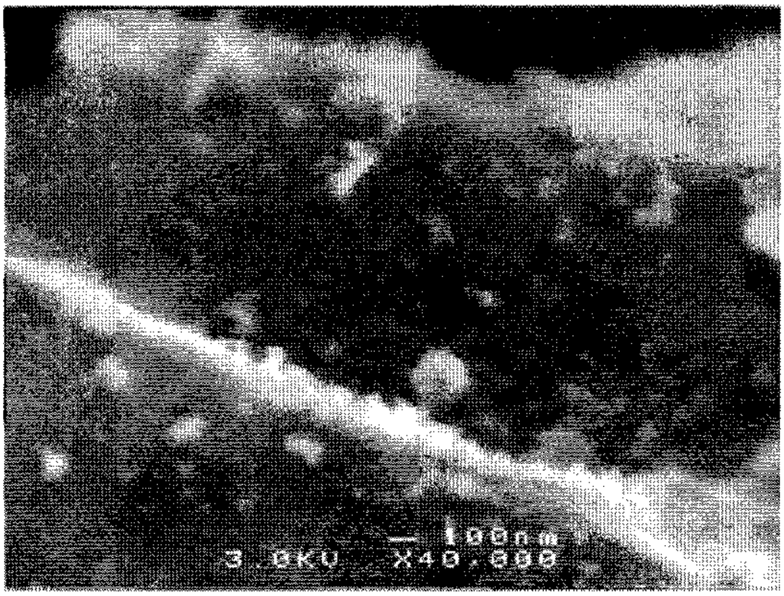

Figure 4.20: FESEM micrograph of the smooth area of a silica particle.

The smooth area has small aggregates on the surface. The structure of these smooth areas is probably the result of a previously aggregated area having been subject to further deposition of colloidal and monomeric silica to produce a dense, continuous mass of impervious silica. This type of growth was also described in Section 1.3. As well as particles having definite areas of separate growth, some particles have both types of growth intermixed, as depicted in Figure 4.21.

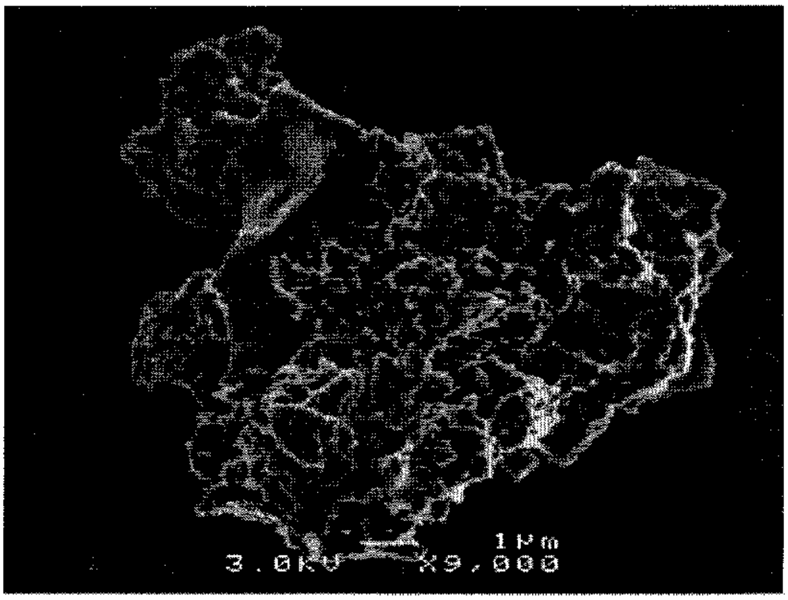

Figure 4.21: FESEM micrograph of a silica aggregate showing further growth.

Particles containing smooth areas of growth would presumably be relatively old particles compared to those particles with only the aggregated structure.

4.3.10.2 Scanning electron microscopy - energy dispersive X-ray analysis (SEM-EDX)

Solid product samples from the end of each residence time from IRN-9 and IRN-11 were set into resin blocks and polished to cross-section the particles so as to expose their internal features. SEM-EDX was used to qualitatively determine the chemical composition of the particles and also the nature and distribution of the impurities present. As with previous examinations, there were no detectable differences between particles from different residence times within the same experiment, even when significant changes in filterability occurred. There was also no difference between particles from different experiments. Once again a sample from IRN-11 will be discussed in further detail.

The resin block contains mostly carbon, with a much lesser amount of oxygen and a trace amount of chloride, the EDX spectrum is shown in Figure 4.22. In this section, elements are listed in decreasing order according to their peak height in the EDX spectrum. It should be noted that this is only a qualitative examination to determine the elements present, not their exact concentrations. Peak height or area is not an accurate method of determining elemental composition because of the dependence of X-ray emission intensity on atomic number and differential absorption of electrons, particularly by the light elements.

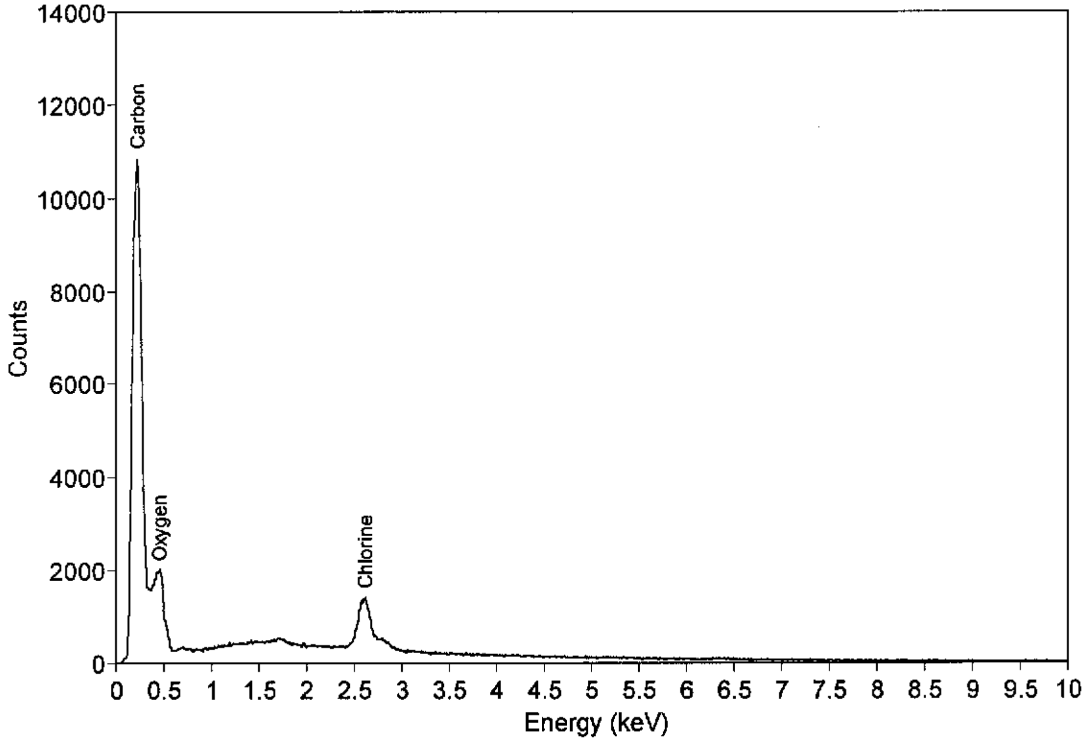

Figure 4.22: EDX spectrum of the resin block.

As would be expected, most of the particles present in the sample are silica and contain silicon, oxygen, carbon and traces of chlorine, aluminium, iron and sulfur. Also present in the spectrum is a silicon double peak, caused by two silicon X-rays hitting the detector simultaneously. The carbon, chlorine and a proportion of the oxygen would no doubt be present in the silica as a result of resin filling the pores within these particles. Carbon also appears in the EDX spectra of all the samples in this section as a result of the samples being coated with carbon to enable imaging without charging. The aluminium and iron are not unexpected impurities based on the bulk chemical analyses discussed in Section 4.3.8. Sulfur is also not unexpected as there is bound to be some entrained zinc sulfate or other sulfate species present in the silica, even though its concentration was below the detection limit of the XRD instrument. The EDX spectrum for the silica particles is shown in Figure 4.23.

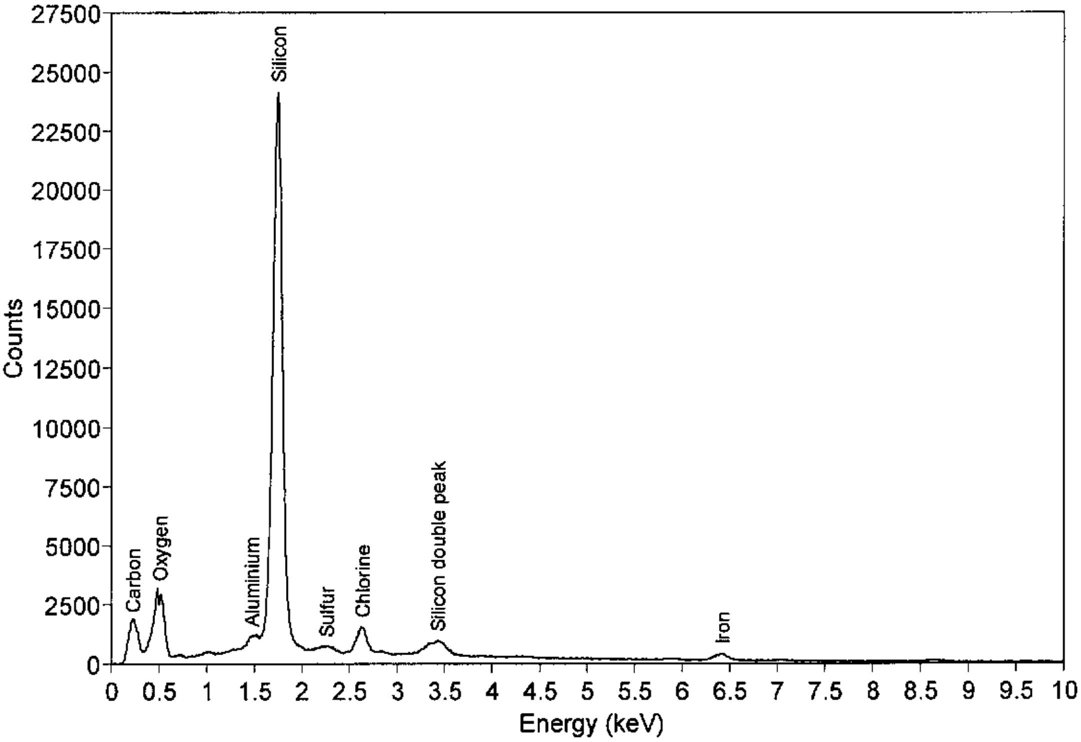

Figure 4.23: EDX spectrum of the silica particles.

Figure 4.24 is a micrograph of a typical silica particle imaged using backscattered electron imaging, as are all micrographs in this section. The silica particle appears grey in colour and occupies most of the image area. The surrounding black areas are resin. The most noticeable feature is the amount of impurities present within the silica particle. Almost all the silica particles have this feature in common. It would appear that the solid impurities present in the natural zinc orthosilicate ore have acted as primary heterogeneous nucleation centres for precipitation, or initial centres for aggregation. Iler (1979) described the deposition of monosilicic acid and higher order silica particles onto the hydroxylated surface of a foreign substrate (Section 1.4.2). This process maybe used to explain the tendency of silica to deposit onto these impurity particles, as is shown in Figure 4.24.

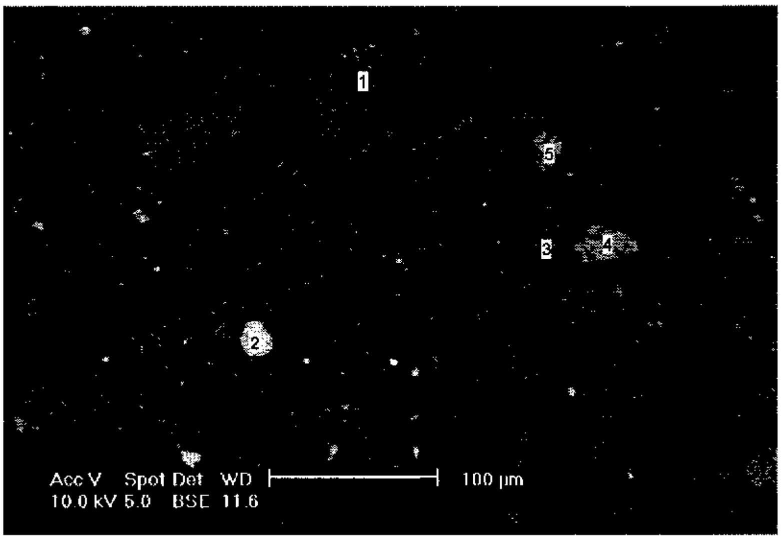

Figure 4.24: SEM micrograph of a typical silica particle containing impurities, imaged using backscattered electron imaging.

The five main areas of impurities present in the silica particle in Figure 4.24 have been labelled and have the following compositions:

1) The EDX spectrum for this impurity is shown in Figure 4.25 and contains peaks for silicon, oxygen, mercury and a silicon double peak. This compound is, or maybe quartz, which has been detected in both the initial ore and the solid product by XRD. The EDX spectrum of a quartz particle in the initial ore is shown in Figure 2.11, and is identical to the EDX spectrum shown here, confirming the quartz particles to be the same.

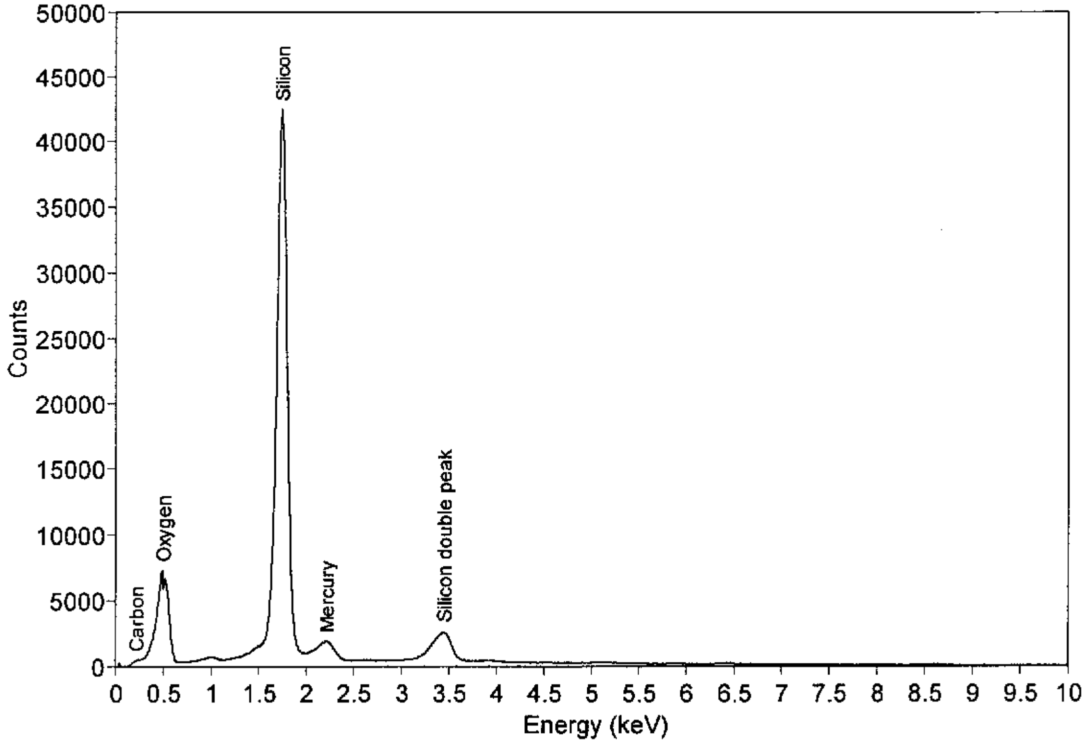

Figure 4.25: EDX spectrum of quartz particles.

Quartz has also been observed associated with the precipitated silica and would appear to be the site for nucleation or aggregation of the silica itself, as is shown in Figure 4.26. The quartz appears brighter in the micrograph than the precipitated silica and has a very distinct morphology. The precipitated silica appears grey in colour while the resin appears black. The difference in brightness between the quartz and precipitated silica is an indication that the precipitated silica is of lower density than the quartz.

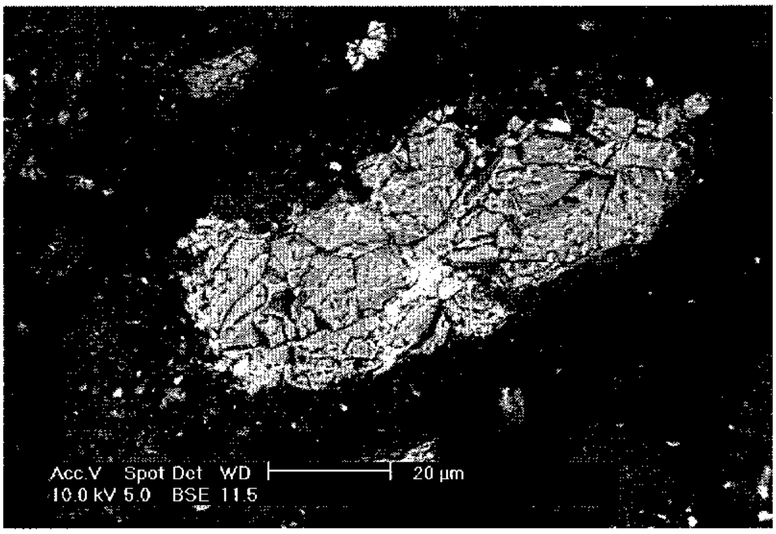

Figure 4.26: SEM micrograph of a silica particle associated with quartz, imaged using backscattered electron imaging.

The brighter areas in impurity region 1 of Figure 4.24, contain silicon, aluminium, oxygen and potassium with traces of magnesium, mercury, iron and sodium. The EDX spectrum is shown in Figure 4.27. These particles are, or maybe the muscovite phase identified by XRD as being present in the precipitation product. Muscovite has also been detected in the natural zinc orthosilicate ore both on its own and associated with quartz. A comparison of the EDX spectrum shown here and that of the muscovite phase in the initial ore (Figure 2.14), reveals them to be very similar. It is therefore concluded that the muscovite passes through the crystalliser without significant dissolution. Muscovite has also been observed associated with the precipitated silica, as depicted in Figure 4.28.

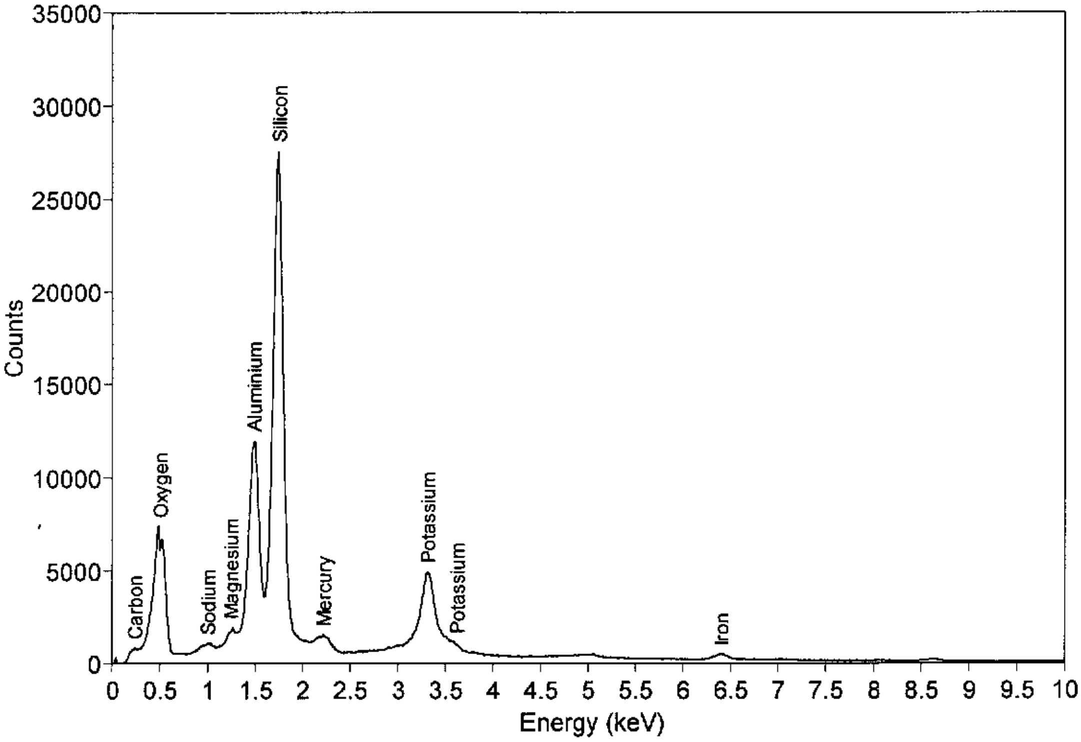

Figure 4.27: EDX spectrum of muscovite particles.

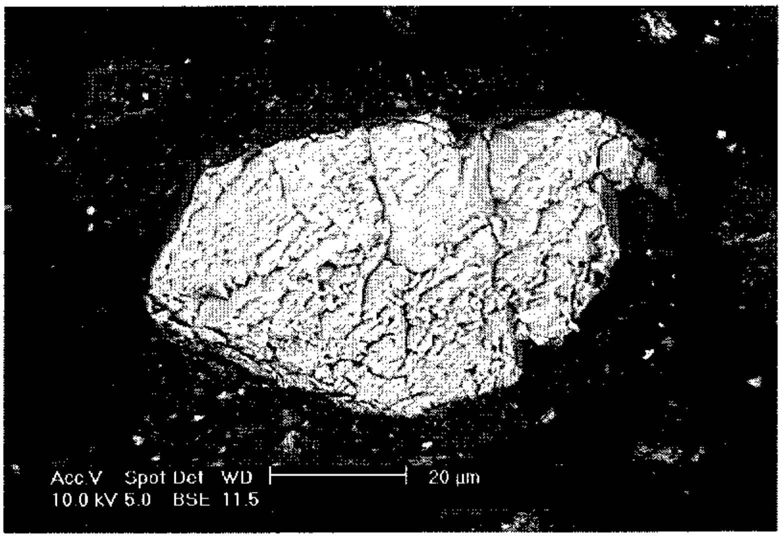

Figure 4.28: SEM micrograph of a silica particle associated with muscovite, imaged using backscattered electron imaging.

The muscovite appears as the brighter, central region in Figure 4.28 and seems to have provided a nucleation or aggregation site for the silica to precipitate onto. The muscovite has a very similar atomic number contrast to that of the pure silica but has a distinct and different morphology.

2) The EDX spectrum for this impurity compound is shown in Figure 4.29. Clearly, it is manganese sulfate, as the EDX spectrum contains manganese, oxygen and sulfur with smaller amounts of potassium, zinc and arsenic. Manganese sulfate was detected in the initial zinc orthosilicate ore, and its EDX is shown in Figure 2.19. While the two EDXs are somewhat dissimilar it is assumed to be the same material in each case. Based on this, it is concluded that the manganese sulfate passes through the crystalliser essentially unreacted. Without knowing which manganese sulfate phase is present, no comment can be made concerning its solubility under the experimental conditions studied. The identity of the manganese sulphate phase could not be determined using the available equipment.

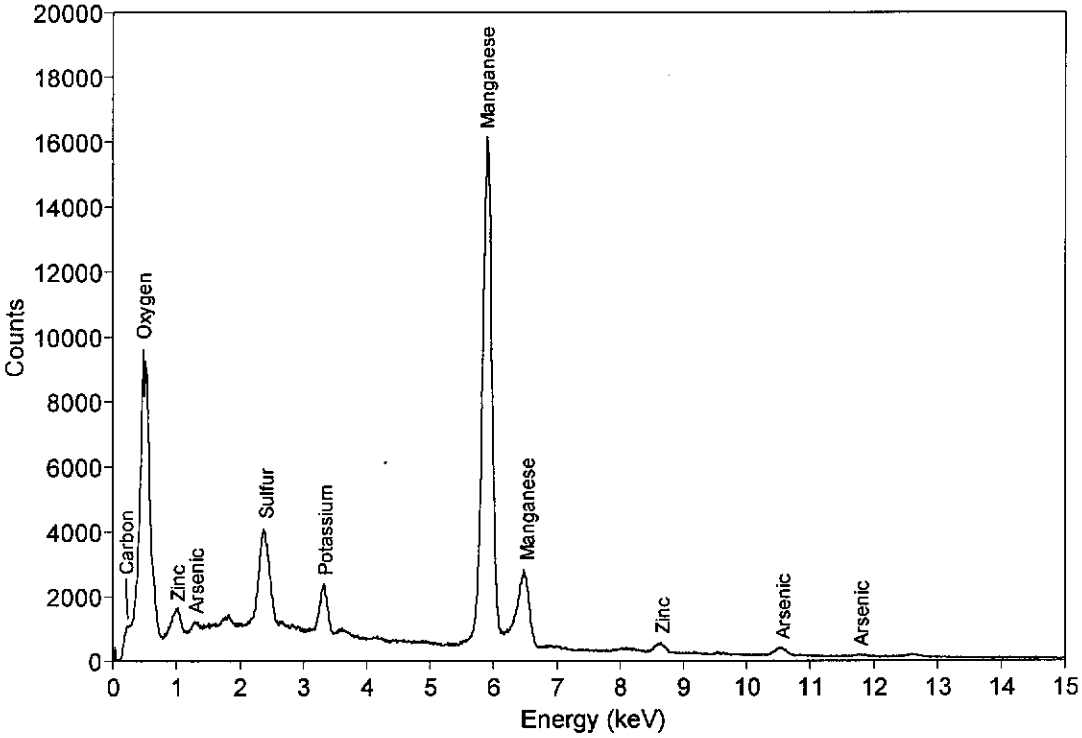

Figure 4.29: EDX spectrum of manganese sulfate particles.

Manganese sulfate particles have also been identified elsewhere in the sample, independent of any other particles and also associated with silica, as shown in Figure 4.30. The manganese sulfate particle, white in the centre of the micrograph, seems to have nucleated or aggregated the silica particle that appears grey. The resin is the black area that surrounds the particles.

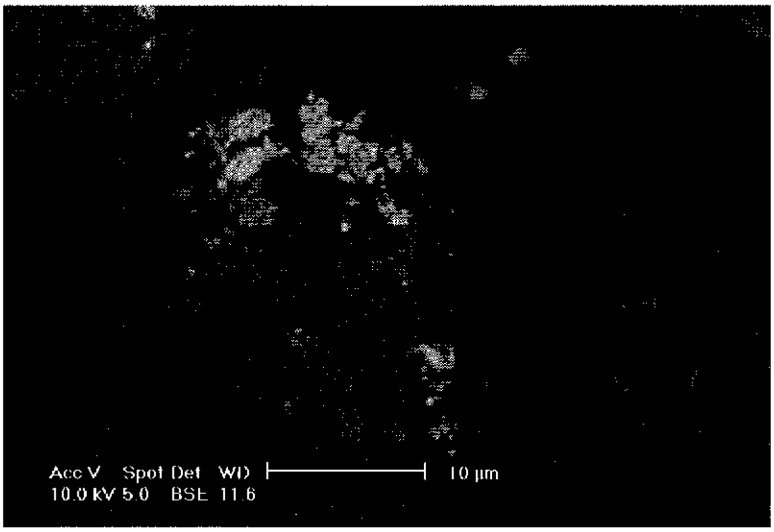

Figure 4.30: SEM micrograph of a silica particle associated with manganese sulfate, imaged using backscattered electron imaging.

3) This impurity compound is muscovite, as described in region 1. On this occasion it contains no entrained impurities.

4) This impurity would undoubtedly be haematite as the EDX spectrum, shown in Figure 4.31, contains iron and oxygen with traces of silicon and carbon. The presence of haematite has been identified by XRD. The natural zinc orthosilicate contains haematite, determined by XRD and SEM-EDX, with the spectrum, shown in Figure 2.13, being very similar to the one shown here in Figure 4.31.

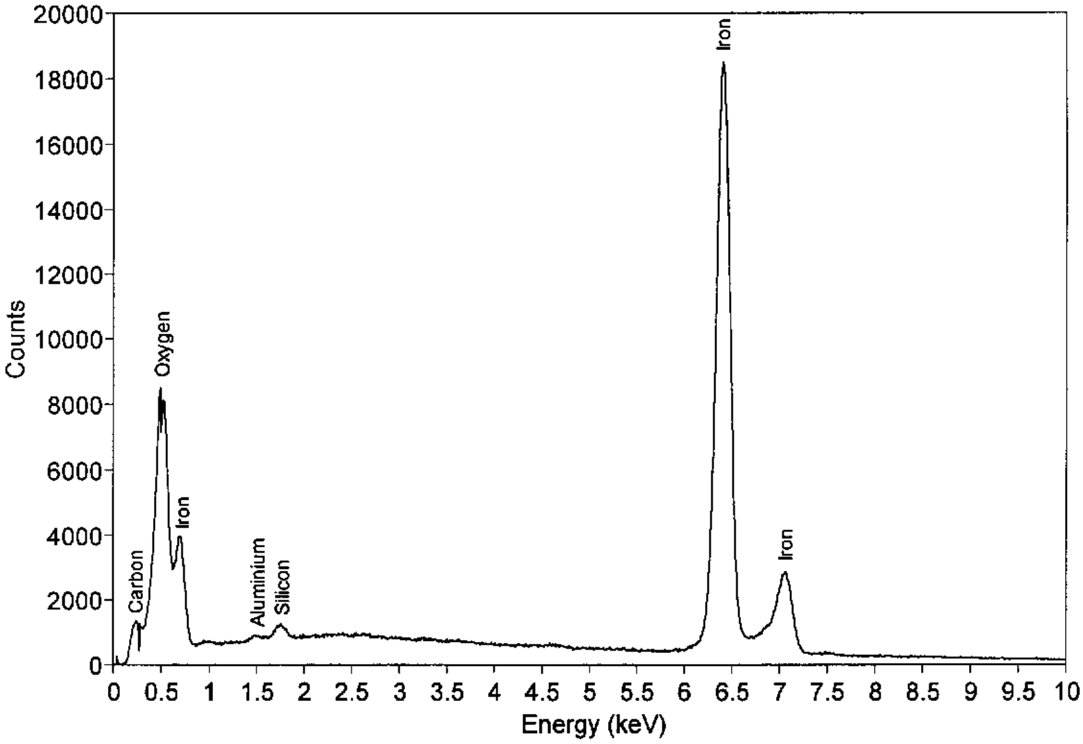

Figure 4.31: EDX spectrum of haematite particles.

Silica has been observed associated with haematite, as is shown in Figure 4.32. The haematite appears as the bright particle in the centre of the micrograph, surrounded by the grey silica which appears to have precipitated or aggregated onto the haematite. The surrounding black regions are the resin. The poor contrast between the silica and the resin in this micrograph is due to the large difference in contrast between these two compounds and the haematite.

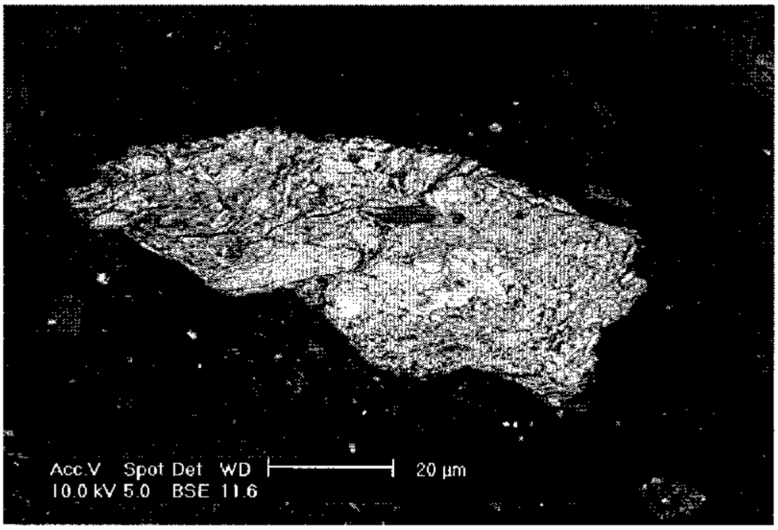

Figure 4.32: SEM micrograph of a silica particle associated with haematite, imaged using backscattered electron imaging.

5) Impurity region 5, in Figure 4.24, has its EDX spectrum shown in Figure 4.33. Manganese, sulfur, silicon and oxygen are present in large concentrations along with smaller concentrations of arsenic, potassium, zinc and carbon. It is not certain what this material is, as it is very similar in composition to the manganese sulfate in impurity region 2 except for the silicon. Since this phase is not present in the initial ore used for the continuous experiments, it is most likely manganese sulfate with some silica precipitating in the pores of the particle. Figure 2.20 shows the manganese sulfate particles present in the initial ore sample to have a very unusual, porous structure containing a calcium/manganese sulfate phase within the pores. It is concluded that the calcium/manganese sulfate phase was dissolved in the crystalliser and silica has precipitated to fill the pores.

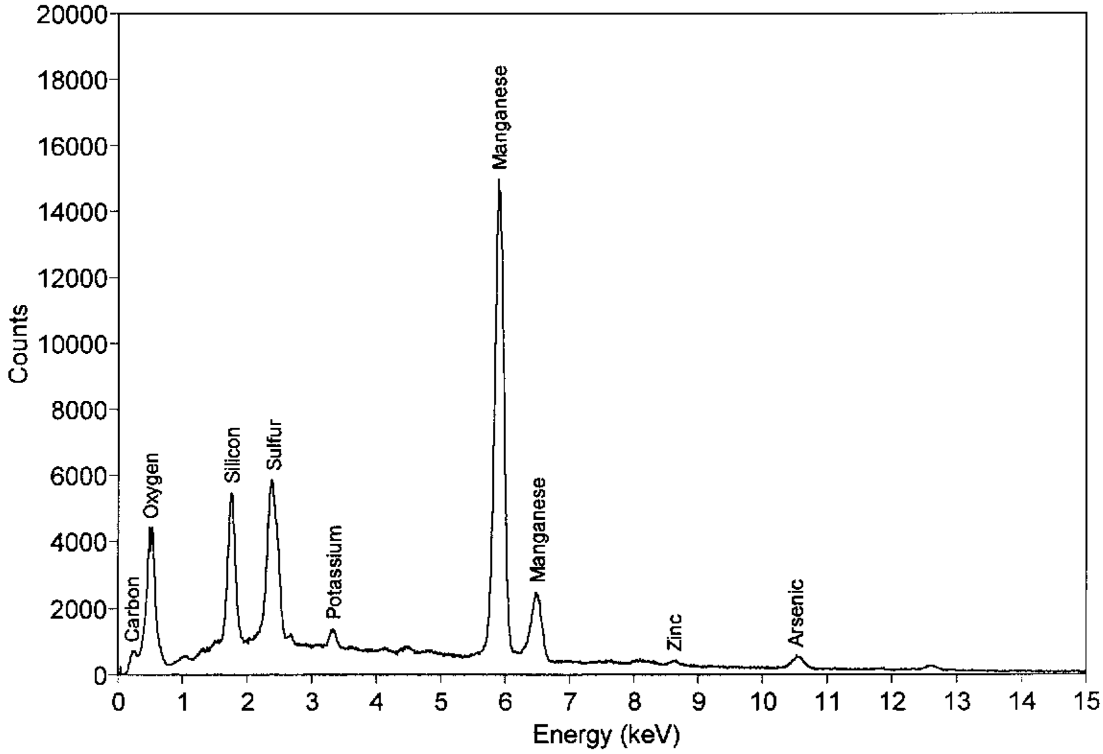

Figure 4.33: EDX spectrum of manganese sulfate containing silicon.

The only other impurity encountered in the samples that doesn't appear in Figure 4.24 has its EDX spectrum shown in Figure 4.34. The compound contains predominantly arsenic and lead, with trace amounts of calcium, oxygen and carbon. A double peak for lead/sulfur is also present in the EDX spectrum. The XRD analysis of the precipitated product from the continuous experiments, Section 4.3.9, identified the presence of anglesite, $PbSO_4$. The initial ore used for these experiments was analysed in Section 2.2 and was found to contain anglesite rich in arsenic. It is therefore concluded that this impurity compound is the arsenic rich anglesite present in the initial ore.

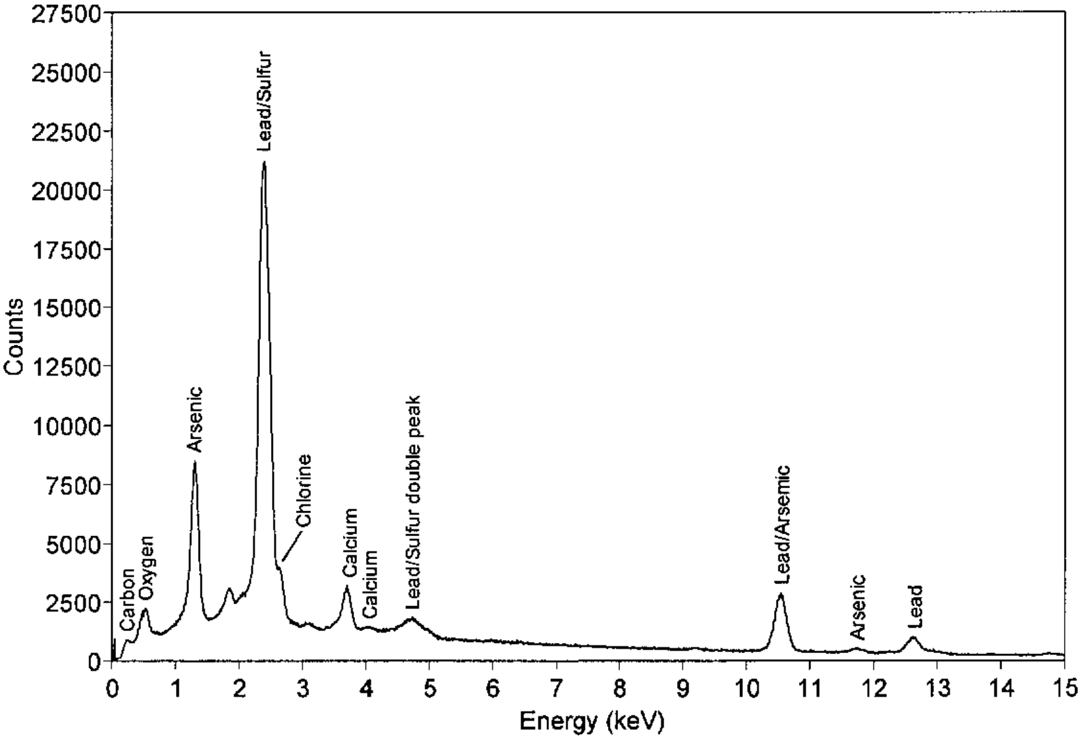

Figure 4.34: EDX spectrum of anglesite.

Figure 4.35 shows a white anglesite particle in the centre of the micrograph that appears to be the nucleation or aggregation centre for the precipitation of a silica particle, that appears grey in colour. The resin appears as the black regions around the other particles. The poor contrast between the silica and the resin in this micrograph is due to the large difference in atomic number contrast between these two phases and the anglesite phase. This image was produced using a mixture of 70% backscattered and 30% secondary electron imaging. Anglesite particles only ever appear associated with silica particles.

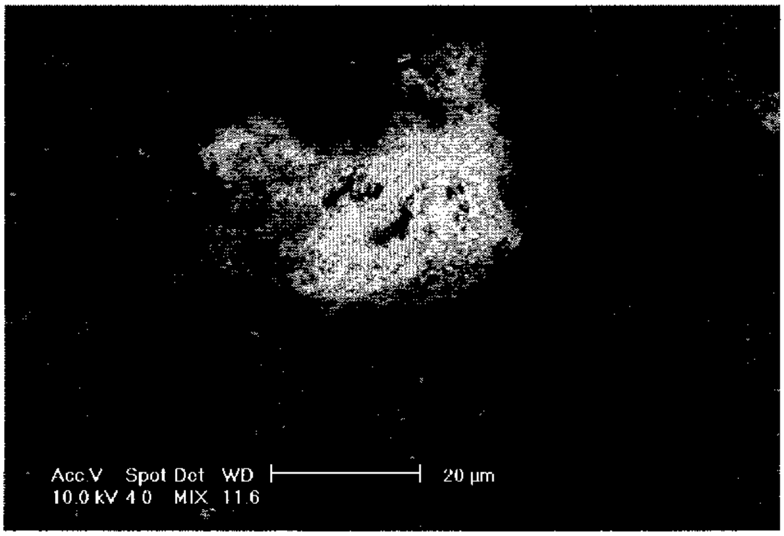

Figure 4.35: SEM micrograph of a silica particle associated with anglesite, imaged using a mixture of 70% backscattered and 30% secondary electron imaging.

SEM-EDX in conjunction with XRD has been used to determine that solid impurities present in the initial ore charge are acting as primary heterogeneous nucleation centres or aggregation centres for silica precipitation or aggregation, respectively. Such impurities are quartz, muscovite, manganese sulfate, haematite and anglesite. While at least one of these phases is soluble in sulfuric acid, it nonetheless appears in the product encapsulated in precipitated silica. In fact, it is most uncommon to see a silica particle that is free of impurities and most particles contain many separate impurity inclusions.

4.3.10.3 Transmission electron microscopy (TEM)

The aim of this study was to determine the cause of the dramatic decrease in filterability when the silica supersaturation ratio rises above S = 2.9. Samples from IRN-9 were chosen for the investigation. At the end of the second residence time of IRN-9, the supersaturation ratio rose above S = 2.9 and remained above this level for the third and fourth residence times (Figure 4.8). As a result of this the filtration performance began to decline. Samples from the end of the third and fourth residence times of IRN-9 were chosen for examination as the filtration rate was 1.03 and 0.01 m^3 m^{-2} h^{-1}, respectively. This is a bigger difference in filtration performance than between the second and third residence time samples. Examination of a range of precipitate sizes from these samples by FESEM revealed no differences in the nature of the particles as a result of the reduction in filterability. In an effort to investigate further the cause of gelling, it was decided to use TEM to study the colloidal particle size range. Two TEM micrographs of samples taken form the end of the third and fourth residence times of IRN-9 are shown in Figure 4.36 and Figure 4.37, respectively.

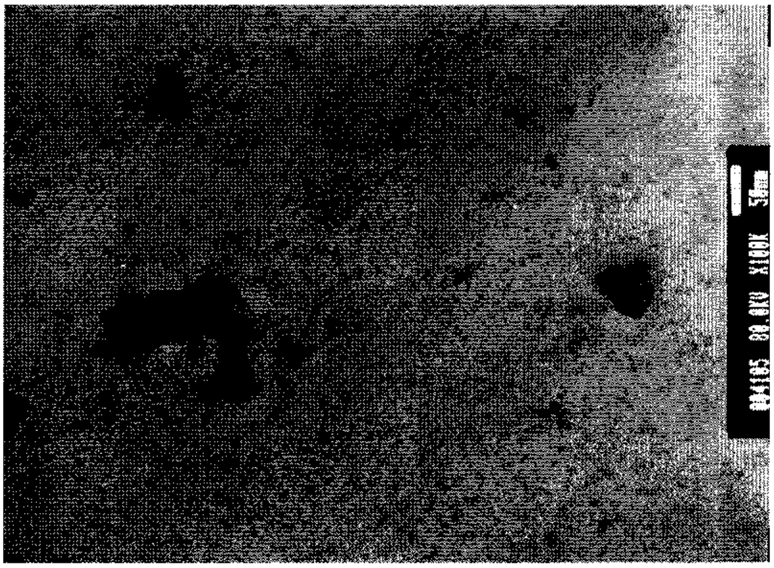

Figure 4.36: TEM micrograph from the third residence time of IRN-9. The scale bar is displayed on the upper right hand side of the micrograph.

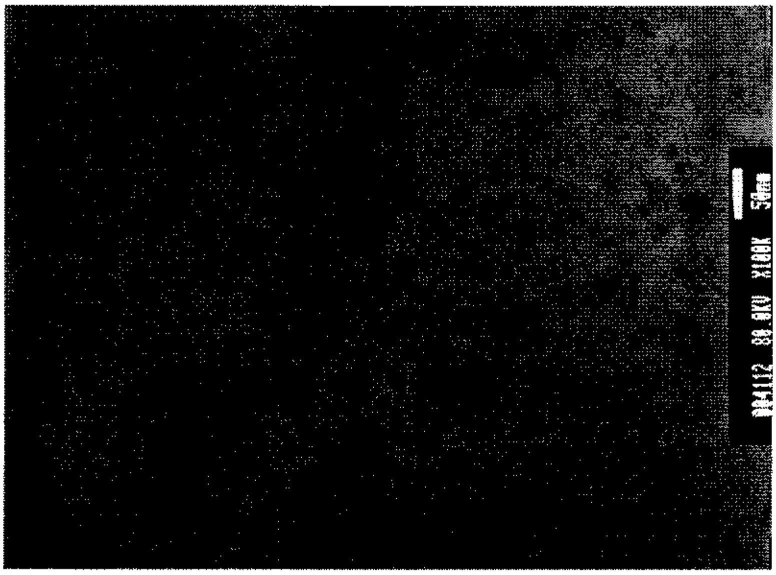

Figure 4.37: TEM micrograph from the fourth residence time of IRN-9. The scale bar is displayed on the upper right hand side of the micrograph.

The sample from the third residence time (Figure 4.36) has many small, discrete particles in the order of 5 to 10 nm in diameter and several larger aggregates of these smaller particles. The sample from the fourth residence time (Figure 4.37) has both the features common to the previous sample but also appears to have a fine network of silica micro-gel present. This tends to give the image a de-focussed, fuzzy appearance, but the central aggregate in the image is proof the micrograph is well focussed. The presence of this micro-gel network explains the source of the filtration problems. This micro-gel network nucleates and forms when the supersaturation increases above $S = 2.9$.

4.4 CONCLUSIONS

The effect of supersaturation on silica precipitation is best described by Figure 4.38. The most important indicator of precipitate quality is filtration performance. Supersaturation in these continuous experiments is difficult to quantify, as it fluctuates until the system reaches steady state. For Figure 4.38 the degree of supersaturation is represented by the flow rate of soluble silica into the reactor vessel. The higher the flow rate the higher the supersaturation. Changing the flow rate of soluble silica into the reactor vessel also impacts on the residence time duration, with the higher the flow rate the shorter the duration of the residence time. These three experiments were conducted using MSMPR conditions.

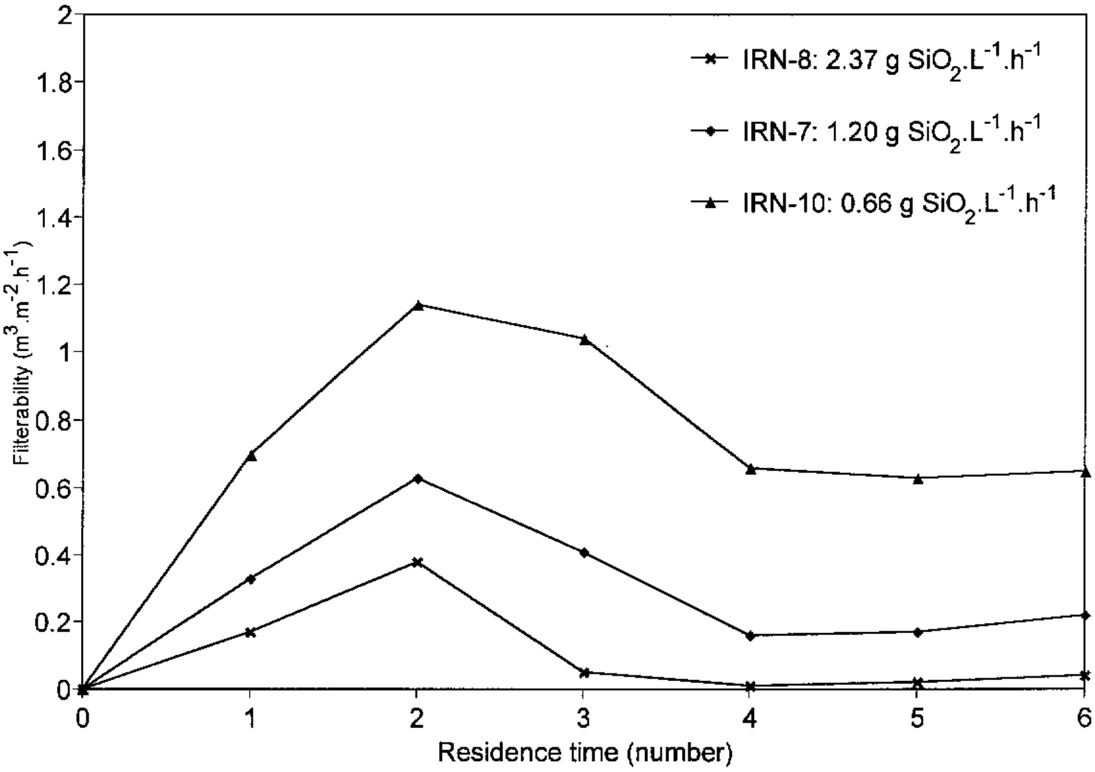

Figure 4.38: Filterability versus residence time number as a function of silica feed rate.

While the filterability is only measured at the end of each residence time, it is given an initial value of zero at the start of the experiment, in Figure 4.38, as it is extremely poor for most of the first residence time. This statement also applies to Figure 4.39. Clearly, in Figure 4.38, a relationship exists between the degree of supersaturation and the filterability of the silica product. At any stage throughout an experiment, the lower the supersaturation the better the filterability. A trend in the filtration performance of the silica product at the end of each residence time is also evident in Figure 4.38. Filterability increases for the first two residence times, decreases for the next two and becomes stable after that (the steady state period). It is clear that using MSMPR conditions requires a very long residence time duration to achieve satisfactory filtration performance at steady state. IRN-10 has a residence time of 29 hours and while the filterability is satisfactory at approximately 0.6 m^3 m^{-2} h^{-1} it is not as high as that defined by Pasminco as being acceptable industrially (Section 4.1). This suggests that an even longer residence time would be required to achieve an acceptable filtration rate using MSMPR conditions. This was not pursued as the effect of hydrodynamics was seen as a more significant area to investigate.

The effect of mixing and product removal conditions on precipitate quality, most importantly filterability, is summarised in Figure 4.39.

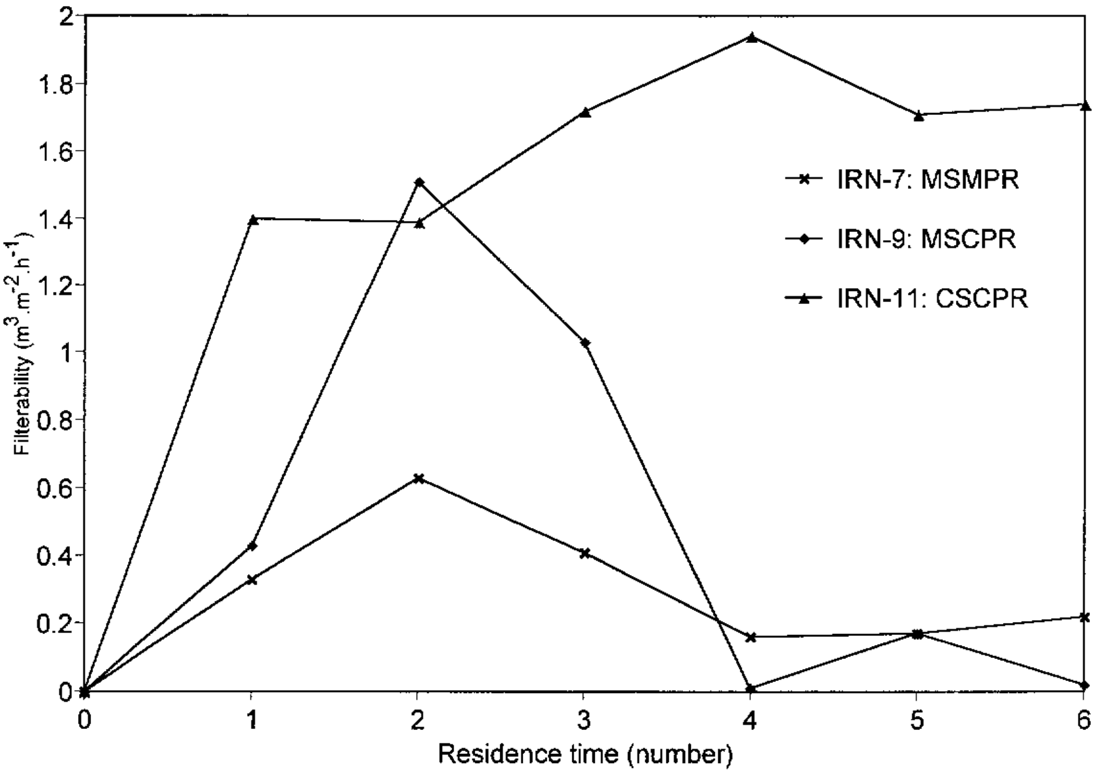

Figure 4.39: Filterability versus residence time number as a function of mixing and product removal conditions in the reactor vessel.

These three experiments were carried out with very similar soluble silica flow rates into the reactor vessel, ranging from 0.96 to 1.20 g SiO_2 L^{-1} h^{-1}. This corresponds to residence times of 20 and 18 hours, respectively. These small differences are thought not to impact greatly upon the results of these experiments or the conclusions drawn from them. The three mixing and product removal conditions studied were MSMPR, MSCPR and CSCPR.

For MSMPR and MSCPR conditions the trend in filterability with residence time is roughly the same as that seen in Figure 4.38 above; however, there are some unexpectedly low results for the steady state period for IRN-9 (MSCPR). Before this period, the filterability is superior with MSCPR conditions. Overall, the more classified the mixing and product removal conditions are, then the better the filtration performance. This is clearly evident in Figure 4.39 and especially with IRN-11 (CSCPR). It should be remembered that the steady state period is the most important, as this represents typical operating conditions. Changing mixing and product removal conditions has much more impact on the filterability than does changing the supersaturation. The conditions used for IRN-11 result in the highest quality product and satisfy most of the quality criteria requested by Pasminco, the most important being filterability (Section 4.1). These operating conditions could therefore be used in industry, with suitable scale-up procedures.

After the above conclusions had been drawn, the most important conclusion from this section of work was made: the acceptance of the following revised hypothesis. "The silica supersaturation limit of S = 2.9 is the gel point for silica. Above this limit silica micro-gel is formed and below this silica precipitate is formed". This has only been tested under the fixed conditions of 50 g L^{-1} sulfuric acid and 95°C, and the supersaturation limit is expected to change with a change in either or both of these variables. The acceptance of this hypothesis is a major step in increasing our knowledge of silica precipitation and has not been reported previously in the literature. This one piece of information explains, quite simply, the precipitation behaviour of silica. There is a distinct change in the morphology/structure at this supersaturation; the reason for this is not known. The gel network that forms when $S > 2.9$ and causes filtration performance to decrease dramatically does not appear to precipitate onto existing particles. TEM examination indicates that a fresh gel network appears to nucleate and render the solution unfilterable. Thus, the filterability is not a function of particle size, contrary to expectations.

The growth of silica particles under these acidic conditions follows the mechanism of Iler (1979). That is, nucleation of colloidal sized particles followed by aggregation to form larger particles. There is evidence of further deposition of monomer and colloidal particles to form dense impervious areas on some of the aggregate particles. It maybe the case that the insoluble impurity particles present in the ore are acting as aggregation centres, rather than nucleation centres. The initial silica particles formed are colloidal in size and then appear to aggregate to form larger particles, almost exclusively containing solid impurity species. PSD analysis indicates that the silica particles are of the same mean size as the insoluble impurity material present in the ore, by the end of the first residence time in a continuous experiment. TEM has been used to indicate the presence of discrete, colloidal silica particles during a continuous experiment. This evidence supports the theory that the solid impurities are indeed centres for silica aggregation, rather than silica nucleation.

The morphology of the silica particles, as examined by FESEM, would be described as irregular but tending towards spherical. The silica particles appear as porous aggregates of colloidal sub-particles. The aggregate sub-structure is made up of particles approximately 50 nm in diameter. The structure appears to be quite dense on the colloidal scale but porous on a larger scale. The somewhat spherical nature of the silica aggregates is most probably a function of attrition caused by collisions between the aggregates and the impeller and also the reactor vessel walls. Attrition is thought to be the cause of there being a bi-modal distribution of particle sizes at steady state. Initial aggregation of particles is centred around the insoluble material in the ore, and under MSMPR conditions this results in a peak at 20 μm. By the time steady state is reached this single peak has transformed into two peaks, the second at 4 μm. CSCPR conditions result in a larger mean size of particles with peaks at 10 and 30 μm. It is thought that under these mixing and product removal conditions the solid portion of the silica product ages, aggregates or grows to a further extent than under MSMPR conditions, resulting in the larger particle sizes. At the lower stirring speed of the CSCPR conditions, the product is also less affected by attrition, which may contribute to the larger particle sizes.

ICP-AES was used to examine both the solid and liquid products from the continuous experiments. The products from all experiments and all residence times within an experiment were very similar in their chemical composition. A very low level of zinc reports to the solid product with greater than 99% remaining in solution. The silica precipitate contains 96% of the silica and is very effective in removing lead and iron and moderately effective in removing aluminium from solution. Arsenic and fluorine, and to a lesser degree aluminium remain in solution. XRD identified four minor crystalline phases present in the solid residue that were also present in the initial ore, as well as, a large amorphous peak from the non-crystalline precipitated silica. These crystalline phases are, in order of approximate decreasing abundance; quartz (SiO_2), haematite (Fe_2O_3), anglesite ($PbSO_4$) and muscovite ($Al_{2.9}H_2KO_{12}Si_{3.1}$). The identification of these phases complements the ICP-AES results. SEM-EDX has confirmed the presence of quartz, muscovite, haematite and arsenic rich anglesite and also identified a manganese sulfate phase present in the solid product. It is concluded that all other impurity phases identified in the natural zinc orthosilicate ore in Section 2.2 are dissolved in the crystalliser and hence do not appear in the solid product.

SEM-EDX has confirmed that these solid impurities are acting as centres for silica aggregation. It is most uncommon to see a silica particle that is free of impurities and most particles contain multiple, separate impurity inclusions. Unfortunately, the synthetic zinc orthosilicate also contains insoluble impurities, so the full impact of these impurity phases cannot be realised by conducting a continuous experiment in the absence of solid impurities.

The MSMPR model, described in Section 1.3, was not applied to IRN-10 to determine the nucleation rate, B, and growth rate, G, of the silica particles. This was due to the aggregation based growth mechanism being so dependent on the foreign solid particles present. This growth mechanism was considered to be too far removed from traditional crystallisation for the MSMPR treatment to be applied.

5.0 CONCLUSIONS

Extensive conclusions have been made at the end of the sections regarding batch and continuous precipitation in Sections 3.4 and 4.4, respectively. For completeness those previous conclusions will be summarised here and further conclusions that have been drawn by combining these previous sections will be presented.

Batch experiments have determined, as would be expected, that the rate of silica precipitation is proportional to the initial silica supersaturation. It is also proportional to the concentrations of sulfuric acid, zinc sulfate, iron (III) sulfate, aluminium sulfate and hydrofluoric acid, and the precipitation temperature, all determined at a fixed silica supersaturation ratio. The role of all these additives appears to be catalytic but the mechanism of catalysis is unknown. Studies on the effect of supersaturation revealed a dramatic change in the precipitate morphology between $S = 2.9$ and $S = 4.3$. At $S = 4.3$ and above, unfilterable, porous, micro-gel particles are formed, while at $S = 2.9$ and below granular, colloidal particles that filter rapidly are formed. The morphology of precipitated silica is independent of the rate of precipitation and is therefore thought to be controlled by chemical means rather than kinetic means, with supersaturation being the most dominant factor.

The presence of silica seed can be used to increase the rate of silica precipitation, with the rate being proportional to the seed solids loading. Seed however, cannot be used to prevent the precipitation of micro-gel from supersaturations ratios of $S = 4.3$ and above. The insoluble impurity phases present in the natural zinc orthosilicate ore appear to be acting as centres for silica aggregation.

Continuous experiments confirmed the relationship between silica supersaturation and precipitate morphology discovered during the batch experiments. However, the supersaturation ratio range for the gel point has been narrowed to $S = 2.9$. This finding does not appear to have been recorded previously, in the literature. Thus, the steady state filtration performance of the silica product is a function of the supersaturation ratio. The steady state filterability was also found to be a function of the mixing and product removal conditions within the reactor vessel, with CSCPR conditions producing better filterability than MSMPR conditions, at the same supersaturation ratio. It is believed that the CSCPR conditions provide the silica precipitate with a longer residence time in the reactor, allowing ageing to form particles with higher filterability.

The growth of silica particles during continuous precipitation (*cf.* industrial operation) has been elucidated by combining the results from a variety of batch and continuous precipitation experiments.

The silica supersaturation rises rapidly during the initial stages of a continuous experiment. This is due to the dissolution rate of the natural zinc orthosilicate ore being much greater than the precipitation rate of silica, as there is insufficient seed surface at this early stage to mop up the dissolved silica. During this period there is nucleation of colloidal silica particles. TEM indicates that colloidal precipitates are present at all stages of a continuous experiment, even in the presence of micro-gel. At some supersaturation ratio well above S = 2.9, a massive, spontaneous precipitation event occurs and the colloidal silica particles are entrained in a micro-gel network, that renders the solution unfilterable. As a result of this de-supersaturation event, the supersaturation ratio is now below S = 2.9. The silica micro-gel tends to aggregate around the insoluble impurity particles present in the reactor from the natural zinc orthosilicate ore, as shown by SEM. The micro-gel now begins to age and densify, as seen in batch experiments, by the aggregation of colloidal silica particles and the deposition of monosilicic acid. By the end of the first residence time the precipitate is filterable. The ageing process is accelerated, in comparison to that occurring in a batch experiment, by the continual presence of a relatively high concentration of monosilicic acid, from the dissolution of the natural zinc orthosilicate ore. This enables rapid filling of pores to densify the silica micro-gel.

Depending on the many factors controlling silica supersaturation, the precipitation can proceed in one of two directions:

If the supersaturation ratio remains below S = 2.9, precipitation will continue with the nucleation of further colloidal particles and aggregation of these colloids; either with other colloidal silica particles, on an existing silica surface or a fresh heterogeneous surface from the dissolving natural zinc orthosilicate ore. TEM, FESEM and SEM has shown this to be occurring. Monosilicic acid liberated from the dissolving ore will deposit in pores in existing particles to form a denser structure and in crevices between freshly aggregated particles cementing them together. All the while, Ostwald ripening is occurring, liberating monosilicic acid and contributing to the growth of silica particles. These growth processes will continue until steady state is reached, whereupon product quality and composition will remain constant.

If the supersaturation ratio rises above S = 2.9, the higher concentration of silica in solution will result in the growth of fresh micro-gel, both on the surface of existing particles and in solution. TEM has been used to image this homogeneous micro-gel formation. This renders the solution, once again, unfilterable. The precipitate quality will not recover from this event if operating conditions are not changed sufficiently to reduce the silica supersaturation ratio to below S = 2.9. Even though the supersaturation ratio will drop below S = 2.9 after the micro-gel formation, it will soon rise above this point again and further micro-gel will form, thus compounding the problem. If the operating conditions are changed and the supersaturation ratio remains below S = 2.9 indefinitely, the precipitate quality will improve as it did during the first residence time.

6.0 IMPLICATIONS FOR INDUSTRY

This section describes, in simple terminology, the implications of this research on the electrolytic zinc industry. In particular, it details the main influences on silica precipitation, their effect on precipitate quality and how to deal with potential problems that may arise.

Silica can be successfully precipitated and separated from strong sulfuric acid solutions using batch or continuous processing. Batch precipitation is very slow and more than likely, uneconomical. However, it can be used to produce a sphericular, silica precipitate in the sub-micron size range if there is economic benefit for such material. Otherwise, an easily separable precipitate can be formed in a reasonable time using continuous processing. The remainder of this section focuses on continuous precipitation.

The most important consideration in the treatment of soluble silica is the supersaturation ratio, or the concentration of silica in solution. If this rises above 1000 mg L^{-1}, expressed as SiO_2, unfilterable silica micro-gel will be produced. If the silica concentration remains below this value, a readily filterable, dense, silica precipitate will be formed. The concentration of silica in solution can be controlled; by the feed rate of soluble silica to the reactor vessel, by the presence of seed and also by the mixing conditions within the reactor vessel itself. A slow stirring speed that allows partial settling of the solids in the reactor vessel produces silica that has a higher filterability than that produced in a well mixed vessel, using the same operating parameters. The conditions used in IRN-11, detailed in Section 4.3.5 using a slower stirring speed than normal, are the most successful undertaken in this study. They would be ideal for use in scaling up to larger industrial scale equipment.

The poor filterability that occurs during the first residence time of operation can be avoided by the addition of a one-off batch of seed at start-up. The seed solids loading can be the same as for normal operation, or less if seed material is in short supply, and combined with a longer residence time to allow the solids loading to build up to a nominal level. Alternatively, a semicontinuous arrangement could be used with no silica product material being removed for the first residence time. This would allow the unfilterable micro-gel to age into a readily filterable silica product, without any poorly filtering product being released beforehand. Obviously, this would require the process to be started with the reactor vessel half full of a starting solution and residence time calculations performed using half the vessel capacity as the volume. At the end of the first residence time, it is envisaged that operation could be switched to continuous, with the residence time slowly changed to suit the full volume of the reactor vessel. This method has not been trialed but is expected to be successful.

If, at some time during operation, silica micro-gel is formed and the filtration rate of the silica product decreases dramatically, a similar semi-continuous mode of operation can be adopted, as that described above. The soluble silica feed rate would be reduced to allow the silica concentration to fall below 1000 mg L^{-1}, while no product material would be released until the silica had aged sufficiently for filtration performance to return to specification. Obviously, additional reactor volume will be required to achieve this. The presence of freshly dissolved silica enhances the rate at which the micro-gel ages to a filterable precipitate. If no further reactor volume is available for the above operation, the feed streams can be shut off completely and the reactor vessel held at operating temperature, 95°C, to allow the ageing process to occur. This however, will be extremely slow, in the order of ten days if the silica concentration had risen to 2000 mg L^{-1}.

7.0 RECOMMENDATIONS FOR FURTHER WORK

While this research has made a considerable contribution to the knowledge of silica precipitation from electrolytic zinc solutions, the following are suggestions for future work:

In terms of fundamentals, the mechanism of silica precipitation requires further work to fully understand the processes occurring. Why is silica micro-gel formed above $S = 2.9$, while silica precipitate is formed at or below this supersaturation ratio? Obviously, the supersaturation is a major factor, but why a different structure precipitates at the different supersaturation ratios is unknown. The mechanism needs to be probed on a molecular scale. This is seen as the single, most important area for further research.

Dynamic light scattering measurements and high resolution TEM imaging of the initial stages of precipitation from the two supersaturation ratios of interest ($S = 2.9$ and $S = 4.3$) would also be useful tools to investigate the mechanism of precipitation. This would enable the initial structure of particles to be determined as a function of supersaturation. In turn, this could be used to determine whether the same, or different mechanisms are operating at the different supersaturations. Infra-red, Raman and ^{29}Si nuclear magnetic resonance spectroscopies could be used to probe the solution chemistry during silica precipitation from these two supersaturation ratios in order to determine the mechanism. Further batch experiments at a range of different temperatures, at the two supersaturation ratios mentioned above, could be used to determine the rate constant and activation energy for precipitation using the Arrhenius equation. Knowledge of the rate constant and activation energy for the precipitation of silica micro-gel and granular silica will determine if there is a different mechanism operating for the precipitation of the two different species.

A series of experiments is needed to determine accurately, the equilibrium solubility of silica over the range of temperatures and sulfuric acid concentrations studied in this project. Equilibrium solubilities are important values, which vary with both temperature and sulfuric acid concentration, and are necessary to determine supersaturation ratios under various conditions. Values should be determined from above the equilibrium solubility, using precipitation experiments; and from below the equilibrium solubility, using dissolution of amorphous silica experiments. The equilibrium solubility should be the same, determined by both methods. However, as noted in Section 1.4.4, the solubility of amorphous silica is very dependent on the type and source of silica used for the experiment.

The relationship between supersaturation and precipitate structure should be investigated further, as a function of temperature and sulfuric acid concentration. In conjunction with the equilibrium solubility, the supersaturation ratio limit for the formation of silica precipitate in preference to micro-gel can be determined. This knowledge will help to formulate a mechanism for precipitation.

It is hoped that a detailed, fundamental investigation, such as that outlined above will lead to the determination of the mechanism of silica precipitation. Much of the equipment described above, was not readily available. Time constraints also prevented the pursuit of the work described. However, the work carried out for this thesis used the most suitable equipment available.

Further experimentation is required to extract the maximum performance from continuous silica precipitation. This entails reducing the residence time and improving the filterability, the thickened solids loading and the water content of the filter cake.

Investigation of the effect of continual seeding on continuous precipitation is needed to determine if a higher solids loading in the reactor vessel will allow shorter residence times, while still adequately controlling supersaturation. The ideal seed material would be silica precipitation product, recycled into the reactor vessel after suitable processing to increase the solids loading. The insoluble phases present in the natural zinc orthosilicate ore should also be investigated as a potentially better seed source than silica. Other readily available solid industrial residues might also be suitable as seeds. A continuous experiment in the absence of any insoluble impurities will indicate how important these particles are in the precipitation process. This poses a significant challenge as to the development of a method for the removal of the solid impurities from the zinc orthosilicate feed material. It should be remembered that both the natural and synthetic zinc orthosilicates contain substantial amounts of insoluble material.

Operation at a higher sulfuric acid concentration will enable a shorter residence time to be used as a result of the subsequent higher precipitation rate experienced at higher acid concentrations, as determined in Section 3.3.2.2. A denser, less porous precipitate with a subsequently improved thickened solids loading and a lower water content of the filter cake may also result. The reasoning behind this is the higher dehydration power and subsequently lower water activity associated with the higher sulfuric acid concentration.

The effect of mixing and product removal conditions should be investigated further as this is not well understood at present and appears to have a significant effect on the precipitate quality. The determination of the residence time distribution for both the liquid and solid portion of the product under MSMPR and CSCPR conditions may provide insight into this phenomenon. Both solid and liquid tracer materials could be used to probe this.

The possibility of using the zinc, iron (III) and aluminium sulfate and hydrofluoric acid additive materials to increase the precipitation rate and also possibly the filterability in continuous processing should not be discounted, as they appear to have a catalytic effect. Thus, a factorial design and optimisation series of experiments (Miller and Miller, 1989) should be performed to determine if there is any interaction between the additives and also determine the optimum level of these additives to maximise the precipitation rate.

While this section describes two very separate areas of research, there is the possibility of some overlap, with conclusions from one section answering questions from the other.

8.0 REFERENCES

Abbruzzese, C. (1981). Caustic leaching of oxidised lead-zinc ores. Hydrometallurgy '81 - S.C.I. Conference (pp. 1-12).

Allen, R.W., Haigh, C.J. and Hamdorf, C.J. (15-05-1970). An improved method of removing dissolved ferric iron from iron-bearing solutions. Australian Patent 424,095. Australia: Electrolytic Zinc Company of Australasia Limited.

Ashman, D.W., Delong, O.J. and Jankola, W.A. (1993). Silica control during zinc calcine leaching at Cominco's Trail operation. In I.G. Matthew (Ed.), World Zinc '93: Proceedings of the International Symposium on Zinc (pp. 217-225). Victoria, Australia: The Australasian Institute of Mining and Metallurgy.

Ball, Y. (1998). Zinc bounces back after four-year low. In P. Gonnella (Ed.), Register of Australian Mining 1997/98 (pp. 322). Subiaco, Western Australia: Resource Information Unit.

Baughman, R.J. (1991). Quartz crystal growth. Journal of Crystal Growth, 112(4), 753-757.

Bell, S. (1997a, August). Zinc underpins Pasminco growth plans. Australia's Mining Monthly, 28-31.

Bell, S. (1997b, August). Zinc sizzles as gold drizzles. Australia's Mining Monthly, 26-28.

Betterton, J.O. (1923). Soluble silica in the preparation of zinc-sulfate solution for electrolysis. Transactions of the American Institute of Mining and Metallurgical Engineers, 69, 159-175.

Bodas, M.G. (1996). Hydrometallurgical treatment of zinc silicate ore from Thailand. Hydrometallurgy, 40(1-2), 37-49.

Bodson, F.J.J. (4-5-1974). Process for the treatment of material containing zinc and silica for the recovering of zinc by the hydrometallurgical way. United States Patent 3,954,937. Angleur, Belgium.

Bratt, G.C. and Gordon, A.R. (1967). Solution purification for the electrolytic production of zinc. Research in chemical and extraction metallurgy (pp. 197-210). Victoria, Australia: The Australasian Institute of Mining and Metallurgy.

Brinker, C.J. and Scherer, G.W. (1990). Sol-gel science: The physics and chemistry of sol-gel processing. Boston: Academic Press.

Bryson, A.W. (1986). Factors that effect the kinetics of nucleation and growth and the purity of goethite precipitates produced from sulphate solutions. In J.E. Dutrizac and A.J. Monhemius (Ed.), Iron Control in Hydrometallurgy (pp. 376-390). Chichester, England: Ellis Horwood Limited.

Carmichael, J.D. (1993). Zinc silicate ore mining by Pasminco Limited at Beltana-Aroona, SA. In J.T. Woodcock and J.K. Hamilton (Ed.), Australasian Mining and Metallurgy. The Sir Maurice Mawby Memorial Volume (2nd ed., pp. 496-498). Victoria, Australia: The Australasian Institute of Mining and Metallurgy.

Chan, S.H. (1989). A review on solubility and polymerization of silica. Geothermics, 18(1/2), 49-56.

Chen, S.L., Dong, P. and Yang, G.H. (1997). The size dependence of growth rate of monodisperse silica particles from tetraalkoxysilane. Journal of Colloid and Interface Science, 189, 268-272.

Davey, P.T. and Scott, T.R. (1975). Formation of β-FeOOH and α-Fe_2O_3 in the goethite process. Transactions of the Institution of Mining and Metallurgy. Section C, 84, 83-86.

Davey, P.T. and Scott, T.R. (1976). Removal of iron from leach liquors by the "Goethite" process. Hydrometallurgy, 2, 25-33.

Demazeau, G. and Lafon, F. (1994). Hydrothermal crystal growth of α-quartz: New specificities correlated to applications. Journal De Physique IV, 4(C2), 13-18.

Demopoulos, G.P., Droppert, D.J. and Van Wert, G. (1985). Options for the immobilization of arsenic as crystalline scorodite. Impurity Control and Disposal in Hydrometallurgical Processes (pp. 57-69).

Demopoulos, G.P., Droppert, D.J. and Van Weert, G. (1995). Precipitation of crystalline scorodite ($FeAsO_4.2H_2O$) from chloride solutions. Hydrometallurgy, 38, 245-261.

Droppert, D.J., Demopoulos, G.P. and Harris, G.B. (1996). Ambient pressure production of crystalline scorodite from arsenic-rich metallurgical effluent solutions. In G.W. Warren (Ed.), EPD Congress: Proceedings of Sessions and Symposia (sponsored by the Extraction and Processing Division-TMS Annual Meeting) (pp. 227-239). California, USA: TMMMS.

Dufresne, R.E. (1976). Quick leach of siliceous zinc ores. Journal of Metals, 2, 8-12.

Dutrizac, J.E. and Kaiman, S. (1976). Synthesis and properties of jarosite compounds. Canadian Mineralogist, 14, 151-158.

Dutrizac, J.E. and Jambor, J.L. (1985). Impurity control during jarosite precipitation. Impurity Control Disposal, Proceedings of the Canadian

Institute of Metallurgy Annual Hydrometallurgical Meeting (pp. 23/1-23/24). Vancouver, British Columbia: Canadian Institute of Metallurgy.

Dutrizac, J.E. (1990). Converting jarosite residues into compact hematite products. JOM: the journal of the Minerals, Metals and Materials Society, 42(1), 36-39.

Elgersma, F., Witkamp, G.J. and van Rosmalen, G.M. (1993). Incorporation of zinc in continuous jarosite precipitation. Hydrometallurgy, 33, 313-339.

Elliot, P. (1991). Minerals of the Beltana mine, Puttapa, South Australia. The Mineralogical Record, 22(November-December), 449-456.

Firkin, G.R. (1980). Lead-zinc smelting at the Sulphide Corporation Pty. Ltd., Cockle Creek, NSW. In J.T. Woodcock (Ed.), Mining and metallurgical practices in Australasia . The Sir Maurice Mawby Memorial Volume (pp. 241-248). Victoria, Australia: The Australasian Institute of Mining and Metallurgy.

Financial Times Energy Yearbook, Mining. 1998 (1997). London: Financial Times Energy.

Fitzgerald, B. (1997, June). Pasminco set for a new Century. The Miner, 4-8.

Fleming, B.A. (1981). Polymerisation kinetics and ionisation equilibria in aqueous silica solutions. (Doctoral dissertation, Princeton University, 1981).UMI Dissertation Services, 3203239.

Frenay, J. (1985). Leaching of oxidised zinc ores in various media. Hydrometallurgy, 15(2), 243-253.

Fugleberg, S.P. and Poijarvi, J.T.I. (5-10-1977). Hydrometallurgical process for the treatment of soluble silicate-bearing materials. Australian Patent 29,385. Outokumpu, Finland: Outokumpu Oy.

Fugleberg, S.P. and Poijarvi, J.T.I. (10-4-1979). Hydrometallurgical treatment of soluble silicate-bearing zinc materials. United States Patent 4,148,862. Outokumpu, Finland: Outokumpu Oy.

Gilmour, R. (1993). Electrolytic zinc production by Pasminco Metals-EZ, Risdon, Tas. In J.T. Woodcock and J.K. Hamilton (Ed.), Australasian Mining and Metallurgy. The Sir Maurice Mawby Memorial Volume (2nd ed., pp. 573-578). Victoria, Australia: The Australasian Institute of Mining and Metallurgy.

Gordon, A.R. (1985). Zinc extraction and Refining. Australasian Institute of Mining and Metallurgy. Scientific and Technological Developments in Extractive Metallurgy, G.K. Williams Memorial Volume (1st ed., pp. 67-86). Victoria, Australia: The Australasian Institute of Mining and Metallurgy.

Greenwood, N.N. and Earnshaw, A. (1989). Chemistry of the Elements. Oxford: Pergamon Press.

Gregory, J. and Nelson, D.W. (1986). Monitoring of aggregates in flowing suspensions. Colloids and Surfaces, 18, 175-188.

Hamilton, J.K. and Woodcock, J.T. (1993). Century zinc deposit of CRA Limited, north west Queensland. In J.T. Woodcock and J.K. Hamilton (Ed.), Australasian Mining and Metallurgy. The Sir Maurice Mawby Memorial Volume (2nd ed., pp. 589-590). Victoria, Australia: The Australasian Institute of Mining and Metallurgy.

Harnby, N., Edwards, M.F. and Nienow, A.W. (Ed.). (1985). Mixing in the process industries. London: Butterworths.

Harnby, N., Edwards, M.F. and Nienow, A.W. (1992). Mixing in the process industries (2nd ed.). Oxford: Butterworth-Heinemann.

Hunter, R.J. (1987). Foundations of colloid science (Vol 1). Oxford: Clarendon Press.

Hurd, C.B. and Letteron, H.A. (1932). Studies on silicic acid gels. I. Measurements on surface tension during setting and the effect of temperature on the time of set. Journal of Physical Chemistry, 26, 604-615.

Hurd, C.B. and Barclay, R.W. (1940). Studies on silicic acid gels. X. The time of set of gel mixtures containing high concentrations of mineral acids. Journal of Physical Chemistry, 44, 847-851.

Hurd, C.B. and Sheffer, H.E. (1941). Studies on silicic acid gels. XI. The effect of concentration of silica upon the time of set. Journal of Physical Chemistry, 45, 588-594.

Hutchison, R.F.S. (1958). Silica gelation in Risdon leach pulp. Proceedings of the Australasian Institute of Mining and Metallurgy, 188(12), 11-25.

Hutchison, R.F.S. and Phipps, P.J. (1977). Formation and particle size of jarosite. The AusIMM Conference (pp. 319-327). Victoria, Australia: The Australasian Institute of Mining and Metallurgy.

Iler, R.K. (1952). Polymerisation of silicic acid: Catalytic effect of fluoride. Journal of Physical Chemistry, 56(6), 680-683.

Iler, R.K. (1979). The chemistry of silica. Solubility, polymerisation, colloid and surface properties, and biochemistry. New York: John Wiley and Sons.

Iler, R.K. (1980). Isolation and characterisation of particle nuclei during the polymerisation of silicic acid to colloidal silica. Journal of Colloid and Interface Science, 75(1), 138-148.

Irving, A.T. (1998). Environmental issues in the development of the Pasminco Century Project. AusIMM '98: the mining cycle (pp. 437-439). Victoria, Australia: The Australasian Institute of Mining and Metallurgy.

It's over: Pasminco ends ocean dumping. (1997, November 2). Environmental Manager, 178, 2.

Johnson, R.S. and Tyson, R.K. (1993). Zinc production by Pasminco Metals-BHAS at Port Pirie, SA. In J.T. Woodcock and J.K. Hamilton (Ed.), Australasian Mining and Metallurgy. The Sir Maurice Mawby Memorial Volume (2^{nd} ed., pp. 569-573). Victoria, Australia: The Australasian Institute of Mining and Metallurgy.

Kershaw, M.G. (1995). Modernisation of the leaching circuit at Pasminco Metals-EZ. Hydrometallurgy, 39, 129-145.

Lide, D.R. (Ed.). (1994). CRC Handbook of Chemistry and Physics (75th ed.). London: CRC Press.

Main, J. (1993). The Century zinc deposit. Carpentaria and Mount Isa Regional Development Forum (pp. 27-30). Mount Isa: North West Queensland branch of the Australasian Institute of Mining and Metallurgy and J.B. Were and Son.

Margulis, E.V. (1983). Behaviour of silica when leaching oxidised material in zinc hydrometallurgy. Tsvetnye metally/Non-ferrous metals, 24(1), 24-28.

Matthew, I.G. and Elsner, D. (1977a). The hydrometallurgical treatment of zinc silicate ores. Metallurgical Transactions B, 8B(3), 73-83.

Matthew, I.G. and Elsner, D. (1977b). The processing of zinc silicate ores-a review. Metallurgical Transactions B, 8B(3), 85-91.

McCristal, T.G., Manning, J. and Sanderson, I. (1998). Conversion of the Pasminco Hobart smelter to paragoethite. In J.E. Dutrizac, J.A. Gonzalez, G.L. Bolton and P. Hancock (Ed.), Zinc and lead processing: Proceedings of an international symposium on zinc and lead processing (pp. 443-453). Calgary, Canada: The Metallurgical Society of CIM.

McDonough, R.J. (1992). Mixing for the process industries. New York: Van Nostrand Reinhold.

Mersmann, A. (Ed.). (1995). Crystallisation technology handbook. New York: Marcel Dekker, Inc.

Miller, J.C. and Miller, J.N. (1989). Statistics for analytical chemistry (2nd ed.). New York: John Wiley and Sons.

Mullin, J.W. (1988). Crystallization and precipitation. In B. Elvers, M. Ravenscroft, J.F. Rounsaville and G. Schulz (Ed.), Ullman's encyclopedia of industrial chemistry (5th ed., pp. 1-46). Weinheim: VCH.

Mullin, J.W. (1993). Crystallization (3rd Rev ed.). Oxford: Butterworth-Heinemann.

Nyvlt, J. (1982a). Industrial crystallization: The state of the art (2nd Rev ed.). Weinhein: Verlag Chemie.

Nyvlt, J. (1982b). Determination of crystallization kinetics from batch experiments. Collection of Czechoslovak Chemical Communications, 47(12), 3384-3392.

Ozkul, T. (1996). Data acquisition and process control using personal computers. New York: Marcel Dekker, Inc.

Pammenter, R.V. (1993). Modernisation and expansion of the electrolytic zinc plant of Pasminco Metals-EZ, Risdon, Tas. In J.T. Woodcock and J.K. Hamilton (Ed.), Australasian Mining and Metallurgy. The Sir Maurice Mawby Memorial Volume (2nd ed., pp. 578-581). Victoria, Australia: The Australasian Institute of Mining and Metallurgy.

Pammenter, R.V., Gilmour, R. and Salmon, P.T. (1993). Production of zinc in the modernised Pasminco Metals - EZ plant, Hobart Tasmania. In I.G.

Matthew (Ed.), World Zinc '93: Proceedings of the International Symposium on Zinc (pp. 287-293). Victoria, Australia: The Australasian Institute of Mining and Metallurgy.

Pryor, E.J. (1965). Mineral Processing (3rd ed.). London: Applied Science Publishers Ltd.

Pus'ko, A.G., Ushakov, N.N. and Khan, O.A. (1979). Chemism and limiting steps of the reaction of zinc orthosilicate with aqueous sulphuric acid solutions. Russian Journal of Applied Chemistry, 52(10), 2052-2057.

Queneau, P.B. and Berthold, C.E. (1985). Silica in hydrometallurgy: An overview. Impurity Control Disposal, Proceedings of the Canadian Institute of Metallurgy Annual Hydrometallurgical Meeting (pp. 13/1-13/21). Vancouver, British Columbia: Canadian Institute of Metallurgy.

Radino, H.L. (5-12-1957). Process of zinc extraction from ores comprising soluble silicates by means of hydrometallurgy. Australian Patent 224,195. Companhia Mercantile Industrial Inga.

Randolph, A.D. and Larson, M.A. (1988). Theory of particulate processes. Analysis and techniques of continuous crystallization (2nd ed.). San Diego, California: Academic Press, Inc.

Rangott, M.F. (1980). Zinc ore mining by Electrolytic Zinc Company of Australasia Ltd, Beltana, S.A. In J.T. Woodcock (Ed.), Mining and metallurgical practices in Australasia. The Sir Maurice Mawby Memorial Volume (pp. 202-204). Victoria, Australia: The Australasian Institute of Mining and Metallurgy.

Read, N. (1995, September). Century set to turn: CRA expects investment payoff. The Miner, 24-25.

Reuter, M.A., Sudholter, S., Kruger, J. and Koller, S. (1995). Synthesis of processes for the production of environmentally clean zinc. Minerals Engineering, 8(1/2), 201-219.

Shaw, D.J. (1980). Introduction to colloid and surface chemistry (3rd ed.). London: Butterworths.

Skoog, D.A., West, D.M. and Holler, F.J. (1988). Fundamentals of analytical chemistry (5th ed.). New York: Saunders College Publishing.

Sohnel, O. and Garside, J. (1992). Precipitation: Basic principles and industrial applications. Oxford: Butterworth-Heinemann Ltd.

Staff of Pasminco Metals-Sulphide Pty Limited. (1993). Lead-zinc smelting at Pasminco Metals - Sulphide Pty Limited, Newcastle, NSW. In J.T. Woodcock and J.K. Hamilton (Ed.), Australasian Mining and Metallurgy. The Sir Maurice Mawby Memorial Volume (2nd ed., pp. 563-568). Victoria, Australia: The Australasian Institute of Mining and Metallurgy.

Stober, W., Fink, A. and Bohn, E. (1968). Controlled growth of monodisperse silica spheres in the micron size range. Journal of Colloid and Interface Science, 26, 62-69.

Terry, B. and Monhemius, A.J. (1983). Acid dissolution of willemite ($(Zn,Mn)_2SiO_4$) and hemimorphite ($Zn_4Si_2O_7(OH)_2.H_2O$). Metallurgical Transactions B, 14B(3), 335-346.

Terry, B. (1983a). The acid decomposition of silicate minerals. Part I. Reactivities and modes of dissolution of silicates. Hydrometallurgy, 10(2), 135-150.

Terry, B. (1983b). The acid decomposition of silicate materials. Part II. Hydrometallurgical applications. Hydrometallurgy, 10(2), 151-171.

Terry, B. (1983c). Specific chemical rate constants for the acid dissolution of oxides and silicates. Hydrometallurgy, 11(3), 315-344.

Waltho, A.E. and Andrews, S.J. (1993). The Century zinc-lead deposit, Northwest Queensland. The Australasian Institute of Mining and Metallurgy - Centenary Conference (pp. 41-61). Adelaide, Australia: Australasian Institute of Mining and Metallurgy.

Waltho, A.E., Allnutt, S.L. and Radojkovic, A.M. (1993). Geology of the Century zinc deposit, northwest Queensland. In I.G. Matthew (Ed.), World Zinc '93: Proceedings of the International Symposium on Zinc (pp. 111-129). Victoria, Australia: The Australasian Institute of Mining and Metallurgy.

Weimer, F.S., Wever, G.T. and Lapee, R.J. (1959). Electrolytic zinc processes. In C.H. Mathewson (Ed.), Zinc: The science and technology of the metal, its alloys and compounds (pp. 174-225). New York: Hafner Publishing Company, Inc.

Wood, J.T., Kern, P.L. and Ashdown, N.C. (1977). Electrolytic recovery of zinc from oxidised ores. Journal of Metals, 29(11), 7-11.

Yatabe, J., Yamada, S., Ikawa, T. and Kageyama, T. (1992). Synthesis of zinc silicate using water glass as raw material. Journal of the Chemical Society of Japan, 5, 565-569.

Zaitsev, V.Y. and Margulis, E.V. (1985). The metallurgy of lead and zinc. Moscow: Metallurgiya.

9.0 APPENDICES

9.1 APPENDIX 1 - LIST OF SYMBOLS AND ACRONYMS

The following is a list of symbols and acronyms used in this thesis.

α = Activity at the surface

α_0 = Activity in the bulk solution

γ = Surface energy

Ω = Ohm

σ = Relative supersaturation

τ = Steady state residence time

Δc = Concentration difference

°C = Degrees Celsius

μm = Microns

$\{H^+\}$ = Hydrogen ion activity (mol cm^{-3})

A = Amps

ADC = Analog to digital converter

B = Nucleation rate

c = Concentration

c* = Equilibrium concentration

CH# = Channel number

$cm^3\ min^{-1}$ = Cubic centimetres per minute

CSCPR = Classified suspension classified product removal

Cw/ccw = Clockwise/counterclockwise

DAC = Digital to analog converter

DIG = Digital

DLVO = Deryaguin-Landau-Verwey-Overbeek

exp = Base of natural logarithms (2.71828)

FESEM = Field emission scanning electron microscopy

g = Grams

G = Growth rate

$g\ cm^{-3}$ = Grams per cubic centimetre

$g\ kg^{-1}$ = Grams per kilogram

$g\ L^{-1}$ = Grams per litre

$g\ L^{-1}\ h^{-1}$ = Grams per litre per hour

GND = Ground

h = Hours

Hz = Hertz

ICP-AES = Inductively coupled plasma-atomic emission spectroscopy

K = Steady state separation coefficient

keV = Kiloelectron volts

kg = Kilograms

$kg\ h^{-1}\ m^{-2}$ = Kilograms per hour per square metre

kPa = Kilopascals

k_s = Specific chemical rate

K_w = Ion-product constant for water

L = Litres

L = PSD as a number function

L h^{-1} = Litres per hour
LLGND = Logic logic ground
M = Moles per litre
m h^{-1} = Metres per hour
m^2 = Square metres
m^3 = Cubic metres
m^3 m^{-2} h^{-1} = Cubic meters per square meter per hour
mA = Milliamps
MB = Megabyte
MHz = Megahertz
mL = Millilitres
mm = Millimetres
mol Zn cm^{-1} s^{-1} = Moles of zinc per centimetre per second
mS cm^{-1} = MilliSiemens per centimetre
MSCPR = Mixed suspension classified product removal
MSMPR = Mixed suspension mixed product removal
n = Population density
n_0 = Population density of nuclei
nm = Nanometres
pH = Potential hydrogen ion concentration
PID = Proportional integral derivative
pK_a = Ionisation constant
PSD = Particle size distribution
r = Radius of curvature
R = Universal gas constant (J mol^{-1} K^{-1})
rpm = Revolutions per minute
S = Supersaturation ratio
SEM = Scanning electron microscopy
SEM-EDX = Scanning electron microscopy-energy dispersive X-ray analysis
S_{met} = Metastable supersaturation ratio
T = Temperature (K)
TEM = Transmission electron microscopy
TTL = Transistor transistor logic
VAC = Volts alternating current
VDC = Volts direct current
V_m = Molar volume
W = Watt
w/w = Weight for weight
XRD = X-ray diffraction

9.2 APPENDIX 2 - MATERIALS AND METHODS

9.2.1 Materials

The following is a list of the reagents used during this project.

Aluminium sulfate, $Al_2(SO_4)_3.16H_2O$ AR grade, BDH.
Ammonium hydroxide, NH_4OH (25% NH_3) AR grade, Ajax.
Ammonium molybdate, $(NH_4)_6Mo_7O_{24}.4H_2O$ AR grade, BDH.
Ammonium molybdate stock solution, 100 g L^{-1} ammonium molybdate (AR grade, BDH) and 53 g L^{-1} ammonium hydroxide (AR grade, Ajax).
Ballotini impact spheres, SiO_2 AH grade, Potters Industries.
Bromo-cresol green, pH indicator grade, BDH.
Cytochrome C from bovine albumin, Biochemika grade, Fluka.
Diluent solution #1, Milli-Q^{TM} water adjusted to pH 2.0 with sulfuric acid (AR grade, Ajax).
Diluent solution #2, Milli-Q^{TM} water containing 50 g L^{-1} sulfuric acid (AR grade, Ajax).
Ethanol, CH_3CH_2OH LR grade, Ajax.
Hydrofluoric acid, HF 40% w/v, AR grade, BDH.
Magnafloc 333 commercial grade, Allied Colloids.
Milli-Q^{TM} water, H_2O.
Potassium iodide, KI AR grade, BDH.
Silica - precipitated, SiO_2 LR grade, Ajax.
Silica - pyrogenic, SiO_2, supplied by Simcoa Operations.
Sodium carbonate, Na_2CO_3 AR grade, BDH.
Sodium hydroxide, NaOH LR grade, Ajax.
Sodium metasilicate, $Na_2SiO_3.5H_20$ AR grade, Ajax.
Sodium metasilicate, $Na_2SiO_3.5H_20$ LR grade, Ajax.
Sodium thiosulfate, $Na_2S_2O_3$ AR grade, Ajax.
Sulfuric acid, H_2SO_4 98% w/v AR grade, Ajax.
Sulfuric acid, H_2SO_4 170 g L^{-1} (Cell room spent electrolyte solution), supplied by Pasminco Group Technical Support from the Pasminco-BHAS zinc/lead smelter.

Sulfuric acid, H_2SO_4 0.41 M (98% w/v AR grade, Ajax) in Milli-Q^{TM} water.

Vitex indicator for iodine LR grade, Ajax.

Zinc chloride, $ZnCl_2$ LR grade, Ajax.

Zinc orthosilicate - natural, Zn_2SiO_4 (mineral name willemite), supplied by Pasminco Group Technical Support from the Pasminco-Beltana mine. Preparation and characterisation described in Section 2.2.

Zinc orthosilicate - synthetic, Zn_2SiO_4 (mineral name willemite), preparation and characterisation described in Section 2.1.

Zinc sulfate, $ZnSO_4$ 320 g L^{-1} (Cell room feed solution), supplied by Pasminco Group Technical Support from the Pasminco-BHAS zinc/lead smelter.

The composition of the major raw materials for the project are listed in Table 9.1. All analytes were determined using ICP-AES except for fluoride which was determined by ion selective electrode measurement (out-sourced to a commercial laboratory), the sulfuric acid concentration which was determined by the titration method detailed in Section 9.2.2.4 and the insoluble material which was determined by weight loss measurement after leaching, described in Section 9.2.2.5. The concentration of all analytes listed for the two types of zinc orthosilicate are total concentrations, with the acid soluble concentration shown in parentheses, where applicable.

Table 9.1: Composition of the major reagents for the project. The concentration of all analytes listed for the two zinc orthosilicate samples are total concentrations, with the acid soluble concentration shown in parentheses, where applicable

Analyte	Cell Room Spent Electrolyte Solution (g L^{-1})	Cell Room Feed Solution (g L^{-1})	Natural Zinc Orthosilicate (% w/w)	Synthetic Zinc Orthosilicate (% w/w)
SiO_2	0.04	0.04	24.5 (19.4)	32.7 (22.6)
Zn	36.8	131	42.3 (41.6)	48.7 (48.7)
As	<1	<1	0.92	<0.02
Pb	<0.005	<0.005	2.0	<0.01
Al	0.03	<0.01	1.7	<0.01
Fe	0.04	<0.01	2.4	0.05
Ge	<1	<1	0.004	<0.01
Sb	<0.1	<0.1	0.025	<0.01
F	<0.1	<0.01	<0.001	<0.001
Mn	9.5	9.0	0.87	<0.01
Ca	0.28	0.38	1.6	0.05
K	6.4	6.0	0.31	<0.04
Mg	6.4	5.7	1.2	0.07
S	102	86.9	<0.05	<0.05
Na	14.5	13.2	0.02	0.04
H_2SO_4	170	0	NA	NA
Total	NA	NA	88.2	93.7
Insoluble material	NA	NA	16.8	10.1

The total percentage compositions for the two types of zinc orthosilicate were calculated to include the additional oxygen present in the zinc orthosilicate (Zn_2SiO_4), as the table only shows the SiO_2 species. The *ca* 10% of material that is unaccounted for in Table 9.1 is thought to consist of oxygen, carbon and hydrogen, present as sulfate, oxide, hydroxide and carbonate species. These elements were not analysed.

The Cell room spent electrolyte and feed solutions are very similar in their minor analyte compositions with the Cell room feed solution having slightly lower concentrations of impurities. Both solutions are impure, as would be expected of industrially sourced solutions. The natural zinc orthosilicate, also as expected, is very impure. The acid soluble zinc and silica (SiO_2) concentrations are 41.6% and 19.4% respectively, well down on the stoichiometric values of 58.7% and 27.0%. However, the ratio of acid soluble zinc to silica is 2.14, very close to the zinc orthosilicate stoichiometric value of 2.17, which indicates that the predominant material is zinc orthosilicate. Many impurities are present in the low percent range with those phases detected by XRD and SEM-EDX, detailed in Section 2.2, being accounted for in this analysis. The only analyte that has a lower concentration than expected is sulfur, as both XRD and SEM-EDX detected several sulfate species. The synthetic zinc orthosilicate has an acid soluble zinc content of 48.7% and an acid soluble silica (SiO_2) content of 22.6%. The ratio of acid soluble zinc to silica is 2.16, extremely close to the previously mentioned stoichiometric value of 2.17, thus indicating that the predominant material is zinc orthosilicate. The major impurities present are sodium, magnesium, calcium and iron, all at concentrations of less than 0.1%. The nature of the insoluble material in the synthetic and natural zinc orthosilicates will be discussed in Section 2.1 and Section 2.2, respectively.

9.2.2 Methods

The following methods of analysis were used during the course of this investigation.

9.2.2.1 Turbidity

Measurement of the liquor turbidity during batch experiments was made directly in the reactor vessel using an Analite 152-APS portable nephelometer with the deflector cone fitted to prevent stray light entering the probe.

9.2.2.2 Inductively coupled plasma-atomic emission spectroscopy (ICP-AES)

For the batch experiments, approximately 2 mL of liquor was removed from the reactor vessel using a syringe and syringe filtered through a Gelman Supor 0.45 μm membrane. The filtered liquor was cooled to 20°C in an ice bath and 0.4 mL diluted with 10 mL of Diluent solution #1 to give a dilution factor of 26. Diluting sample aliquots to below equilibrium silica solubility and acidifying them to the isoelectric point, pH 2.0, stops further reaction, as silicic acid reactivity is lowest at this pH and silicic acid is stable in this concentration range (Fleming, 1981). The sample was later analysed using a Varian Liberty 220 ICP-AES. Analytes determined were silica (SiO_2), zinc and any additive that was under examination during that particular experiment. For example, aluminium if aluminium sulfate had been used as an additive. For the continuous experiments, the same procedure was used; however, the analytes determined were silica (SiO_2), zinc, germanium, arsenic, antimony, lead, aluminium and iron. Other one-off samples were analysed for their analytes of interest.

Solid samples were digested using a borate fusion followed by leaching of the melt with weak nitric acid (5%). The resulting solution was analysed using ICP-AES for the particular analytes of interest.

9.2.2.3 Monosilicic acid concentration

Approximately 2 mL of liquor was removed from the batch reactor and cooled to 20°C in ice. Between 0.1 and 5.0 mL of liquor, depending on concentration, was analysed for monosilicic acid concentration using Iler's (1980) Molybdic acid colourimetric method at 410 nm. The UV-Visible instrument used was a Hewlett Packard 8452A Diode Array Spectrophotometer. The procedure involved adding the following solutions to a 25 mL volumetric flask and swirling to ensure proper mixing; 2.5 mL of ammonium molybdate stock solution, 12.5 mL of Milli-Q^{TM} water and 5 mL of the 0.41 M sulfuric acid solution. The time was recorded and between 0.1

and 5.0 mL of sample or standard for analysis was added and the flask made up to volume with Milli-Q™ water. The solution was analysed after 2 minutes had elapsed since sample addition and the monosilicic acid concentration determined by comparison with a range of standards. A 200 mg L^{-1} solution of monosilicic acid (expressed as SiO_2) was produced from sodium metasilicate, AR grade, and Diluent solution #1. This was serially diluted twice to produce two additional standards of 100 and 50 mg L^{-1} monosilicic acid, expressed as SiO_2.

9.2.2.4 Sulfuric acid concentration

The filtered liquor (2 mL) for analysis was diluted with 18 mL of Milli-Q™ water containing 2.5 g of potassium iodide. The solution was allowed to stand for 5 minutes before the dropwise addition of sodium thiosulfate solution (28.30 g L^{-1} in Milli-Q™ water), with stirring, until a straw colour was reached. At this point, approximately 0.5 g of Vitex indicator for iodine was added and the sodium thiosulfate addition continued until the solution turned colourless. A further 1 mL of sodium thiosulfate solution was added. This first stage removed from the liquor the iron, which interferes with the sulfuric acid determination.

To the liquor from the first stage was added 5 drops of bromo-cresol green indicator solution (1.0 g L^{-1} in 90% ethanol and 10% Milli-Q™ water), upon which the solution turned yellow. The indicator solution was prepared by dissolving 0.05 g of bromo-cresol green in 5 mL of Milli-Q™ water, then adding 45 mL of ethanol. The yellow solution for analysis was titrated with sodium carbonate (10.81 g L^{-1} in Milli-Q™ water) until the green end point was reached. The concentration of sulfuric acid, in g L^{-1}, was calculated by multiplying the titre by five, a determinate error of approximately 1% is associated with this value. This method was supplied by Pasminco.

9.2.2.5 Insoluble material

The percentage, by weight, of insoluble material in the two zinc orthosilicate reagents was determined by leaching an accurate weight of the solid, about 1.0 g, in 1000 mL of Milli-Q^{TM} water containing 50 g L^{-1} sulfuric acid at 95°C for one hour, with stirring. The large volume of acid ensured the concentration of dissolved silica was kept below equilibrium solubility to prevent silica precipitation. The insoluble residue was filtered, washed with Milli-Q^{TM} water, air dried at 110°C for 24 hours and weighed. The following calculation provides the percentage insoluble material:

$$\text{Insoluble material} = (\text{Mass}_{\text{Insoluble material}} / \text{Mass}_{\text{Initial sample}}) \times 100$$

Masses are in g while the insoluble material is presented as a % value with a determinate error of approximately 1%.

9.2.2.6 Sulphuric acid consumption

The sulfuric acid consumed during the dissolution of synthetic zinc orthosilicate was determined by leaching an accurate mass of the solid, about 10.0 g, in 1000 mL of Milli-Q^{TM} water containing approximately 55 g L^{-1} sulfuric acid at 95°C for one hour, with stirring. The acidity of the solution was determined, using the method in Section 9.2.2.4, before and after the zinc orthosilicate dissolution and the acid consumption calculated using the following equation:

$$\text{Acid consumption} = \text{Acidity}_{\text{Initial}} - \text{Acidity}_{\text{Final}} / \text{Mass}_{\text{Solid}}$$

Acid consumption is expressed in units of $g_{\text{Sulfuric acid}}\ g_{\text{Solid}}^{-1}$, acidity is in units of g L^{-1} and mass in g. A determinate error of approximately 2% is associated with the acid consumption value.

9.2.2.7 Transmission electron microscopy (TEM)

Samples were removed at various stages of an experiment to observe the morphology of the silica precipitate. An Alltech, 3 mm diameter, 200 mesh copper grid with a continuous formvar carbon film was treated with a 1.0 g L^{-1} solution of Cytochrome C at pH 3.0 and allowed to air dry prior to use (Iler, 1979). This step rendered the surface of the grid positively charged, enabling dispersion of the negatively charged silica particles and preventing induced aggregation. Approximately 0.5 mL of liquor was removed from the batch reactor and a single drop placed on a treated grid which was washed with three drops of Milli-Q^{TM} water and allowed to air dry at room temperature. For the continuous experiments, 0.5 mL of liquor was diluted with 5 mL of Diluent solution #2. The solution was mixed well and one drop placed on a pre-treated grid, which was washed with three drops of Milli-Q^{TM} water and allowed to air dry. The samples were examined using a JEOL JEM 2000FX II TEM operating with an accelerating voltage between 80 and 200 keV.

9.2.2.8 Scanning electron microscopy (SEM)

Samples collected on TEM grids, described in Section 9.2.2.7, were imaged using the Philips XL30 scanning electron microscope, by fixing the grid to an aluminium stub with carbon paste. These samples did not require carbon coating to enable imaging. Some bulk powdered samples were mounted in round epoxy resin blocks 30 mm in diameter. The powdered samples were mixed with resin and placed in 6 mm holes within the block. After curing, the blocks were ground and polished to cross-section the particles. These blocks were carbon coated, fixed to an aluminium stub and electrically grounded to the stub with carbon paste. The particles within the block were analysed for their chemical composition using the EDAX DX4 energy dispersive X-ray analysis system.

9.2.2.9 Field emission scanning electron microscopy (FESEM)

Samples that were collected on TEM grids according to the procedure described in Section 9.2.2.7, were imaged using a JEOL JSM-6300F scanning microscope by mounting the grid to an aluminium stub using carbon paste. The instrument was operated with an accelerating voltage of 3 keV. The samples did not require carbon coating.

9.2.2.10 X-ray diffraction (XRD)

X-ray diffraction measurements were made using an APD Philips x'pert system, with a cobalt, long fine focus X-ray tube. Samples were finely ground using a mortar and pestle prior to analysis.

9.2.2.11 Particle size distribution (PSD)

Slurry samples collected from the continuous experiments were diluted in an aqueous sodium hexametaphosphate solution and analysed using a Malvern Mastersizer X instrument. The PSD was determined in the range 0.1 to 600 μm or 1 to 600 μm, depending on the instrument configuration.

9.2.2.12 Filtration rate

At the end of each batch experiment, approximately 50 mL of liquor was removed from the reactor and vacuum filtered through a 0.45 μm Gelman Supor membrane. The volume of sample was measured using a measuring cylinder. The diameter of available filter membrane was 36 mm, and the level of vacuum was -65 kPa. By measuring the time taken from the appearance of the first drop of filtrate collected until the filter cake was free of surface moisture, the filtration rate could be calculated using the following equation:

$$\text{Filtration rate} = \text{Volume}_{\text{Sample}} / \text{Area}_{\text{Filter}} / \text{Time}_{\text{Filtration}}$$

The filtration rate is expressed as $m^3\ m^{-2}\ h^{-1}$, while the volume is expressed in m^3, the area in m^2 and the time in h. This simplistic procedure, ignoring differences in solids loadings between samples, allowed a qualitative determination of a relative filtration rate between silica products from the batch experiments. This method was satisfactory for the present purpose as the difference in filtration rates between silica micro-gel and colloidal silica is enormous.

For the continuous experiments, the filtration rate was determined at the end of each residence time. A Buchner funnel holding a Whatman 541 filter paper was used which provided a diameter of 57 mm of available filter.

Once again the vacuum level was -65 kPa. The filtration rate was determined as above for the batch experiments. The thickness of the filter cake was also measured, and the filtrate clarity determined using an Allied Colloids Clarity wedge. The clarity wedge is filled with filtrate and the last number visible through the liquor is recorded as the liquor clarity. The wedge is numbered from 1 to 46 with the higher the number the clearer the liquor.

A very fine membrane was employed in filtration tests for the batch experiments to ensure colloidal silica was retained. Whatman filter paper was used for the continuous experiments as it provided more meaningful results for Pasminco. The difference in filtration media resulted in the filtration rate using the Supor membrane being about 65% of that using the paper, for a sample of the same slurry. This value will depend on the particle size distribution of the sample compared to the pore size in the membrane and paper filter. The filtration rate determined using this method has a determinate error of approximately ±5%.

9.2.2.13 Solids loading

The solids loading was determined in conjunction with the filtering test. The filter cake remaining from the filtration test was washed with Milli-Q^{TM} water, the volume being half that of the original slurry sample for the filtering test. The filter cake was air dried at 110°C for 24 hours and weighed. The solids loading is calculated according to the following equation:

$$\text{Solids loading} = \text{Mass}_{\text{Filter cake}} / \text{Volume}_{\text{Initial sample}}$$

The solids loading is expressed in g L^{-1}, while the mass is in g and the volume is in L. There is a determinate error of ±5% associated with this value.

9.2.2.14 Water content

The water content of the filter cake after filtering was carried out in conjunction with the determination of the solids loading. The mass of the wet filter cake after washing was measured and then again after drying. The water content of the filter cake was calculated using the relationship:

$$\text{Water content} = ((\text{Mass}_{\text{Wet filter cake}} - \text{Mass}_{\text{Dry filter cake}}) / \text{Mass}_{\text{Wet filter cake}}) * 100$$

Masses are in g with water retention expressed as a percentage. A determinate error of ±10% is associated with this value.

9.2.2.15 Settling rate

The settling test was carried out in a 500 mL measuring cylinder, internal diameter 48 mm, standing in a toughened glass tank filled with water, maintained at 95°C using a Grant heater/circulator. A 0.05% flocculant solution was produced by adding 0.25 g of Magnafloc 333 over the course of 30 minutes to a gently agitated 500 mL glass bottle containing 250 mL of Milli-Q^{TM} water. Following the addition of the solid flocculant, the sides of the bottle were washed down with a further 250 mL of Milli-Q^{TM} water and agitation continued for 24 hours. The flocculant solution was prepared approximately 24 hours beforehand to allow for complete hydration and stored in a dark cupboard until ready for use.

The slurry for testing (500 mL) was placed in the measuring cylinder and the temperature allowed to reach equilibrium. The slurry was homogenised by swiftly moving a plunger through the slurry. The 316 stainless steel plunger consisted of a flat disc, 40 mm in diameter with 20, 4 mm holes in it, welded to a 400 mm long shaft, 4 mm in diameter. The flocculant solution (20 mL) was added to the measuring cylinder, giving an overall concentration of 0.002%, and mixed by plunging the plunger down and up three times. The plunger was removed and a timer started. The solid/liquid interface height was recorded as a function of time for one hour. At this point the supernatant clarity was determined using the clarity wedge (Section 9.2.2.12), and the thickened solids loading was calculated. This entailed filtering, washing, drying and weighing the settled solids to determine the solids loading with the equation described in Section 9.2.2.13. The settled volume is used in the equation, not the initial volume of sample as used in Section 9.2.2.13. The settling rate was determined by measuring the gradient of the initial part of the curve on a plot of time in hours versus settled distance in meters. This provides a settling rate with units of m h^{-1}. This method was supplied by Pasminco.

9.3 APPENDIX 3 - CONTINUOUS CRYSTALLISER CONSTRUCTION

A general description of the continuous crystalliser, a detailed description of the reactor vessel and draft tube and the operation of the crystalliser are given in Section 4.2. This appendix details the finer aspects of the crystalliser, its construction and characterisation of the mixing and product removal conditions.

9.3.1 Reactor vessel lid and fittings

As mentioned in Section 4.2.2 the reactor vessel lid is constructed from 316 stainless steel. A plan view, dimensional drawing of the lid is shown in Figure 9.1. The individual ports and fittings used to secure the various components to the reactor vessel lid will now be discussed, in the numerical order they appear in Figure 9.1. The fittings associated with the reactor vessel lid were manufactured from a range of materials. 316 stainless steel was used for most fittings and for all those welded to the lid of the reactor vessel. The remaining fittings were manufactured from Teflon or polypropylene, when a higher degree of chemical inertness or a softer material, respectively, was required. Figure 9.2 shows cross sectional, dimensional drawings of these fittings. The O-ring seals used are nitrile rubber.

The lid is secured to the reactor vessel, through four ports labelled 1 in Figure 9.1, by four 316 stainless steel bolts (4.5 x 25 mm) with washers and wing nuts.

The O-ring seal between the lid and reactor vessel is manufactured from nitrile rubber cord (2 mm in diameter) cut and glued to form the required diameter O-ring.

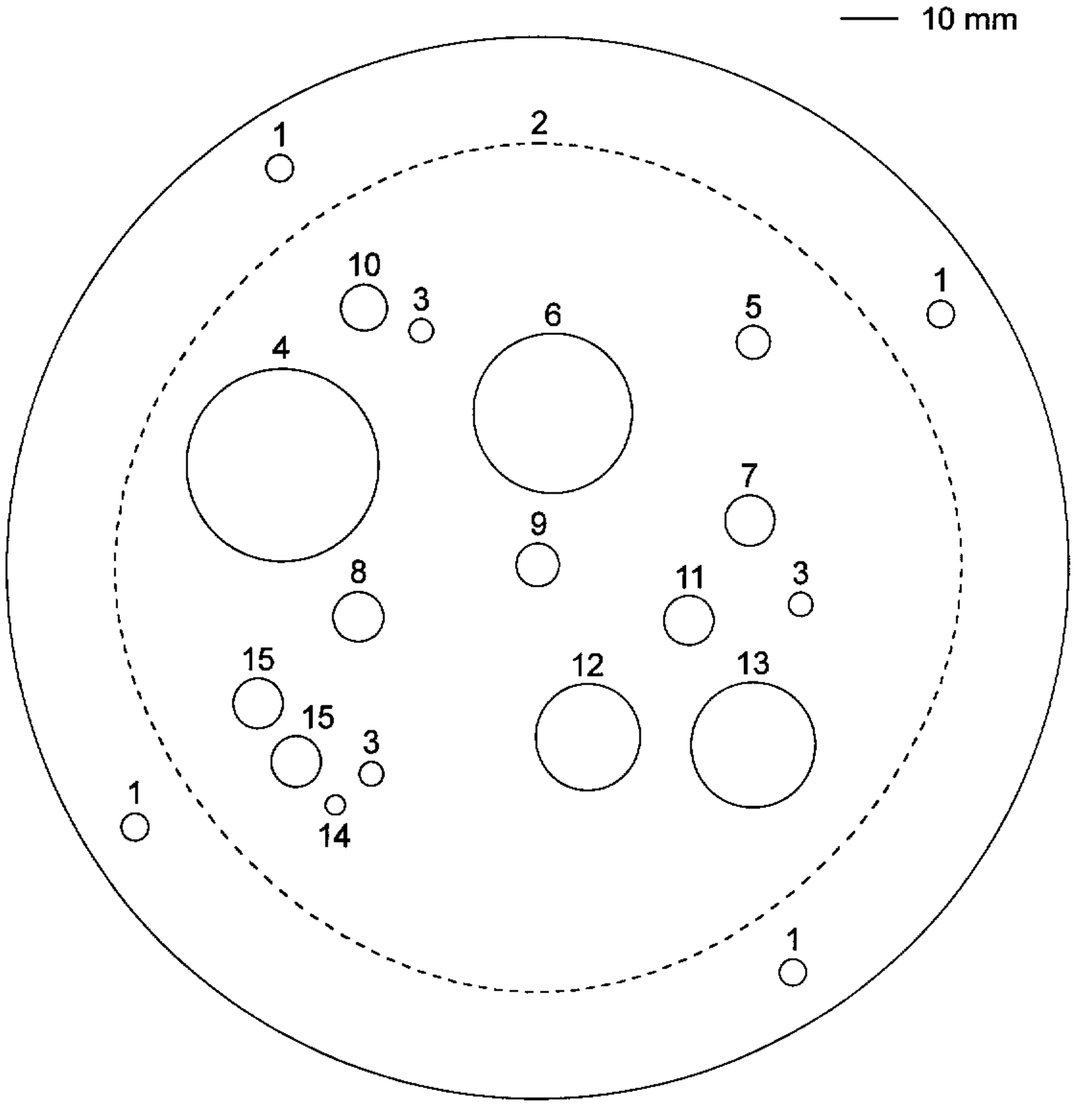

1	Fixing to secure lid to reactor vessel, 5.0 mm.
2	Groove on underside of lid for O-ring seal, 160 mm.
3	Draft tube support shafts, 4.5 mm.
4	pH electrode/conductivity sensor, 34.0 mm.
5	Temperature compensation probe for pH, 6.5 mm.
6	Immersion heater, 29.0 mm.
7	Product return, 7/16" UNF.
8	Ore slurry input, 7/16" UNF.
9	Impeller shaft, 9.0 mm.
10	Temperature probe, 9.0 mm.
11	Acid input, 7/16" UNF.
12	Liquor level sensing electrode, 1/2" BSP.
13	Dual-surface condenser, 23.0 mm.
14	Product removal, 3.5 mm.
15	Spare port, 7/16" UNF.

Figure 9.1: Plan view, dimensional drawing of the reactor vessel lid.

As mentioned in Section 4.2.2 the draft tube is suspended from the lid by three, 316 stainless steel support shafts through the three ports labelled 3, in Figure 9.1. The shafts are 4 mm in diameter and are threaded (4 mm metric thread) and fitted with 316 stainless steel-nylon lock nuts and washers on both sides of the lid.

The pH electrode and the conductivity sensor share the same port in the lid, hole number 4 in Figure 9.1, and only one can be used at any time. The conductivity sensor simply screws (3/4" BSP thread) into the stainless steel fitting that is welded to the underside of the lid and seals onto an O-ring. When the pH electrode is to be used, a polypropylene insert is screwed into the conductivity sensor fitting and the pH electrode, wrapped in Teflon tape to form a seal, is pressed into the insert. Figure 9.2 A shows the fitting and insert in detail.

The temperature compensation probe for the pH transmitter, located in port 5 in Figure 9.1, is secured by a 316 stainless steel fitting that is welded to the top of the lid. Detail of the fitting is shown in Figure 9.2 B. A small stainless steel grub screw (2 mm) is used to secure the shaft of the probe which is wrapped in Teflon tape to create a seal. When pH is not being used to measure acidity and the temperature compensation probe is not in use, a plug is inserted to seal the fitting. Detail of this plug is also shown in Figure 9.2 B.

The immersion heater, located in port number 6 in Figure 9.1, simply presses into the reactor vessel lid. A seal is formed and evaporation prevented by wrapping the shaft of the immersion heater with Teflon tape where it fits into the lid.

The product return tubing (Masterflex - Norprene peristaltic pump tubing, size 17, 6.4 mm internal diameter) enters the reactor vessel via a 316 stainless steel fitting shown in detail in Figure 9.2 C.

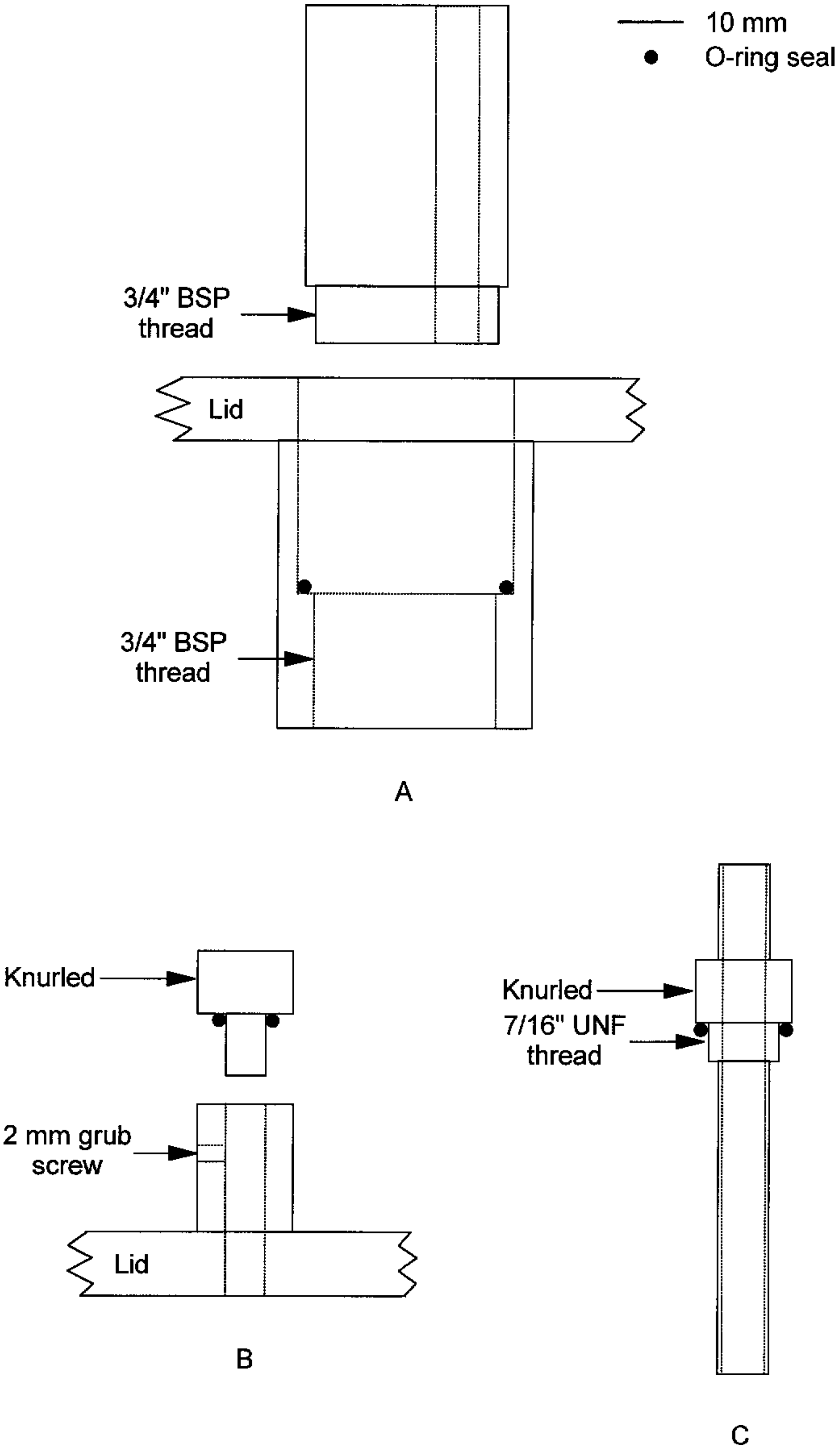

Figure 9.2 A-C: Cross-sectional view, dimensional drawings of the fittings for the reactor vessel lid.

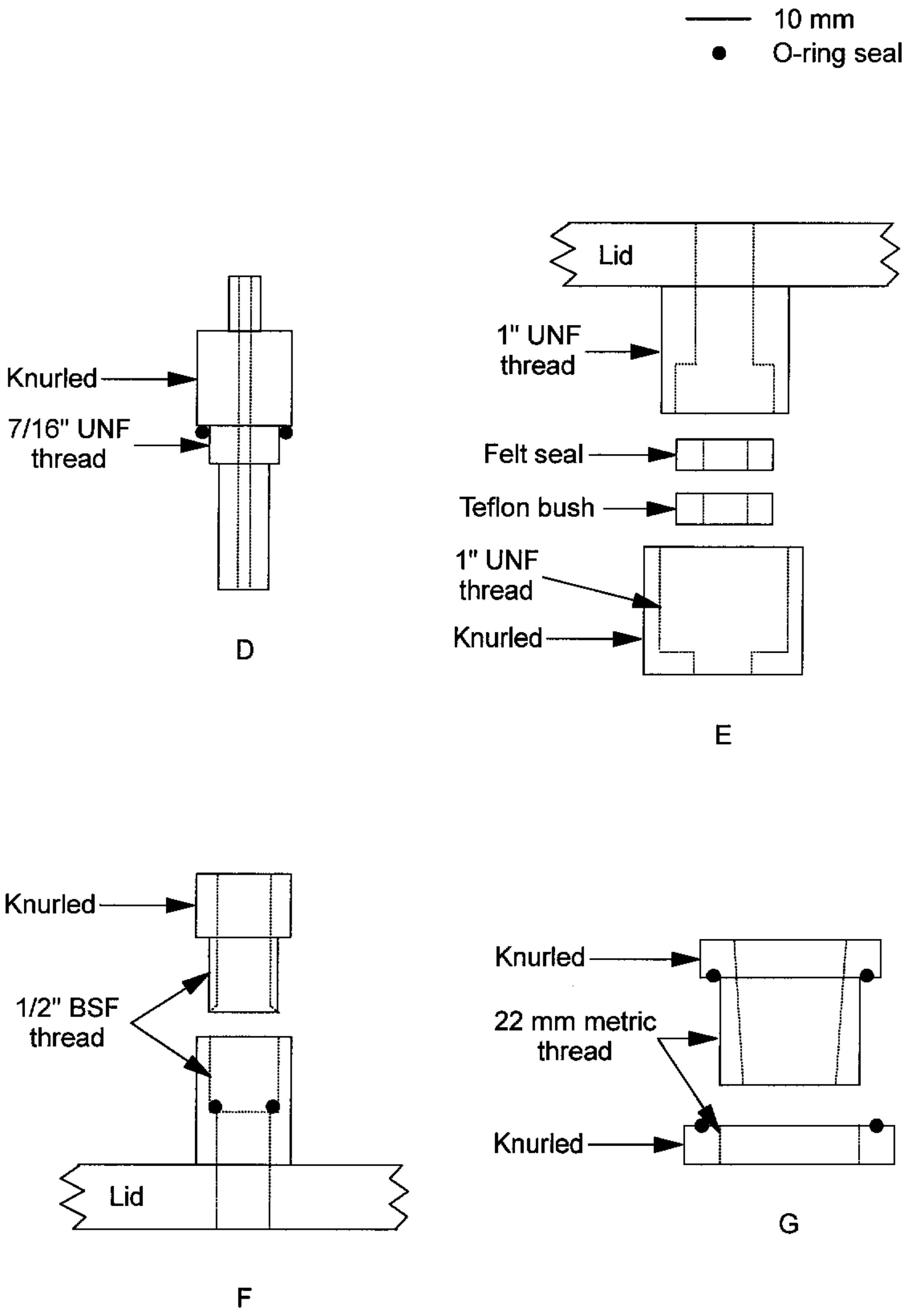

Figure 9.2 D-G: Cross-sectional view, dimensional drawings of the fittings for the reactor vessel lid.

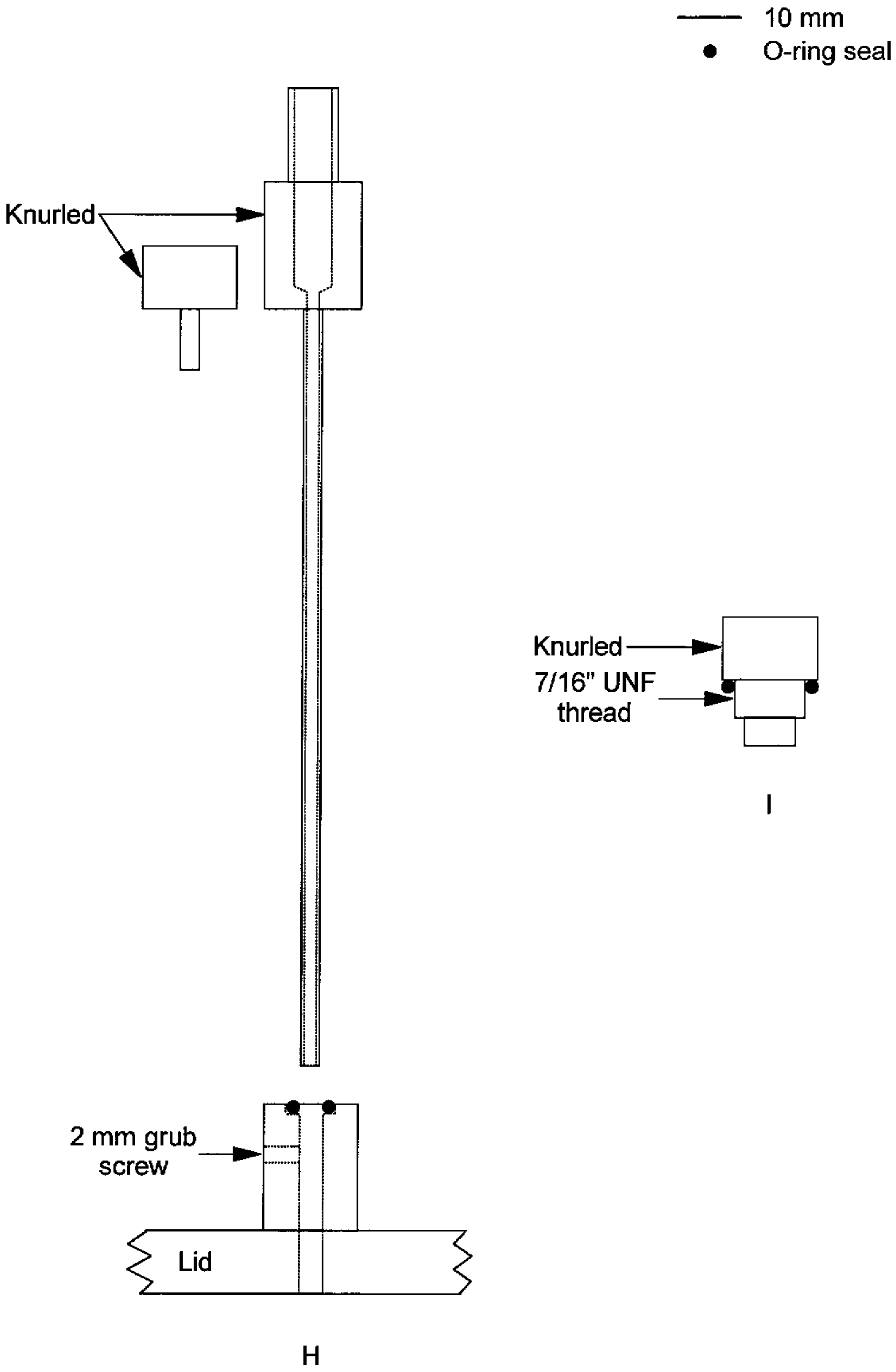

Figure 9.2 H-I: Cross-sectional view, dimensional drawings of the fittings for the reactor vessel lid.

The peristaltic pump tubing fits tightly over the fitting while the fitting itself screws (7/16" UNF thread) into the lid, port 7 in Figure 9.1, and a seal is formed by the O-ring.

The Ore slurry and Cell room spent electrolyte reagents feed into the reactor vessel through ports 8 and 11, respectively, in Figure 9.1. The peristaltic pump tubing (Masterflex - Norprene peristaltic pump tubing, size 14, 1.6 mm internal diameter) used to deliver the reagents, fits over the end of a Teflon fitting that itself screws (7/16" UNF thread) into the lid and is sealed by an O-ring. Detail of the fitting is shown in Figure 9.2 D. Teflon was used for these two fittings as the Cell room spent electrolyte, containing concentrated sulfuric acid, was found to corrode earlier fittings manufactured from 316 stainless steel. This was due to the lid and its fittings reaching a temperature close to that of the reactor vessel itself.

A stuffing box is used to seal the impeller shaft within the lid and uses a Teflon bush to compress a felt washer to create the seal. A diagram showing greater detail of the stuffing box is shown in Figure 9.2 E. The stuffing box is welded to the underside of the lid. Both the Teflon bush and felt washer fit tightly on the rotating impeller shaft and therefore wear out regularly, requiring replacement after each experiment.

The temperature probe, located in port 10 in Figure 9.1, is secured by a 316 stainless steel fitting that is welded to the top of the lid. This fitting is shown in detail in Figure 9.2 F and uses a screw down section to compress an O-ring around the shaft of the temperature probe to form a seal. Due to the mass of the temperature transmitter mounted on top of the temperature probe shaft, a boss head clamp is also required to secure the temperature probe and transmitter.

The liquor level sensing electrode, port 12 in Figure 9.1, screws (1/2" BSP thread) into the lid and seals using a silicone rubber washer.

The dual-surface condenser is connected to the reactor vessel lid using a polypropylene fitting, port 13 in Figure 9.1. The fitting is threaded (22 mm metric thread) and is secured to the lid by means of a nut on the underside of the lid, detail of both are shown in Figure 9.2 G. The fitting and the nut contain O-rings for sealing. The lower ground glass joint (Quickfit 19/26) of the condenser is wrapped in Teflon tape and firmly pressed into the tapered fitting, with the outside of the joint also being wrapped in Teflon tape. Polypropylene was used for this fitting as it is much softer than stainless steel and is therefore more compatible with a glass fitting.

Product removal, port 14 in Figure 9.1, is through a fitting shown in detail in Figure 9.2 H. Peristaltic pump tubing (Masterflex - Norprene peristaltic pump tubing, size 17, 6.4 mm internal diameter) fits tightly over the top of the fitting while another fitting welded to the top of the lid uses a grub screw to secure the fitting and an O-ring to seal it. The narrow tubing allows for a very high product removal velocity. When the crystalliser is being operated in batch mode and product removal is not needed, the plug shown in Figure 9.2 H is used to seal the fitting. All fittings used for product removal are manufactured from 316 stainless steel.

Two spare ports, labelled 15 in Figure 9.1, are sealed by a solid threaded (7/16" UNF thread) plug, manufactured from 316 stainless steel, that screws into the lid and uses an O-ring to produce a seal. Detail of these plugs are shown in Figure 9.2 I. These ports are used for observation at present, but maybe used in future for extra reagent addition points.

9.3.2 Electronic components of the crystalliser

The basic electronic components of the crystalliser are shown in Figure 4.2, the schematic diagram and Figure 4.1, the photograph of the crystalliser.

The Control computer is a 486 IBM© compatible personal computer with 32 MB of random access memory, a 250 MB hard disc and a clock speed of 25 MHz. Installed in the Control computer is a Computer Boards Incorporated CIO-DAS1600/16 data acquisition board which has 16 high speed-16 bit analog input channels, two-12 bit analog output channels, 32 digital input/outputs and three-16 bit counters.

The data acquisition board in the Control computer is connected by a DB37 ribbon cable to a Computer Boards Incorporated CIO Mini 37 screw terminal board housed in the Transfer box, which is a diecast aluminium alloy enclosure measuring 250 x 250 x 100 mm. All electrical connections to the Control computer are made through the screw terminal board. Table 9.2 describes the pin allocations for the data acquisition board.

Table 9.2: DB37 pin allocations for the Computer Boards Incorporated CIO-DAS1600/16 data acquisition board. Those pins not shown are not used with this setup.

Pin Number	Signal	Value	Allocation
3	DIG OUT CH3	TTL	Product pump cw/ccw
4	DIG OUT CH1	TTL	Product pump on/off
7	GND	0 VDC (earth)	Product pump cw/ccw Product pump on/off Immersion heater on/off Product removal valve on/off Liquor level high/low Acid pump on/speed/off Acid flow rate Ore slurry pump on/speed/off Ore slurry flow rate
9	DAC CH0	10 VDC	Acid pump on/speed/off
19	LLGND	0 VDC (earth)	pH
22	DIG OUT CH2	TTL	Product removal valve on/off
23	DIG OUT CH0	TTL	Immersion heater on/off
25	DIG IN CH0	TTL	Liquor level high/low
27	DAC CH1	10 VDC	Ore slurry pump on/speed/off
28	LLGND	0 VDC (earth)	Conductivity
29	LLGND	0 VDC (earth)	Temperature
33	ADC CH4	10 VDC	Conductivity
34	ADC CH3	5 VDC	Ore slurry flow rate
35	ADC CH2	5 VDC	Acid flow rate
36	ADC CH1	10 VDC	Temperature
37	ADC CH0	10 VDC	pH

A full wiring diagram for the crystalliser is shown in Figure 9.3. A description of the individual components follows this, in the order they appear in Figure 9.3.

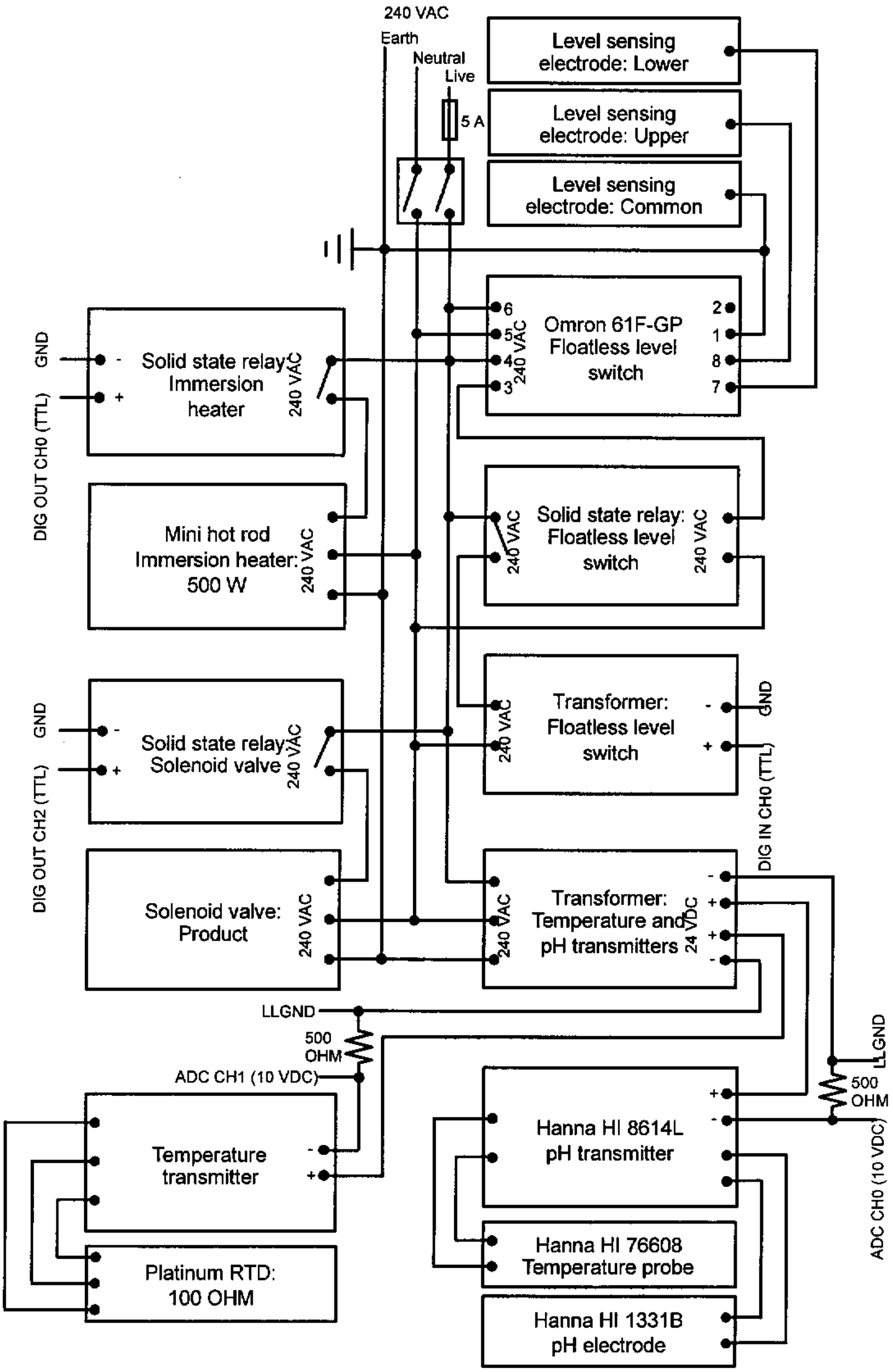

Figure 9.3 Wiring diagram for the continuous crystalliser.

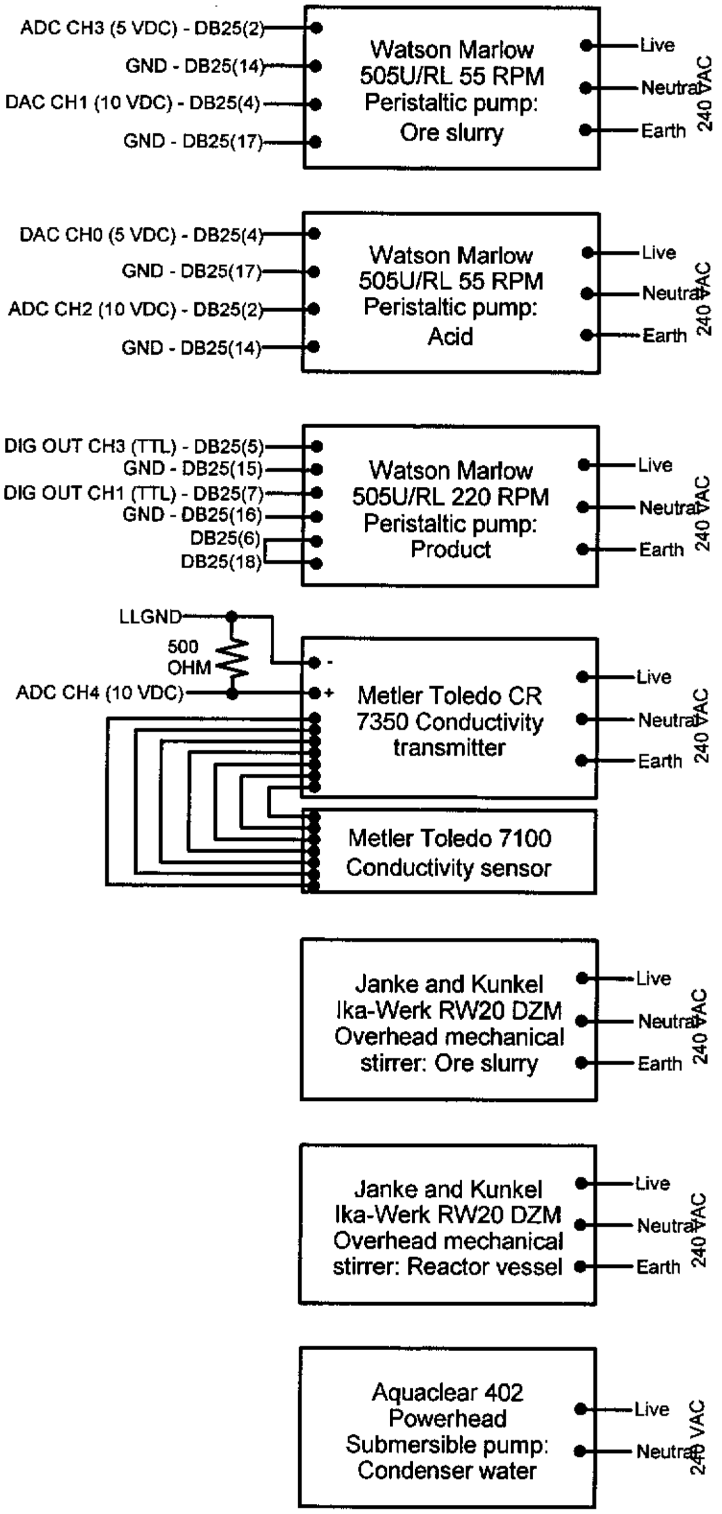

Figure 9.3 Wiring diagram for the continuous crystalliser.

Mains power, 240 Volt alternating current (VAC), enters the Transfer box with a 5 Amp (A) Slow-blow fuse on the live wire, while an illuminated rocker switch is used to switch the power supply. The earth wire is grounded to the Transfer box itself.

An Omron 61F-GP Floatless level switch is housed in the Transfer box and operates on 240 VAC power. Connected to this by a jack plug in the bottom of the Transfer box are the three, 316 stainless steel, Level sensing electrodes which are contained in a single housing that screws into the reactor vessel lid. When the liquor in the reactor vessel reaches the upper Level sensing electrode a 240 VAC signal is sent from the Floatless level switch through the Solid state relay (240 VAC/240 VAC) to the Transformer (Arlec 240 VAC/TTL) where it is reduced to a TTL signal suitable for the Control computer. The Solid state relay is needed to remove a massive voltage spike that disrupts the electrical system when the Floatless level switch becomes energised. When the liquor in the reactor vessel falls below the Lower level sensing electrode the circuit becomes de-energised and the Transformer TTL output returns to zero.

A solid state relay (TTL/240 VAC) that is energised by the Control computer is located in the Transfer box and is used to switch power to the immersion heater. The 500 W Mini hot rod immersion heater is manufactured from vitrisol glass and is 200 mm long. It is connected to the solid state relay by a domestic three-pin plug and socket that is located on the bottom of the Transfer box.

Another solid state relay (TTL/240 VAC) that is energised by the Control computer is installed in the Transfer box and is used to switch the Solenoid valve for product removal. The solenoid valve is a three-way 316 stainless steel unit that is switched using 240 VAC power and is connected to the solid state relay in the same way as the immersion heater.

A transformer (240 VAC/24 VDC x 2 channel) is housed in the Transfer box and supplies both the temperature and pH transmitters with 24 VDC power.

The industrial style temperature transmitter is mounted inside a plastic enclosure fixed to the top of the temperature probe and operates on 24 VDC while transmitting a 4 to 20 mA signal proportional to the temperature. The temperature probe consists of a Platinum RTD (100 Ω) mounted in a Teflon coated 316 stainless steel tube 8.5 mm in diameter and 300 mm long. The transmitter with attached probe is connected to the transformer in the Transfer box through a jack plug in the bottom of the Transfer box. The inclusion of a 500 Ω precision wire wound resistor in the negative wire forces the current loop to become a voltage loop (2-10 VDC) which is proportional to the temperature and is logged by the Control computer.

The pH transmitter is from Hana Instruments, model HI8614L with a digital display and operates on 24 VDC while transmitting a 4 to 20 mA signal proportional to the pH. It is hard-wired to the Transfer box and the use of a 500 Ω precision wire wound resistor allows the 2 to 10 VDC signal to be logged to the Control computer in the same fashion as that from the temperature transmitter. A Hana Instruments HI1331B glass, liquid filled pH electrode is used. The temperature compensation probe was reconstructed from a Hana Instruments HI76608 probe inserted into a Teflon coated 316 stainless steel tube 6 mm in diameter and 250 mm in length. These two probes are connected to the transmitter using BNC connectors.

The three peristaltic pumps were supplied by Watson Marlow and are 505U/RL models. The pumps are controlled either manually or with digital (TTL) remote control of stop/start and direction, analog (0 to 10 VDC) remote control of pump speed and analog output (0 to 5 VDC) of pump speed. Table 9.3 shows the DB25 pin allocations for the pumps, each of which are connected to the Transfer box by individual DB25 ribbon cables. The Ore slurry and Acid pumps have a maximum speed of 55 rpm while that of the Product pump is 220 rpm. The Ore slurry and Acid pumps are configured to receive On/speed/off control from the Control computer while the pump speed is logged to the computer. The Product pump is configured to receive

On/off and Cw/ccw (clockwise/counter clockwise) control from the Control computer while pump speed is set manually.

Table 9.3: DB25 pin allocations for the Watson Marlow 505U/RL 55/220 rpm peristaltic pump. Those pins not shown are not used in the current setup.

Pin Number	Signal	Value	Allocation
2	Output	5 VDC	Flow rate
4	Input	10 VDC	On/speed/off
5	Input	TTL	Cw/ccw
6	Link	NA	Cw/ccw
7	Input	TTL	On/off
14	Output	0 VDC (earth)	Flow rate
15	Input	0 VDC (earth)	Cw/ccw
16	Input	0 VDC (earth)	On/off
17	Output	0 VDC (earth)	On/speed/off
18	Link	NA	Cw/ccw

The conductivity transmitter is a Metler Toledo model CR7350 with digital display and transmits the conductivity signal as a 4 to 20 mA signal. As with the other two transmitters, a 500 Ω precision wire wound resistor is used to convert the current loop into a 2 to 10 VDC signal proportional to the conductivity that is logged by the Control computer. The conductivity transmitter is hard-wired to the Transfer box but operates on a separate 240 VAC power supply. The conductivity sensor is a Metler Toledo model 7100 that is connected to the transmitter by a jack plug.

The two overhead mechanical stirrers are Janke and Kunkel Ika-Werk model RW20 DZM with digital display of the speed, which is variable between 60 and 2000 rpm. The first stirrer is used to agitate the ore slurry, while the second is used to agitate the reactor vessel. Neither of the stirrers are connected to the control computer and both operate on 240 VAC power.

An Aquaclear 402 Powerhead submersible pump is used to circulate cooling water through the condenser, attached to the reactor vessel. The pump, rated at 1000 L h^{-1} with no head pressure, operates on 240 VAC independently of the Control computer.

9.3.3 Control software for the crystalliser

The software used on the Control computer to run the continuous crystalliser is Labtech Notebook Pro for Windows, version 8.1, a general purpose data acquisition and control package which is quite powerful and simple to use (Ozkul, 1996). The software is graphically programmed by constructing a flow chart from the various function blocks available to execute the individual steps required to control each stage of the process. A diagram of the software program used to control the continuous crystalliser is shown in Figure 9.4. Each individual step is represented by a function block in the program. This program is used to control the crystalliser and also log the operating conditions to a file and print them to a printer in real-time. This enables unattended operation, allows for the operating conditions to be checked for consistency throughout the experiment and provides a permanent electronic record. The program can be broken down into seven separate operations designated 1 to 7 in Figure 9.4, each of which will be discussed in turn.

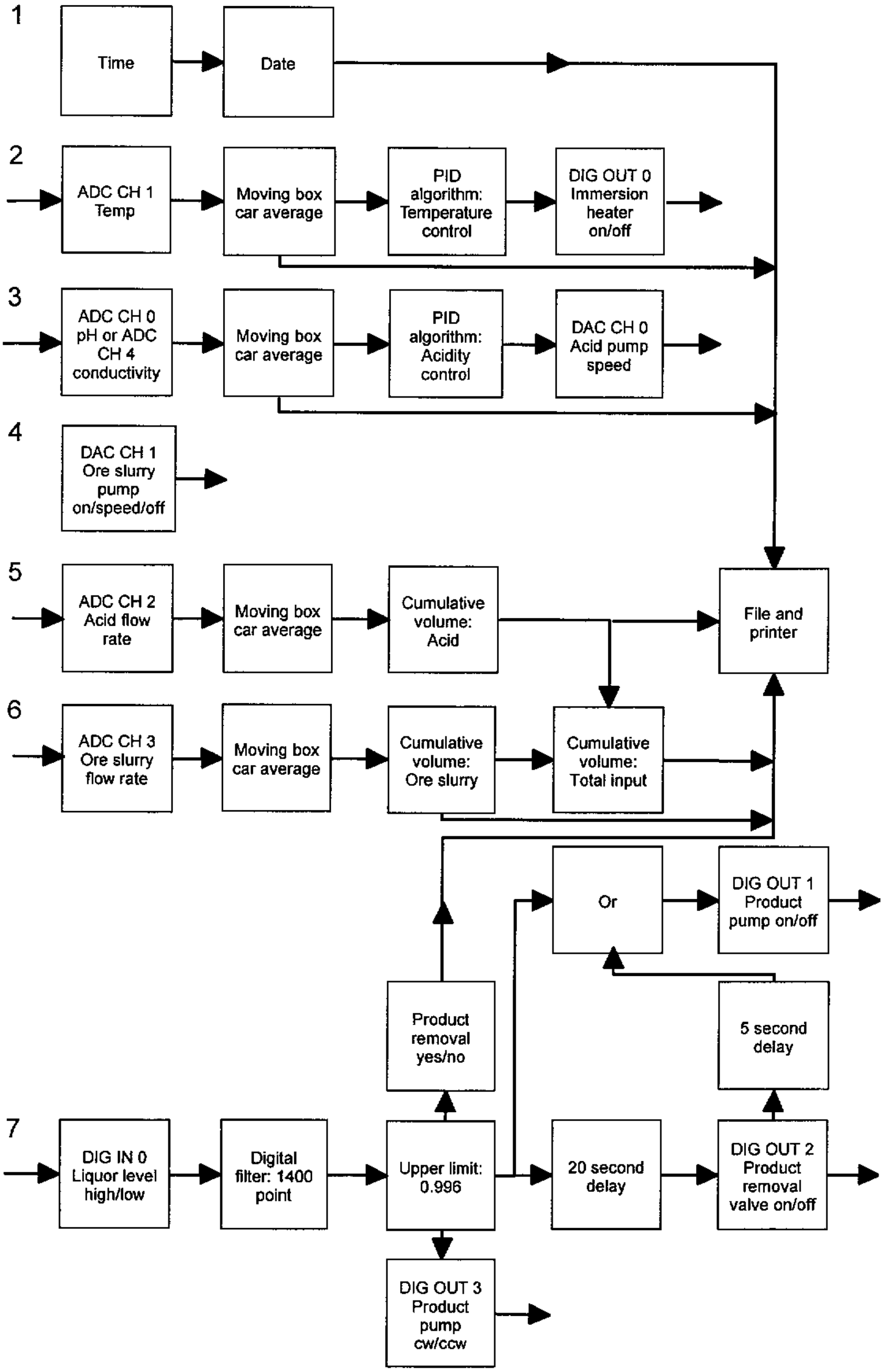

Figure 9.4: Schematic diagram of the software program used to control the continuous crystalliser.

Operation 1 writes the time and the date to the printer and the log file. This is achieved by using two Time blocks, the first configured to output time in 24 hour format and the second configured to output the date. Both of these Time blocks are written to the Log block and printer at 0.0028 Hz *ie.* approximately at six minute intervals. This is necessary to cross check the operating conditions at a particular time during the progress of the experiment or after it has finished.

The writing of all data to the Log file and printer in the following operations is done so via an X arithmetic block sampling at 0.0028 Hz. These blocks simply transfer information, and are necessary as the data blocks are operating at higher frequencies than the Log blocks which only log at the frequency to which they are written, not to a desired frequency.

Operation 2 controls the operating temperature of the crystalliser. The temperature signal is read in as a 2-10 VDC signal at 50 Hz using an Analog input block. The signal is transferred to a Moving average block, also sampling at 50 Hz, where a moving box car average is performed with a box size of 50. This eliminates most of the noise from the signal. A linear function is applied (scale = 12.51 and offset = -24.19) to the signal to convert the voltage to a temperature. The Moving average block is sampled by a Transfer block, at 0.0028 Hz, which writes the temperature to the Log block, the printer and also a PID block, at 1 Hz. The PID block uses a closed loop Proportional, Integral and Derivative algorithm ($P = 0.02$, $I = 1.90\times10^{-4}$ and $D = 3.19$) to determine when to switch on the Immersion heater to maintain the set-point temperature, which is defined in this block. A Digital output block, operating at 1 Hz, samples the PID block and outputs a TTL signal to switch on and off the Immersion heater. This block is needed as the PID block has an analog output function only.

Operation 3 controls the acidity of the crystalliser, measured as pH or conductivity. In the same fashion as Operation 2, the pH or conductivity is inputed as a 2-10 VDC signal using an Analog input block. This voltage is averaged to reduce noise and scaled to convert to a pH value (scale = 1.78

and offset = -3.79) or a conductivity (scale = 63.23 and offset = 133.13, units of mS cm^{-1}) using a Moving average block. Once again a PID block is used, this time to determine when to switch on and off and how fast to run the Acid pump. If pH control is used, the PID values used are 2.50×10^3, 1.00×10^{-8} and 0.00, respectively and if conductivity control is used the values are 500, 1.00×10^{-3} and 0.00, respectively. The PID block outputs a 0-10 VDC analog signal directly to the pump. At 0 VDC the pump is switched off. Above 0 VDC the pump is switched on with its speed being proportional to the voltage supplied with maximum speed being at 10 VDC. The set-point pH or conductivity can be altered by keyboard input while the program is running via a link to a Microsoft Excel© file.

Operation 4 sets the flow rate for the Ore slurry pump. An Analog output block operating at 1 Hz reads a voltage, ASCII real value, from a file and outputs this directly to the Ore slurry pump. The voltage corresponds to a pump speed which in turn corresponds to a known ore slurry flow rate. This function allows for the ore slurry flow rate to be altered in any way necessary throughout the experiment.

Operation 5 is used to measure the total volume of Spent electrolyte dosed into the crystalliser. The speed of the Acid pump is inputted as a 0-5 VDC signal using an Analog input block sampling at 50 Hz. As with Operations 2 and 3 the Analog input block is sampled by a Moving average block to reduce noise and linearly convert the signal to a flow rate (mL min^{-1}), scale = 5.12 and offset = -0.49. An Integral block, operating at 50 Hz, samples the Moving average block, sums all previous values and applies a scale factor of 3.33×10^{-4} to produce the cumulative volume (mL) of acid dosed into the crystalliser, which is written to the Log file and printer at 0.0028 Hz.

Operation 6 works in exactly the same manner as Operation 5 to determine the cumulative volume of ore slurry dosed into the crystalliser. In this case the Moving average block has scale and offset values of 4.75 and -0.38, respectively. The cumulative volume of ore slurry is written to the Log file and printer and also to an X + Y arithmetic block where it is combined with the cumulative volume of acid to give the total cumulative volume of reagents dosed to the crystalliser.

The final operation, number 7, is used to activate the Product pump when the reactor vessel is full. A Digital input block, sampling at 1 Hz, as are all blocks in this particular operation, reads the TTL signal from the Liquor level sensing electrode. A 1400 point Digital filter block is used to dampen the signal and prevent premature product removal caused by liquor splashing onto the electrode and falsely activating the cycle. The filter must be activated for 1400 seconds, approximately 23 minutes, before the next block is activated. This is an Upper limit block set at 0.996 and is used to prevent the product removal circuit prematurely switching off the same way that the Digital filter is used to prevent premature activation of the circuit. Four blocks are simultaneously sampled by the Upper limit block, the first is a Programmable block that records when product removal is taking place and writes this information to the file and printer. The second is a Digital output block that changes the direction of the Product pump from counter clockwise to clockwise. The third is a boolean Or block which feeds into a Digital output block that switches on and off the Product pump. The fourth block sampled by the Upper limit block is a Lag block with a delay time of 20 seconds. This block, which is used to allow the liquor in the Product loop to homogenise with that in the reactor, then feeds into another Digital output block which opens and closes the Product removal valve to enable product removal. This block is sampled by another Lag block, this time with a five second delay, which in turn is sampled by the aforementioned Or block. The Or block ensures that the Product pump remains switched on when either or both the Upper limit block or the five second Lag block are active.

9.3.4 Characterisation of the mixing and product removal conditions in the reactor vessel

A series of Wash-out tests (Harnby, Edwards and Nienow, 1992; Nyvlt, 1982a) were carried out to characterise the mixing and product removal conditions in the crystalliser itself. Three sets of conditions were defined for this project; mixed suspension mixed product removal (MSMPR), mixed suspension classified product removal (MSCPR) and classified suspension classified product removal (CSCPR).

The wash-out tests involve removing a sample of product slurry from the crystalliser and determining the solids loading of both the sample and the remaining contents of the crystalliser. The Steady state separation coefficient, K, is simply the ratio of these two solids loadings. Obviously a K value of 1 indicates the sample has the same solids loading as the crystalliser contents. By analysing the PSDs of the product sample and the crystalliser contents it is possible to determine when isokinetic withdrawal has been achieved. This satisfies one of, and the most difficult to achieve, requirements for MSMPR operation.

The two classified conditions were chosen to simulate the operating conditions used by Pasminco in their pilot plant trials, while the MSMPR conditions were chosen as a benchmark to investigate the effect of mixing and product removal conditions on the precipitation of silica.

In this instance, a slurry of Ballotini impact spheres in water was used for the wash-out tests. These spheres were chosen as they are made of amorphous silica and hence closely represent the actual precipitate to be produced in the crystalliser in terms of morphology and density. Equal masses of two size fractions (37 to 45 and 90 to 106 μm) of Ballotini impact spheres were mixed together to produce a slurry with a solids loading of approximately 40 g L^{-1}. The water was weighed as this is more accurate than using a measuring cylinder. Hence, solids loadings were actually determined as g kg^{-1} of water and not g L^{-1}. Once again, these conditions were chosen based upon information supplied by Pasminco. The particle size fractions were chosen with regard to the sieve sizes available. Although it is expected to produce particles smaller than the size range used for characterisation of the reactor vessel, a smaller size fraction was not chosen as it was considered harder to achieve isokinetic withdrawal with larger particle sizes. A slurry sample of about 100 mL was taken from the crystalliser using the product pump and loop and collected in a 100 mL measuring cylinder. The sample was then weighed, filtered through a 0.45 μm membrane and dried in an oven at 110°C. A similar volume of water to that which was removed as the sample was accurately weighed and placed into the crystalliser to approximately maintain the original volume. It would be undesirable for the volume to drop significantly, as this would change the mixing and product removal conditions. It would be drastic if the volume dropped below the top of the draft tube as slurry circulation would stop altogether. After the variable of interest had been changed, a further slurry sample was taken and the process repeated. Up to ten samples were taken before the process was stopped and the slurry filtered, dried and weighed. The dry samples were then weighed. From the initial masses of spheres and water, the mass of the sample, the mass of spheres in the sample and the mass of water added to the crystalliser, the Steady state separation coefficient can be determined. An example calculation is outlined below.

Initial mass of water in reactor (g)	= 2137.04
Initial mass of silica in reactor (g)	= 81.15
Sample mass (g)	= 94.91
Mass of silica in sample (g)	= 3.41
Mass of water in sample (g)	94.91 - 3.41 = 91.50
Sample solids loading (g kg^{-1} of H_2O)	3.41 / (91.50 / 1000) = 37.27
Initial tank solids loading (g kg^{-1} of H_2O)	81.15 / (2137.04 / 1000) = 37.97
Final tank solids loading (g kg^{-1} of H_2O)	(81.15 - 3.41) / ((2137.04 - 91.50) / 1000) = 38.00
Mass of water added to reactor (g)	= 89.42
Final mass of water in reactor (g)	2137.04 - 91.50 + 89.42 = 2134.96
Final mass of silica in reactor (g)	81.15 - 3.41 = 77.74
Steady state separation coefficient (K)	37.27 / ((37.97 + 38.00) / 2) = 0.981

Wash-out tests were used to determine the optimum height of the draft tube in the crystalliser required to provide the minimum stirring speed for homogeneous solids suspension. The results of this work are shown as a graph in Figure 9.5.

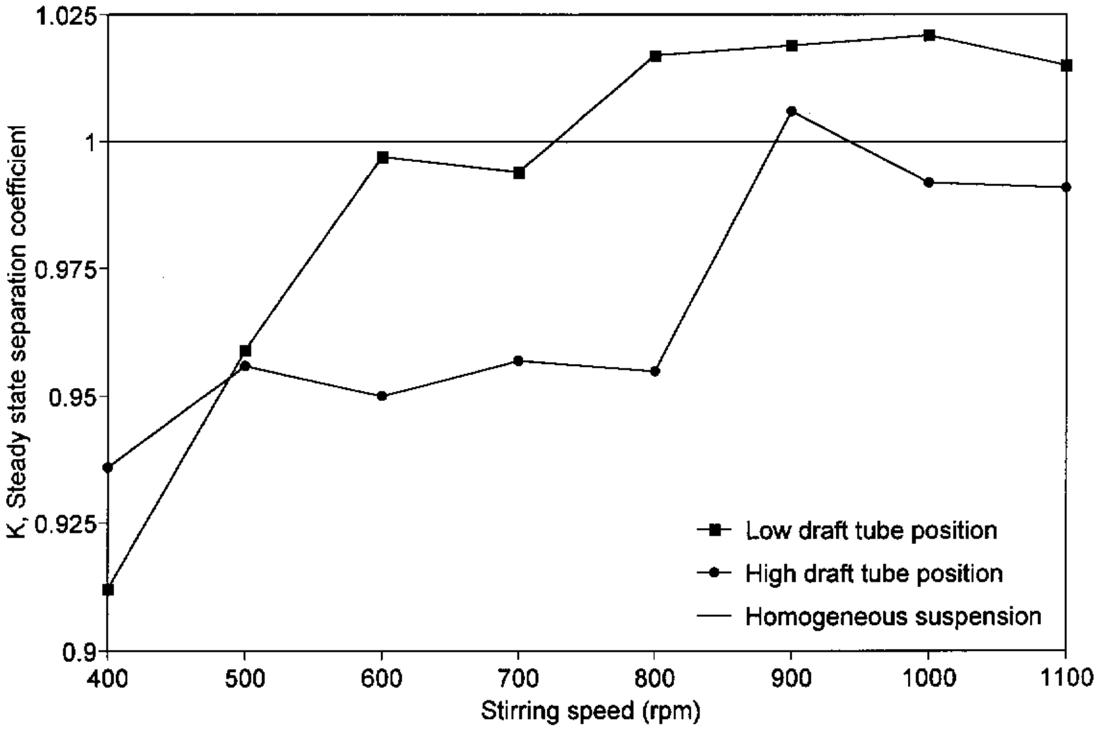

Figure 9.5: Steady state separation coefficient, K, versus stirring speed, showing minimum stirring speed for homogeneous suspension. Highest and lowest draft tube positions shown.

Of the six different draft tube positions trialed, two are represented in Figure 9.5. The high draft tube position represents the location in the crystalliser of the draft tube where the highest minimum stirring speed for homogeneous suspension was located. Similarly, the low draft tube position is where the lowest minimum stirring speed for homogeneous suspension is located. From the graph it is clear that the two draft tube positions provide minimum stirring speeds of 600 and 900 rpm for the low and high positions, respectively.

Further wash-out tests were carried out to determine the optimum location and depth of the product tube and also the speed of the product pump for the low draft tube position. This series of wash-out tests used K as a quality parameter as well as the PSD of the slurry. By determining K and comparing the distribution of the size fractions with that of the crystalliser contents, it was possible to achieve isokinetic product withdrawal, and hence MSMPR conditions. The optimum location of the product tube is clearly shown in

Figure 9.1, while the optimum length of the product tube is 120 mm, as shown in Figure 9.2 H, which defines the depth at which product withdrawal occurs. The speed of the product pump to achieve isokinetic product withdrawal was determined to be 175 rpm. These conditions were tested for reproducability by another wash-out test consisting of five replicate samples, these results are plotted in Figure 9.6. It was previously specified, that the initial slurry for the wash-out tests contained equal masses of the two particle size ranges 37 to 45 and 90 to 106 μm. However, Figure 9.6 and the following two figures concerning wash-out tests, show three particle size fractions in both the reactor and the samples. It is thought that the Ballotini impact spheres were in an agglomerated state when they were sieved into the two particle size ranges and then became dispersed to form the three particle size ranges upon mixing with water and agitation during the wash-out test. It is thought that the differences in the ratios of the three particle size fractions between the wash-out tests will not seriously affect their outcomes when compared with each other.

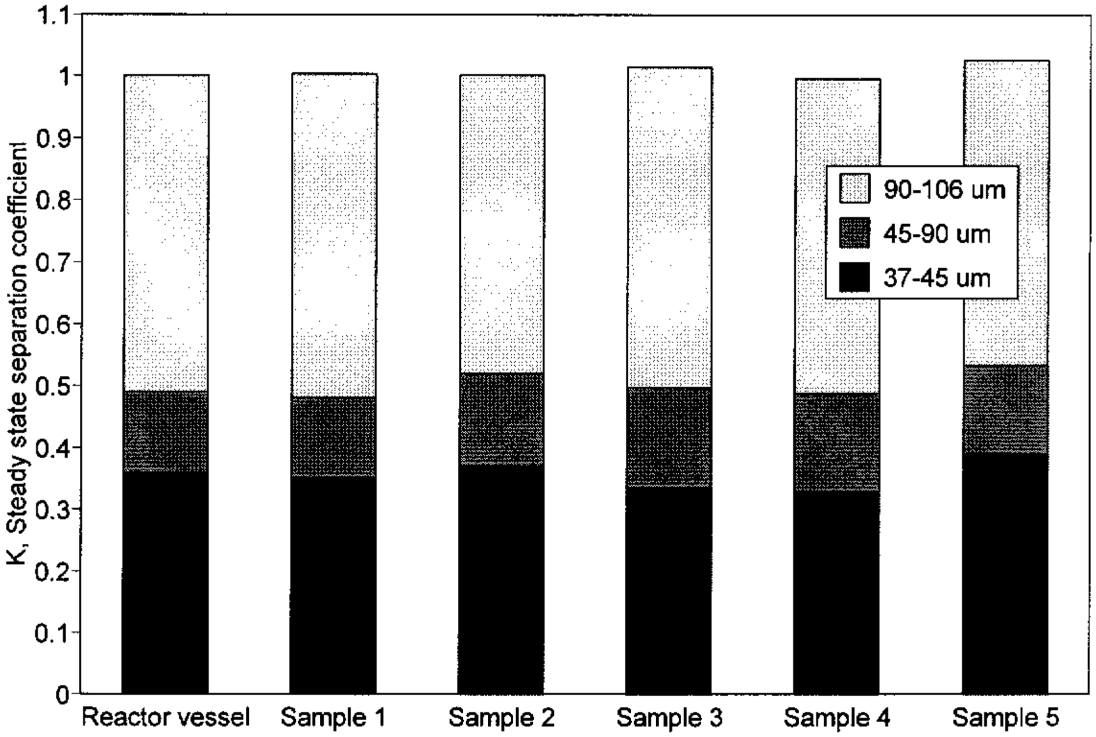

Figure 9.6: Verification of isokinetic product withdrawal and MSMPR conditions. Steady state separation coefficient, K, versus crystalliser contents and sample replicate number. PSD is also displayed.

The two other mixing and product removal arrangements used for this project were a simple change from MSMPR conditions and required far fewer wash-out tests to achieve. MSCPR conditions, as the acronym suggests, have the same mixing conditions as MSMPR conditions but with classified product removal. The product was classified by reducing the speed of the product pump from 175 to 125 rpm, this resulting in non-isokinetic product withdrawal. The graph in Figure 9.7 shows the product properties: The K values are very close to 1.00 but the particle size fractions have become classified with a smaller proportion of the largest fraction and a larger proportion of the intermediate fraction being removed. Removal of the smallest fraction of the product is representative, and is thus remains essentially the same as with MSMPR conditions.

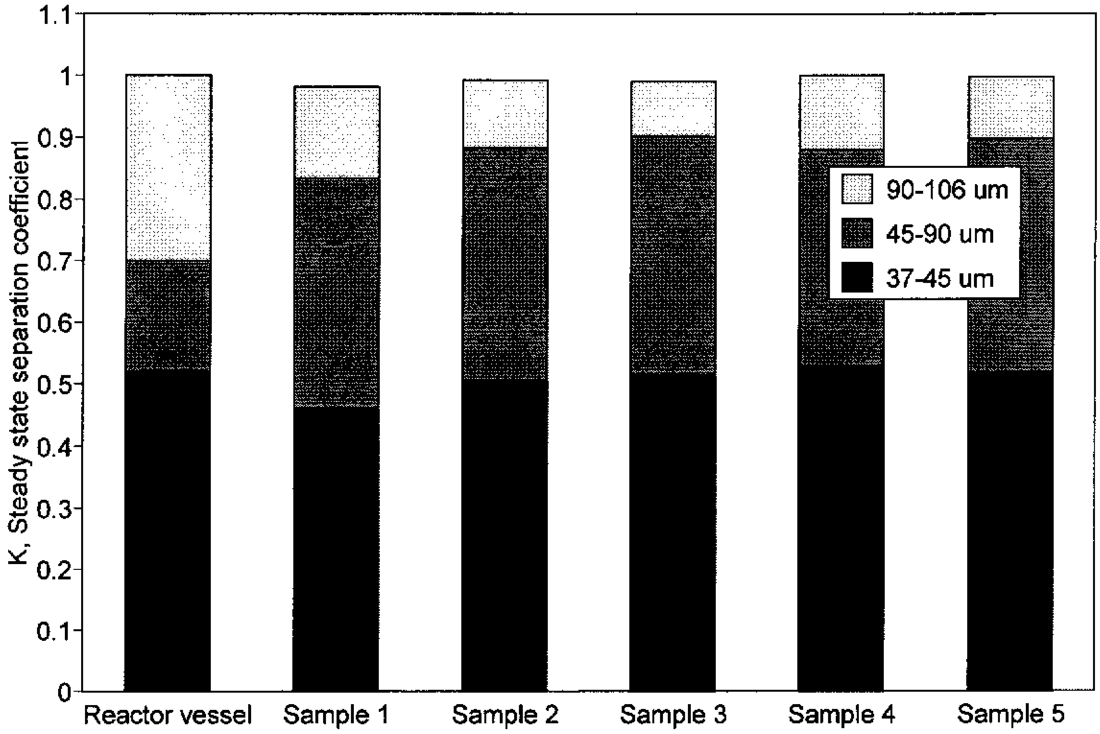

Figure 9.7: Verification of non-isokinetic product withdrawal and MSCPR conditions. Steady state separation coefficient, K, versus crystalliser contents and sample replicate number. PSD is also displayed.

The CSCPR conditions were obtained by slowing the stirring speed in the crystalliser to 200 rpm, well below the minimum stirring speed for homogeneous suspension, and also by further reducing the product pump speed from MSCPR conditions to 50 rpm. Figure 9.8 shows the resulting product properties of a wash-out test with five replicates taken under these conditions. Clearly K has been reduced to approximately 0.10 for the product, while the smallest size fraction almost exclusively makes up the product particle size fraction distribution.

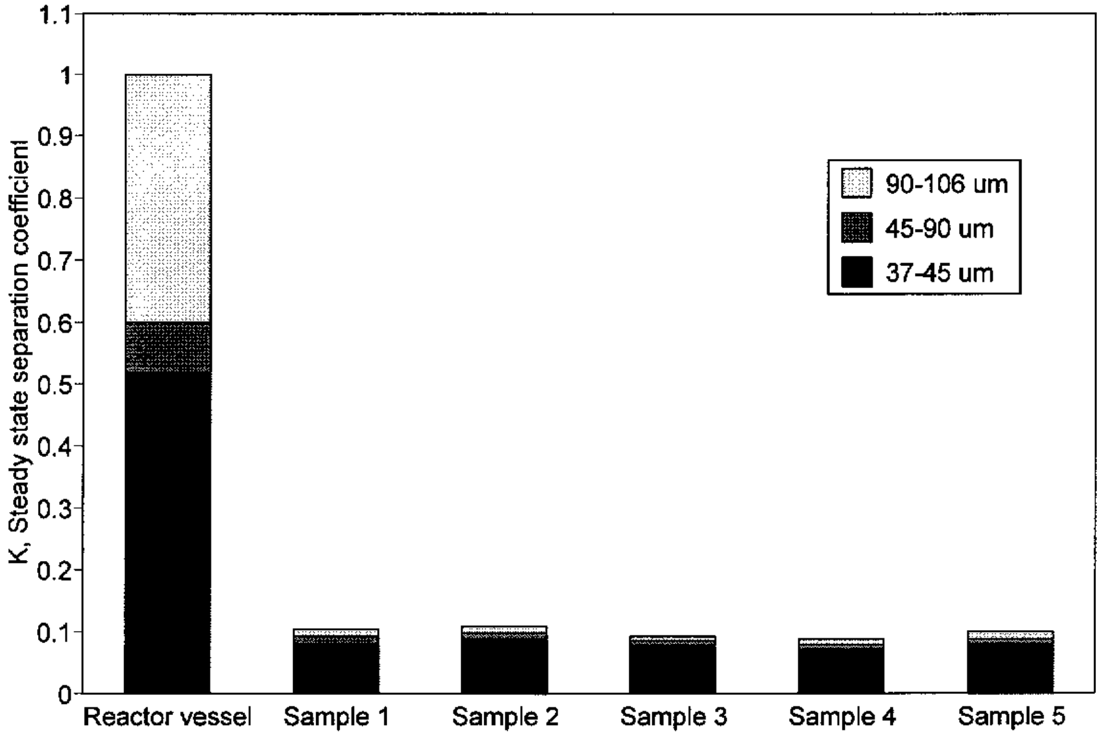

Figure 9.8: Verification of non-isokinetic product withdrawal and CSCPR conditions. Steady state separation coefficient, K, versus crystalliser contents and sample replicate number. PSD is also displayed.

Table 9.4 summarises the three sets of mixing and product removal conditions used in the continuous crystalliser for this project. Well over 100 wash-out tests were carried out to determine these conditions.

Table 9.4: Mixing and product removal conditions used in the continuous crystalliser.

Mixing and Product Removal Condition	Impeller Stirring Speed (rpm)	Product Pump Speed (rpm)
MSMPR	600	175
MSCPR	600	125
CSCPR	200	50